ATOM INTERFEROMETRY IN A TWIN LATTICE

WITH MORE THAN A THOUSAND PHOTON RECOILS

Dissertation zur Erlangung des akademischen Grades
Doktor der Naturwissenschaften (Dr. rer. nat.)
im Fachbereich Physik und Elektrotechnik
der Universität Bremen

vorgelegt von

Martina Gebbe, M.Sc.

Erstgutachter	Prof. Dr. Claus Lämmerzahl
Zweitgutachter	Prof. Dr. Ernst M. Rasel
Tag der Disputation	20. März 2020

Universität Bremen

QUANTUS

ZENTRUM FÜR
ANGEWANDTE RAUMFAHRTTECHNOLOGIE
UND MIKROGRAVITATION

ZARM

ABSTRACT

Atom interferometers represent a well-proven tool for precision measurements and are used for a variety of applications ranging from geodesy and inertial navigation to fundamental questions in physics. State-of-the-art sensors typically operate with laser-cooled atoms, which exhibit a relatively large spatial and momentum width. The systematic uncertainties associated with the latter can be overcome by employing Bose-Einstein condensates (BECs). The sensitivity of an atom interferometer can be enhanced by the interrogation time as well as by a large momentum separation of the atomic wave packets. Hereby, a small atomic velocity width is crucial to achieve high-fidelity manipulation.

Within this thesis, the realization of a novel beam splitter for the transfer of large momentum on an ultra-cold atom cloud is presented. The condensate is generated in a miniaturized atom-chip based setup and its expansion rate is further reduced by delta-kick collimation. The beam splitting light field consists of two counterpropagating lattices with orthogonal polarizations. In such a twin lattice, the efficient combination of double Bragg diffraction with Bloch oscillations promises to overcome current limitations of large momentum transfer. Bloch transfer efficiencies of more than 99.9% per photon recoil ($\hbar k$) can be achieved and, thus, excellent scalability is provided. The symmetry of the twin lattice enables the suppression of systematic errors. These features allow for the realization of a symmetric Mach-Zehnder-type geometry, where contrast can be observed up to a maximum splitting of $408\,\hbar k$ corresponding to a total transfer of $1632\,\hbar k$. To our knowledge, this represents the largest momentum separation in an atom interferometer reported so far.

A detailed experimental and theoretical study reveals that the current limitations are solely caused by technical properties of the experiment. In particular, light field distortions arising due to the diffraction of the laser beam at different apertures cause a dephasing leading to a contrast decay. The results open up new routes for the miniaturization of inertial quantum sensors as well as for gravitational wave detectors.

In addition, the combination of an atom-chip trap with an optical dipole trap is investigated, which serves as a pathfinder experiment for atom interferometry in optical waveguides. Waveguides allow extending the interrogation time without an increase of the interferometer region. Optimizing the spatial overlap of both traps as well as the temporal sequence, the BEC can be transferred into the dipole trap with an efficiency of over 99%. Such a setup also has applications in future atom-chip experiments featuring two atomic species, whose interactions can only be controlled in a purely optical trap.

ZUSAMMENFASSUNG

Atominterferometer bilden ein bewährtes Werkzeug für Präzisionsmessungen. Mögliche Anwendungsgebiete sind vielfältig und reichen von Geodäsie und Trägheitsnavigation bis hin zu grundlegenden Fragen der Physik. Modernste Sensoren arbeiten typischerweise mit lasergekühlten Atomen, die eine relativ große räumliche Ausdehnung sowie Impulsbreite besitzen. Die damit verbundenen systematischen Unsicherheiten können mithilfe von Bose-Einstein-Kondensaten (BECs) überwunden werden. Die Empfindlichkeit eines Atominterferometers wird abgesehen von der Interrogationszeit durch eine große Impulsseparation der atomaren Wellenpakete gesteigert. Eine geringe atomare Geschwindigkeitsbreite ist dabei entscheidend für eine hocheffiziente Manipulation.

Im Rahmen dieser Arbeit wird die Realisierung eines neuartigen Strahlteilers vorgestellt, mit welchem große Impulse auf eine ultrakalte Atomwolke übertragen werden können. Das Kondensat wird in einem miniaturisierten Atomchip-basierten Aufbau erzeugt und dessen Expansionsrate durch Delta-kick-Kollimation weiter reduziert. Das Lichtfeld für die Strahlteilung besteht aus zwei gegenläufigen Gittern mit orthogonalen Polarisationen. In einem solchen Zwillingsgitter wird Doppel-Bragg-Beugung effizient mit Bloch-Oszillationen kombiniert. Diese Methode erscheint vielversprechend, um die derzeitigen Begrenzungen bei der Übertragung großer Impulse zu überwinden. Durch das Erreichen von Bloch-Transfereffizienzen von mehr als 99,9% pro Photonenrückstoß ($\hbar k$) wird eine ausgezeichnete Skalierbarkeit gewährleistet. Darüber hinaus ermöglicht die Symmetrie des Doppelgitters die Unterdrückung systematischer Fehler. Diese Eigenschaften erlauben die Realisierung einer symmetrischen Mach-Zehnder-Geometrie, in der Kontrast bis zu einer maximalen Separation von $408\hbar k$ beobachtet werden kann. Insgesamt werden dabei $1632\hbar k$ übertragen. Nach unserem Kenntnisstand stellt dies die größte bisherige Impulstrennung in einem Atominterferometer dar.

Eine detaillierte experimentelle und theoretische Studie zeigt, dass vor allem technische Eigenschaften des Experiments die derzeitigen Ergebnisse limitieren. Insbesondere Störungen des Lichtfelds, die durch die Beugung des Laserstrahls an verschiedenen Aperturen entstehen, führen zu Dephasierung und einem damit verbundenem Kontrastabfall. Die hier erzielten Ergebnisse eröffnen neue Möglichkeiten für die Miniaturisierung inertialer Quantensensoren sowie für Gravitationswellendetektoren.

Außerdem wird die Kombination einer Atomchipfalle mit einer optischen Dipolfalle im Hinblick auf Atominterferometrie in Lichtwellenleitern untersucht. In diesen kann die Interrogationszeit verlängert werden, ohne den Interferometerbereich zu vergrößern. Durch Optimierung der räumlichen Überlagerung beider Fallen sowie der zeitlichen Sequenz kann das BEC mit einer Effizienz von über 99% in die Dipolfalle geladen werden. Ein solcher Aufbau soll auch in zukünftigen Atomchip-Experimenten mit zwei verschiedenen Atomsorten verwendet werden. Deren Wechselwirkungen untereinander können nur in einer rein optischen Falle kontrolliert werden.

CONTENTS

1 INTRODUCTION

Precision measurements constitute an essential part of modern-day science, helping us to gain insight into the most essential aspects of nature. A more accurate knowledge about fundamental constants and physical variables such as rotations or accelerations leads to a better understanding of our universe, which is currently described by the theories of general relativity and quantum mechanics. Today, one of the most sensitive measurement techniques is based on the interference of electromagnetic waves. A tremendous enhancement of these interferometers occurred in the aftermath of the invention of the laser in the 1960s, which allowed to utilize light with unique coherence properties [1].

Ultimately, this led to the development of devices with unprecedented sensitivity such as the gravitational wave detector LIGO (Laser Interferometer Gravitational-Wave Observatory) which is capable of dissolving relative length changes as small as $\Delta L/L = 10^{-23}$ between two interferometer arms. To achieve such sensitivities, quantum phenomena are employed, such as squeezing to improve the performance beyond the quantum shot-noise limit [2]. In September 2015, following decades of work and improvement, LIGO could, for the first time, directly observe gravitational waves emitted by the merger of two black holes [3]. The discovery was awarded the Nobel prize in 2017, opening up outstanding opportunities to observe the universe from a new perspective.

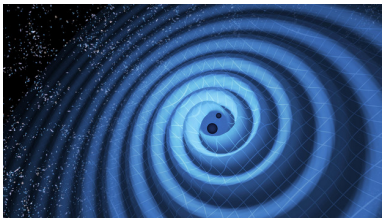

Fig. 1.1: Merger of two black holes. Image credit: LIGO/T. Pyle

1.1 Atomic quantum sensors

Beginning in the late 1970s, the development in laser technology boosted the field of cold atom experiments, making it possible to achieve temperatures of few microkelvins and to study gases with velocities of centimeters per second [4–7]. The application of ultra-cold atoms significantly contributed to the advancement of atomic clocks [8, 9], which until today serve as highly precise standards for the definition of time. Cold clouds of atoms also constitute a highly sensitive test matter wave, perfectly suited for interferometric measurements. Inspired by the work on neutron interferometers [10, 11], atom interferometry started its advent in the year 1991 [12–15]. Some of the pioneering experiments employed material slits [12] or crystalline gratings [13] for the diffraction of atoms, while Bordé and Chu operated their devices with counterpropagating laser beams [14, 15]. Reversing the roles of light and matter compared to an optical interferometer, the atomic wave packet is split, redirected,

and brought to interference by the application of laser pulses. Compared to matter gratings, optical lattices [16, 17] greatly benefit from the ability to adjust their properties like depth and velocity in an easy manner. Today, light pulses are usually employed instead of stationary optical lattices since they feature a better control of interaction time and temporal shape [15].

Atom interferometers impressively demonstrate the wave nature of atoms essential to quantum mechanics as well as the coherent superposition of two atomic states over macroscopic distances. The observed interference phase depends on the evolution of the atomic wave function, which is determined by the potential probed by the atom. Hereby, the cold atoms represent an ideal test mass for a variety of forces.

Enormous progress during the past years has led to the development of high-precision atom interferometers, which are now commonly used as inertial sensors competing with the sensitivity of classical devices. Compared to macroscopic test masses atoms offer several advantages like an excellent control and manipulation capability of their velocity and position. Besides, they do not suffer from manufacturing imperfections or mechanical wear, and their small spatial extent reduces systematic effects caused by gravity gradients or tidal forces. Quantum gravimeters are able to measure the local gravitational acceleration with an accuracy of up to $10^{-9}g$ [18–20] and even emerged as commercially available products offering inertial on-site measurements [21, 22]. Other applications include gyroscopes [23–25] determining, for example, Earth's rotation or gradiometers [26, 27], where the differential signal of two spatially separated experiments is read out. Their extreme sensitivities and drift-free operation make inertial quantum sensors ideally suited for Earth observation and navigation.

Atom interferometers also represent a promising tool to address and test fundamental topics in physics [28], searching for deviations from the standard model. Incorporating the interface between gravity and quantum mechanics, they constitute a complementary way of probing general relativity by comparing the free-fall rate of different atomic species or isotopes [29–31]. Other subjects include tests of dark energy theories [32] as well as the examination of quantum phenomena such as the Aharanov-Bohm effect [33] or a measurement of the Casimir force [34].

1.1.1 Large momentum transfer

The sensitivity of an atom interferometer typically scales with the enclosed space-time area. A large effort is therefore made to increase the interrogation time up to several seconds by realizing atomic fountains in large vacuum structures [35] or by suspending the atoms against gravity using an optical or magnetic waveguide [36–38]. The progress of developing compact and robust sensors allows to conduct experiments under microgravity conditions [39–41] or even in space [42, 43] to achieve unperturbed evolution on large time scales.

The differential momentum between the two interferometer arms is another crucial factor for enhancing the device's sensitivity. One strives to develop efficient beam splitters to transfer multiple photon recoils ($n \cdot \hbar k$) onto the atomic wave packet. Here, k defines the wave vector. Large momentum transfer is particularly relevant in the geometry used for measurements of the fine-structure constant α [44–46]. Since α is derived from the measurement of the photon recoil energy, its precision scales quadratically with the number of transferred photon recoils within a beam splitter. Large momentum transfer also increases the sensitivity of

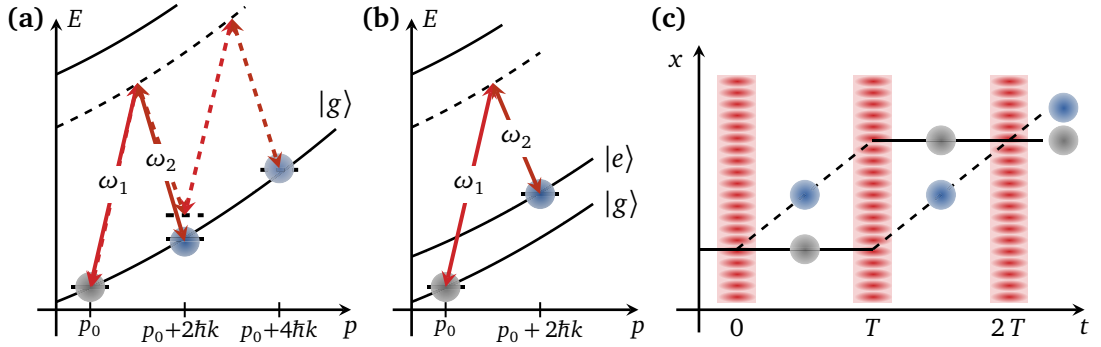

Figure 1.2: (a) First (——) and second order (- - -) Bragg diffraction between different momentum states. (b) Raman diffraction involving an internal state change. (c) Mach-Zehnder type atom interferometer, where the atom cloud is split, redirected and recombined by the application of three laser pulses separated by a pulse interval T.

inertial sensors [27, 47] and allows to shorten the interrogation region for the improvement of compact portable devices [19, 48].

Novel areas of application include gravitational wave detection on ground [49–51] and in space [52, 53], where atom interferometers can contribute to the detection of fascinating astrophysical phenomena. In these instruments, the wave-packet momentum separation $\Delta p = n\hbar k$ is a key factor to achieve the required precision. Their strain sensitivity covers the infrasound domain, allowing to bridge the gap around $0.1 - 10\,\mathrm{Hz}$ between present ground- and future space-based detectors based on optical interferometry [54]. While current classical devices only permit the observation of binary systems at the very end of their lifetime, detection in the infrasound band would enable to observe these sources years before their coalescence [52, 55]. A sensor consists of two atom interferometers, which are separated by a long baseline L and operated with common lasers. The propagation of the laser pulses between both parts is modified in the presence of a gravitational wave generating a differential phase shift. In case of a symmetric three-pulse sequence as described in Ref. [50] it yields

$$\Delta\phi_{\mathrm{GW}} = 2nkhL\,[\cos(\omega T) - 1], \tag{1.1}$$

where T is the interrogation time, h the strain and ω the angular frequency of the gravitational wave. To reach the extreme sensitivities required for such devices, proposals assume splittings as large as $1000\,\hbar k$ [50, 56].

Table 1.1 lists several techniques for reaching large momentum transfer in an atom interferometer by coherently manipulating the atomic motion with laser pulses. While stimulated Raman transitions comprise a change of the internal state, the application of Bragg diffraction solely alters the momentum state of an atom. Each method comes with certain benefits. Raman pulses impose lower requirements on the atomic momentum distribution and enable velocity filtering. By contrast, Bragg diffraction allows for higher-order transitions and can be implemented in the same system as Bloch oscillations, which correspond to an adiabatic acceleration in an optical lattice. The ability of Bragg diffraction to drive sequential multi-photon transitions resulted in benchmark experiments demonstrating momentum splittings of $\Delta p = 102\,\hbar k$ in an atom interferometer [57]. In this case, population loss caused by the limited beam splitter efficiencies lead to a residual atom number of 10% and restricted the maximum momentum separation [57].

Method	Momentum splitting Δp
Multiphoton Bragg	$24\hbar k$ [71], $102\hbar k$ [57], $90\hbar k$ [47]
Double Bragg	$8\hbar k$ [68]
Sequential Raman	$6\hbar k$ [72], $4\hbar k$ [24]
Double Raman	$8\hbar k$ [66], $4\hbar k$ [67]
Adiabatic Bragg/Raman	$10\hbar k$ [73], $30\hbar k$ [74]
Kapitza-Dirac & Bragg	$112\hbar k$ [75]*
Raman/Bragg & Bloch	$10\hbar k$ [60], $24\hbar k$ [62], $80\hbar k$ [59]
Dual-lattice Bloch	$240\hbar k$ [69]

* Three-path contrast interferometer

Table 1.1: Methods for the generation of large momentum transfer along with the maximum separation achieved in an atom interferometer.

The high transfer efficiencies achievable with Bloch oscillations, therefore, constitute a promising candidate for a scalable beam splitter. Besides, the method is robust against intensity and frequency fluctuations, requires less laser power compared to higher-order Bragg transitions, and even offers the possibility for a faster scaling in acceleration sensitive measurements [58]. By combining Bragg pulses with Bloch oscillations in a waveguide, fringe visibility could be demonstrated in an atom interferometer with a momentum separation of $80\hbar k$ [59]. However, as pointed out already in Ref. [60], a major drawback of Bloch oscillations constitute light shifts between the different interferometer arms which reduce the interferometric contrast. This can be overcome by accelerating both arms simultaneously, as suggested in Ref. [61] and realized in Ref. [62] in a dual-lattice setup with two beams and three frequency components. Also, during Bragg or Raman beam splitting, diffraction phases [63–65] arise and have to be accounted for [46]. They can be suppressed along with other systematic effects in a symmetric geometry formed by double Bragg or Raman diffraction [66–68]. These symmetric implementations, however, could only demonstrate a splitting of up to $8\hbar k$ at a contrast below 29%. Very recently, the realization of a symmetric dual-lattice interferometer was reported that ideally exhibits zero diffraction phase [69]. Hereby, retroreflection of a beam containing three frequency components forms two independently accelerated optical lattices, which can form beam splitter, mirror, or recombination pulses via control of the differential laser phase. In this way, contrast could be observed up to a momentum splitting of $240\hbar k$. Proposals also exist for a dual lattice acting as a waveguide, which is able to pull the two interferometer arms apart, hold them at a given distance and recombine them [70]. Such a sensor would exhibit a high sensitivity while occupying a small volume.

1.1.2 Bose-Einstein condensates

In 1995, the development of laser cooling peaked in the realization of a new state of matter, where quantum degeneracy is reached in form of a Bose-Einstein condensate (BEC) [76–78]. Predicted decades earlier by Bose and Einstein [79, 80], the realization of macroscopic quantum objects allows to investigate quantum mechanics at a new level. In analogy to an

optical laser, the matter waves are characterized by unique coherence properties allowing to observe high-contrast interferences fringes over the extent of the condensate [81].

Up to date, the vast majority of state-of-the-art quantum sensors operate with laser-cooled Alkali atoms. They are typically manipulated with Raman transitions, which impose less stringent requirements on the momentum width of the atomic ensemble and can be exploited for velocity selection [82]. The reluctance to employ condensed sources is motivated by two major restrictions. The process of reaching quantum degeneracy with an evaporation cycle is time-consuming and leads to large atom losses. This results in a lower atom flux compared to thermal ensembles, which in turn degrades the sensitivity of an atomic sensor. Recently, however, there has been large progress concerning the BEC flux. Atom-chip technologies allow for fast and efficient evaporation enabling high-flux sources with 10^5 atoms per second [83] approaching those of current sensors based on velocity selected laser-cooled atoms.

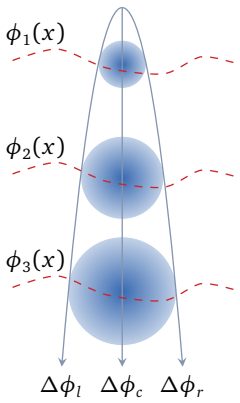

Fig. 1.3: The expansion of an atom cloud in a distorted wavefront leads to different phase shifts across the cloud.

Another downside arises from the high densities of a BEC, which lead to significant atomic interactions causing mean-field shifts in an atom interferometer [84, 85]. These can be mitigated via tuning the atomic interactions with Feshbach resonances [84] or by waiting a sufficiently long time after release of the condensate to achieve a conversion of mean-field energy into kinetic energy. Hereby, it is instrumental to employ a technique called delta-kick collimation [40, 86] to minimize the duration of free expansion prior to interferometry. It is beneficial to start with a larger initial expansion to achieve a rapid conversion and alleviation of mean-field energy. During the collimation via a magnetic or optical lens, kinetic energy is converted into potential energy and the expansion can be almost stopped resulting in a small final momentum width.

If these limitations can be overcome, the properties of condensed sources offer a lot of advantages and potential for matter-wave interferometry:

- Owing to their small momentum width, high beam-splitter efficiencies can be achieved, reaching an interferometric contrast close to 100% [87, 88]. BECs are particularly relevant for large momentum transfer via multiphoton Bragg transitions or Bloch oscillations where they allow for a high-fidelity transfer with low atom losses [57, 59].

- Condensed sources permit lowering the effect of a variety of systematics associated with the spatial extent and expansion of the atomic ensemble. This includes one of the major uncertainties in present atom interferometers induced by wavefront aberrations [89, 90], as depicted in Figure 1.3. Similarly, small clouds decrease dephasing due to spatial variations of the laser intensity [91]. Again, these features are especially crucial for multiphoton processes, which are more susceptible to dephasing processes [71]. A small expansion rate also represents a key requirement for reaching ultra-long free evolution times as anticipated in future space missions [41–43, 52].

- The point-source character of BECs along with a spatially resolved detection allows to detect spatial features in the interference pattern to reveal more details about phase shifts or systematic effects [35, 92].

- The phase sensitivity of an atom interferometer is limited by shot noise, which scales with the atom number N as $1/\sqrt{N}$. BECs offer the possibility of exceeding the classical limit by using squeezed states with a reduced uncertainty [93, 94]

1.2 The QUANTUS collaboration

The work within this thesis is part of the QUANTUS (Quantengase unter Schwerelosigkeit) project, which aims to develop miniaturized and robust sensors for the application in microgravity environments and, ultimately, in space. Space platforms not only provide ultra-long interrogation times but also offer a relatively quiet environment undisturbed by seismic noise. These properties are promising for the realization of ultra-cold atom sensors with unprecedented sensitivity to test fundamental physics such as the equivalence principle at a new level or perform inertial measurements for the observation of the Earth [95]. The absence of gravity allows to realize ultra-shallow traps along with smaller expansion rates of the atomic ensembles and to study exotic geometries by forming spherical or ellipsoidal shell condensates [96, 97]. The technologies required for the development of spaceborne sensors can also be applied to improve the evolution of compact and robust mobile devices operating in the fields of geodesy, geophysics, and navigation.

The QUANTUS collaboration consists of several generations of experiments, each accompanied with significant technological progress advancing the field of ultra-cold gases in weightlessness. All of these experiments apply an atom chip to produce the magnetic fields required for BEC generation. Its small size and power consumption make it a crucial ingredient in building compact and efficient devices. In 2007, the first generation QUANTUS-1 created the first Bose-Einstein condensate of ^{87}Rb in the microgravity environment of the drop tower of Bremen, which features a drop tube of 110 m and a corresponding free fall duration of 4.7 s. Further pathfinder experiments in microgravity include the application of delta-kick collimation and atom interferometry with long interrogation times [40] making use of the spatial coherence properties of the condensate. Lately, the apparatus is exploited for the investigation of new interferometer topologies on ground [68, 88] which is not only applicable to subsequent generations but leads to innovative methods for BEC interferometry in general. Some of these novel techniques will be presented in this thesis.

Further miniaturization allowed the integration of the second generation drop tower experiment, QUANTUS-2, into a smaller and lighter capsule. The experiment is suitable for catapult operation to double the microgravity time to 9.4 s. Additionally, the device will be extended to a dual-species source permitting the simultaneous cooling and manipulation of ^{87}Rb and a potassium isotope. An advanced cooling setup along with an elaborated atom chip enables an ultra-high atom flux making it the fastest BEC machine in the world [83]. Extensive drop-tower studies of delta-kick collimation via magnetic lensing could enhance the former results and achieve effective temperatures of tens of picokelvin [98, 99]. Complementary to the QUANTUS drop-tower experiments, the PRIMUS project follows a different approach by employing an optical dipole trap instead of an atom chip for trapping and cooling [100, 101].

The seconds of microgravity time in the drop tower can be extended to few minutes onboard a sounding rocket as realized within the MAIUS (matter-wave interferometry in microgravity) missions. After years of development to meet the harsh requirements of a rocket launch

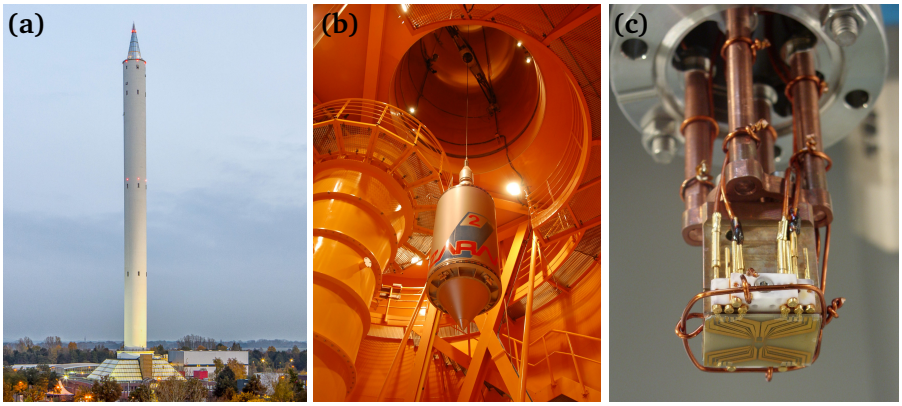

Figure 1.4: (a) Drop tower in Bremen (source: [102]). QUANTUS-2 capsule within the drop tower (b) and image of the QUANTUS-1 atom chip (c), both photographies by H. Müntinga.

along with the subsequent autonomous operation, the first mission MAIUS-1 was successfully launched in January 2017 [41]. During the six minutes of free fall, the first Bose-Einstein condensate in space was generated, and a variety of other atom-optics experiments were demonstrated. Already two successor missions are planned, aiming to perform dual-species experiments with rubidium and potassium and investigate their interactions in a magnetic as well as in an optical dipole trap.

In 2018, the CAL (Cold atom laboratory) experiment set off for the ISS to provide the first continuous platform for ultracold gases in microgravity. The mission comprises the creation and investigation of degenerate gases as well as ultracold mixtures of ^{87}Rb, ^{39}K, and ^{41}K [42]. As a successor of MAIUS and CAL a joint project between NASA and DLR was initiated in 2016. The multi-user facility BECCAL is still in the planning phase and will be equipped with different isotopes (^{87}Rb, ^{85}Rb,^{39}K,^{40}K,^{41}K) to study their interactions and perform dual-species atom interferometry [43]. Based on the MAIUS design, it will additionally feature high magnetic fields and shaped optical potentials to address a variety of topics in fundamental physics as well as inertial sensing.

1.3 Scope of this thesis

The work presented here aims at the development of new methods for the coherent manipulation of Bose-Einstein condensates with optical lattices, concerning in particular large momentum transfer. Two major effects typically restrict the transfer of a large number of photon recoils within an atom interferometer. On the one hand, limited beam splitter efficiencies lead to significant atom losses as well as spurious ports, lowering the signal-to-noise ratio of the measurement. Additionally, the accumulation of phases unequal in both interferometer arms arises due to the prolonged interaction with the light field. They lead to dephasing and reduction of the interferometric contrast.

Within this thesis, a novel scalable and symmetric beam splitter is investigated, which is able to overcome the limitations mentioned above and to reach unprecedented momentum separation in an atom interferometer. The new technique consists of an efficient combination of double Bragg diffraction and Bloch oscillations for large momentum transfer. Both methods

can be driven in a relatively simple setup, where a single beam with two frequency components of orthogonal polarization is retroreflected and forms a twin lattice. A retroreflected geometry features the advantage of suppressing laser phase noise and wavefront distortions. In case of a vanishing velocity in beam splitter direction, it directly entails the symmetric diffraction through a double Bragg process, which automatically doubles the momentum transfer and has already been implemented successfully in a quantum tiltmeter [68]. Owing to the small momentum width of the Bose-Einstein condensate, which is further reduced by the method of delta-kick collimation, efficiencies of 98.8% per $\hbar k$ can be realized. Double Bragg diffraction, however, only serves for the initial beam splitting. Exploiting the twin lattice, the superposition of two momentum states is simultaneously accelerated utilizing Bloch oscillations, which not only allows for much larger transfer efficiencies but is also more robust against laser intensity fluctuations compared to Bragg or Raman diffraction [88, 103]. We call the combination of both techniques a twin-lattice beam splitter offering excellent scalability by the application of Bloch oscillations as well as a symmetric geometry for the suppression of systematic effects such as diffraction phases and AC-Stark shifts caused by laser intensity noise. Based on the work in Ref. [68], it allows to span a symmetric Mach-Zehnder-type atom interferometer, which exhibits an increased scaling factor due to the transfer of a multiple of photon momenta. The scaling of the coherence is investigated statistically. The evaluation reveals that the contrast is currently not limited fundamentally but by technical features of our device, which can be overcome rather easily in a dedicated setup. The implementation of the twin-lattice interferometer, along with the contrast analysis, has been published in Ref. [104].

In addition, an optical dipole trap is studied regarding future atom interferometry experiments in optical waveguides [37, 38]. A waveguide promises to achieve long interrogation times without increasing the interferometer baseline and is therefore ideally suited for the integration in miniaturized sensors. Furthermore, future MAIUS and BECCAL missions will be equipped with a dipole trap that enables to control the atomic interactions with Feshbach resonances [105]. In dual-species experiments with rubidium and potassium, this is crucial for an efficient evaporation of potassium [106] and an improved spatial overlap of both species [107]. It also offers the possibility of transferring the atoms away from the atom chip to suppress disturbances arising from the chip's surface or its mass. However, the combination of an atom chip with a purely optical trap has not been investigated in detail so far. The presented work includes a first evaluation of loading a Bose-Einstein condensate from a chip-based trap into a purely optical trap by extending the QUANTUS-1 experiment with a new laser system far-detuned from resonance. For an efficient transfer, a good spatial overlap, as well as an optimized sequence, is required.

This thesis starts with an introduction into the theoretical concepts of light-pulse atom interferometry in chapter 2, where particular emphasis is placed on Bragg diffraction, Bloch oscillations and the Mach-Zehnder-type interferometer scheme. Chapter 3 gives a short description of the QUANTUS-1 experiment together with a closer look at the high-power laser system employed for coherent manipulation of the atomic ensemble via Bragg and Bloch processes. Precision interferometry requires a well-prepared atomic cloud exhibiting a small momentum width, offset velocity and insensitivity to magnetic fields. Next to the preparation sequence, chapter 4 provides a detailed characterization of double Bragg diffraction and Bloch oscillations in a twin lattice. The chapter is extended by the presentation of some

interesting techniques for future interferometer geometries. Combining these ingredients large momentum interferometry in a twin lattice can be realized, which is presented in chapter 5. Its contrast is analyzed in detail both experimentally and theoretically. Chapter 6 describes the setup and loading of the optical dipole trap within the QUANTUS-1 experiment. The thesis closes with a summary and outlook in chapter 7.

The results presented in this thesis could only be achieved in a collaborative effort. The QUANTUS-1 experiment was operated together with M. Gersemann and S. Abend, while the theoretical simulations concerning atoms in optical lattices were carried out by J.-N. Siemß. The experiments on the optical dipole trap were performed in collaboration with S. Kanthak. Within the scope of this thesis, the author is in particular responsible for the optimization of the large momentum beam splitter and the experimental realization of the twin-lattice interferometer. All experimental data evaluation was performed by the author.

ATOM OPTICS AND INTERFEROMETRY 2

This chapter gives an overview of the theory which is essential for the realization large momentum atom interferometry in QUANTUS-1. Light pulses, in particular Bragg diffraction, serve as beam splitters for the atomic wave packet creating a coherent superposition of different quantum states (sec. 2.1). In addition, momentum transfer is also possible by means of Bloch oscillations which offer a very efficienct way of manipulating the atomic velocity (sec. 2.2). Through the combination of beam splitters an interferometer geometry can be spanned allowing the measurement of inertial forces acting on the atoms (sec. 2.3). Among the availability of different topologies the Mach-Zehnder inteferometer is widely employed in atom interferometry consisting in its simplest form of three light pulses.

2.1 Light-pulse manipulation

Light-pulse atom interferometers were first operated with two-photon Raman transitions [15] coupling two different hyperfine states. This technique is still widely used in atom interferometry and is especially suitable for thermal atoms from optical molasses due to its lower requirements on momentum distribution. Compared to Bragg diffraction, Raman transitions enable the use of short pulses which lead to a reduced velocity selectivity. Additionally, the existence of two different states allows both a state-selective read-out during detection as well as a state-selective removal of spurious atoms, a so-called "blow-away". Alternatively, Bragg transitions can be driven to couple different momentum states [16, 108]. The absence of an internal state change suppresses systematic effects such as AC Stark shifts and makes it possible to apply this method to atomic species without hyperfine splitting of the ground state [109, 110]. In addition, it is possible to drive higher-order transitions and realize Bloch oscillations in the same laser system.

In the following chapter the tools for light-pulse atom interferometry are introduced starting with the simple model of a two-level atom in an optical field. This already gives rise to an important result, namely the so-called Rabi oscillations of the atomic cloud between different states (sec. 2.1.1). A more profound description does not only include the energy but also the momentum of the atoms which is changed via the atom-light interaction by means of a two-photon process (sec. 2.1.2). Bragg diffraction is one example of such a process (sec. 2.1.3), where the internal state is not changed. In an appropriate setup it can be extended to a symmetric beam splitter, a technique named double Bragg diffraction, featuring advantages like the suppression of the laser phases (sec. 2.1.4).

2.1.1 Two-level atom in a light field

We consider a two-level atom having a ground and an excited state, $|g\rangle$ and $|e\rangle$, with corresponding energies ω_g and ω_e and energy difference $\omega_{eg} = \omega_e - \omega_g$, which couples to an electromagnetic field $\mathbf{E} = \mathbf{E}_0 \cos(\omega t + \phi)$ (see Fig. 2.1(b)). Neglecting spontaneous emission the Hamiltonian can be written as the sum of an internal Hamiltonian given by the eigenfunctions $|g, e\rangle$ and eigenenergies $\omega_{e,g}$, and an interaction Hamiltonian defined by the light field [111]

$$\hat{H} = \hbar\omega_e |e\rangle \langle e| + \hbar\omega_g |g\rangle \langle g| - \mathbf{dE}. \tag{2.1}$$

Here, $\mathbf{dE}$ is the coupling term between the electromagnetic field $\mathbf{E}$ and the atomic dipole moment $\mathbf{d} = |e|\mathbf{r}_e$, $\mathbf{r}_e$ being the vector from the nucleus to the electron's position. The time-dependent Schrödinger equation describes the time evolution of a quantum state, i.e. our atomic wave function $|\Psi(t)\rangle$

$$i\hbar \frac{\mathrm{d}}{\mathrm{d}t} |\Psi(t)\rangle = \hat{H} |\Psi(t)\rangle . \tag{2.2}$$

The ansatz for the wave function consists of a linear combination of eigenfunctions, where the rapidly oscillating terms $\omega_{e,g}$ have been factored out to remain with slowly oscillating coefficients $c_{e,g}$:

$$|\Psi(t)\rangle = c_e(t)\mathrm{e}^{-i\omega_e t} |e\rangle + c_g(t)\mathrm{e}^{-i\omega_g t} |g\rangle . \tag{2.3}$$

We assume that the detuning δ of the laser frequency ω from resonance is much smaller than the transition frequency

$$\delta = (\omega - \omega_{eg}) \ll \omega_{eg}, \tag{2.4}$$

and can therefore apply the rotating wave approximation (RWA), neglecting the rapid oscillating terms of order $(\omega_{eg} + \omega)$ compared to the terms of order δ. By inserting (2.3) into (2.2), the probability P for an atom to be in state $|g\rangle$ or $|e\rangle$ can be calculated

$$P_e = |c_e(t)|^2 = \frac{1}{2}\left(\frac{\Omega_{\mathrm{eg}}}{\Omega_{\mathrm{eff}}}\right)^2 [1 - \cos(\Omega_{\mathrm{eff}} t)], \tag{2.5}$$

$$P_g = |c_g(t)|^2 = \frac{1}{2}\left(\frac{\Omega_{\mathrm{eg}}}{\Omega_{\mathrm{eff}}}\right)^2 [1 + \cos(\Omega_{\mathrm{eff}} t)], \tag{2.6}$$

where Ω_{eg} and Ω_{eff} represent the Rabi frequencies at resonance ($\delta = 0$) and out of resonance ($\delta \neq 0$), respectively. Ω_{eg} can also be expressed as a function of the light field intensity I in terms of the saturation intensity I_{sat} for a specific transition and its natural linewidth Γ

$$\Omega_{\mathrm{eg}} = \frac{\langle e|\mathbf{d}\cdot\mathbf{E}|g\rangle}{\hbar} = \sqrt{\frac{I[I_{\mathrm{sat}}]}{2}}\Gamma, \tag{2.7}$$

$$\Omega_{\mathrm{eff}} = \sqrt{\delta^2 + |\Omega_{\mathrm{eg}}|^2}. \tag{2.8}$$

We observe the well-known behavior of the population probability $P_{e,g}$ oscillating at the Rabi frequency. For an nonzero detuning δ the oscillation frequency increases, whereas the amplitude of the oscillations decreases as depicted in Fig. 2.1(a). For zero detuning we distinguish two cases which are important for the implementation of an interferometer: A π-pulse of length $t = \pi/\Omega_{\mathrm{eg}}$ will invert the occupation probability corresponding to a mirror pulse, while a $\pi/2$-pulse of duration $t = \pi/2\Omega_{\mathrm{eg}}$ creates an equal superposition between both states, thus establishing a beam splitter.

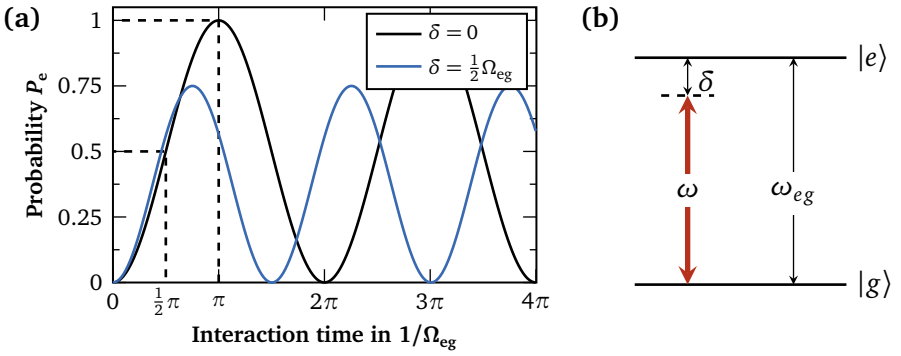

Figure 2.1: Rabi oscillations of the probability amplitude P_e (a) in an ideal two-level system (b) for the resonant case ($\delta = 0$) and for nonzero detuning ($\delta = \frac{1}{2}\Omega_{eg}$). The latter leads to oscillations with higher frequency and lower amplitude. In case of zero detuning two interaction times are marked. They correspond to a $\pi/2$-pulse acting as a beam splitter and a mirror pulse of duration π/Ω_{eg}.

2.1.2 Two-photon transitions and external degrees of freedom

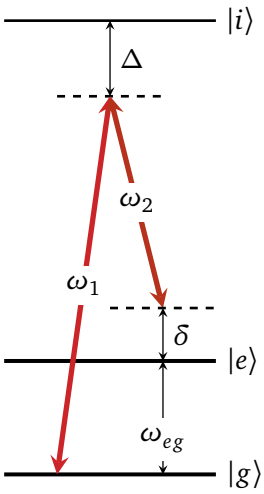

Fig. 2.2: Two-photon transition between states $|g\rangle$ and $|e\rangle$ via an intermediate level $|i\rangle$. The transition is detuned by Δ to suppress spontaneous emission.

One-photon Rabi oscillations can only be driven if both excited and ground state have a long lifetime τ ($\tau > 1/\Omega_{\text{eff}}$). Otherwise, spontaneous emission will lead to large atom losses. Single-photon transitions have recently been proposed and realized in atom interferometry [53, 112]. However, they are difficult to drive since they require a laser system featuring a high frequency stability and large laser powers to achieve sufficiently high Rabi frequencies. Therefore, two-photon transitions are commonly employed to drive Rabi oscillations via an intermediate state $|i\rangle$, which does not need to have a long lifetime, since it is only populated virtually. In the following we generally assume long-lived states and neglect spontaneous emission.

In the description so far, the external degrees of freedom have been neglected. In order to take into account the momentum spread of an atomic cloud the wave packets are represented as the sum of momentum plane-wave states [111]. For each component, the momentum transfer due to an interaction with the electromagnetic field can be calculated. At last, the atomic ensemble is given by the integral over all momentum states $\int \mathrm{d}^3\mathbf{p}\,|\mathbf{p}\rangle\langle\mathbf{p}|$.
The two-photon transitions are driven by two light fields $\mathbf{E_1}$ and $\mathbf{E_2}$:

$$\begin{aligned}\mathbf{E}_1 &= \mathbf{E}_{0,1}\cos(\omega_1 t - \mathbf{k}_1\mathbf{x}),\\ \mathbf{E}_2 &= \mathbf{E}_{0,2}\cos(\omega_2 t - \mathbf{k}_2\mathbf{x}).\end{aligned} \tag{2.9}$$

The interaction term between atoms and light field can be written using the closure relation:

$$1\cdot \mathrm{e}^{\pm ikx} = \int \mathrm{d}^3\mathbf{p}\mathrm{e}^{\pm ikx}\,|\mathbf{p}\rangle\langle\mathbf{p}| = \int \mathrm{d}^3\mathbf{p}\,|\mathbf{p}\pm\hbar k\rangle\langle\mathbf{p}|\,. \tag{2.10}$$

This simply implies that the absorption or emission of a photon of wave vector $\mathbf{k}$ changes the atom's total momentum by $\hbar\mathbf{k}$. The atomic velocity is altered by the recoil velocity $\mathbf{v}_{\text{rec}} = \hbar\mathbf{k}/m$ associated with the recoil energy of $E_r = \hbar\omega_r = \hbar\mathbf{k}^2/(2m)$.

The external and internal degrees of freedom are coupled, since an atom can only change states by absorption or stimulated emission of photons. In a two-photon process an atom in state $|g,\mathbf{p}\rangle$ can be transferred via the intermediate state $|i\rangle$ to $|e, p+\hbar\mathbf{k}_1-\hbar\mathbf{k}_2\rangle$. The momentum transfer $\hbar\mathbf{k}_{\text{eff}}$ during this process is given by the difference of both wave vectors $\mathbf{k}_{\text{eff}} \equiv \mathbf{k}_1 - \mathbf{k}_2$, which is maximized for counterpropagating laser beams, when both wave vectors point in opposite directions. The energies of these states are shifted by the Doppler effect and the recoil energy:

$$E_{|g,\mathbf{p}\rangle} = \hbar\omega_g + \frac{\mathbf{p}^2}{2m}, \tag{2.11}$$

$$E_{|e,\mathbf{p}+\hbar\mathbf{k}_{\text{eff}}\rangle} = \hbar\omega_e + \frac{(\mathbf{p}+\hbar\mathbf{k}_{\text{eff}})^2}{2m}. \tag{2.12}$$

The detuning of the effective laser frequency $\omega_{12} = \omega_1 - \omega_2$ from the transition is assumed to be small compared to the two-photon detuning Δ relative to the intermediate state $|i\rangle$ and equals

$$\delta_{12} = \omega_{12} - \left(\omega_{eg} + \frac{\mathbf{p}\mathbf{k}_{\text{eff}}}{m} + \frac{\hbar\mathbf{k}_{\text{eff}}^2}{2m}\right) = \delta - \left(\frac{\mathbf{p}\mathbf{k}_{\text{eff}}}{m} + \frac{\hbar\mathbf{k}_{\text{eff}}^2}{2m}\right). \tag{2.13}$$

The Hamiltonian for the full three-level system including the external degrees of freedom is then given by

$$\hat{H}(t) = \hbar\omega_e |e\rangle\langle e| + \hbar\omega_g |g\rangle\langle g| + \hbar\omega_i |i\rangle\langle i| + \frac{\mathbf{p}^2}{2m} - \mathbf{d}(\mathbf{E}_1 + \mathbf{E}_1). \tag{2.14}$$

The system can be solved as before by writing the atomic wave-function $|\Psi\rangle$ as a linear combination of eigenfunctions similar as in (2.3) and inserting it into the time-dependent Schrödinger equation (2.2) [113]. As a result, the population probability for the excited state is given by

$$P_e(t) = \frac{1}{2}\frac{\Omega_{12}^2}{\Omega_{12}^2 + (\delta_{12} - \delta^{AC})^2}\left[1 - \cos\left(\sqrt{\Omega_{12}^2 + (\delta_{12} - \delta^{AC})^2}\,t\right)\right] \tag{2.15}$$

$$= \frac{1}{2}\frac{\Omega_{12}^2}{\Omega_{\text{eff}}^2}\left[1 - \cos(\Omega_{\text{eff}}t)\right]. \tag{2.16}$$

Where the following quantities have been defined:

Two-photon Rabi frequency:

$$\Omega_{12} = \frac{\Omega_{g i,1}^{*}\Omega_{ei,2}}{2\Delta} = \frac{\Gamma\sqrt{I_1[I_{\text{sat}}]I_2[I_{\text{sat}}]}}{4\Delta[\Gamma]}. \tag{2.17}$$

The Rabi frequency of a two-photon light field with intensities I_1 and I_2 and two-photon detuning Δ. It consists of the multiplication of $\Omega_{gi,1}$ and $\Omega_{ei,2}$, which are the one-photon frequencies corresponding to the transitions from $|i\rangle$ to $|g\rangle$ with light field $\mathbf{E}_1$ and from $|i\rangle$ to $|e\rangle$ with $\mathbf{E}_2$, respectively.

AC-Stark Shift: The interaction between a light field and an atom not only leads to a state transfer, but also influences the atomic energy structure. In the presence of a light field with Rabi frequency Ω and detuning Δ to the transition the eigenenergies experience a frequency shift of $\Omega^2/(4\Delta)$ [114]. In our case, where two light fields act on two transitions, four contributions have to be taken into account and a differential AC-Stark shift can be calculated [113]

$$\delta^{AC} = \left(\frac{|\Omega_{ei,1}|^2}{4(\Delta-\omega_{eg})} + \frac{|\Omega_{ei,2}|^2}{4(\Delta+\delta)}\right) - \left(\frac{|\Omega_{gi,1}|^2}{4(\Delta)} + \frac{|\Omega_{gi,2}|^2}{4(\Delta-\omega_{eg}-\delta)}\right). \tag{2.18}$$

With a proper choice of intensity ratio I_1/I_2 and two-photon detuning Δ the differential AC-Stark shift can be compensated.

Effective Rabi frequency: The effective coupling of this system including a detuning δ_{12} and an AC-Stark shift δ^{AC} is then given by $\Omega_{\text{eff}} = \sqrt{\Omega_{12}^2 + (\delta_{12}-\delta^{AC})^2}$.

Spontaneous emission

So far, the states were assumed to be of long lifetime and spontaneous emission was neglected. However, in a real system it can only be suppressed by operating at a larger detuning Δ from the intermediate state $|i\rangle$ and leads to atom losses during the coherent beam splitting process. The rate of spontaneous decay depends on the light field intensity I and the detuning Δ expressed in units of the natural linewidht Γ and saturation intensity I_{sat}.

$$P_{\text{sp}} = \frac{\Gamma}{2}\frac{I[I_{\text{sat}}]}{(2\Delta[\Gamma])^2}. \tag{2.19}$$

Since Eq. (2.19) scales quadratically with Δ, whereas the Rabi frequency in (2.17) exhibits a linear scaling, spontaneous emission can be suppressed with $1/\Delta$. To keep the Rabi frequency constant, the laser intensity has to be increased accordingly.

2.1.3 Bragg diffraction

Bragg diffraction was first known as the scattering of electromagnetic radiation from crystals [117, 118]. In atom interferometry, analogously, an atomic beam is diffracted from a light grating. During the process, the absorption and emission of a photon changes the atom's momentum state while the internal state remains constant (Fig. 2.3(a)). Bragg diffraction represents a special case of the Kapitza-Dirac effect [119]. Diffraction to a single momentum state is only valid for a thick grating, i.e. relatively long interaction times. For smaller interaction lengths a transition to the Raman-Nath regime takes place, where several momentum states are populated (Fig. 2.3(b)). In contrast to Raman diffraction, where two phase-locked lasers are required to couple the different hyperfine states, Bragg diffraction is relatively simple to implement experimentally, since the frequency difference between two momentum states lies in the kHz regime and a single laser can be employed.

For Bragg diffraction the results from the previous section 2.1.2 simplify since the atoms do not change their internal states. The two-photon resonance condition becomes

$$\delta_{12} = 0 \qquad \Leftrightarrow \qquad \delta = \frac{\mathbf{p}\mathbf{k}_{\text{eff}}}{m} + \frac{\hbar\mathbf{k}_{\text{eff}}^2}{2m} \equiv \omega_{\text{D}} + \omega_{\text{eff}}. \tag{2.20}$$

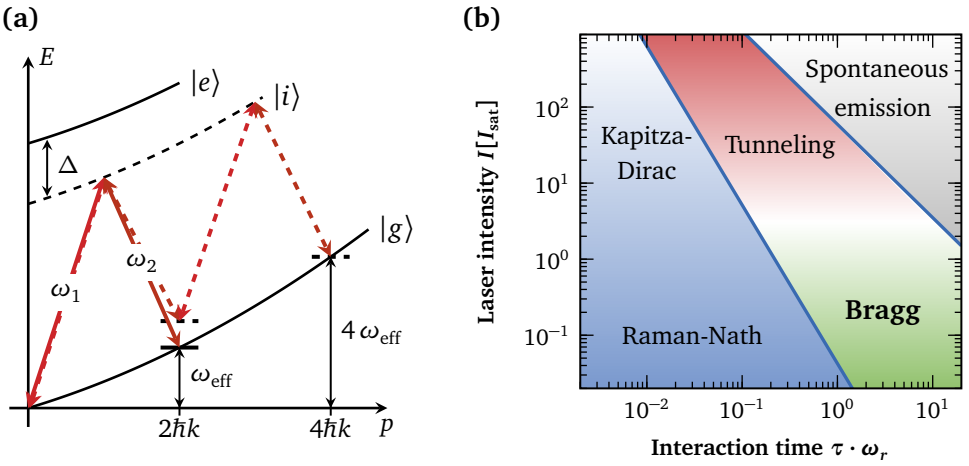

Figure 2.3: (a) Schematic representation of Bragg diffraction. Via a two-photon process with detuning $\delta = 4\omega_r \equiv \omega_{\text{eff}}$ an atom is transferred to another momentum state receiving $2\hbar k$. Via a second order process with $\delta = 2\,\omega_{\text{eff}}$ and four photons involved (dashed lines) the momentum transfer can be doubled. (b) Depending on the interaction length τ and the laser intensity I different diffraction regimes can be defined [115]. Only the Bragg regime features diffraction into a single momentum state. Elsewhere, losses into other momentum states or spontaneous emission processes occur. Adapted from [116].

Given that the frequency difference between the two laser beams is very small we can write $\mathbf{k} \equiv \mathbf{k}_1 \approx \mathbf{k}_2$ and $\mathbf{k}_{\text{eff}} \approx 2\hbar\mathbf{k}$. In a single first-order Bragg process, the kinetic energy of an atom changes by $\omega_{\text{eff}} \equiv 4\omega_r = \hbar k_{\text{eff}}^2/(2m)$.

Because of the absence of internal state coupling we have set $\omega_{eg} = 0$. Since the detuning δ between both frequencies is typically very small ($\delta \ll \Delta$), the differential AC-Stark term δ^{AC} in (2.18) can be neglected. In the resonant case ($\delta_{12} = 0$), an atom initially in momentum state $|\mathbf{p}\rangle$ is transferred to state $|\mathbf{p} + 2\hbar\mathbf{k}\rangle$ with probability

$$P_{\mathbf{p}+2\hbar\mathbf{k}}(t) = \frac{1}{2}[1 - \cos(\Omega_{12} t)]. \tag{2.21}$$

Higher order diffraction

The sensitivity of an atom interferometer can be enhanced by enlarging the momentum transfer onto the atomic cloud. This can either be done by the application of sequential first order pulses or by performing higher order diffraction, where multiple photon pairs are scattered simultaneously as illustrated in Figure 2.3(a). In that case, the transferred momentum is $2n\hbar\mathbf{k}$, n being the order of the diffraction process. The detuning between the two laser frequencies is adjusted to $\delta = \omega_D + n \cdot \omega_{\text{eff}}$.

Bragg transitions up to the order of $n = 12$, corresponding to a large momentum transfer of $24\hbar k$, have been realized in an atom interferometer [71]. Compared to single diffraction, the multiphoton process imposes higher demands on laser intensity and is more sensitive to wave front distortions and phase noise [71]. In the deep Bragg regime, which holds for long interaction times so that the optical lattice fulfills the condition of a thick grating, it is

possible to transfer atoms into single higher order state. The effective Rabi frequency of a process of order n depends on the laser intensity via the two-photon Rabi frequency Ω_{12} [71]

$$\Omega_{\text{eff}} = \frac{\Omega_{12}^n}{(8\omega_r)^{n-1}} \frac{1}{[(n-1)!]^2}. \tag{2.22}$$

However, operation in this regime requires a very narrow velocity distribution of the atoms. Furthermore, interaction time in an experiment is limited and desired to be small. For shorter interaction times one operates in the quasi-Bragg regime featuring a relaxed velocity selectivity. Here, one has to take into account losses into other diffraction orders, which might result in much lower diffraction efficiencies. However, when applying smooth envelope functions along with carefully chosen pulse durations and intensities it is still possible to create beam splitters with an efficiency close to 100% in the quasi-Bragg regime [120].

Recently, Rabi frequencies for first and higher order Bragg diffraction were calculated in the Bloch-band picture [65]. Experimental results agreed well with these calculations while Eq. (2.22) failed for higher intensities. The Bloch-band structure will be explained in sec 2.2.2.

Momentum width and pulse shaping

So far, the calculations did not consider the momentum spread of the atomic cloud. Depending on the velocity selectivity of a pulse, which increases with its width, parts of the cloud might not get diffracted (Fig. 2.4(a)). For higher order transitions the requirements on momentum spread are even stricter. A momentum spread causes a damping of the Rabi oscillations, since different momentum components of a cloud experience different effective Rabi frequencies. An extensive numerical discussion about the importance of momentum width for single Bragg diffraction is given in [87].

It has been shown, that the simple switching on and off of the electromagnetic potential, a box-shaped pulse, is not the best option for efficient beam splitting of clouds with finite momentum spread. Better results can be achieved by applying smooth envelope functions for the laser intensity [120]. In addition, smooth pulse shapes have been shown to suppress high-frequency phase noise [121] as well as two-photon light shifts in a retroreflective geometry [122].

The Rabi oscillations in sec. 2.1.1 were calculated for a pulse of rectangular form with constant field amplitude E_0 and duration τ

$$I(t) = \begin{cases} I_0 & |t| \leq \frac{\tau}{2} \\ 0 & |t| > \frac{\tau}{2} \end{cases} \tag{2.23}$$

The Fourier transform of such a pulse is given by a sinc function

$$\tilde{I}(f) = I_0 \tau \,\text{sinc}(\pi \tau f), \tag{2.24}$$

which determines the probability of an atom with Doppler shift f to be diffracted to another momentum state. We compare the box-shaped pulse with a Gaussian pulse

$$I(t) = I_0 \exp\left(-\frac{t^2}{2\sigma_t^2}\right), \tag{2.25}$$

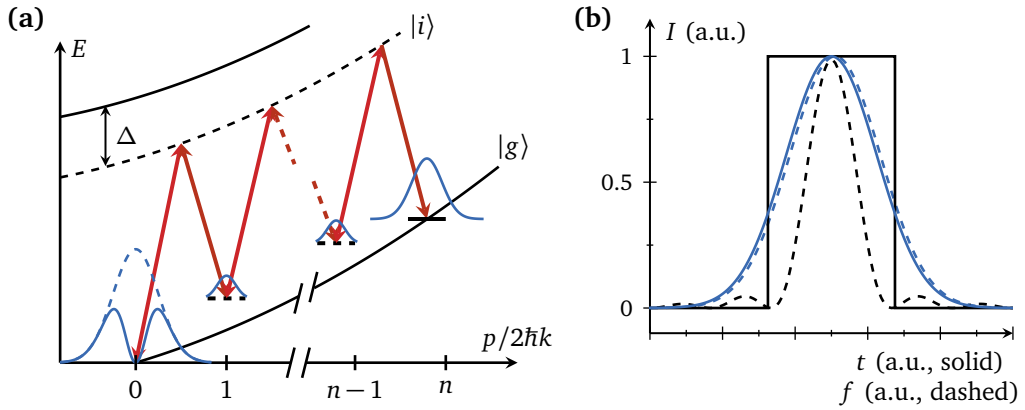

Figure 2.4: (a) Higher order Bragg process for a cloud with finite momentum width. Due to the pulse's velocity selectivity the cloud can not be transferred with 100% efficiency and atoms are lost to other diffraction orders. (b) Box (—) and Gaussian-shaped (—) intensity pulse along with the corresponding Fourier transform (dashed).

which contains its form in Fourier space

$$\tilde{I}(f) = I_0\sqrt{2\pi}\sigma_t \exp\left(-\frac{f^2}{2\sigma_f^2}\right) \qquad \text{with } \sigma_f = \frac{1}{2\pi\sigma_t}. \tag{2.26}$$

Since the velocity distribution of the atom cloud is approximately of Gaussian shape the Gaussian pulse increases the momentum overlap between pulse and atoms. For equal maximum intensities and pulse areas, a Gaussian pulse exhibits a broader momentum acceptance than the central peak of the sinc function of a box pulse. Additionally, a sinc function features sidebands which might overlap with higher-order momentum states and cause losses into these states. For pulse shapes with a time-dependent Rabi frequency, the pulse area is defined via the integral over time. For a π-pulse this yields for example

$$\int \mathrm{d}t\Omega(t) = \pi. \tag{2.27}$$

Long pulse durations ($1/\tau \ll \sigma_v$, σ_v being the momentum width of the atomic ensemble) can be used in order to spectroscopically analyze the cloud's momentum. In this way, only a narrow part of the cloud is selected. By scanning the detuning δ across the cloud, a momentum profile of the atoms can be obtained. Very short pulse durations will lead to a transition into the Raman-Nath or Kapitza-Dirac regime corresponding to thin gratings (Fig 2.3(b)). The small momentum selectivity of these regimes leads to the population of many diffraction orders [123].

2.1.4 Double Bragg diffraction

Retroreflection is commonly employed in fountains for high-precision atom interferometers [18, 35], since the common beam path leads to a suppression of laser phase noise and wave-front distortions. At the same time, the mirror serves as inertial reference. In these experiments, only one pair of counterpropagating beams is resonant due to the Doppler shift.

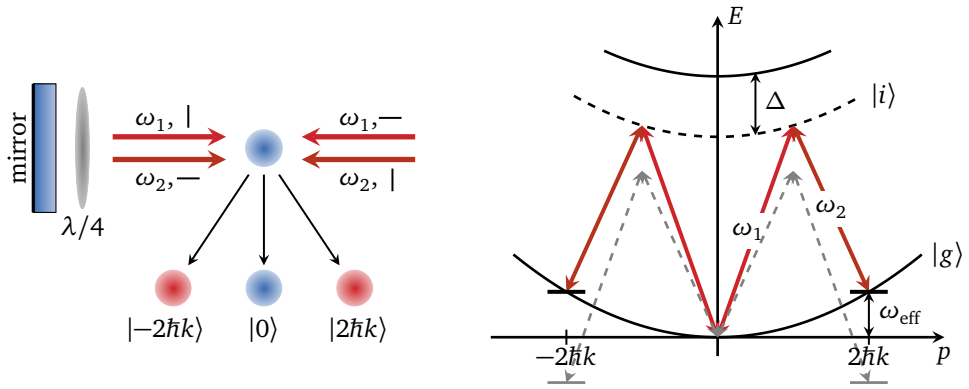

Figure 2.5: Via a double Bragg process a cloud with nonzero velocity gets symmetrically diffracted into two momentum states with opposite velocity. Two counterpropagating lattices with orthogonal linear polarization are formed by reflecting a beam with two frequency components off a mirror passing a quarter-wave plate twice. In the energy parabola on the right not only the resonant first order process but also one of the non-resonant cases is shown.

In case of a vanishing velocity in beam splitter direction or in weightlessness, the atom cloud can interact with both beam pairs and simultaneous Bragg or Raman transitions with opposite momentum transfer occur [66, 68]. They intrinsically double the momentum separation in a beam splitter and lead to the suppression of systematic effects such as the AC-Stark shift or laser phase noise. Here, we focus on the case without an internal state change, so-called double Bragg diffraction. First- and second-order double Bragg diffraction was first realized within the QUANTUS-1 experiment [68] and a more detailed analysis can be found in [124, 125].

A scheme of double Bragg diffraction is depicted in Fig. 2.5. By choosing appropriate polarizations for the two laser beams, disturbances due to copropagating transitions as well as standing waves can be suppressed. Incoming polarizations are orthogonal and rotated by 90 degrees after passing a quarter-wave plate twice and being retroreflected from a mirror.

In contrast to single diffraction, Rabi oscillations take place in an effective three-level system, which ,among other things, leads to a higher velocity selectivity compared to single diffraction. For double diffraction in the deep Bragg regime, the effective Rabi frequency system reads $\Omega_{\text{eff}} = \sqrt{2}\Omega_{\text{DD}} = \sqrt{2}\Omega_{12}/2$ [124]. In contrast to single Bragg diffraction, the term $\pi/2$ pulse is now used when an equal superposition of the states $|\pm 2\hbar k\rangle$ is reached, while a π pulse corresponds to a population transfer from $|-2\hbar k\rangle$ to $|+2\hbar k\rangle$ and vice versa. When we leave the deep Bragg regime and take non-resonant transitions into account the ideal Rabi oscillations are modulated. Off-resonant processes induce a fast oscillation with frequency $2\omega_{\text{eff}}$ and small amplitude on top of the slow Rabi oscillation as will be experimentally demonstrated in section 4.2.1. The frequency $2\omega_{\text{eff}}$ corresponds to the energy difference between the off-resonant and the resonant process (Fig. 2.5). The simultaneously resonant and off-resonant coupling of a momentum state is a new feature of double Bragg diffraction .

2.2 Optical lattices

Bloch oscillations initially emerged in the context of electrons in a crystal, where the quantum theory by Bloch and Zener predicted an oscillating instead of a uniform motion in the presence of a static electric field [126, 127]. The period of these oscillations is given by the lattice period d and the static electric force F as $T_B = 2\pi\hbar/dF$. In natural crystals the time between scattering events from electrons at lattice defects is much smaller than the Bloch period. Therefore, Bloch oscillations have not been observed in a bulk crystal so far. A periodic potential can also be created by interfering two light beams to form a standing wave. Indeed, cold neutral atoms in an optical lattice exhibit a similar behavior compared to electrons in a crystal. In 1996, Bloch oscillations of atoms have been observed for the first time in the groups of Salomon and Raizen [128, 129]. Lately, the realization of more than 28 000 Bloch oscillations has been demonstrated owing to the high coherence of this technique in combination with an optical cavity [130]. In contrast to solid state systems, the depth and velocity of an optical lattice can easily be changed and does not suffer from dissipation or scattering due to defects or particle interactions.

Compared to Bragg or Raman diffraction, Bloch oscillations allow for much higher transfer efficiencies of 99.97% per $\hbar k$ [103] and therefore present a well suitable tool to transfer a large amount of momentum onto an atomic cloud. Bloch oscillations are frequently used in recoil measurements [45, 46], to probe gravity [130–132] or for coherent acceleration within an atom interferometer [60, 62].

After an introduction to the dipole potential (sec. 2.2.1) the band structure of an optical lattice will be derived following the notation of [129, 133] (sec. 2.2.2). In the presence of a uniform force this leads to a periodic atomic motion, the so-called Bloch oscillations, which can also be explained in a quantum optics description (sec. 2.2.3). Atom loss is mainly caused by two mechanisms, namely interband transitions calculated with the Landau-Zener formalism and spontaneous emission (sec. 2.2.4). In case of the dipole potential and spontaneous emission the particular case of a twin lattice is treated, i.e. two identical counterpropagating lattice with orthogonal polarizations.

2.2.1 Dipole potential

The periodic potential of an optical lattice results from the dipole force, due to the interaction of the induced atomic dipole moment with the intensity gradient of the light field [134]. The electric dipol moment $\mathbf{d}$ is proportional to the electric field $\mathbf{E}$ and depends on its frequency ω via the complex polarizability $\alpha(\omega)$ as $\mathbf{d}(\omega) = \alpha(\omega)\mathbf{E}$. The field shifts the potential energy of the atomic state proportional to the local laser intensity $I(\mathbf{r})$.

$$V_{\text{dip}} = -\frac{1}{2}\langle \mathbf{d}\cdot\mathbf{E}\rangle \propto -\text{Re}[\alpha(\omega)]\cdot I(\mathbf{r}) \qquad \text{with} \qquad I(\mathbf{r}) = \frac{1}{2}\epsilon_0 c|\mathbf{E}|^2, \tag{2.28}$$

where ϵ_0 is the vacuum permittivity and the angular brackets denote the temporale average over the rapidly oscillating terms. The real part of the polarizability corresponding to the

in-phase component of the dipole oscillation is therefore responsible for the conservative dipole force

$$\mathbf{F}_{\mathrm{dip}}(\mathbf{r}) = -\nabla V_{\mathrm{dip}}(\mathbf{r}) = \frac{1}{2\epsilon_0 c}\mathrm{Re}[\alpha(\omega)]\nabla I(\mathbf{r}). \tag{2.29}$$

In turn, the imaginary part of the polarizability describing the out-of-phase component gives rise to the scattering or spontaneous emission rate

$$P_{\mathrm{sp}} = \frac{1}{\epsilon_0 c\hbar}\mathrm{Im}[\alpha(\omega)]I(\mathbf{r}). \tag{2.30}$$

The polarizability can be derived using a classical oscillator model. One obtains the same results in a semiclassical approach by treating an atomic two-level system with transition frequency ω_{eg} and linewidth Γ:

$$\alpha(\omega) = 6\pi\epsilon_0 c^2 \frac{\Gamma/\omega_{eg}^2}{\omega_{eg}^2 - \omega^2 - i(\omega^3/\omega_{eg}^2)\Gamma}. \tag{2.31}$$

Here, $\Gamma \propto |\langle e|\mathbf{d}|g\rangle|^2$ can be understood as a damping rate associated with the spontaneous decay rate of the excited level. Eq. (2.31) only holds in the limit of low saturation, i.e. neglibible population in the excited state which is reached for large detunings $\Delta = \omega - \omega_{eg}$ and low scatterings rates P_{sp}.

Based on the previous considerations the following expression for the dipole potential can be derived

$$V_{\mathrm{dip}}(\mathbf{r}) = -\frac{3\pi c^2}{2\omega_{eg}^3}\left(\frac{\Gamma}{\omega_{eg}-\omega} + \frac{\Gamma}{\omega_{eg}+\omega}\right)I(\mathbf{r}). \tag{2.32}$$

Since the laser frequency is typically not too far away from the atomic resonance ($|\Delta| \ll \omega_{eg}$) the rotating wave approximation can be applied, resulting in

$$V_{\mathrm{dip}}(\mathbf{r}) = \frac{3\pi c^2}{2\omega^3}\frac{\Gamma}{\Delta}I(\mathbf{r}). \tag{2.33}$$

Similarly one finds for the scattering rate

$$P_{\mathrm{sp}}(\mathbf{r}) = \frac{3\pi c^2}{2\hbar\omega^3}\frac{\Gamma}{\Delta}I(\mathbf{r}) = \frac{V_{\mathrm{dip}}(\mathbf{r})}{\hbar\Delta[\Gamma]}, \tag{2.34}$$

which can be rewritten into Eq. (2.19).

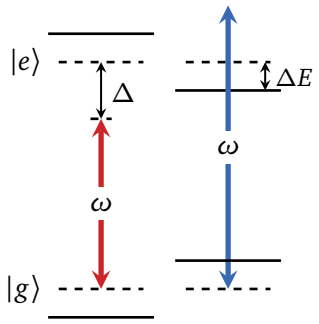

Fig. 2.6: AC Stark level shifting due to a red ($\Delta < 0$) or blue ($\Delta > 0$) detuned optical dipole potential.

The dipole potential corresponds to the AC-Stark or light shift of the ground state introduced in section 2.1.2, which shifts the energy states of an atom in the presence of a light field (Fig. 2.6)

$$V_{\mathrm{dip}} = \Delta E_g = \frac{\hbar\Omega^2}{4\Delta} = \frac{\hbar\Gamma}{8}\frac{I[I_{\mathrm{sat}}]}{\Delta[\Gamma]}. \tag{2.35}$$

It can be expressed in terms of the saturation intensity I_{sat} and the linewidth Γ using (2.7). Like the two-photon Rabi frequency, the dipole potential scales with I/Δ allowing the suppression

of spontaneous emission with $1/\Delta$. For a red detuning ($\Delta < 0$) the dipole potential is negative and leads to an attractive interaction with the atoms, which accumulate in potential minima where the intensity is at a maximum. For a blue detuning ($\Delta > 0$), atoms are repelled by high-intensity regions and a potential minimum corresponds to a minimum of the intensity.

An optical lattice in one dimension can either be formed by interfering two laser beams traveling in opposite direction of same intensity I and wavelength λ or by retroreflecting a single beam at a mirror. Due to the interference of the amplitudes the dipole potential of the resulting standing wave increases by a factor of four and has a periodicity of $\lambda/2 = \pi/k$

$$V(x) = V_0 \cos^2(kx) = 4 \cdot V_{\text{dip}} \cos^2(kx) = \frac{V_0}{2}(1 + \cos(2kx)). \tag{2.36}$$

The lattice period is usually much smaller than the diameter of a cold atom cloud and the wavefunction thus occupies more than a hundred of lattice sites [135]. Commonly, the amplitude V_0 of the potential is given in units of the recoil energy $E_r = \frac{(\hbar k)^2}{2m} = \hbar\omega_r$

$$V_0[E_r] = 4 \cdot \frac{\hbar\Gamma}{8} \frac{I[I_{\text{sat}}]}{\Delta[\Gamma]} \frac{1}{E_r} = \frac{\Gamma}{2\omega_r} \frac{I[I_{\text{sat}}]}{\Delta[\Gamma]}. \tag{2.37}$$

Twin-lattice potential

In a double diffraction setup, the light field is created by two laser beams with frequencies ω_1, ω_2 having orthogonal polarization (see Fig. 2.5). Through retroreflection at a mirror and passing a quarter-wave plate twice two counterpropagating lattices of orthogonal polarization are formed. In this setup, two atom clouds can be simultaneously accelerated by means of Bloch oscillations. Because of the simultaneous transfer in opposite directions, we will call such a configuration a twin lattice. Assuming equal field amplitudes $E_1 = E_2 \equiv E_0$ the incident light field can be described by

$$\mathbf{E}(x,t) = E_0 \left[\boldsymbol{\epsilon_1} \cos(\omega_1 t - k_1 x) + \boldsymbol{\epsilon_2} \cos(\omega_2 t - k_2 x)\right], \tag{2.38}$$

where the vectors $\boldsymbol{\epsilon_1}, \boldsymbol{\epsilon_2}$ indicate the polarization. Their scalar product is zero in case of orthogonal polarizations and equals 1 for parallel vectors. We now want to take into account imperfections by assuming that the polarizations of the incident components are no longer perfectly orthogonal to each other, i.e. $\boldsymbol{\epsilon_1} \cdot \boldsymbol{\epsilon_2} \neq 0$. The polarization error is defined by the scalar product $\sigma_{\text{pol}} \equiv |\boldsymbol{\epsilon_1} \cdot \boldsymbol{\epsilon_2}|/2$. With $\Delta\omega = \omega_1 - \omega_2$ and $k \equiv k_1 \approx k_2$ the dipole potential after retroflection and passage of the quarter-wave plate becomes

$$\begin{aligned} V_{\text{twin}}(x,t) = {} & V_0 \cos^2(kx - \tfrac{\Delta\omega}{2}t) + V_0 \cos^2(kx + \tfrac{\Delta\omega}{2}t) \\ & + V_0 \frac{\sigma_{\text{pol}}}{(1-\sigma_{\text{pol}})} \left[2\cos(kx + \tfrac{\Delta\omega}{2}t) \cdot \cos(kx - \tfrac{\Delta\omega}{2}t)\right], \end{aligned} \tag{2.39}$$

where all terms oscillating at twice the laser frequency ($2\omega_{1,2}, \omega_1 + \omega_2$) have vanished in the rotating wave approximation. Apart from the ideal twin lattice $\left(\propto \cos^2(kx \pm \Delta\omega t/2)\right)$ imperfect polarizations lead to an additional interference term. For a more intuitive understanding of the impact of this parasitic contribution, we write the interference term as the sum of a standing lattice $V_{\text{St}} \propto \cos^2(kx)$ and a beat term without spatial modulation $V_{\text{b}} \propto \sin^2(\frac{\Delta\omega}{2}t)$:

$$\left[2\cos(kx + \tfrac{\Delta\omega}{2}t) \cdot \cos(kx - \tfrac{\Delta\omega}{2}t)\right] = 2\cos^2(kx) - 2\sin^2(\tfrac{\Delta\omega}{2}t) \equiv V_{\text{St}} + V_{\text{b}}. \tag{2.40}$$

We will see later on that the interfence term acts as a standing lattice in terms of momentum transfer on the atoms.

2.2.2 Band structure in an optical lattice

The periodicity of an optical lattice $V(x+d) = V(x)$ leads to a band structure of the atomic energy spectrum. According to the Bloch theorem [136] the corresponding eigenenergies $E_n(q)$ and eigenstates $|n,q\rangle$ (Bloch states) are labeled by a discrete band index n and a continuous quasimomentum q. The eigenfunctions Ψ are given as a superposition of plane waves e^{iqx} with amplitude $u_{n,q}(x)$

$$\Psi_{n,q}(x) = \langle x|n,q\rangle = e^{iqx} u_{n,q}(x). \tag{2.41}$$

$|u_{n,q}\rangle$ exhibits the same periodicity as the potential $V(x)$ and satisfies the Schrödinger equation

$$\hat{H}_q\,|u_{n,q}\rangle = E_n(q)\,|u_{n,q}\rangle \quad \text{with} \quad \hat{H}_q = \frac{(p+\hbar q)^2}{2m} + V(x) \tag{2.42}$$

The Bloch states $|n,q\rangle$ and eigenenergies $E_n(q)$ are periodic in q. Due to the periodicity of $2\pi/d$ the quasimomentum q is conventionally restricted to the first Brillouin zone $]-\pi/d, +\pi/d]$. For an optical lattice these limits can be expressed by the wave vector k corresponding to $]-\hbar k, +\hbar k]$ in momentum space.

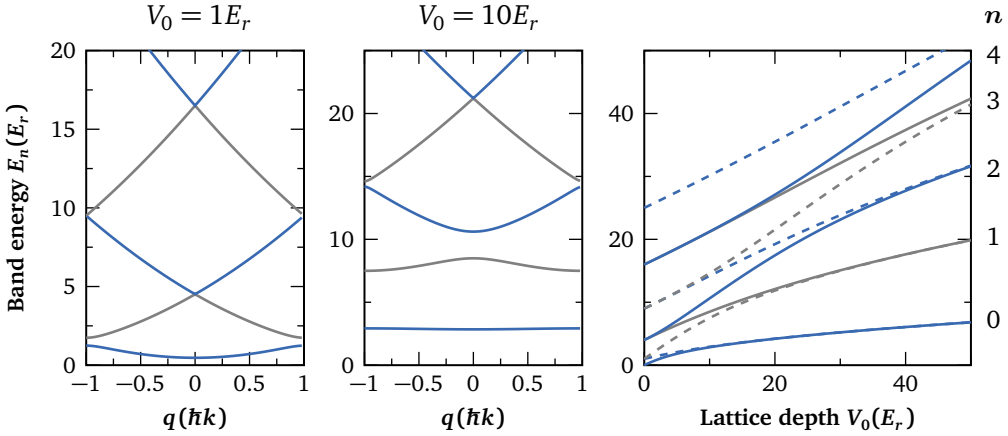

Figure 2.7: Band structure of an optical lattice of depth $V_0 = 1E_r$ and $10E_r$ for the first Brillouin zone as a function of the quasimomentum q. Band energy E_n depending on the lattice depth V_0 for $q = 0$ (—— and ——) and $q = \pm 1$ (- - - and - - -). Adapted from [116].

The band structure in the frame of the optical lattice is depicted in Figure 2.7 for the first Brillouin zone. A Bose-Einstein condensate [135] or a velocity filtered thermal cloud [129, 133] exhibit a momentum spread much smaller than $2\hbar k$ and the atomic states can therefore be well represented as discrete points on the energy parabola. For very shallow lattices ($V_0 < 1E_r$) the dispersion relation between band energy E_n and quasimomentum q is similar to the momentum-energy parabola of a free particle. With increasing lattice depth the band structure progressively flattens out starting with the lowest bands and the band gap tends to become constant across the Brillouin zone.

While the Bloch states are delocalized eigenfunctions, the so-called Wannier functions are localized at individual lattice sites [137, 138] and might represent are more convenient basis

especially in the limit of deep lattices. The Wannier functions of a particle at lattice site l in the n^{th} Bloch band are obtained by integration of the Bloch states over the quasimomentum

$$\psi_{n,l} = \int_{-\pi/d}^{\pi/d} \mathrm{e}^{-iqx_l} \Psi_{n,q}(x). \tag{2.43}$$

2.2.3 Coherent acceleration via Bloch oscillations

In the presence of a constant external force F the stationary Bloch states $\langle n, q\rangle$ are no longer solutions to the Schrödinger equation with the new Hamiltonian

$$\hat{H} = \frac{p^2}{2m} + V(x) - Fx. \tag{2.44}$$

The quasi-momentum becomes time-dependent $q(t) = q(0) + Ft/\hbar$ but the waveform of the eigenfunction is preserved

$$\Psi(x,t) = \mathrm{e}^{iq(t)x} u(x,t). \tag{2.45}$$

The time evolution of the spatially periodic function $u(x,t)$ is described by the time-dependent Schrödinger equation with Hamiltonien $\hat{H}_{q(t)}$

$$i\hbar \frac{\mathrm{d}}{\mathrm{d}t} |u(t)\rangle = \hat{H}_{q(t)} |u(t)\rangle . \tag{2.46}$$

If the adiabatic approximation can be applied

$$|\langle n,q| \frac{\mathrm{d}}{\mathrm{d}t} |n',q\rangle| \ll |E_n(q) - E_{n'}(q)|/\hbar \quad (n \neq n') \tag{2.47}$$

the new eigenstate equals the former stationary Bloch state $|n, q(t)\rangle$ up to an oscillating phase factor

$$|u(t)\rangle = \exp\left[-i \int_0^t \mathrm{d}\tau \frac{E_n(q(\tau))}{\hbar}\right] |n, q(t)\rangle . \tag{2.48}$$

For this approximation to be valid the force F has to be weak enough to prevent population transfer into higher energy bands. Transitions are most probable when the quasimomentum reaches the edge of the Brillouin zone ($q = \hbar k$). For the fundamental band $n = 0$ and a shallow lattice $V_0 \ll 10E_r$ the adiabaticity criterion then reads

$$|F| \frac{\lambda}{2} \ll \frac{\pi}{8} \frac{V_0^2}{E_r}. \tag{2.49}$$

Since the quasimomentum increases linearly in time the periodicity of the wave function $\Psi(x,t)$ corresponds to the time required for the quasimomentum to scan the full Brillouin zone. The Bloch period is therefore given by

$$T_B = \frac{2\pi\hbar}{d|F|}. \tag{2.50}$$

The mean velocity of a particle in state $|n, q(t)\rangle$ depends on q and exhibits the same periodicity as $E_n(q)$

$$\langle v \rangle_n(q) = \frac{1}{\hbar} \frac{\mathrm{d}E_n(q)}{\mathrm{d}q}. \tag{2.51}$$

Due to the uniform evolution of the quasimomentum it oscillates in time around a mean value of zero. This periodic motion, depicted in Figure 2.8, represents the so-called Bloch oscillations.

The applied force does not have to be an external one, like gravity, but can also be realized by introducing a frequency difference $\Delta\omega$ between the two laser waves, which increases linearly in time. In the laboratory frame the light field can no longer be treated as a standing wave, while it is still stationary in an accelerated frame. In the lattice frame, the atoms experience a constant inertial force

$$F = -ma = -\frac{m}{2k} \frac{\mathrm{d}}{\mathrm{d}t} \Delta\omega(t) = -\frac{m}{2k} \alpha, \tag{2.52}$$

where $\alpha = \frac{\mathrm{d}}{\mathrm{d}t} \Delta\omega$ is the chirp rate of the lattice. For an efficient transfer the rate α has to fulfill the adiabaticity condition $\alpha \ll \Omega_{12}^2$.

In the laboratory frame, the atomic velocity in the fundamental band $n = 0$ linearly increases during the acceleration of the lattice. The crossing of a Brillouin-zone does not change the band index of an atom. Atoms in higher bands with energies larger than the potential depth V_0, however, act as nearly free particles. At each boundary of the Brillouin-zone they travel to the next higher band and are not accelerated in the laboratory frame.

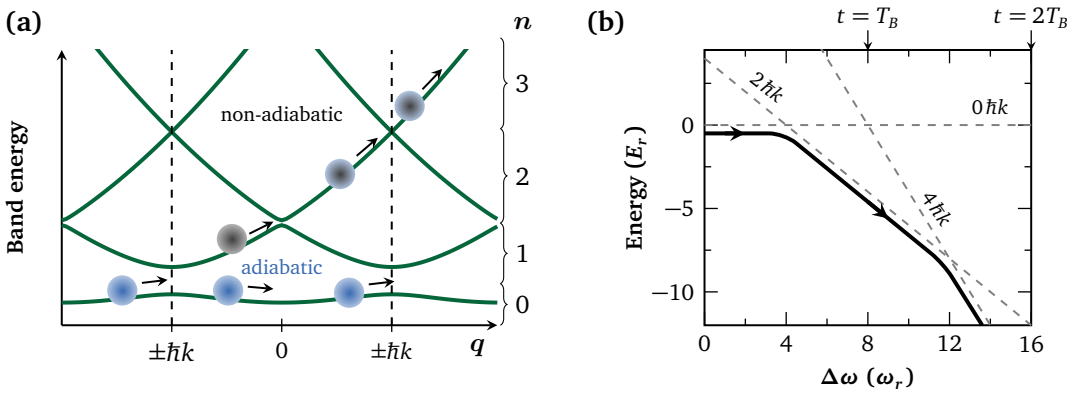

Figure 2.8: (a) Bloch oscillations of atoms in an optical lattice with $V_0 = 3E_r$. In the presence of a uniform force the quasimomentum q of atoms in the fundamental band increases linearly across the Brillouin zone leading to an adiabatic acceleration. If the force it too strong, non-adiabatic transitions into higher bands occur. Adapted from [60]. (b) Bloch oscillations can be interpreted as adiabatic passages between momentum states. At avoided crossings a momentum transfer of $2\hbar k$ occurs.

Adiabatic-rapid-passage approach

Alternatively, Bloch oscillations can also be described in a quantum-optics approach without using the concept of a band theory [133]. Here, they correspond to an adiabatic rapid passage

between momentum states and can be interpreted as sequential Bragg scattering, where the momentum change of the atom is decribed by absorption of a photon from one beam and stimulated emission of a photon into the other beam. These two-photon transitions happen at avoided crossings between the fundamental and first excited band (Fig. 2.8(b)).

As the frequency difference $\Delta\omega$ of the laser beams increases in time, transitions to higher momentum states sequentially become resonant for $\Delta\omega = 4(2j+1)E_r/\hbar$ with $j = 0, 1, 2, ...$ At each resonance the atoms gain a momentum of $2\hbar k$ and are accelerated in direction of the beam with higher frequency. Starting with a vanishing atomic velocity ($j = 0$) and $\Delta\omega = 0$, atoms are repeatedly transferred from state $|p = 2j\hbar k, E = 4j^2E_r\rangle$ to $|p = 2(j+1)\hbar k, E = 4(j+1)^2E_r\rangle$. For a constant chirp rate α the time required for a momentum transfer of $2\hbar k$ brings us again to the Bloch period with a force $F = m\alpha/2k$

$$T_B = \frac{8E_r}{\hbar\alpha} = \frac{2\hbar k}{ma}. \tag{2.53}$$

2.2.4 Transfer efficiency

Landau-Zener theory

To calculate the efficiency of the coherent transfer via Bloch oscillations the Landau-Zener formalism is applied. For a lossless acceleration the atoms have to stay in the fundamental band and not perform transitions into bands with higher energy.

The band gap between band n and $n+1$ decreases with n and is therefore largest between the fundamental and first excited band. Since the probability for interband transitions decreases exponentially with the band gap, an atom that has done the first transition will continue to travel into higher and higher bands and will not be accelerated in the laboratory frame. The critical point for transitions to other bands is at the ends of the Brillouin zone $q = k$ where the band gap has its smallest value. The rate for interband transitions between band n and n' is given by the Landau-Zener formula [126, 133]

$$\eta = \exp\left\{-\frac{\pi}{2\alpha}(\Omega_{\mathrm{bg}}^{nn'})^2\right\}, \tag{2.54}$$

where $\Omega_{\mathrm{bg}}^{nn'} = (E_n - E_{n'})/\hbar$ corresponds to the band gap at the edge of the Brillouin zone ($q = k$) and α is chirp rate of the lattice.
In the weak binding limit the band gap between fundamental and first band matches the two-photon Rabi frequency $\Omega_{\mathrm{bg}}^{01} \simeq \Omega_{12} = V_0/2\hbar = V_0[E_r]\omega_r/2$ (see Fig. 2.9). The probability for atoms to stay in the fundamental band after n crossings of the Brillouin zone can be written as the survival probability for one oscillation to the power of n

$$\eta_{\mathrm{LZ}} = \left[1 - \exp\left\{-\frac{\pi}{8\alpha}(V_0[E_r]\omega_r)^2\right\}\right]^n. \tag{2.55}$$

For large lattice depths ($V_0 > 10E_r$), the first band gap keeps increasing with V_0, however, slower than linearly and Eq. (2.55) underestimates the atomic losses. Furthermore, the lowest bands become essentially flat so that transitions not only take place at zone boundaries. Landau-Zener theory, however, is only valid if the initial coupling around $q = 0$ is negligible and the Bloch state is close to a plane wave. Therefore, only an effective transfer efficiency after n oscillations can be specified for high lattice depths.

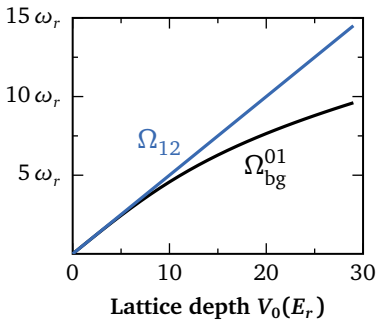

Fig. 2.9: Band gap Ω_{bg}^{01} versus Rabi frequency Ω_{12}.

Coherent acceleration with Bloch oscillations in the tight-binding limit is investigated in [139] using numerical simulations. These calculations show that the Bloch state, which corresponds to the eigenstate of the Hamiltonian without a force, is not the optimal state exhibiting the highest transfer efficiency. A better solution is presented by the Wannier-Bloch state [138], which is the eigenstate of the evolution operator $U = \exp\left(-i\frac{HT_B}{\hbar}\right)$. Experimentally, this state can be prepared by an adiabatic acceleration. Alternatively, similar efficiencies can be reached when introducing a phase shift to the lattice.

Landau-Zener theory also does not take into account resonantly enhanced tunneling [116, 140]. In the tilted potential of an accelerated lattice the tunneling probability is enhanced, when the energy of an atom in one site approximately equals the excited energy level of a neighboring lattice site. At such resonances a dip in the transfer efficiency occurs, since the tunneled atom is not accelerated anymore.

In Ref. [61] a calculation for a superposition of two different momentum states, of which only one is to be accelerated, is performed. In case of a momentum separation of $2\hbar k$ one has to find a compromise between adiabatically accelerating atoms in the fundamental band and a non-adiabatic acceleration for atoms in the second excited band. The efficiency is the product of the probability for an atom to stay in the fundamental band η_{00} and the probability for the other atom to move into the third excited band η_{23}

$$\eta = \eta_{00}\eta_{23} = \left(1 - \exp\left\{-\frac{\pi}{2\alpha}(\Omega_{bg}^{01})^2\right\}\right) \cdot \exp\left\{-\frac{\pi}{2\alpha}(\Omega_{bg}^{23})^2\right\}. \tag{2.56}$$

The best efficiencies can be achieved for small values of acceleration corresponding to large acceleration durations τ_{acc}.

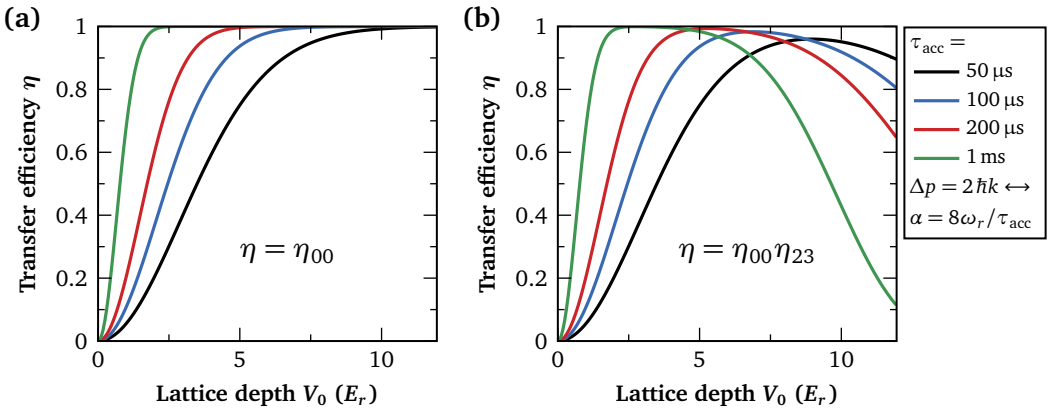

Figure 2.10: Transfer efficiency in an optical lattice according to the Landau-Zener theory for a transfer of $\Delta p = 2\hbar k$ and different acceleration durations τ_{acc} as a function of the lattice depth V_0. Comparison of (a) acceleration in the fundamental band of a single lattice and (b) acceleration of a superposition of momentum states $0\hbar k$ and $2hk$. The latter can be interpreted as the influence of a parasitic lattice.

One encounters a similar situation for a retroreflected lattice featuring two counterpropagating parts, i.e. a twin lattice, where atoms should be accelerated by one lattice and not

be disturbed by the other. In Fig. 2.10 the transfer efficiency in a single lattice is plotted for an atom in the fundamental band compared to a superposition of two atomic momentums states $0\hbar k$ and $2\hbar k$. The latter can be interpreted as the effect a parasitic lattice with an offset velocity of $2\,v_{\mathrm{rec}}$ has on the transfer. If the lattice velocity deviates by $4\,v_{\mathrm{rec}}$ or more from the atomic motion its influence is negligible.

Spontaneous emission

In addition to Landau-Zener tunneling to higher bands, losses occur due to spontaneous emission events. In contrast to Bragg diffraction, they often cannot be neglected during Bloch oscillations because of larger interaction times τ_{acc} with the optical lattice. With a spontaneous emission rate of P_{sp} the residual fraction of atoms is equal to

$$\eta_{\mathrm{Sp}} = \mathrm{e}^{-P_{\mathrm{Sp}}\tau_{\mathrm{acc}}}. \tag{2.57}$$

We evaluate the spontaneous emission rate (2.34) for an atom in a Bloch state of an optical lattice by taking the average of the potential $\langle V(x)\rangle$

$$P_{\mathrm{Sp}} = \frac{\omega_r}{\Delta[\Gamma]}\frac{\langle V(x)\rangle}{E_r} = \frac{\omega_r}{\Delta[\Gamma]}V_0[E_r]\langle\cos^2(kx)\rangle. \tag{2.58}$$

In the tight-binding limit ($V_0 \gg E_r$) it is valid to assume that atoms are located in a single lattice well [44]. In case of a red detuned lattice ($\Delta < 0$), where atoms are trapped in high intensity regions, $\langle\cos^2(kx)\rangle \approx 1 - \frac{1}{2\sqrt{V_0[E_r]}}$ and the spontaneous emission rate becomes

$$P_{\mathrm{Sp,red}} = \frac{\omega_r V_0[E_r]}{\Delta[\Gamma]}\left(1 - \frac{1}{2\sqrt{V_0[E_r]}}\right). \tag{2.59}$$

For a blue detuned lattice ($\Delta > 0$), $\langle\cos^2(kx)\rangle \approx \frac{1}{2\sqrt{V_0[E_r]}}$ resulting in a suppressed spontaneous emission since atoms accumulate in regions with minimum intensity

$$P_{\mathrm{Sp,blue}} = \frac{1}{2\sqrt{V_0[E_r]}}\frac{\omega_r V_0[E_r]}{\Delta[\Gamma]}. \tag{2.60}$$

Spontaneous emission in a twin lattice

The calculations in the previous section only hold for the spontaneous emission rate in a single lattice. Here, we will consider the special case of spontaneous scattering in a blue-detuned twin lattice where additionally the contrapropagating twin as well as the contributions arising from imperfect polarization have to be taken into account. First, the spontaneous emission rate for atoms copropagating with one of the twins at a speed of $v_{\mathrm{BEC}} = \frac{\Delta\omega}{2}k$ is evaluated. We write the potential V_{twin} (Eq. (2.39)) in the rest frame of these atoms by substituting $x \to x + \frac{\Delta\omega}{2k}t$

$$\begin{aligned} V_{\mathrm{twin}}(x,t) = {} & V_0\cos^2(kx) + V_0\cos^2(kx + \Delta\omega t) \\ & + V_0\frac{\sigma_{\mathrm{pol}}}{(1-\sigma_{\mathrm{pol}})}\left[2\cos(kx + \Delta\omega t)\cdot\cos(kx)\right]. \end{aligned} \tag{2.61}$$

We use the mean intensity seen by an atom to calculate the average scattering rate. As detailed in the previous section 2.2.4 one finds for the first term $\langle\cos^2(kx)\rangle \approx \frac{1}{2\sqrt{V_0[E_r]}}$. Since the time scale of the rate $\frac{\omega_r}{\Delta[\Gamma]E_r}$ (Eq. (2.58)) is typically much slower than the frequencies within the cosine arguments we can temporally average over the other terms which results in $\langle\cos^2(kx+\Delta\omega t)\rangle = \frac{1}{2}$ and $\langle[2\cos(kx+\Delta\omega t)\cdot\cos(kx)]\rangle = 0$. Therefore, we find for an atom copropagating with one of the twins a total emission rate of

$$P_{\text{twin}} = \frac{V_0[E_r]\omega_r}{\Delta[\Gamma]}\left(\frac{1}{2\sqrt{V_0[E_r]}}+\frac{1}{2}\right). \tag{2.62}$$

In the same manner, the spontaneous emission rate for an atom at rest can be calculated ($v_{\text{BEC}} = 0$)

$$\begin{aligned} P_{0\,\hbar\mathrm{k}} &= \frac{V_0[E_r]\omega_r}{\Delta[\Gamma]}\Big[\langle\cos^2(kx-\Delta\omega t/2)\rangle + \langle\cos^2(kx+\Delta\omega t/2)\rangle \\ &\quad + \frac{\sigma_{\text{pol}}}{(1-\sigma_{\text{pol}})}\langle 2\cos^2(kx) - 2\sin^2(\Delta\omega/2t)\rangle\Big] \\ &= \frac{1}{2}+\frac{1}{2}+\frac{\sigma_{\text{pol}}}{(1-\sigma_{\text{pol}})}\left(\frac{1}{\sqrt{V_0[E_r]}}-1\right). \end{aligned} \tag{2.63}$$

2.3 Atom interferometry

Interferometry with electro-magnetic waves is widely employed in science and industry for high-precision measurements. Applications range from the early measurement of the speed of light to prove the existence of an aether [141] up to the recent detection of gravitational waves [3] utilizing instruments with unprecedented sensitivity. The wave nature of atoms and in particular the high coherence properties of Bose-Einstein condensates make atom interferometry a promising tool where the roles of light and matter are reversed compared to traditional optical interferometers.

A commonly employed scheme to measure for example the gravitational acceleration, represents the so-called Mach-Zehnder-type interferometer [66, 85, 88] in analogy to its optical counterpart. Following the notation introduced in section 2.1.1 the interferometer consists of a sequence of three pulses, namely a $\pi/2$, a π and another $\pi/2$-pulse to split, redirect and recombine the atomic wave packet. The pulses can be realized either with Bragg or Raman transitions. The first pulse at $t = 0$ splits the atomic wave function to create a coherent superposition of two different states. In case of Bragg diffraction, the superposition consists of two momentum states $|p_0\rangle$ and $|p_1\rangle$ separated by two or more photon recoils. During a free evolution time of T the clouds separate spatially along the interferometer arms. The second pulse at $t = T$ acts as

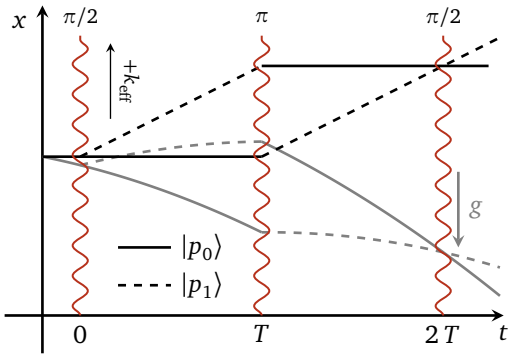

Fig. 2.11: Mach-Zehnder interferometer without (—) and with gravity (—).

mirror reversing the momentum states. Ideally, both trajectories perfectly overlap at $t = 2T$, when a third pulse leads to a coherent recombination of the atomic ensemble to project the phase information onto the population in each state and create an interference pattern. The existence of external forces like gravity can break the symmetry of the interferometer geometry which results in the accumulation of a phase difference after the propagation along the different trajectories. In Figure 2.11 the atomic trajectories of a Mach-Zehnder are plotted in a space-time-diagramm with and without the influence of an external acceleration.

2.3.1 Sensitivity to inertial forces

The total phase difference in an atom interferometer can be expressed as the sum of three contributions [18] arising from the free evolution, the interaction with the light field and the separation of the wave packets

$$\Delta\phi = \Delta\phi_{\text{path}} + \Delta\phi_{\text{light}} + \Delta\phi_{\text{split}}. \tag{2.64}$$

The first contribution $\Delta\phi_{\text{path}}$ stems from the free evolution between laser pulses and is described by the classical action given by the Lagrangian $\mathscr{L}$

$$S_{\text{cl}} = \int_0^{2T} \mathscr{L}[z(t), \dot{z}(t)]\mathrm{d}t. \tag{2.65}$$

As long as $S_{\text{cl}} \gg \hbar$ the phase difference between paths A and B then yields

$$\Delta\phi_{\text{path}} = (S_{\text{cl}}^{\text{B}} - S_{\text{cl}}^{\text{A}}). \tag{2.66}$$

This contribution vanishes for a uniform gravitational field ($\mathscr{L} = \frac{1}{2}mv^2 - mgz$). To take into account a linear gravitational gradient γ, the Lagrangian is extended by the term $\frac{1}{2}m\gamma z^2$ [18]. The second term $\Delta\phi_{\text{light}}$ emerges due to the interaction with the laser beams. If the atomic state changes during such an interaction at time t_i and position z_i, the local laser phase $\phi_i = k_{\text{eff}} z_i - \omega_{\text{eff}} t_i$ is imprinted on the atomic wave function. For a Mach-Zehnder interferometer we find

$$\Delta\phi_{\text{light}} = (\phi_1^{\text{A}} - \phi_2^{\text{A}}) - (\phi_2^{\text{B}} - \phi_3^{\text{B}}). \tag{2.67}$$

The third contribution, the separation phase $\Delta\phi_{\text{split}}$, vanishes if the interferometer closes properly in space and the wave packets perfectly overlap at the exit ports. Without any external forces the symmetry of the Mach-Zehnder interferometer leads to a vanishing phase shift $\Delta\phi = 0$. In the presence of a uniform gravitational field the symmetry is broken and the phase shift yields

$$\Delta\phi_{\text{grav}} = k_{\text{eff}} g T^2 \approx 2kgT^2. \tag{2.68}$$

This simple formula is already a very good approximation for the phase shift within a gravimeter. The sensitivity towards accelerations scales linearly with the momentum separation nk_{eff} and quadratically with the time T between interferometer pulses. Therefore, the product $nk_{\text{eff}}T^2$ is also named scaling factor. In other words, the sensitivity increases with the space-time area A which is enclosed by the two interferometer trajectories.

The phase shift in Eq. (2.68) has been derived under the assumption of vanishing pulse durations. For box pulses of duration τ for a $\pi/2$-pulse and 2τ for a π-pulse slight modifications of order τ/T arise [142]

$$\Delta\phi_{\text{grav}} = 2kgT^2\left[1+\left(1+\frac{2}{\pi}\right)\frac{2\tau}{T}+\frac{2}{\pi}\left(\frac{2\tau}{T}\right)^2\right]. \tag{2.69}$$

Whenever an interferometer encloses a finite spatial area it becomes sensitive to rotations, which is the well-known Sagnac effect. The sensitivity towards a rotational rate of $\mathbf{\Omega}$, caused e.g. by the rotation of the Earth, reads

$$\Delta\phi_{\text{rot}} = \frac{2m}{\hbar}\mathbf{\Omega}\cdot\mathbf{A} = 2\mathbf{\Omega}\cdot(\mathbf{v}_0\times\mathbf{k}_{\text{eff}})T^2, \tag{2.70}$$

where $\mathbf{v}_0$ is the initial velocity and $\mathbf{A}$ the vector normal to the enclosed area, whose length is proportional to its size.

The response of an atom interferometer to noise contributions, caused e.g. by laser phase fluctuations or vibrations, can be calculated using the sensitivity function formalism [142, 143].

Light shifts

For the calculation of the phase from light interactions $\Delta\phi_{\text{light}}$, additional contributions due to one- or two-photon lights shifts leading to an offset phase have been neglected. A one-photon light shift, namely the differential AC-Stark shift δ_{AC} (see sec. 2.1.2) is caused by the differential AC Stark effect between the different states. In case of Raman diffraction it can be compensated for by choosing an appropriate intensity ratio I_1/I_2 of the two laser beams. Given the operation in a single internal state, the AC-Stark shift is intrinsically suppressed in Bragg diffraction. However, here, one has to consider diffraction phases caused by the coherent coupling of atoms to unwanted momentum states [63, 64]. Additionally, in retroreflected geometries two-photon light shifts might arise due to couplings with the off-resonant photon pair. The impact of these off-resonant transitions has been studied for Raman and Bragg [122, 144]. For the latter, it can be suppressed when using Gaussian shaped pulses instead of rectangular ones.

2.3.2 Increasing the scaling factor

Through the application of multiphoton processes, i.e. higher n^{th} order processes, the scaling factor, i.e. the space-time area, can be increased by a factor n. If double diffraction is used for beam splitting, a symmetric Mach-Zehnder type interferometer is realized (see Fig. 2.12(a)), where several systematic effects such as diffraction phases ideally cancel out. Compared to single diffraction the double diffraction scheme intrinsically doubles the momentum transfer ($n = 2$) and, thus, the sensitivity towards the gravitational acceleration

$$\Delta\phi = 4kgT^2. \tag{2.71}$$

Instead of using higher order transitions, the sensitivity can also be increased by using sequential pulses [68, 125]. Thus, the order n changes during the interferometer. Assuming a

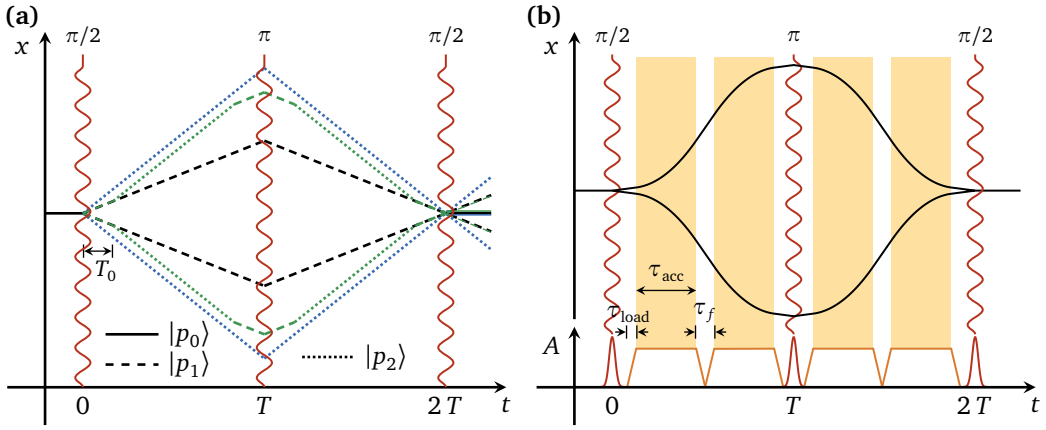

Figure 2.12: Increased scaling factor in different Mach-Zehnder topologies. (a) Symmetric interferometer with first (——), sequential (——) and second-order (——) double diffraction. (b) By inserting Bloch oscillations with a constant acceleration one not only increases the enclosed space-time area but also achieves a faster scaling with time T.

double diffraction interferometer, where the sequential pulses are separated by a time T_0, the phase difference yields

$$\Delta\phi = 8kgT(T - T_0). \tag{2.72}$$

The general formula for an interferometer with N sequential pulses of order n and separated by T_0 [142] yields

$$\Delta\phi = 2n(N+1)kgT \cdot (T - NT_0). \tag{2.73}$$

The space-time area of an interferometer can be determined by integration over the temporal distance Δx of the two interferometer trajectories $A = \int \Delta x(t)\mathrm{d}t$. In a Mach-Zehnder configuration, the two paths exhibit a constant velocity difference Δv. The space-time area therefore scales with the square of the interrogation time T as $\Delta v T^2$. In contrast, in a Ramsey-Bordé interferometer [60, 62] the two trajectories mainly exhibit a constant displacement Δx during T resulting in a sensitivity scaling linearly with T. Based on these two commonly used schemes one can think of an improved scaling towards acceleration with T^3 by increasing the separation with a constant acceleration Δa by means of Bloch oscillations [58]. Regardless of an enhanced scaling behavior the addition of multiple Bloch oscillations in an interferometer will increase the momentum separation and, thus, its sensitivity.

We calculate the phase shift for a symmetric interferometer with Bloch oscillations as depicted in Figure 2.12(b). After an initial separation via double Bragg diffraction both clouds are loaded into a copropagating lattice during τ_{load} and accelerated by n_B Bloch oscillations over a time τ_{acc}. Following a duration τ_f which is required for unloading, a potential free evolution time as well as reloading into the lattice, both momentum states are decelerated before their velocities are reversed via a double diffraction π-pulse. In the second interferometer half, the acceleration and deceleration via Bloch oscillations is repeated until a final $\pi/2$ pulses recombines the momentum states for interferometric readout. The phase shift due to an external acceleration $\boldsymbol{a}$ is given by

$$\Delta\phi = 2 \cdot \left(n + n_B \cdot \frac{\tau_{\mathrm{acc}} + \tau_f}{T} \right) 2\mathbf{k} \cdot \mathbf{a}T^2. \tag{2.74}$$

A constant acceleration rate $\Delta a_B = \frac{4n_B\hbar k}{m\tau_{\mathrm{acc}}}$ between both interferometer arms corresponds to a constant Bloch period $T_B = \tau_{\mathrm{acc}}/n_B$. Therefore, when τ_{acc} or T increases, so does the number of Bloch oscillations. In the limit where τ_{load} and τ_f are significantly smaller than τ_{acc} we can approximate $\tau_{\mathrm{acc}} \approx T/2$ and (2.74) becomes

$$\Delta\phi = 4\mathbf{k}\cdot\mathbf{a}T^2 + \frac{\mathbf{k}\cdot\mathbf{a}T^3}{2T_B}, \tag{2.75}$$

showing an explicit T^3-scaling for a constant Bloch period T_B.

One can even think about further pushing the scaling by applying a constantly increasing relative acceleration, which would lead to a phase contribution scaling with T^4 [58]. The maximum adiabatic acceleration rate which can be achieved increases quadratically with laser power [133]. In case of a twin lattice, the corresponding small initial acceleration and lattice depth are beneficial to lower the influence of the non-resonant lattice on the atomic cloud.

2.3.3 Phase readout

The differential interferometer phase $\Delta\phi$ is read out by analyzing the relative population in one of the momentum states, e.g. $|p_1\rangle$ with an additional momentum of $2\hbar k$.

$$P_{|p_1\rangle} = P_0 + \frac{A}{2}\cos(\Delta\phi), \tag{2.76}$$

where P_0 corresponds to the mean value of $P_{|p_1\rangle}$ and A to the amplitude of the fringe as depicted in Figure 2.13. In case of a double diffraction interferometer, the signal $P_{|p_1\rangle}$ is given by the relative population in the outer momentum states $|\pm 2\hbar k\rangle$ relative to the total population in all output ports $|-2\hbar k\rangle, |0\hbar k\rangle$ and $|+2\hbar k\rangle$. The sinusoidal course of the population $P_{|p_1\rangle}$ for a linear phase scan is called a "fringe".

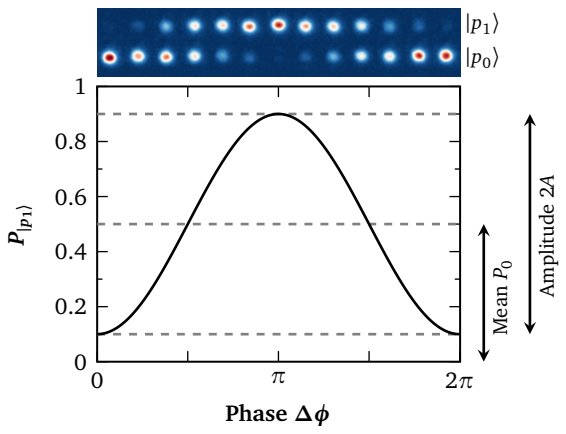

Fig. 2.13: Interferometer fringe with exemplary density images of the population in two momentum states and contrast determination $C = A/P_0$.

The interferometric contrast C is an important property since it directly influcence the sensitivity of a measurement. For a given interferometer signal P, the contrast C is determined by the amplitude A and mean P_0 and can also be expressed by the minimum P_{min} and maximum P_{max} values of $P_{|p_1\rangle}$

$$C = \frac{A}{P_0} = \frac{P_{\mathrm{max}} - P_{\mathrm{min}}}{P_{\mathrm{max}} + P_{\mathrm{min}}}. \tag{2.77}$$

The phase resolution of a fringe measurement and, thus, the sensitivity of an atom interferometer is intrinsically limited by the quantum projection noise [145], also called shot noise, which originates from the statistical nature of quantum mechanics. Since

the determination of the atom number N is essentially a Poisson process, the signal-to-noise ratio (SNR) scales with $\sqrt{N}$. For an atom interferometer with contrast C the quantum projection noise is given by

$$\sigma_{\mathrm{qpn}} = \frac{1}{\mathrm{SNR}} = \frac{1}{C\sqrt{N}}. \tag{2.78}$$

The uncertainty of an acceleration measurement is therefore given by the shot noise σ_{qpn} and the scaling factor $nk_{\mathrm{eff}}T^2$ [18]

$$\Delta a = \frac{1}{C\sqrt{N}nk_{\mathrm{eff}}T^2}. \tag{2.79}$$

From this formula it is obvious that the measurement sensitivity will not only gain through an increase of the scaling factor, but also through the operation with a large number of atoms and a higher contrast. Apart from shot noise, other intrinsic noise sources might arise from the beam splitter itself, caused for example by laser intensity fluctuations or from the detection process.

3 EXPERIMENT

I'm old. Not obsolete.

— Terminator

The QUANTUS-1 experiment has been designed to produce and observe Bose-Einstein condensates (BECs) for the first time in extended free fall in a microgravity environment. For the operation in the drop tower facility of Bremen all components required for BEC generation have been integrated into a capsule with a diameter of 0.6 m and a payload height of 1.73 m. Apart from miniaturization, the components are characterized by low mass and power consumption as well as robustness against mechanical stress and thermal fluctuations. Additionally, the experiment is remotely controllable and can be supplied independently via batteries.

In 2007, the first BEC in microgravity was successfully created with the QUANTUS-1 experiment [146]. Subsequent studies in the drop tower include the investigation and implementation of delta-kick collimation as well as atom interferometry with long interrogation times [40]. On ground, a quantum tiltmeter was demonstrated [68] as well as a gravimeter with an atomic fountain to prolong the time-of-flight [88]. For the latter, the apparatus has been equipped with an external high-power fiber laser system, which enables the realization of Bloch oscillations. Up to date, the experiment is a reliable source for Bose-Einstein condensates and produces up to $1.5 \cdot 10^4$ condensed ^{87}Rb atoms in a cycle time of 15 s.

In the following chapter, the different sub-systems including the vacuum chamber, the laser system, and the control system of the QUANTUS-1 capsule are presented briefly (sec. 3.1). A detailed description can be found in former work [125, 147–149]. Furthermore, the experimental sequence for BEC generation and the theory of Bose-Einstein condensation is introduced (sec. 3.2). A focus is set on the high power laser system employed for interferometry along the vertical and horizontal direction to perform gravimetry and symmetric large momentum transfer, respectively (sec. 3.3).

3.1 QUANTUS-1 capsule

Fig. 3.1 shows the QUANTUS-1 capsule with its seven different segments. The vacuum chamber is situated in the center of the capsule along with electronics for current control and photodiodes. The vacuum system stretches across two platforms further above. A constantly operating ion-getter pump (IGP) and a passive getter keep the pressure below 10^{-10} mbar. Apart from the IGP these platforms also house the main control system, current drivers and electronics. The laser system including its control electronics is installed on the top platform

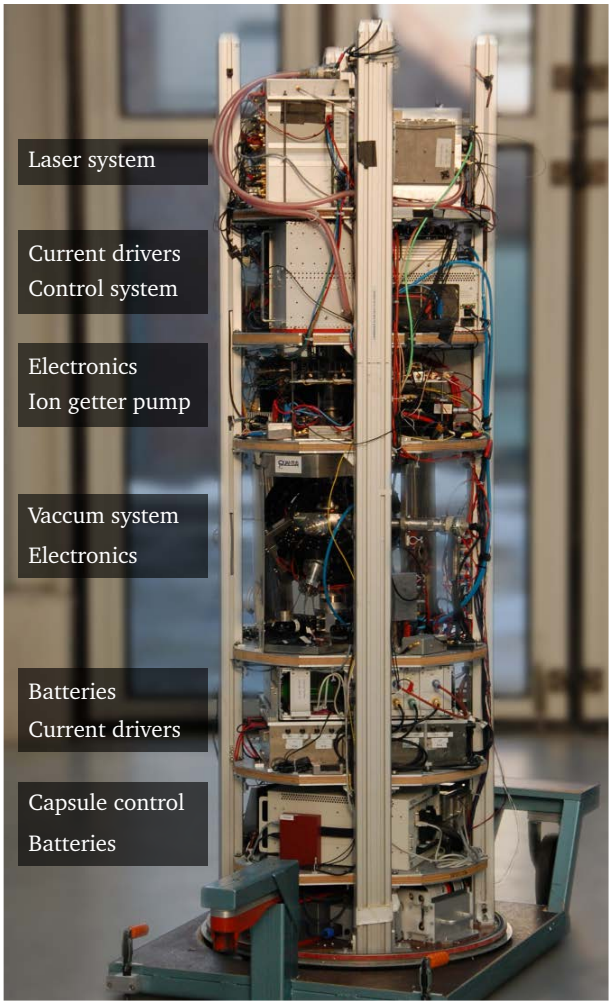

Figure 3.1: The QUANTUS-1 drop capsule with its seven segments. The main purpose of each section is written alongside. Trapping, cooling and manipulation of the rubidium atoms takes place in the vacuum chamber in the center (photography by H. Müntinga).

to allow access for alignment. Below the vacuum chamber precision current drivers for driving magnetic fields are integrated. To reduce the maintenance effort their supply has recently been changed from batteries to power-supply units since an independent operation is no longer necessary. The two lowest sections house the capsule control system, power supply, and sensor packs for monitoring and are common to every drop-tower capsule.

3.1.1 Vacuum chamber

The ultra-high vacuum (UHV) chamber consists of a six-way cross extended by two tubes at an angle of 45° as illustrated in Figure 3.2(a). At its ends, anti-reflection coated viewports are integrated. The vacuum system is made of non-magnetic stainless steel to minimize inductivity and its components are connected via robust copper seals (CF type). It is solely attached to the platform above to prevent mechanical stress which might lead to leakage. All magnetic coils as well as optical assemblies are directly fixed to the chamber to guarantee a rigid alignment.

The largest coil pair, the so-called MOT coils, is connected in anti-Helmholtz configuration and provides a magnetic field gradient for the magneto-optical trap (MOT) during the initial cooling phase. The coil pairs in x, y, and z direction are labeled K1, Bias and K2, respectively, and create homogeneous offset fields. All detection optics are integrated along the x direction. The axis is shared with two cooling beams which are superposed with the detection light on polarizing beam splitters (PBS). Together with two other laser beams reflected at an angle of 45° from the chip surface all six beams for 3D cooling are thus provided (see Fig. 3.5). The interferometer beams are aligned horizontally and vertically, in y and z direction. In the latter case, the chip serves as retroreflector.

At the bottom of the chamber, an electrical feedthrough supplies the rubidium dispenser mounted inside the chamber. Around the vacuum chamber, a μ-metal shielding consisting of seven individual parts is installed which suppresses external magnetic fields by a factor of roughly 40 [147].

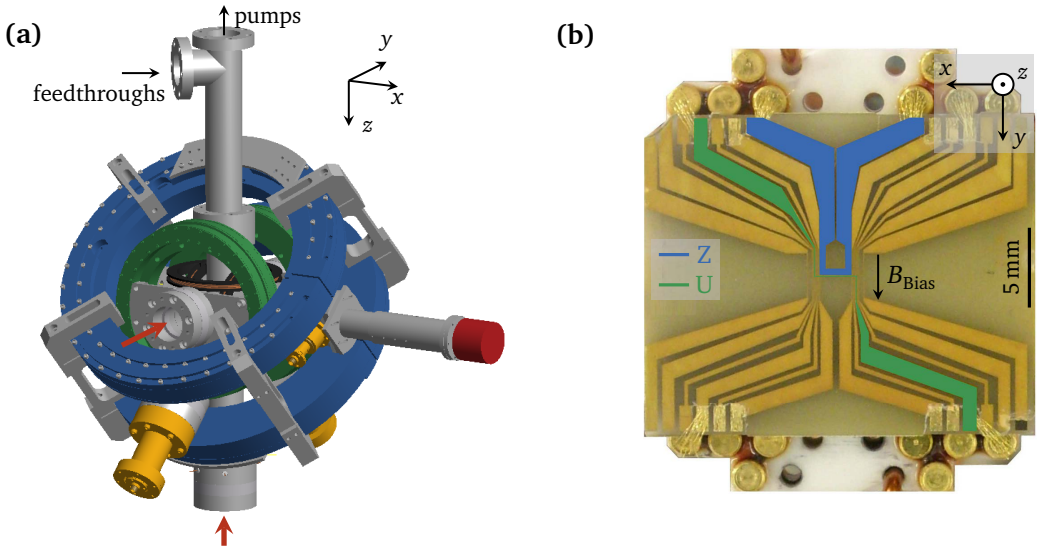

Figure 3.2: (a) Vacuum chamber with highlighted MOT coils (■), Bias coils (■), MOT telescopes (■) and camera for detection (■). Horizontal and vertical interferometry accesses are marked by thick red arrows. The associated optics are not included for clarity. (b) Photograph of the atom chip with Z-type (—) and U-type (—) wire configuration. An offset field can be generated by the Bias coils.

Atom chip

The main ingredient for fast and efficient BEC production within the QUANTUS-1 experiment is an atom chip located at the top of the vacuum chamber and aligned horizontally. Compared to macroscopic coils atom chips exhibit a small size, low power consumption and provide high spatial confinement of the atomic ensemble [150, 151]. The latter is important for high collision rates during the evaporation process. Figure 3.2(b) shows the atom chip surface featuring different structures. The two highlighted ones of U and Z shape are used for the creation of a quadrupole field and a Ioffe-Pritchard trap [152, 153], respectively. The Z-wire is additionally used as an antenna for a radio frequency signal required for evaporative cooling

and magnetic state transfer. The structures are bonded to gold contacts ending in Copper wires covered in Kapton. On top of the conductive paths a dielectric coating with a reflectance of roughly 85% for a wavelength of 780 nm serves as a mirror for laser beams employed for cooling and interferometry. The chip is mounted on a copper structure which acts as a heatsink and is fixed to a vacuum flange containing an electrical feedthrough with a D-sub-9 connector for the power supply.

To minimize current noise, the atom chip as well as the coils are driven by low-noise current sources `BCSP-7` by `HighFinesse`. Until october 2018, they have been supplied by a set of lead-acid batteries. Currently, the chip drivers are powered with customized power supplies fabricated by `HighFinesse`, whereas the coil drivers are supplied by commercial power-supply units (`R&S HMP4040`). To protect the atom chip from high currents, which might cause serious damages, fuses and safety electronics are installed in the electronic circuit [125].

Magnetic trap

In the presence of a magnetic field **B** the energy of an atom with a magnetic dipole moment is shifted by

$$U = g\mu_B m_F |\mathbf{B}|, \tag{3.1}$$

where g is the Landé factor, μ_B the Bohr magneton and m_F the magnetic quantum number belonging to the hyperfine state $|F\rangle$ [114]. By applying an inhomogeneous magnetic field which causes a magnetic dipole force $\mathbf{F} = \nabla U$ atoms can either be trapped in a magnetic maximum ($g_F m_F < 0$) or a magnetic minimum ($g_F m_F > 0$). The most simple trap configuration with a magnetic field minimum, the quadrupole trap, can be realized with a pair of anti-Helmholtz coils. However, it features a vanishing magnetic field in the center which leads to atom losses due to Majorana spin-flips [154, 155].

A Ioffe-Pritchard trap (IPT), first discussed by Ioffe [152] and later demonstrated by Pritchard for neutral atoms [153, 156], is broadly used in the field of atom trapping. It features an axial symmetry and is characterized by a nonzero minimum to suppress Majorana transitions as well as a harmonic potential in the vicinity of the trap center of the form

$$V(x,y,z) = \frac{m}{2}(\omega_x x^2 + \omega_y y^2 + \omega_z z^2), \tag{3.2}$$

where $\omega_{x,y,z}$ are the respective trap frequencies.

Magnetic traps can also be generated by wire structures in combination with an external homogeneous bias field. The magnetic field created by an infinitely thin wire along the x-axis carrying a current I_0 depends on the distance r perpendicular to the wire axis (Fig. 3.3). Its magnitude, gradient and curvature are given by [157]

$$B(r) = \frac{\mu_0}{2\pi}\frac{I_0}{r}, \qquad B'(r) = -\frac{\mu_0}{2\pi}\frac{I_0}{r^2}, \qquad B''(r) = \frac{\mu_0}{\pi}\frac{I_0}{r^3}. \tag{3.3}$$

For small values of r the magnetic field features a strong gradient and curvature beneficial for a high atomic confinement. The local minimum required for trapping atoms can be created by an additional homogeneous field B_y in y direction, perpendicular to the wire axis. At distance z_0 a guide for neutral atoms with zero magnetic field is formed

$$z_0 = \frac{\mu_0}{2\pi}\frac{I_0}{B_y}. \tag{3.4}$$

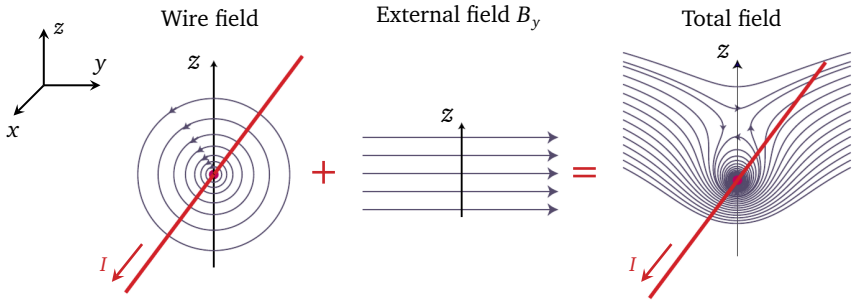

Figure 3.3: Composition of the magnetic field used for two-dimensional trapping, generated by a wire and an external field. Adapted from [150].

Close to the center of this 2D trap the total field can be approximated by a two-dimensional quadrupole field with gradient $B'(z_0) = -\frac{\mu_0}{2\pi}\frac{B_y^2}{I_0}$. By adding another homogeneous field B_x in x direction, the trap can be transformed into a Ioffe-Pritchard guide exhibiting a nonzero minimum.

In case of the QUANTUS-1 atom chip 3D confinement is produced by the U and Z wire in combination with a uniform field B_{Bias} provided by the Bias coils in y direction. The central wire segment along the x-axis and the bias field produce a two-dimensional quadrupole trap as stated before. The additional bent components in y direction provide axial confinement, which is weaker than the confinement in radial direction. In case of the U-shaped wire the magnetic fields of the two bent wires point in opposite direction and cancel each other. The resulting 3D quadrupole trap with a vanishing magnetic field in the center is used as a chip MOT. Since the fields of the bent components of the Z wire add up, the zero minimum vanishes and a chip-based Ioffe-Pritchard trap is created.

3.1.2 Laser system for cooling, trapping and detection

The laser system for cooling, trapping, and detection is installed in a water-cooled aluminum block in the top section of the capsule. Robust and compact distributed feedback (DFB) diodes with a line width of approximately 3 MHz generate the laser light. The laser system consists of the following four modules which are connected via single-mode polarization-maintaining (PM) fibers

- A **reference** laser is stabilized by modulation transfer spectroscopy [160] to the transition $|5^2S_{1/2}, F = 3\rangle \rightarrow |5^2P_{3/2}, F' = 4\rangle$ of ^{85}Rb.
- A DFB diode, the so-called **cooling** laser, is amplified by a tapered amplifier (TA) and provides light for cooling, detection, and pumping of ^{87}Rb. During the MOT phase, the laser is red-detuned by 23 MHz from resonance. Afterwards, it is used to optically pump different Zeeman states into $|F = 2, m_F = 2\rangle$ by using a cycling transition $|F = 2, m_F = j\rangle \rightarrow |F = 2, m_F = j + 1\rangle$. Finally, the laser is tuned to resonance for detection. A direct-digital synthesizer (DDS) provides the reference frequency for the offset lock with the master laser and allows for fast switching between the different frequencies.

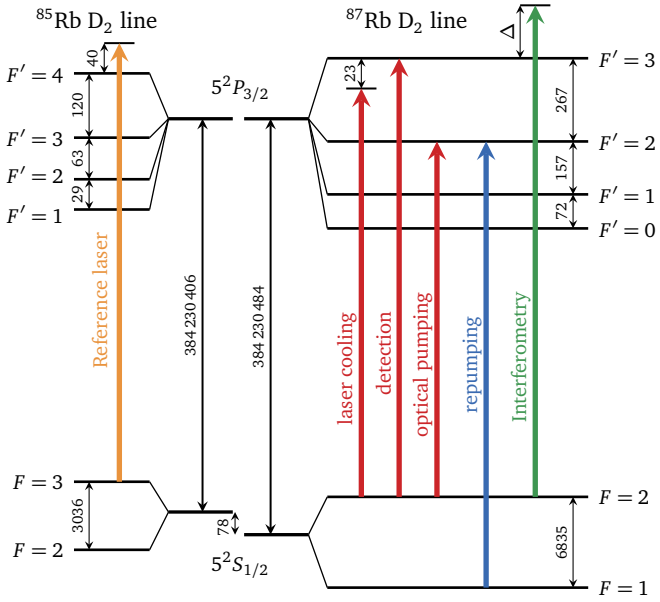

Figure 3.4: Scheme of the D_2 transition of ^{85}Rb and ^{87}Rb including hyperfine structure. All frequencies are given in MHz [158, 159]. The colored arrows depict the laser frequencies employed in the experiment. Each color resembles one laser source.

- A so-called **repumper** laser is stabilized to the reference laser via electronic offset locks to $|F = 1\rangle \rightarrow |F' = 2\rangle$ of ^{87}Rb. The laser transfers atoms back to the cooling cycle, which have been lost to the hyperfine state $|F = 1\rangle$.

- Light from the three modules described above is guided to a module for **distribution** and switching of the laser light. Within this module, a few mW of the repumping and cooling light are split off and superimposed with the reference laser on one photodiode each for frequency stabilization. Another fraction of the cooling light is separated and coupled into an optical fiber serving both for detection and optical pumping. The rest of the cooling light is divided into four beams, superimposed with the repumper and coupled into four fibers. The paths for repumping, cooling, and detection each house an acousto-optic modulator (AOM) for intensity adjustment. In addition, mechanical shutters in front of each output can completely block the light.

From the distribution module, five PM fibers, four for cooling and one for detection, are guided to the vacuum chamber. They are attached to the respective viewports where they are collimated to a $1/e^2$ diameter of 16 mm and 10 mm, respectively. The laser frequencies employed within the QUANTUS-1 experiment are depicted in Fig. 3.4 with respect to the D_2 transitions of ^{85}Rb and ^{87}Rb.

Absorption detection

The optics for detection are arranged along the x direction resulting in an image acquisition of the $y-z$ plane. The detection light, resonant to the $|5^2S_{1/2}, F = 2, m_F = 2\rangle \rightarrow |5^2P_{3/2}, F = 3, m_F = 3\rangle$ transition and of σ^+ polarization, is collimated via a lens to a $1/e^2$ diameter of 10 mm and an approximate intensity of 0.25 mW/cm^2 (0.15 I_{sat}). The atom's

shadow is projected onto a CCD camera (`Grasshopper GS3-U3-15S5M-C`) by a single imaging lens with $f = 80\,\mathrm{mm}$. The image sensor has a resolution of 1384×1032 pixels with a pixel size of $6.45\,\mu\mathrm{m}$. The corresponding extent of 6.7 mm in z direction sets a limit to the maximally observable time-of-flight of the atomic cloud.

During detection, a quantization field of 8 G is generated by the K1 coils parallel to the detection axis. In each sequence two images are taken with an interval of 200 ms, namely an atom image I_{atom} including the shadow of the cloud and a beam image I_{beam} in the absence of any atoms. Both images are corrected by a dark image I_{dark} recorded once a day with all lasers switched off. The two-dimensional atomic density distribution n is reconstructed via substracting atom and beam image which allows the elimination of beam distortions such as interferences.

Beer's law describes the absorption of an incident beam with intensity I detuned by Δ from resonance for a two-level atom with cross-section σ_0 [159, 161]

$$\frac{\mathrm{d}I}{\mathrm{d}x} = -n\sigma_0 \frac{1}{1 + I[I_{\mathrm{sat}}] + 4(\Delta[\Gamma])^2} I \equiv -n\sigma(I)I. \tag{3.5}$$

where I_{sat} is the saturation intensity, Γ the natural linewidth and $\sigma(I)$ the effective cross section including saturation correction. The column density $\tilde{n}(y,z)$, i.e. the atomic density integrated perpendicular to the camera, can be extracted from the detected intensities in the three recorded images

$$\tilde{n} = \frac{1}{\sigma_0}(1 + 4(\Delta[\Gamma])^2)\left[\ln\left(\frac{I_{\mathrm{beam}}}{I_{\mathrm{atom}}}\right) + \frac{I_{\mathrm{beam}} - I_{\mathrm{atom}}}{I_{\mathrm{sat}}}\right]. \tag{3.6}$$

In order to account for the actual response of the atoms, an effective saturation intensity $I_{\mathrm{sat}}^{\mathrm{eff}} = \alpha^* I_{\mathrm{sat}}$ is required. The dimensionless parameter α^* considers corrections caused e.g. by imperfect polarization of the imaging beam or different Zeeman states.

From the absorption image, parameters such as particle number and size of the atom cloud are calculated by fitting a suitable function to the integrated column density [125]. Whereas the form of a Bose-Einstein condensate ideally equals an inverted parabola, a thermal background is of Gaussian shape. A combination of both can be described by a bimodal distribution. Absolute atom numbers and sizes, however, are prone to errors in context with magnification and atomic density calculation. Furthermore, atom number fluctuations in the order of 10-20% occur due to shot-to-shot variations of experimental parameters.

If a beam splitter is applied or an atom interferometer is realized, one does not detect a single atom cloud but rather different, spatially separated momentum states. In order to measure the diffraction efficiency, i.e. the relative population between two states, one can fit two individual Gaussians to determine the absolute atom number in each state. Since the offset of the Gaussian fit critically depends on the size and position of the selected image region, it is usually not common for both of these fits. This leads to an uncertainty in the calculated relative population of both states. Alternatively, it is possible to fit a function consisting of two Gaussian distributions with identical offset to the absorption image [125], a so-called double Gaussian fit. This evaluation suffers from less noise compared to two individual fits.

3.1.3 Control

The computer installed in the drop capsule enables remote control of the experiment [147]. A PXI system (`National Instruments, PXI-1000B`) operating with a `LabVIEW` Real-Time system controls the experimental sequence and allows for a timing precision on the µs level. Different digital and analog inputs and outputs are provided by extension cards to control laser frequencies, electronic switches, and current sources. The radio frequency signals required for evaporation and magnetic state transfer are controlled via a self-built DDS card (`AD9958`). The same type is used to control the AOMs for frequency and intensity shaping of the interferometry pulses. A timed sequence can be created via a graphical user interface on an external system and is loaded into the memory of the PXI system via Ethernet.

3.2 Generation of Bose-Einstein condensates

3.2.1 Experimental sequence for BEC generation

In the following, a typical experimental sequence for BEC generation is sketched. It consists of trapping and cooling thermal rubidium atoms in a magneto-optical trap, transfer to a chip-based Ioffe-Pritchard trap and final phase transition to a Bose-Einstein condensate via forced radio-frequency (RF) evaporation. The sequence was optimized in previous work [147, 148] and has only undergone slight modifications since then.

Magneto-optical trap and transfer to chip trap

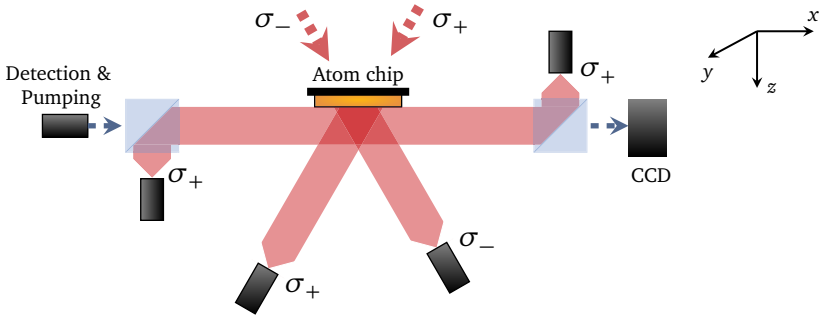

Figure 3.5: Scheme of the cooling light for the magneto-optical trap in QUANTUS-1 formed by four laser beams with circular polarization. Two of them are reflected from the atom chip at an angle of 45°. The detection axis is sketched as well.

A sequence starts with a 3D magneto-optical trap (MOT) [162, 163] which is loaded from the background gas with ^{87}Rb. During the MOT, dispensers evaporate rubidium to increase its partial pressure in the chamber. Absorption of the counterpropagating cooling light, red-detuned with respect to the $|F = 2, m_F = 2\rangle \rightarrow |F' = 3, m_F = 3\rangle$ transition, decelerates the atoms. Two counterpropagating beams in x direction along with two beams reflected from the atom chip provide cooling in all three dimensions as illustrated in Figure 3.5. Additionally, a magnetic quadrupole field produced by the anti-Helmholtz coils confines the atoms locally. During the MOT the repumping laser retrieves atoms relaxed into $|F = 1\rangle$ back to the cooling

cycle. Loading from the background vapor requires a relatively long MOT duration of 10 s compared to setups with an additional 2D-MOT [83] and results in $2 \cdot 10^7$ atoms at a temperature of 200 μK.

Afterwards, the dispenser is turned off and the trap center is moved closer to the atom chip by a shift of the magnetic offset fields. A MOT based on the U-wire is formed which features a smaller trap volume but also a better confinement for better position control compared to the macroscopic MOT. Due to the small lifetime the trap center is moved shortly afterwards to the position of the Ioffe-Pritchard trap with about $1 \cdot 10^7$ remaining atoms in the trap.

Optical molasses and state preparation

The minimum temperature T_D in a MOT is fundamentally limited by the Doppler limit $T_D = \hbar\Gamma/(2k_B)$ with linewidth Γ, which equals 145 μK in case of ^{87}Rb [164]. Lower temperatures required for efficient loading of the magnetic trap can be reached through an optical molasses, also known as polarization gradient cooling [165]. Due to its sensitivity to magnetic forces, all magnetic fields are switched off and residual fields are compensated with the coil pairs in x, y, and z direction (K1, Bias, K2). The short molasses phase of 4 ms results in $6 \cdot 10^6$ atoms at a temperature of 20 μK.

Up to now, the atomic ensemble is constituted of different hyperfine states. For trapping in a purely magnetic trap, the atomic ensemble is optically pumped during 0.7 ms into the state $|5^2S_{1/2}, F = 2, m_F = +2\rangle$ which exhibits the highest magnetic moment within the $5^2S_{1/2}$ level. For the transfer solely the σ^+ polarized pumping beam along the x direction is employed.

Evaporation and release trap

Laser cooling does not suffice to reach the required phase-space density for Bose-Einstein condensation. The final step towards the phase transition is therefore achieved via evaporative cooling [166]. Evaporation takes place in a Ioffe-Pritchard trap produced by the Z-wire with $I_Z = 2A$ and a bias field. An additional magnetic field in x direction $I_{K1} = 1.6A$ lifts the trap floor. The Z-wire serves as an antenna for a radio frequency f_{evap}, which is resonant to the most energetic atoms and drives a spin-changing transition. The atomic state is thereby switched to a high-field seeking one which are expelled from the trap. The following rethermalization requires a high collision rate and results in a reduced temperature. During the whole evaporation cycle of 1.24 s, f_{evap} is ramped down stepwise from 40 MHz to 1.83 MHz. This evaporation process results in large losses with a final atom number of 25 000 and a condensate fraction of roughly 50%.

I_{Bias}	f_x (Hz)	f_y (Hz)	f_z (Hz)
0.36 A	17	47	31
0.6 A	18	131	127
1 A	43	344	343

Table 3.1: Release trap frequencies for different geometries taken from [125].

After evaporation the trap is adiabatically decompressed to increase its lifetime and decrease the expansion rate during free evolution. At the same time, f_{evap} is ramped up again to expel residual thermal atoms. Finally, atoms are transferred to the release trap. Its trap frequency can be adjusted with the bias current I_{Bias} as summarized in Table 3.1. The trap frequencies are measured via variation of the duration of the release trap (sec. 4.1.1). For a free evolution

of the condensate, all magnetic fields are switched off except for a weak homogeneous field in x direction remaining as a quantization axis.

3.2.2 Bose-Einstein condensates

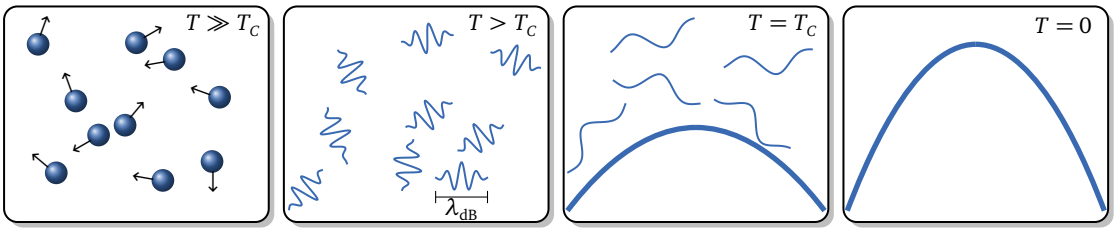

Figure 3.6: Phase transition to a Bose-Einstein condensate. As the temperature decreases, the wave packets of the bosonic particles begin to spatially overlap resulting in a macroscopic matter wave [167].

Bose-Einstein condensates (BEC) represent a unique state of matter where quantum phenomena can be investigated on macroscopic scales. The statistical appearance, characterized by a macroscopic occupation of the lower energy state, was already predicted in 1924 by Bose and Einstein [79, 80]. Experimental demonstration was not done before 1995, when three groups almost simultaneously achieved condensation in dilute atomic gases for rubidium [76], sodium [77], and lithium [78]. Following the notation of [164] a brief overview of the theory of Bose-Einstein condensation is given here.

The phenomenon relies on the wave-particle duality where particles with mass m are described by the thermal de Broglie wavelength

$$\lambda_{\mathrm{dB}} = \sqrt{\frac{2\pi\hbar^2}{m k_{\mathrm{B}} T}}, \tag{3.7}$$

where k_B is the Boltzmann constant. In a vivid picture, quantum effects can be observed when λ_{dB}, which is decreasing with temperature T, becomes comparable to the mean interparticle spacing $n^{-1/3}$, depending on the density n [167]. In other words, Bose-Einstein condensation occurs, when the wave packets of bosonic particles start to spatially overlap and the system can be described by a single wave function (Fig. 3.6). This is given for a phase-space density of $\rho = n\lambda_{\mathrm{dB}}^3 \geq 2.612$. The critical temperature T_C for Bose-Einstein condensation is approximately given by

$$T_C \approx n^{2/3} \frac{2\pi\hbar^2}{m k_{\mathrm{B}}}. \tag{3.8}$$

Quantum behavior in atomic gases can thus only be observed for low temperatures and sufficiently high densities.

Non-interacting Bose gas in a harmonic trap

A BEC of dilute atomic gases is usually generated in a trap, which is approximately harmonic around its center. The simple treatment of a non-interacting Bose gas in a harmonic potential already yields important properties such as transition temperature and condensate fraction.

For this purpose, the density of states $g(\epsilon)$ has to be derived. The Bose distribution describes the mean occupation number in thermodynamic equilibrium depending on the energy ϵ of a single-particle state and the chemical potential μ

$$f(\epsilon) = \frac{1}{\mathrm{e}^{(\epsilon-\mu)/k_\mathrm{B}T} - 1}. \tag{3.9}$$

μ corresponds to the energy required to add a particle to the ensemble and it cannot be larger than the ground state energy ϵ_0 which would result in an unphysical negative occupation. For an anisotropic harmonic potential according to Eq. (3.2) the density of states $g(\epsilon)$ is given by

$$g(\epsilon) = \frac{\mathrm{d}G(\epsilon)}{\mathrm{d}\epsilon} = \frac{\epsilon^2}{2\hbar^3\omega_x\omega_y\omega_z}. \tag{3.10}$$

In the limit of a large particle number N ($N \to \infty$) we can approximate $\epsilon_0 \approx 0$ and calculate the atom number in excited states N_ex through integration over the occupation number $f(\epsilon)$ and the density of states $g(\epsilon)$

$$N_\mathrm{ex} = \int_0^\infty f(\epsilon)g(\epsilon)\mathrm{d}\epsilon. \tag{3.11}$$

N_ex reaches its largest value for $\mu = 0$. Exactly before the phase transition at temperature T_C the total number of particles N is accomodated in excited states. Evalutating the integral in (3.11) at $\mu = 0$ yields the critical temperature T_C

$$\begin{aligned} N = N_\mathrm{ex}(T_C, \mu = 0) &= \zeta(3)\left(\frac{k_\mathrm{B}T_C}{\hbar\bar{\omega}}\right)^3 \\ k_\mathrm{B}T_C &= \frac{\hbar\bar{\omega}N^{1/3}}{[\zeta(3)]^{1/3}} \approx 0.94\hbar\bar{\omega}N^{1/3}, \end{aligned} \tag{3.12}$$

with the Riemann zeta function $\zeta(\alpha) = \sum_{n=1}^{\infty} n^{-\alpha}$ and the geometric mean of the trap frequencies $\bar{\omega} = (\omega_x\omega_y\omega_z)^{1/3}$. For typical trap frequencies of $\bar{\omega} \approx 2\pi \cdot 100\,\mathrm{Hz}$ and an atom number of 10^4 the transition temperature is $T_C \approx 100\,\mathrm{nK}$. Below the transition temperature the number of particles in the condensate N_0 is determined solely by the temperature T

$$N_0 = N\left[1 - \left(\frac{T}{T_C}\right)\right]. \tag{3.13}$$

The corresponding ground-state wave function, which describes the condensate in an anisotropic harmonic oscillator is given by

$$\phi_0(\mathbf{r}) = \frac{1}{\pi^{3/4}(a_1a_2a_3)^{1/2}}\mathrm{e}^{-x^2/2a_x^2}\mathrm{e}^{-y^2/2a_y^2}\mathrm{e}^{-z^2/2a_z^2} \quad \text{with} \quad a_i = \sqrt{\frac{\hbar}{m\omega_i}}, \tag{3.14}$$

where a_i is the width of the wave function in one dimension. The condensate's width a_i changes considerably when taking into account atom-atom interactions as illustrated in the next section.

Gross-Pitaevskii equation and Thomas-Fermi approximation

So far, interparticle interactions have been neglected. The interaction strength between two particles at low energies depends on the scattering length a and is given by $g = \frac{4\pi\hbar^2 a}{m}$. A cloud of alkali vapours is dilute in the sense that particle separations are large compared to the scattering length a. In this case, the properties of a Bose gas at zero temperature are described by the Gross-Pitaevskii equation. In a mean-field or Hartree-Fock approximation we write the total N-particle wave function as the product of normalized single-particle wave functions

$$\Psi(\mathbf{r_1}, \mathbf{r_2}, ..., \mathbf{r_N}) = \prod_{i=1}^{N} \phi(\mathbf{r_i}). \tag{3.15}$$

For an effective interaction $g\delta(\mathbf{r} - \mathbf{r}')$ between two nearby atoms the Hamiltonian in an external potential $V(\mathbf{r})$ yields

$$H = \sum_{i=1}^{N} \left[\frac{\mathbf{p}_i^2}{2m} + V(\mathbf{r_i}) \right] + g \sum_{i<j} \delta(\mathbf{r_i} - \mathbf{r_j}). \tag{3.16}$$

Minimization of the mean energy under the condition of a constant particle number, i.e. $\int |\phi(\mathbf{r})|^2 \mathrm{d}\mathbf{r} = 1$ results in the time-independent Gross-Pitaevskii equation

$$\left(-\frac{\hbar^2}{2m}\nabla^2 + V(\mathbf{r}) + U_0 |\psi(\mathbf{r})|^2 \right) \psi(\mathbf{r}) = \mu\psi(\mathbf{r}), \tag{3.17}$$

where $\psi(\mathbf{r}) = \sqrt{N}\phi(\mathbf{r})$ is the condensate wave function and $n(\mathbf{r}) = |\psi(\mathbf{r})|^2$ is the density of particles. The Gross-Pitaevskii equation has the same form as the Schrödinger equation, where the potential is composed of an external contribution V and a non-linear term $U_0|\psi(\mathbf{r})|^2$ describing the mean-field potential of the other atoms. The eigenvalue is the chemical potential μ, which is only equal to the energy per particle for $g = 0$.

In a harmonic trap with a large number of atoms and repulsive interactions, the kinetic energy is small compared to the potential one. In the Thomas-Fermi approach, the kinetic term $\frac{\hbar^2}{2m}\nabla^2$ in (3.17) is neglected. For $\mu \geq V(\mathbf{r})$ one receives as solution

$$n(\mathbf{r}) = |\psi(\mathbf{r})|^2 = [\mu - V(\mathbf{r})]/U_0, \tag{3.18}$$

while $\psi = 0$ for $\mu < V(\mathbf{r})$. The atomic density profile therefore corresponds to an inverted parabola. Eq. (3.18) describes a uniform gas with density $n(\mathbf{r})$, where the energy μ for adding a particle to the system is constant over the cloud and is given by the sum of the external potential $V(\mathbf{r})$ and the interaction term $U_0 n(\mathbf{r})$. In case of a harmonic potential (3.2) the cloud size is given by the Thomas-Fermi radius R_i, which is inversely proportional to the trap frequency ω_i

$$R_i^{\mathrm{TF}} = \frac{1}{\omega_i}\sqrt{\frac{2\mu}{m}} = \left(\frac{15N\hbar^2 a}{m^2\omega_i^2} \right)^{1/5} \quad \text{with} \quad \mu = \frac{\hbar\bar{\omega}}{2}(15Na)^{2/5}\left(\frac{m\bar{\omega}}{\hbar} \right)^{1/5}. \tag{3.19}$$

Free expansion of the BEC

After release from the confining potential, in free fall, mean-field energy is converted into kinetic energy and the Thomas-Fermi approximation is no longer valid for describing the expansion of the condensate. The temporal evolution of the condensate is determined by solving the time-dependent Gross-Pitaevskii equation. This can be done via a scaling approach [168, 169], where the initial size of the ensemble $R_i(t=0)$ merely increases by a scaling parameter $\lambda_i(t)$

$$R_i(t) = R_i(0)\lambda_i(t). \tag{3.20}$$

Hereby, the scaling parameters should satisfy the following differential equations

$$\ddot{\lambda}_i = \frac{\omega_i^2(0)}{\lambda_i\lambda_x\lambda_y\lambda_z} - \omega_i^2(t)\lambda_i. \tag{3.21}$$

If the trap is switched off instantaneously at time $t=0$ upon release, $\omega_i(t>0)=0$ and the solutions to the differential equations yield

$$\lambda_i(t) = \sqrt{1+\omega_i^2(0)t^2}. \tag{3.22}$$

Experimental proof of Bose-Einstein condensation can be achieved through its characteristic shape during free expansion. Anisotropic trap frequencies initially lead to an anisotropic spatial spread of the cloud, which is inversely proportional to the respective trap frequencies. During free expansion mean-field energy causes an expansion rate increasing with the trap frequencies which leads to an inversion of the aspect ratio [76, 77]. In contrast, thermal atoms spread isotropically.

1D reduced Gross-Pitaevskii model

In the scope of this thesis experimental measurements of Bose-Einstein condensates in an optical lattice are compared to numerical calculations. These are based on an effective 1D reduced Gross-Pitaevski model [170, 171] which is derived from the time-dependent 3D Gross-Pitaevski equation describing the dynamics of the N-particle wave function $\Psi(\mathbf{r},t)$ [164]

$$i\hbar\frac{\partial}{\partial t}\Psi(\mathbf{r},t) = \left[-\frac{\hbar^2}{2m}\nabla^2 + V(\mathbf{r},t) + gN|\Psi(\mathbf{r})|^2\right]\Psi(\mathbf{r}) \tag{3.23}$$
$$\text{with} \qquad \int |\Psi(\mathbf{r})|^2 \mathrm{d}\mathbf{r} = 1.$$

The 1D reduced Gross-Pitaevski model represents a simplified description for Bose-Einstein condensates in potentials with cylindrical symmetry of the form

$$V(\mathbf{r}) = V_x(x,t) + \frac{1}{2}m\left(\omega_y^2(t)y^2 + \omega_z^2(t)z^2\right). \tag{3.24}$$

Compared to a 3D model it leads to a significant reduction of computation time required for numerical calculations while still providing a very good agreement with the experimental data.

In the following we will consider the potential of an optical lattice created by Gaussian shaped laser beams travelling along the x direction. In the axial direction the periodic potential is described as

$$V_x(t) = V_0 \cos^2(kx + \phi(t)). \tag{3.25}$$

The confinement in the transverse direction is much weaker and given by

$$V_\perp(t) = -A(t) \exp\left\{-2\left(\frac{y^2}{w_y^2(x,t)} + \frac{z^2}{w_z^2(x,t)}\right)\right\}. \tag{3.26}$$

Due to the divergence of the beam profile the beam waist $w_{y,z}$ depends on the axial position x. In a harmonic approximation it is given by the transverse trapping frequencies $\omega_{y,z}$

$$w_{y,z}^2(t) = \frac{4A}{m\omega_{y,z}^2}. \tag{3.27}$$

For the variational approach the following separation ansatz for $\Psi(\mathbf{r})$ is chosen

$$\Psi(x,y,z,t) = \phi(x,t) G_{\eta_y}(y,t) G_{\eta_z}(y,t), \tag{3.28}$$

where G_i are Gaussian functions with widths $\eta(x,t)$. Evaluation of the quantum least action principle results in a set of three coupled equations which can be used to find a numerical solution for the dynamics of BECs in an optical lattice [171].

3.3 High-power laser system

You find beauty in a well-aligned optical system.

— Fortune cookie.

In the QUANTUS-1 experiment, a commercial frequency-doubled fiber laser system (`NKT Koheras BOOSTIK`) serves as a light source for interferometry. The high power system enables the implementation of higher-order Bragg diffraction as well as manipulation in an optical lattice via Bloch oscillations and, thus, offers a lot of possibilities to explore advanced interferometer schemes. Additionally, it allows for the operation at large detunings Δ from atomic resonance to lower spontaneous emission. The operation at a center wavelength of 1560 nm, which is widely used in telecommunication, offers a range of sophisticated commercially available lasers along with corresponding components such as modulators or switches [173].

Fig. 3.7: High power laser system `NKT Koheras BOOSTIK` consisting of a narrow linewidth laser on top of an amplifier with an output power of 10-15 W (image by NKT Photonics [172]).

The 19-inch rack system contains an Erbium-doped fiber laser (`ADJUSTIK E15`) with an output power of 40 mW. It features low phase and frequency noise (3.2 µrad/$\sqrt{\text{Hz}}$/m @ 100 Hz) as well as an ultra-narrow linewidth below 100 Hz and provides a thermal tuning

range of roughly ±1 nm. It is supplemented by a 10 W fiber amplifier. Due to a malfunction of the amplifier in august 2017, the system was replaced by another BOOSTIK system consisting of an ADJUSTIK C15 in combination with a 15 W amplifier. The ADJUSTIK C15 offers the lowest intensity noise within the product range. Compared to the E15 it exhibits lower output power (> 10 mW), larger phase noise (36 µrad/$\sqrt{\text{Hz}}$/m @ 100 Hz) and a broader linewidth, which is stated to be smaller than 15 kHz. The measurements presented within this thesis have been obtained with both of these systems.

The 10 W of 1560 nm light, emitted from the Boostik system, are frequency doubled in a Toptica SHG PRO which houses a bow-tie cavity to resonantly enhance the laser power. Its length is stabilized via the Pound-Drever-Hall method [174] to ensure large enhancement factors. In combination with a non-linear optic crystal comparably large conversion efficiencies of 40%-60% can be achieved. Electronics for locking and temperature control are accommodated in a 19-inch rack (Toptica Sys DC 110). Up to 5 W of 780 nm light is distributed, coupled into fibers and guided to the experiment (see sec. 3.3.1). At the vacuum chamber variable optical assemblies ensure a proper adjustment of the collimated laser beams relative to the atomic ensemble (sec. 3.3.2).

3.3.1 Distribution module

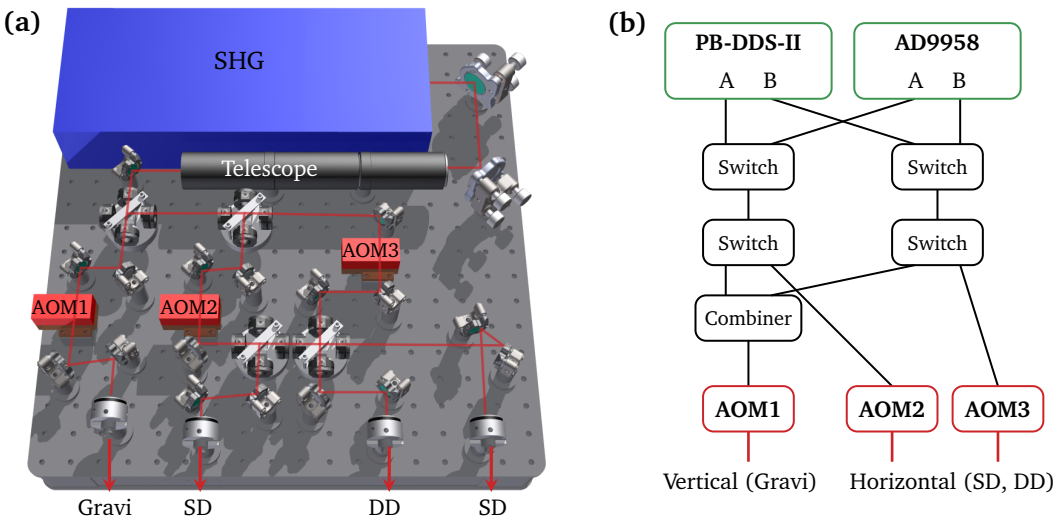

Figure 3.8: (a) Distribution module for splitting and coupling the light into four fibers for interferometry along gravity (Gravi) as well as for single diffraction (SD) and double diffraction (DD) in the horizontal direction. (b) The RF frequencies for the AOMs are either provided by a PulseBlasterDDS-II-300-AWG or a self-built Analog Device AD9958. Each device features two independent output channels A and B.

The frequency-doubling stage (SHG) as well as the components for distributing and switching the light are mounted on a breadboard (Thorlabs Nexus, Fig. 3.8(a)) featuring a high thermal stability and damping against vibrations. These properties are important for the stability of the optomechanical components and the cavity lock. After leaving the SHG the laser beam's size is reduced via a 4:1 telescope to a diameter of roughly 1 mm. Via half-wave plates and polarizing beam-splitter (PBS) cubes the light is distributed to three AOMs (AA

Opto Electronic MT80-A1.5-IR) which diffract light at a base frequency of 80 MHz. The distribution module offers different possibilities for beam splitting:

- A single AOM generates the light field for beam splitting in the vertical direction which contains two frequency components with parallel polarization and a power of approximately 300 mW.
- The other two AOMs serve for manipulation of the atomic clouds along the horizontal direction.
  - For symmetric double diffraction along the y-axis, two frequency components generated by two independent AOMs are superimposed on a PBS with orthogonal polarization. The combined beams are coupled into a single fiber with a total power of up to 1.2 W.
  - Two other fiber outputs each provide light with one frequency component for single diffraction with a power of 100 mW in each fiber.

The laser light is guided to the vacuum chamber via polarization-maintaining single mode fibers (SuK PMC-850-5,1-NA13-3-APC-700-P). Bi-stable shutter devices (Uniblitz TS6B) with reflective AlMgF2 coatings can completely block the light in front of each output.

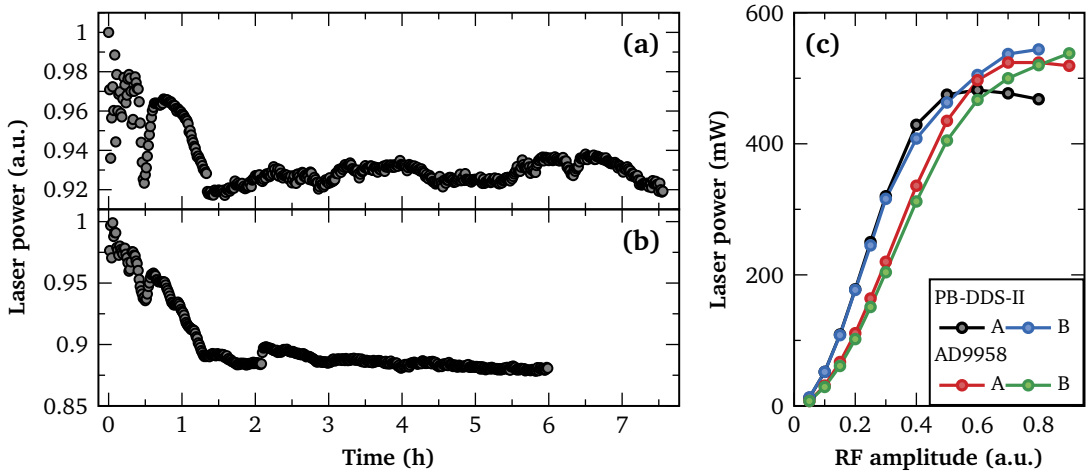

Figure 3.9: Temporal development of the laser power for (a) a measurement of the total laser power emitted from the SHG and (b) laser power in front of a fiber output behind a PBS. (c) Laser power in the fiber parametrized by the RF amplitude of the AOMs. The RF signal is generated either by the PulseBlasterDDS-II or the AD9958.

To test the stability of the system the laser power is measured for several hours directly after turning-on. A photodiode is placed behind a mirror situated in between the SHG and the telescope to estimate the temperal evolution of the total laser power (Fig. 3.9(a)). Another sensing head is positioned between a PBS and a fiber coupler (Fig. 3.9(b)). Both measurements show increased fluctuations of up to 8% and 12%, respectively, during the first two hours of operation. Measurements of the SHG input power indicate that these are mostly caused by the fiber amplifier and not the SHG. After the warm-up phase, fluctuations do not exceed the 2% level. The system therefore provides a stable basis for atomic manipulation. All

critical measurements presented in the next chapters were performed at least two hours after power-on of the laser system.

Control

The AOMs for controlling the intensity, the relative frequency and phase of the light pulses can be driven by two different devices (Fig. 3.8(b)). Each source is based on direct digital synthesizers (DDS) and features two independent channels.

- A pulse generator (`PulseBlasterDDS-II-300-AWG, SpinCore`) receives its commands via USB from a small computer inside the capsule. The parameters for the pulse sequence are sent via Ethernet from an external computer. The `PulseBlaster` features a resolution of 13 ns and can in principle create pulses with arbitrary temporal envelopes. In its current configuration it provides Box or Gaussian shaped pulses with constant frequency.
- A self-assembled device (`Analog Devices AD9958`) controlled via Ethernet allows to drive linear amplitude and frequency ramps for the implementation of Bloch oscillations. Its DDS exhibits a sample rate of 250 kHz corresponding to a time resolution of 4 μs.

Using `MiniCircuits` switches controlled via TTL signals it is possible to alternate between both devices during an experimental sequence. Exemplary fiber output powers for the laser light employed for horizontal symmetric beam splitting, i.e. the twin lattice, are depicted in Fig. 3.9(c) for both devices and both channels A and B.

	`PulseBlaster`	`AD9958`	`ArbStudio`	`MOGLabs`
Amplitude	Box, Gaussian	Linear ramp	Arbitrary	
Frequency	Constant	Linear ramp		Arbitrary
Resolution	13 ns	4 μs	up to 4 ns	up to 16 ns
Use	Bragg pulses	Bloch oscillations	Ampl. shaping	Freq. shaping
	For twin-lattice interferometry			
		In combination for tanh pulses		In the future

Table 3.2: Overview of the different devices which drive the AOMs to control the amplitude and frequency of the interferometry light.

Since the `PulseBlaster` does not provide frequency shaping and the `AD9958` can only perform linear ramps at a limited sample rate of 250 kHz two new devices have been combined to facilitate arbitrary amplitude and frequency shaping. An arbitrary waveform generator (`ArbStudio 1104`) with a sample rate of up to 250 MHz modulates the amplitude of any frequency source via an attenuator (`MiniCircuits ZMAS-3`). The frequency signal either originates from the `AD9958` or, recently, also from an RF synthesizer (`MOGLabs XRF021`) having a sample rate of 65 MHz. A combination of `ArbStudio` and `AD9958` enabled the successful demonstration of tanh-shaped pulses with linear frequency ramps for high-fidelity atomic manipulation (sec. 4.4.2). However, the operation is currently limited by the relatively large response time of the attenuators in the order of $20 - 30\,\mu s$. Therefore, unless otherwise

specified, a combination of `PulseBlaster` and `AD9958` has been employed to control the AOMs. An overview of all devices is given in Table 3.2.

3.3.2 Optical assembly

The optomechanics attached to the vacuum chamber are based on a `Thorlabs` cage system providing an easy and flexible solution for mounting optics and aligning the laser beams for beam splitting. In the experiment, beam splitting can be performed either in horizontal y direction or vertically along the z-axis.

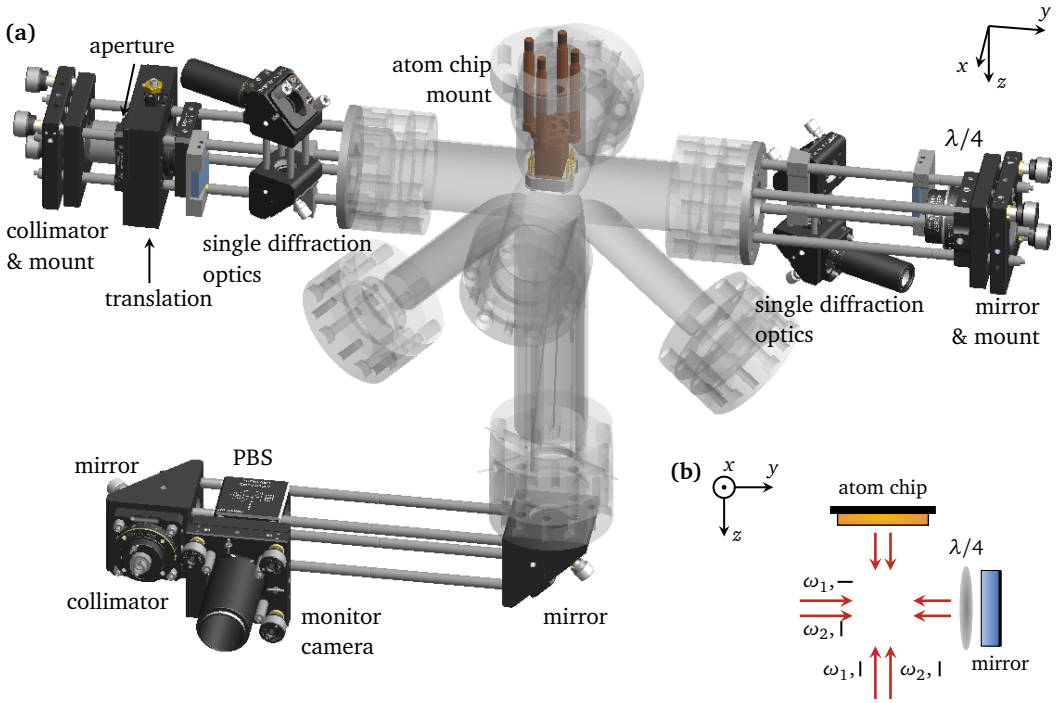

Figure 3.10: Optical assembly for beam splitting along the horizontal and vertical direction (a). In horizontal direction, a retroreflected light field along the y-axis forms the twin lattice to drive double Bragg diffraction and Bloch oscillations. Different optomechanis enable an alignment of the beam. At an angle of 6° with respect to the y-axis additional optics allow the realization of single diffraction processes. The optics for gravimetry along the z-axis are mounted at the bottom viewport. (b) Schematic view of the beam splitting light fields.

Fig. 3.10(a) depicts the optomechanis for horizontal manipulation with double Bragg diffraction and large momentum transfer in a twin lattice. A pre-collimated fiber collimator (`Thorlabs F810APC-780`) expands the beam containing two frequency components with orthogonal polarization up to a diameter of 7.5 mm. A large beam size is required since the atoms are falling tranversely through the beam during the interrogation time. On the other hand, increasing the diameter of the beam also reduces its intensity. With an available power of up to 1.2 W the current beam size provides sufficiently large lattice depths for atomic manipulation. Two mounts (`Thorlabs ST1XY-A` and `KC1-T`) enable $x-z$ translation and angular adjustment of the laser beam. An iris diaphragm (`CP20S`) allows variation of the aperture between 0.8 mm and 20 mm. After travelling through the vacuum chamber, the beam

is retroreflected from a dielectric mirror (BB1-E03 mounted in KC1-T) passing a quarter-wave plate (WPQ10M-780) twice. In this way, an incoming polarization is rotated by 90° and two counterpropagating lattices of orthogonal polarization are generated.

In addition to the optical assembly for symmetric beam splitting described above, components were added to enable single diffraction with an angle of rougly 6° with respect to the y-axis. At each side of the vacuum chamber two adjustable right-angle mirror mounts (KCB05) with half-inch mirrors direct a laser beam onto a square mirror (Newport 07SD520BD.2). The mounts are aligned in a way, that both beams overlap. The main purpose of this additional optics is to move the atomic position away from the chip center. The latter is necessary for vertical beam splitting, where the chip is used as retroreflector. Hereby, defects in the center of the chip surface distort the beam splitting light field.

The components for vertical beam splitting are fixed below the vacuum chamber below the viewport. The beam is collimated to a diameter of 3.3 mm (SuK 60FC-4-A15-02) and can be aligned via two right-angle mirror mounts (Thorlabs KCB1E) in order to guarantee a reflection at an angle of 90° from the chip surface. A polarizing beam splitter (CCM1-PBS252/M) is integrated in the beam path to clean the polarization. At one port a webcam is installed to observe and optimize the MOT during BEC generation.

Adjustment

Efficient manipulation via double Bragg diffraction requires a vanishing atomic velocity in beam direction. In a gravitational field, the beam therefore needs to be aligned horizontally. A non-horizontal alignment by an angle α leads to a projection of the gravitational acceleration onto the beam splitter direction and, thus, to a nonzero velocity $g\,t_{\mathrm{tof}} \cdot \sin\alpha$, which increases with time-of-flight. In contrast to single Bragg diffraction an offset motion in beam splitter direction can not be compensated by an adjustment of the transition frequency, which is fixed at $\omega_{\mathrm{eff}} = 15.084\,\mathrm{kHz}$ for ^{87}Rb. A proper alignment is achieved via deflecting the beam with a pentaprism off a liquid surface which serves as inertial reference (Fig. 3.11(a)). A pentaprism ensures a diffraction angle of 90°. The beam reflected from the water surface is then overlapped with the incident beam for horizontal alignment. Afterwards, the mirror is adjusted in order to achieve perfect retroreflection 3.11(b). This is done by overlapping the incident and reflected beam.

For beam splitting along the vertical axis, in particular for gravity measurements, a proper alignment of the beam and the atom chip, serving as mirror and inertial reference, is required. First, perfect retroreflection is achieved, so that the beam hits the atom chip at an angle of 90°. This is done by first overlapping the incoming beam with the beam that has been reflected from the atom chip via a pentaprism (Fig. 3.11(c)). Then this beam is aligned by means of a liquid surface via tilting the whole capsule (Fig. 3.11(d)). In the end, the beam runs parallel to the gravitational acceleration below the horizontally aligned atom chip (Fig. 3.11(e)). The procedure was first described in [175].

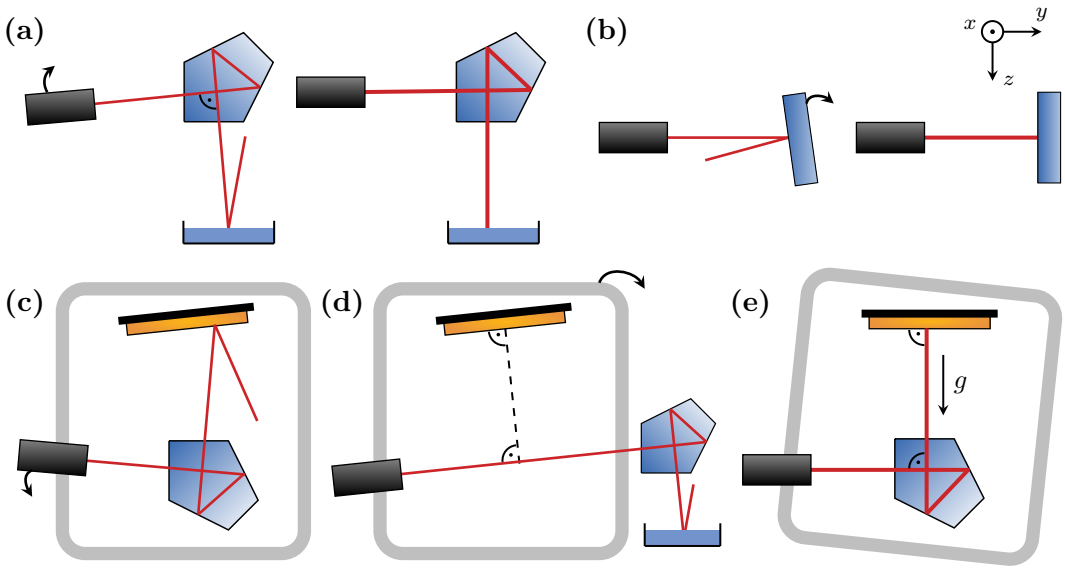

Figure 3.11: (a-b) Beam alignment for horizontal atomic manipulation. After aligning the collimator horizontally by means of a water surface, the retroflection mirror is orientated for a perfect overlap between incoming and reflected beam. (c-e) Alignment of the beam and atom chip for gravimetry along the vertical direction. First, the beam is reflected perpendicularly from the chip surface (c,d). By tilting the whole capsule the atom chip can be positioned horizontally (d). Hereby, a liquid surface serves as reference similar as in (a). Final orientation of atom chip and light field (e).

Polarization

For beam splitting in the horizontal direction two lattices with linear orthogonal polarization are employed to prevent the generation of standing waves which disturb the momentum transfer on the atomic ensemble (see sec. 4.3.3). The implementation of perfect orthogonality, however, is difficult in an experiment, where all optical components might have an influence on the light field. The experimental quality of polarization is investigated via a polarization analyzer (`SuK SK010PA-VIS/NIR`) at different positions along the beam.

The light emitted from the PM fibers features linear polarizations with an extinction ratio of roughly 30 dB and a relative angle of $\Delta = (90 \pm 1)^\circ$ between both frequency components ω_1, ω_2. Passing through the vacuum chamber including both vacuum windows, however, degrades the extinction ratio to roughly 25 dB and rotates both polarizations by approximately $\delta\varphi = -5^\circ$. The quarter-wave plate is adjusted by optimizing the beam splitting efficiency of a double diffraction process. It reaches its maximum if both components of a two-photon process have linear polarizations corresponding to a 90° rotation of both frequency components. Since an adjustment requires a detectable difference in transfer efficiency between two different positions of the quarter-wave plate, this procedure features an uncertainty of roughly 2°, resulting in a relative angle of $\Delta = (90 \pm 3)^\circ$. After passing the vacuum chamber for the second time, the extinction ratio decreases to 20 dB. The vacuum windows lead to another rotation by $\delta\varphi$, keeping the relative angle at $\Delta = (90 \pm 3)^\circ$. In consequence, the polarization of the light fields at the atomic position is not perfect, mainly because of the vacuum windows and an uncertainty in the position of the quarter-wave plate. This gives rise to standing waves and effects the transfer efficiency in the twin lattice.

An in-situ method for the characterization of vacuum windows is presented in Ref. [176]. Hereby, microwave spectroscopy with cold atoms allows to calculate the polarization of the incident light field. In the experiment, an incident polarization with an extinction ratio of 60 dB exhibited a maximum ellipticity $\epsilon = 0.0064$ corresponding to an extinction ratio of 15 dB after passing a standard CF63 viewport.

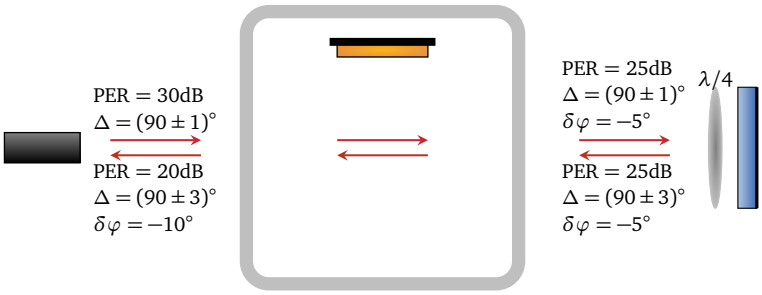

Figure 3.12: Polarization measurement of the horizontal beam splitting light field. Passing through the vacuum chamber and the optics leads to a degradation of the linear polarization extinction ratio (PER) and changes the relative angle Δ as well as the absolute angle $\delta\varphi$ of the two frequency components ω_1, ω_2 within one beam.

TECHNIQUES FOR INTERFEROMETRY 4

The realization of an interferometer with large momentum transfer requires different methods which are explained and characterized within this chapter. The interferometry sequence in QUANTUS-1 starts with a state preparation of the atoms (sec. 4.1) including an optimized release from the magnetic trap as well as a collimation of the atomic cloud with a magnetic lens and a transfer to the non-magnetic state.

The retroreflected twin-lattice geometry along with the vanishing horizontal velocity of the atoms gives rise to symmetric diffraction into opposite momentum states. In section 4.2 the implementation of the so-called double Bragg diffraction is described and analyzed in detail, which constitutes the basis of a large momentum transfer interferometer serving to split, redirect and recombine the atomic wave function. Large accelerations are achieved via Bloch oscillations allowing for much higher transfer efficiencies than Bragg diffraction (sec. 4.3). Compared to a single lattice, the transfer in a twin lattice is additionally influenced by non-resonant contributions, i.e. the contrapropagating lattice as well as interference terms acting as a standing wave. The chapter closes with the description of some extended diffraction techniques which might be implemented in future interferometer geometries (sec. 4.4).

4.1 State preparation

The first 15 ms of each sequence are reserved for state preparation of the atomic cloud to provide an optimal source for atom interferometry. Optimally, the release from the magnetic trap (sec. 4.1.1) results in a zero offset velocity along the horizontal direction. A non-zero velocity degrades the symmetry and efficiency of the double diffraction beam splitter. The release trap also determines the initial mean-field and kinetic energy of the atomic ensemble (see sec. 3.2.2). Mean-field energy, caused by atomic interactions, leads to unwanted phase shifts in an atom interferometer [84, 85].

Large initial expansion rates are beneficial for subsequent magnetic lensing, which reduces the atomic velocity during the conversion of kinetic into potential energy (sec. 4.1.2). A small momentum width not only leads to higher diffraction efficiencies [87] but also results in a smaller spatial extent, lowering systematic uncertainies associated with the cloud's size [91]. During magnetic trapping, release and lensing the atoms occupy the state $|F = 2, m_F = +2\rangle$. However, this makes them also susceptible to any parasitic magnetic fields leading to additional accelerations. To decrease their influence the atoms are transferred to the state $|F = 2, m_F = 0\rangle$ via an adiabatic rapid passage prior to interferometry (sec. 4.1.3).

4.1.1 Release from magnetic trap

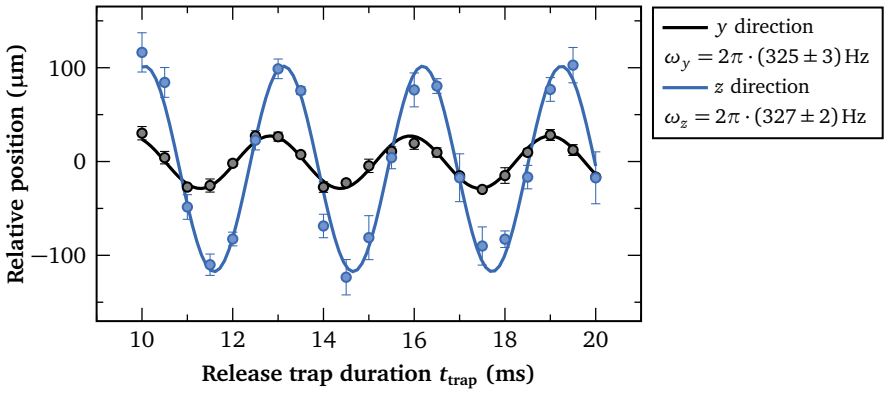

Figure 4.1: In the final release trap the atomic position and velocity oscillates with the trap duration t_{trap}. These dipole oscillations are monitored via the atomic position after a free evolution time of $t_{\text{tof}} = 34\,\text{ms}$.

Prior to the release into free fall the atoms are trapped inside a final decompressed trap, where they undergo dipole oscillations. Depending on the frequency $\omega_{x,y,z}$ and duration t_{trap} of the trap, the atoms oscillate around the minimum of the trapping potential. In beam splitter direction y, the center-of-mass position oscillates around y_0 with amplitude $A_{y,0}$ as

$$y_{\text{trap}}(t_{\text{trap}}) = y_0 + A_{y,0}\sin(\omega_y t_{\text{trap}} + \phi_0). \tag{4.1}$$

Differentiating (4.1) gives us the velocity within the trap which is proportional to the trap frequency ω_y

$$v_y(t_{\text{trap}}) = A_{y,0}\omega_y \cos(\omega_y t_{\text{trap}} + \phi_0). \tag{4.2}$$

After release and a free fall duration of t_{tof}, the atomic position evolves as

$$y(t_{\text{trap}}, t_{\text{tof}}) = y_{\text{trap}}(t_{\text{trap}}) + A_{y,0}\omega_y \cos(\omega_y t_{\text{trap}} + \phi_0)t_{\text{tof}}. \tag{4.3}$$

These dipole oscillations are shown in Figure 4.1 as a function of t_{trap}. For double Bragg diffraction a vanishing offset velocity along the beam splitting axis y is important for efficient and symmetric manipulation. In the absence of any offset motion the lowest center-of-mass velocity is found for $\cos(\omega_y t_{\text{trap}} + \phi_0) = 0$, i.e. at midfringe position.

By fitting a cosine to the measurement data the trap frequencies are determined to be $\omega_{y,z} = 2\pi \cdot (325, 327)\,\text{Hz}$. In the current setup, the movement along the third direction x can not be observed. The trap frequency along the detection axis x has been measured in an ealier setup and equals $\omega_x = 2\pi \cdot 43\,\text{Hz}$ [125]. The measurements shown above have been realized for a trap with a bias current of $I_{\text{Bias}} = 1\,\text{A}$ (steep trap), which is positioned relatively close to the atom chip (see Fig. 4.2). Due to its large trap frequencies this trap exhibits high initial expansion rates as well as a fast conversion of mean-field energy to kinetic energy and is therefore well suited for magnetic lensing. When changing the bias field the trap center moves away from the chip. In the presence of gravity, the shallowest trap realizable in QUANTUS-1 features a bias current of $I_{\text{Bias}} = 0.36\,\text{A}$ and trap frequencies of $\omega_{x,y,z} = 2\pi \cdot (18, 46, 31)\,\text{Hz}$

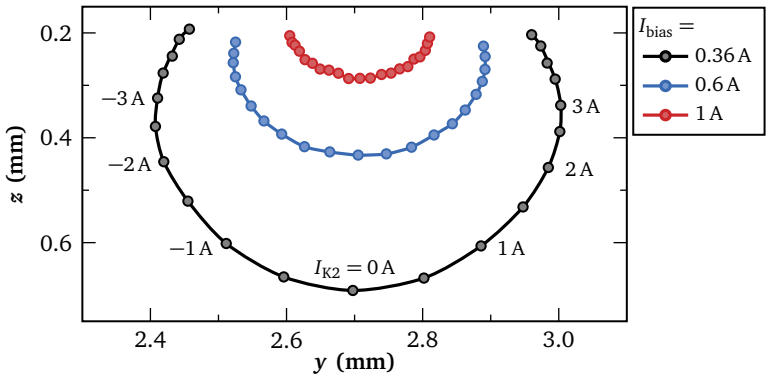

Figure 4.2: The release point of the final trap can be moved in the $y-z$ plane by changing the currents through the Bias coils I_{Bias} and the K2 coils I_{K2}. The data points have been obtained for three different bias currents $I_{\text{Bias}} = 0.36, 0.6, 1\,\text{A}$ and a scan of I_{K2} ranging from $-5\,\text{A}$ to $5\,\text{A}$ in steps of $0.5\,\text{A}$.

leading to the lowest expansion rates. During the first 10 ms after release, however, the expansion in this trap is non-linear due to mean-field driven acceleration [149].

While the Bias coils move the trap center along the z-axis, changing the current of the K2 offset coils, whose magnetic field points into the z direction, shifts the atomic position circularly in the $y-z$ plane. This is shown in Figure 4.2 for three different bias currents $I_{\text{Bias}} = 0.36\,\text{A}$, $0.6\,\text{A}$, and $1\,\text{A}$ and a K2 current I_{K2} ranging from $-5\,\text{A}$ to $5\,\text{A}$. In case of the shallowest trap ($I_{\text{Bias}} = 0.36\,\text{A}$) a change in I_{K2} shifts the initial BEC position by up to $\pm 300\,\mu\text{m}$ in y direction. For the steep trap ($I_{\text{Bias}} = 1\,\text{A}$) the possible shift only corresponds to $\Delta y = \pm 100\,\mu\text{m}$. In addition, a higher K2 current leads to higher trap frequencies [177]. Shifting the position of the trap center will be exploited in chapter 6 to optimize the spatial overlap between magnetic chip trap and optical dipole trap.

4.1.2 Delta-kick collimation

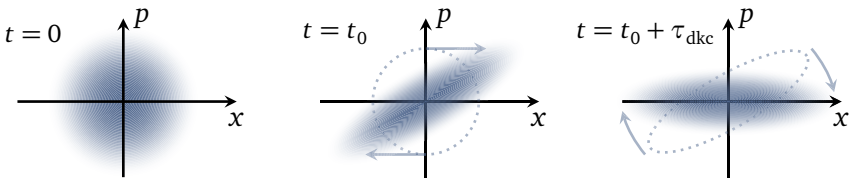

Figure 4.3: The phase-space distribution of an atomic cloud in a harmonic trap is initially Gaussian. The distribution is sheared during free expansion and rotated after delta-kick collimation.

With a technique known as delta-kick collimation (DKC) [178, 179] the expansion rate of an atomic cloud, in particular the mean-field driven expansion of a BEC, can be reduced. Low expansion rates are particularly important when it comes to large time-of-flights t_{tof} as in microgravity environments or large atomic fountains. Here, they are crucial for minimizing the spatial extent of the atomic cloud in order to obtain sufficient densities at the time of detection and decrease systematic errors arising due to laser intensity and wavefront inhomogeneities across the cloud [91]. Additionally, DKC enables larger beam splitting efficiencies and a

reduction of the time which is required to separate different atomic momentum states for spatial detection.

DKC is performed by switching on the magnetic trap potential again some time t_0 after release of the condensate, which leads to dipole oscillations. The magnetic trap is switched off shortly afterwards, when an atom has arrived at the turning point of the potential where its motion stops. In this way, kinetic energy is converted into potential energy. Due to the similarity to an optical lens collimating light, the method is called a magnetic lens. The condition for optimal lensing reads

$$\omega^2 \tau_{\mathrm{dkc}} = 1/t_0, \tag{4.4}$$

where ω is the frequency of the harmonic potential, t_0 the time prior to switching the potential on and τ_{dkc} the duration of the lens [178]. For an atomic ensemble with finite spatial and velocity spread, the velocity after the kick will not be completely zero.

The process is shown in Fig. 4.3, where a cloud of particles with an initial Gaussian distribution is released from a magnetic trap, then captured again after an expansion time t_0. In phase space, this corresponds to a shear during free evolution and a rotation for a duration τ_{dkc} towards the position axis. In this way, DKC ideally minimizes the expansion energy by increasing the spatial spread. Thus, the phase-space density will be the same as before the kick.

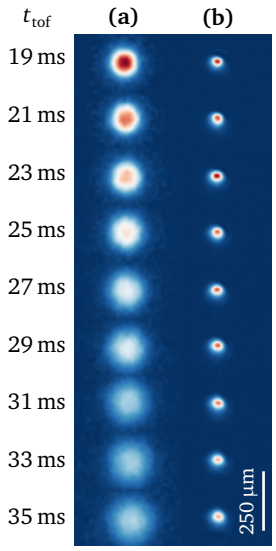

Fig. 4.4: Time-of-flight series of a BEC from a steep trap without (a) and with DKC (b).

Experimentally, DKC is realized by release from a steep trap ($\omega_{x,y,z} = 2\pi \cdot (43, 325, 327)$ Hz, $I_{\mathrm{Bias}} = 1$ A) featuring a fast conversion of mean-field into kinetic energy and high expansion rates. These properties are beneficial to quickly achieve a linear correlation between momentum and position to perform efficient collimation. If the magnetic trap is switched on after $t_0 = 5.4$ ms for a duration of $\tau_{\mathrm{dkc}} = 300$ µs the expansion rate of the atomic cloud in y and z direction can be reduced by a factor of roughly 8 corresponding to expansion rates in horizontal and vertical direction of $\sigma_{v_y} = 0.18\,\mathrm{mm/s} = 0.30\,\hbar k/m$ and $\sigma_{v_z} = 0.26\,\mathrm{mm/s} = 0.44\,\hbar k/m$ (Fig. 4.4 and 4.6). These values are a factor of three below the expansion rates of a cloud released from the shallow trap in QUANTUS-1. Therefore, higher beam splitting efficiencies are expected when operating with the delta-kick collimated ensemble [87].

Figure 4.5 illustrates the influence of DKC on the position and velocity scatter of the source. Here, the position scatter corresponds to the standard deviation of the center position of an atomic cloud calculated for a set of 40 data points. A velocity scatter manifests itself in an increasing position scatter with time-of-flight. The position and velocity scatter in y direction can be significantly reduced with the application of DKC. This is beneficial for the beam splitter of the twin-lattice interferometer which acts along the y direction.

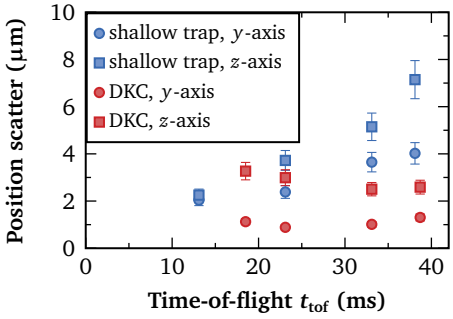

Fig. 4.5: Position scatter with/without DKC.

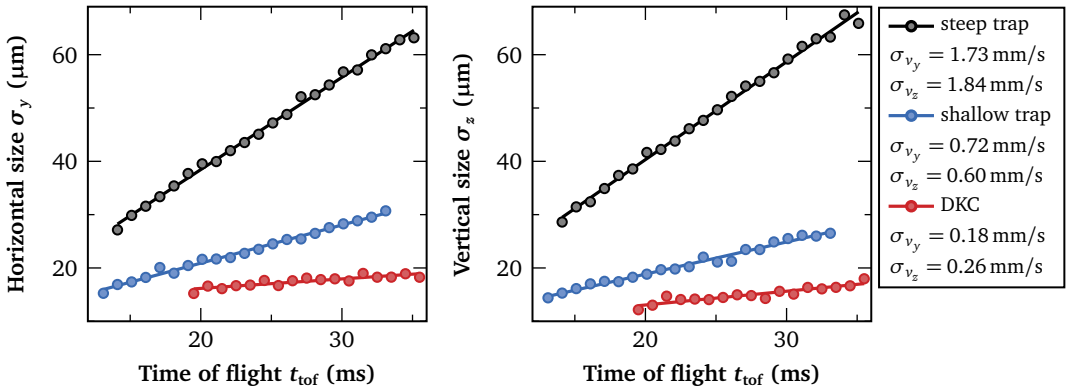

Figure 4.6: Expansion rates of a cloud released from a steep trap ($I_{\text{Bias}} = 1A$, ——), a shallow trap ($I_{\text{Bias}} = 0.36A$, ——) and a delta-kick collimated ensemble from a steep trap (——) in y and z direction.

Due to the asymmetry of the elongated atom-chip based potential only the two radial axis, which have very similar trap frequencies, can efficiently be collimated. In addition, the chip potential is in general not harmonic, which becomes more relevant for increasing cloud sizes and time-of-flights. The anisotropies and anharmonicities of the magnetic lens have not been investigated in detail for QUANTUS-1, however, a thorough analysis has been carried out for the similar experiment QUANTUS-2 [98, 99].

4.1.3 Magnetic state transfer

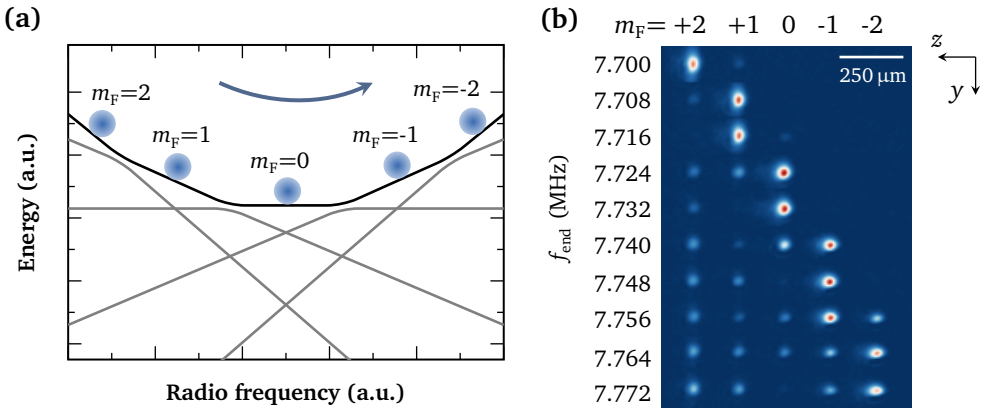

Figure 4.7: State tranfer to the non-magnetic state. (a) Scheme of the radio frequency coupling to the different Zeeman substates of $|F = 2\rangle$ for ^{87}Rb. (b) Density plots of the atomic population for different end frequencies f_{end}. The magnetic substates were separated via Stern-Gerlach-type deflection and the absorption images are rotated by 270 degrees.

In order to efficiently capture atoms in a magnetic trap, the atoms are transferred to the state which is susceptible to magnetic fields $|F = 2, m_F = +2\rangle$. After release from the magnetic trap one usually wants to reduce the influence of residual magnetic fields, which might lead to additional accelerations and phase shifts inside an atom interferometer.

Therefore, the atoms are transferred via an adiabatic rapid passage (ARP) to the non-magnetic state $|F = 2, m_F = 0\rangle$. While the linear dependency vanishes in this case, one still

has to pay attention to higher order contributions which can not be neglected in high precision experiments. The transfer is achieved via a radio frequency emitted from the atom chip which couples to the different magnetic substates. As it is swept over the multiple resonances, population transfer occurs at points of avoided crossings as illustrated in Fig. 4.7(a). For more details on the implementation of the ARP in QUANTUS-1 see [125, 149, 180].

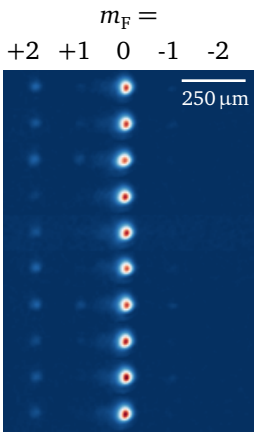

Fig. 4.8: The efficiency of the state transfer into $m_F = 0$ is on the order of 90-95%.

A typical ARP sequence exhibits a total duration of 9 ms. During the first 4 ms a homogeneous bias field is ramped up to a value of 10.5 G in order to lift the degeneracy of the magnetic substates. The frequency of a radio-frequency pulse of 4 ms duration is then linearly increased from the start frequency $f_{\text{start}} = 7.7\,\text{MHz}$ to the end frequency f_{end} coupling to the different magnetic substates. The final 1 ms is consumed by linearly switching off the bias field. Fig. 4.7(b) shows the populations in the magnetic substates as a function of the end frequency f_{end} of the chirp. The different substates are separated spatially by applying an inhomogeneous magnetic field to perform Stern-Gerlach-type deflection.

In case of an optimized configuration with $f_{\text{end}} = 7.732\,\text{MHz}$ around 5-10% of the atoms remain with non-zero magnetic moment, which result from losses during each avoided crossing (Fig. 4.8). The variations stem from fluctuations of the radio frequency amplitude and the magnetic field environment. Without the application of an inhomogeneous magnetic field, all Zeeman states will spatially overlap at detection. In an atom interferometer the residual atoms with nonzero magnetic moment will lead to a slight loss of contrast due to their dephasing. This can be easily circumvented by applying Stern-Gerlach-type deflection to push these atoms away from the $m_F = 0$ output ports.

4.2 Double Bragg diffraction

In a twin-lattice interferometer double Bragg processes serve for symmetric beam splitting, reversion of the atomic velocity and recombination. The use of a Bose-Einstein condensate in combination with an optimized state preparation by delta-kick collimation and an accurate laser beam alignment allows for high transfer efficiencies of almost 100% (sec. 4.2.1). The beam splitter stability of double diffraction is investigated. By choosing appropriate pulse durations at the cost of a smaller momentum acceptance a high pulse stability can be reached (sec. 4.2.2). First order double Bragg diffraction features a symmetric momentum transfer of $\pm 2\hbar k$. The total transfer of $4\hbar k$ can be enlarged by employing either higher order pulses or by driving successive single Bragg processes (sec. 4.2.3).

4.2.1 Rabi oscillations

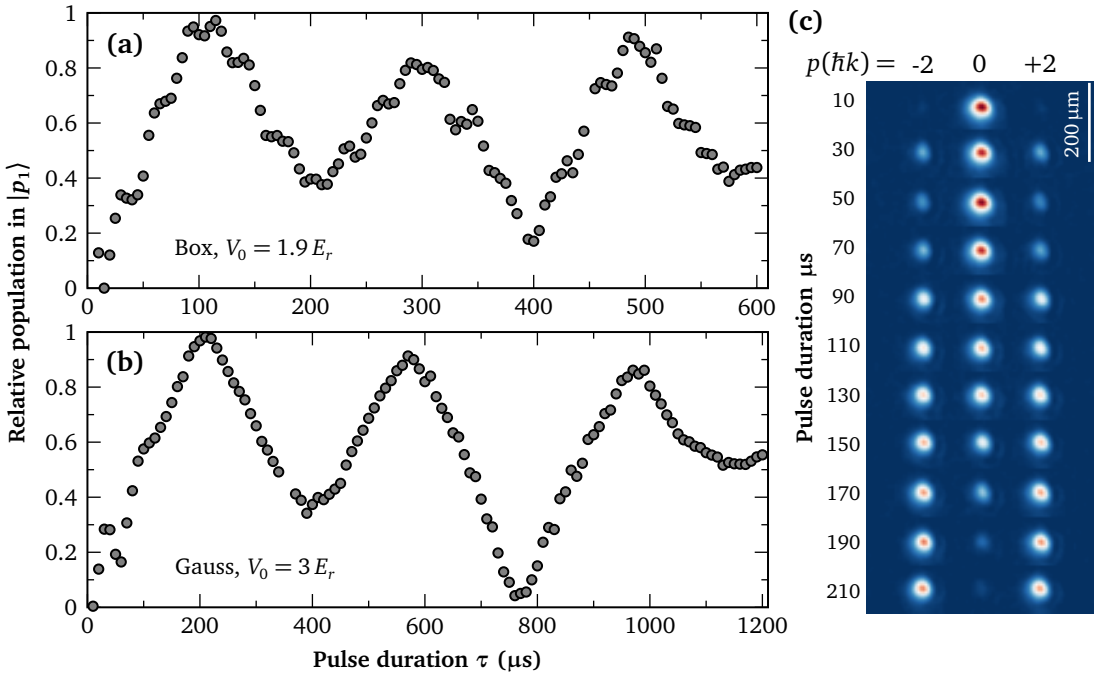

Figure 4.9: Rabi oscillations for first order double Bragg diffraction. The relative population $|p_1\rangle$ in both momentums states $|\pm 2\hbar k\rangle$ is measured depending on the pulse duration τ for a box (a) and Gaussian (b) shaped pulse with lattice depths $V_0 = 1.9\,E_r$ and $3\,E_r$, respectively. In case of a Gaussian pulse the width σ_t equals $\tau/8$. Given the double diffraction process oscillations occur with frequency $2\,\Omega_{\text{eff}} = 2\sqrt{2}\Omega_{\text{DD}}$, with modulations at Ω_{eff} and $2\omega_{\text{eff}}$ [68]. A Gaussian shaped pulse suppresses the modulation at $2\omega_{\text{eff}}$. (c) Density plots for double Bragg diffraction and different Gaussian pulse durations.

The realization of Rabi oscillations, i.e. the measurement of the relative population in $|p_1\rangle$ (corresponding to the diffraction efficiency) depending on the pulse duration τ, represents a good way to characterize a beam splitter. For double diffraction, the relative population in $|p_1\rangle$ represents the sum of momentum states $+2\hbar k$ and $-2\hbar k$ normalized to the total atom number in states $0\,\hbar k$ and $\pm 2\,\hbar k$

$$P_{|p_1\rangle} = \frac{N_{-2\hbar k} + N_{+2\hbar k}}{N_{-2\hbar k} + N_{0\hbar k} + N_{+2\hbar k}}. \tag{4.5}$$

For lower detection noise, the atom number in each state is not calculated individually, but the diffraction efficiencies $P_{+2\hbar k} = N_{+2\hbar k}/(N_{0\hbar k} + N_{+2\hbar k})$ and $P_{-2\hbar k} = N_{-2\hbar k}/(N_{0\hbar k} + N_{-2\hbar k})$ are determined via double Gaussian fits (sec. 3.1.2). From this the total diffraction efficiency is calculated

$$P_{|p_1\rangle} = \frac{P_{+2\hbar k} + P_{-2\hbar k} - 2P_{+2\hbar k}P_{-2\hbar k}}{1 - P_{+2\hbar k}P_{-2\hbar k}}. \tag{4.6}$$

Fig. 4.9 shows Rabi oscillations for first order double Bragg diffraction for a box (a) and Gaussian (b) shaped pulse. In Fig. 4.9(c) the corresponding density plots are shown for a pulse with a Gaussian envelope, which in our setup is defined in a way, that the Gaussian

width σ_t equals $\tau/8$. The detuning δ between both laser beams is fixed at frequency $\omega_{\text{eff}} = 2\pi \cdot 15.084\,\text{kHz}$.

Due to the small momentum spread and offset velocity of the delta-kick collimated cloud, atoms can be transferred from $|0\hbar k\rangle$ to $|\pm 2\hbar k\rangle$ with an efficiency of almost 99%. The finite momentum width of the ensemble causes a dispersion of the Rabi frequency leading to a damping of the oscillations. A double diffraction $\pi/2$ pulse is defined as the total transfer from $|0\hbar k\rangle$ into $|\pm 2\hbar k\rangle$, whereas a single diffraction $\pi/2$ pulse corresponds to the creation of a superposition in $|0\hbar k\rangle$ and $|2\hbar k\rangle$. Therefore, oscillations occur at twice the effective double diffraction Rabi frequency $2\,\Omega_{\text{eff}}$, where $\Omega_{\text{eff}} = \sqrt{2}\Omega_{\text{DD}} = \sqrt{2}\Omega_{12}/2$. Measuring this frequency allows the determination of the lattice depth $V_0[E_r] = \frac{4}{\sqrt{2}\omega_r}\Omega_{\text{eff}}$.

For a box shaped pulse, the first minimum is observed at $2\pi/(2\Omega_{\text{eff}}) = 200\,\mu\text{s}$ (Fig. 4.9(a)). From this we can calculate $\Omega_{\text{eff}} = 2\pi \cdot 2.5\,\text{kHz}$ and $V_0 = 1.9\,E_r$. However, the relative population in $\pm 2\hbar k$ at $\tau = 200\,\mu\text{s}$ only drops to 40%, while it falls below 20% at $\tau \approx 400\,\mu\text{s}$. This demonstrates the modulation at Ω_{eff} caused by a nonzero offset momentum p_0 and/or momentum width σ_v due to the three-level dynamics of double Bragg diffraction [68]. In addition, high-frequency components with small amplitude and a period of $33\,\mu\text{s} = 2\pi/(2\omega_{\text{eff}})$ are visible on top of the slow Rabi oscillations. They occur due to an off-resonant coupling of momentum states and can be suppressed by using Gaussian shaped pulses [120, 124]. The off-resonant processes are sketched in Fig. 2.5. In case of a Gaussian shape the pulse area and, thus, the Rabi frequency is determined by integration of the laser intensity over time (see sec. 2.1.3) and the measurement reveals a lattice depth of $V_0 \approx 3\,E_r$.

Rabi oscillations are also employed to measure the lattice depth along the beam profile. In case of double diffraction the atoms fall through the horizontally aligned Gaussian-shaped beam. Therefore, the Rabi frequency and lattice depth vary depending on the vertical position of the atoms during the pulse. The latter can be changed by applying the pulse at different points in time after release from the chip trap. In Fig. 4.10 the measured lattice depth is displayed for different vertical distances from the atom chip corresponding to different time-of-flights t_{tof} before the application of the Bragg pulse. The minimum t_{tof} before a pulse equals 14.4 ms given by the time required for magnetic lensing and non-magnetic state transfer.

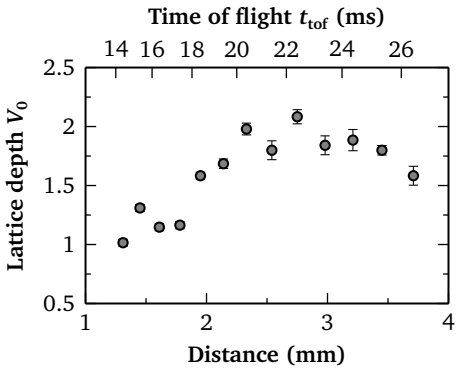

Fig. 4.10: Measured lattice depths along the beam profile for different distances from the atom chip.

4.2.2 Pulse duration, stability and imperfect polarizations

In terms of pulse durations shorter times are usually more convenient since they lead to a broader momentum acceptance and thus lessen the requirements on the atomic source. On the other hand, the frequency width of a pulse should not be too short in order to avoid addressing other states separated by $2\hbar k$ in momentum space. In Figure 4.11(a) a measurement is shown, where the relative population in $|\pm 2\hbar k\rangle$ is recorded for three different Gaussian shaped pulses with duration $\tau = 130, 200$ and $300\,\mu\text{s}$ and corresponding Gaussian width $\sigma_t = \frac{\tau}{8}$. It can

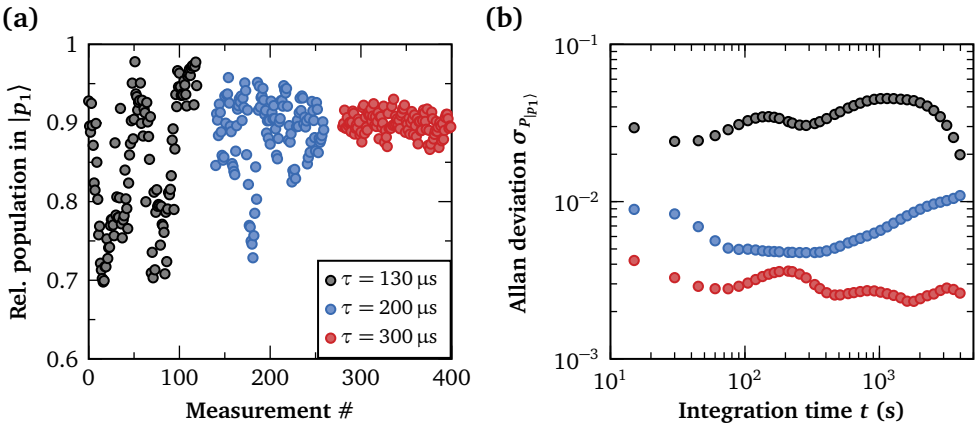

Figure 4.11: Measurement of the double diffraction first order pulse stability for Gaussian pulses with different durations $\tau = 130, 200$ and $300\,\mu s$. (a) Repeated measurements of the relative population in $|\pm 2\hbar k\rangle$. (b) Overlapping Allan deviation for these pulse durations obtained in separate longterm measurements. For each pulse duration a different laser intensity is used.

be easily seen that shorter pulse durations lead to an increased beam splitter noise $\sigma_{P_{|p1\rangle}}$. The stability of a diffraction pulse is important, since temporal changes of the beam splitter efficiency decrease the interferometric contrast and lead to variations of the interferometer signal which can mistakenly be interpreted as a phase change.

The longterm stability is analyzed by the Allan deviation [181] which is defined as

$$\sigma_y(t) = \sqrt{\frac{1}{2}\langle (y_{n+1} - y_n)^2 \rangle} \tag{4.7}$$

for two subsequent data points y_n and y_{n+1}. It describes the noise and the possible gain in stability that can be achieved after integration of the data for a time t. Figure 4.11(b) illustrates the overlapping Allan deviation calculated with data from separate longterm measurements. The data confirms the superior stability when applying longer pulse durations. For pulse lengths of $\tau = 300\,\mu s$ a beam splitter noise of $\sigma_{P_{|p1\rangle}} = 0.0025$ can be achieved after an integration time of $t = 500\,s$, while the noise increases for $\tau = 200\,\mu s$ and $130\,\mu s$ by a factor of roughly 2 and 10, respectively.

The twin lattice light field is generated by superimposing two beams which have a small path difference. This may lead to a differential phase $\Delta\phi_{\text{laser}} = \phi_1 - \phi_2$ between both frequency components. Variations in the path difference caused e.g. by thermal fluctuations will cause $\Delta\phi_{\text{laser}}$ to vary over time. In turn, this will impact the pulse area, since the light field is modulated at a rate $\Delta\omega$ (Eq. (2.39)). For first order Bragg diffraction ($\Delta\omega = \omega_{\text{eff}} = 2\pi \cdot 15.084\,\text{kHz}$) the modulation period equals $2\pi/\omega_{\text{eff}} = 67\,\mu s$. As illustrated in Fig. 4.12 fluctuations of the relative phase $\Delta\phi_{\text{laser}}$ will have a severe impact on the pulse area, as long as the pulse duration is not significantly larger than $67\,\mu s$. The graph shows Gaussian shaped pulses with $\sigma_t = \tau/8$ modulated with ω_{eff} according to

$$I(t) = I_0 \exp\left(-\frac{t^2}{2\sigma_t^2}\right) \cdot \cos^2\left(\frac{\omega_{\text{eff}}}{2} t + \Delta\phi_{\text{laser}}\right). \tag{4.8}$$

The pulse area of a Gaussian pulse of duration $\tau = 130\,\mu s$ varies up to 50% depending on the relative laser phase $\Delta\phi_{\text{laser}}$. For $\tau = 200\,\mu s$ and $300\,\mu s$ the variations are only in the order of 5% and <1%, respectively.

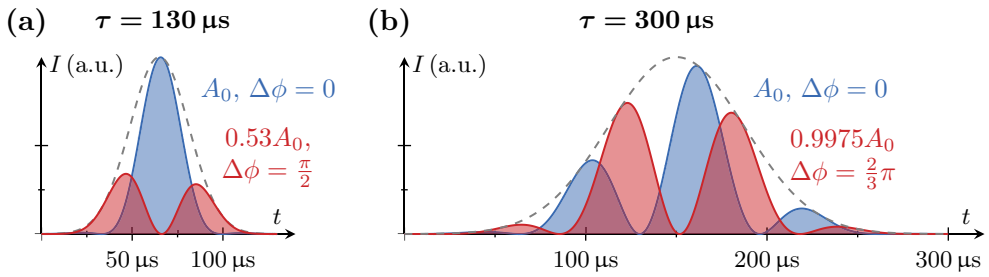

Figure 4.12: Amplitude modulation of a Gaussian pulse of length $\tau = 130\,\mu s$ and $\tau = 300\,\mu s$ at $\Delta\omega = 2\pi \cdot 15\,kHz$ according to (4.8). Notations indicate the corresponding pulse area A_0 for different relative laser phases $\Delta\phi$.

For non-ideal polarizations, standing waves arise in the twin-lattice setup. Atoms with $0\hbar k$ can also be scattered by standing waves into momentum states $\pm 2\hbar k$. However, this transition exhibits a detuning of ω_{eff} from resonance. Therefore, longer pulse durations, which lower the momentum acceptance, also reduce the influence of standing waves.

To sum up, longer pulse durations minimize diffraction by standing waves as well as fluctuations of the pulse area caused by amplitude modulation in our twin-lattice setup. In our case, a choice of $\tau = 300\,\mu s$ leads to stable beam splitting efficiencies, while the corresponding momentum width of the pulse is still sufficient to transfer more than 99% of our delta-kicked BEC. The influence of a change of $\Delta\phi_{\text{laser}}$ for parallel incoming polarizations will be investigated in the next section.

Parallel incoming polarizations

As experimentally confirmed, polarizations in the twin-lattice setup are not perfect (sec. 3.3.2) and lead to a standing wave as well as a time-dependent beating term (Eq. (2.39)). To examine possible disturbances, the beam splitting setup along the vertical direction is used, where these contributions (V_{St} and V_{b}) are not suppressed due to parallel incoming polarizations. In the vertical direction, their influence is usually highly suppressed by the Doppler shift of the gravitationally accelerated atom cloud. The Doppler shift leads to a high-frequency amplitude modulation as well as far off-resonant standing wave transitions.

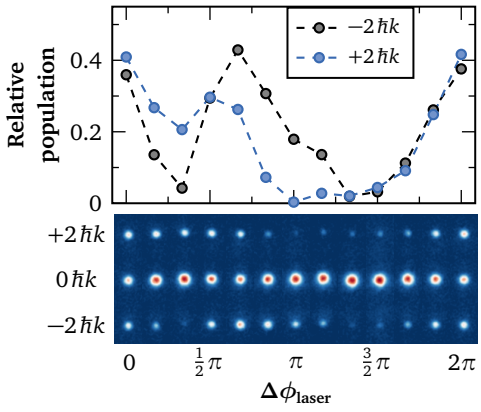

Fig. 4.13: Diffraction in the vertical direction (parallel incoming polarizations) in dependence of the relative laser phase $\Delta\phi_{\text{laser}}$.

A box pulse of duration $\tau = 50\,\mu s$ and detuning $\delta = 2\pi \cdot 15\,kHz$ is applied directly after release where the Doppler shift is close to zero. At the end of the pulse, after 50 µs of free fall, the shift equals $\omega_{\text{D}} = 2\pi \cdot 0.6\,kHz$. The relative population of the momentum states is measured as a function of the relative phase $\Delta\phi_{\text{laser}}$ between both frequency components of

the light field. The latter is adjusted by the AOM. Compared to the horizontal direction, the relative laser phase for beam splitting along gravity is fixed, since both frequencies components are generated by a single AOM.

Given the vanishing velocity in beam splitter direction, double diffraction into neighboring momentum states $\pm 2\hbar k$ occurs as shown in Figure 4.13. The diffraction shows an asymmetry between $+2\hbar k$ and $-2\hbar k$, since the atomic velocity is not completely zero. At the end of the pulse, gravity has accelerated the atoms up to a velocity of 0.5 mm/s. As opposed to standard Bragg diffraction, the relative population in the momentum states oscillates with $\Delta\phi_{\text{laser}}$ because of the standing wave and the amplitude modulation. This $\Delta\phi_{\text{laser}}$-dependence is the reason for the instability examined in the previous section. We will see later on, the standing wave contribution V_{St} also limits the transfer efficiency with Bloch oscillations (see sec. 4.3.3).

4.2.3 Higher-order double Bragg diffraction

In order to enlarge the momentum transfer with double Bragg diffraction, higher diffraction orders n can be adressed to achieve a symmetric momentum splitting of $n \cdot 4\hbar k$ between both clouds. The detuning between both laser beams equals $\delta = n \cdot \omega_{\text{eff}}$ for a pulse of order n. The requirements on laser intensity increase with higher diffraction orders.

Larger momentum separation can also be achieved by employing sequential first order pulses, which can be advantageous when the available laser power is limited. Starting with double diffraction, each of these sequential pulses increases the momentum splitting by $4\hbar k$. Fig. 4.14 contrasts the efficiencies obtained with first and higher order double Bragg diffraction as well as with sequential single Bragg pulses for different momentum transfer $n \cdot 2\hbar k$. In each case, the efficiency has been optimized by adjusting the laser power and pulse duration. For $n = 3$ (corresponding to $12\hbar k$) the diffraction efficiency for higher order double diffraction drastically decreases to 50% and below. The larger momentum selectivity, the necessity of a vanishing center-of-mass velocity as well non-resonant transitions makes it even harder to find suitable parameters for higher-order double Bragg processes compared to single diffraction. In general, the efficiencies obtained with successive pulses exceed those of higher order diffraction. Despite the additional time required for each pulse ($\tau = 300\,\mu$s), they are therefore the preferred technique of choice when it comes to larger momentum transfer by means of double Bragg diffraction.

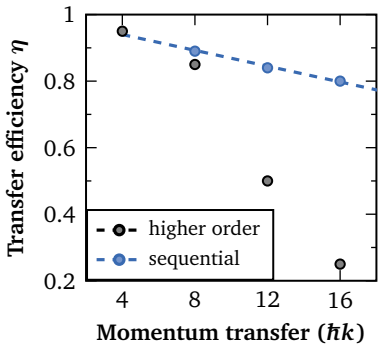

Fig. 4.14: Transfer efficiency for higher order and sequential double Bragg diffraction.

4.3 Bloch oscillations

Compared to Bragg or Raman diffraction, Bloch oscillations feature much higher efficiencies of 99.97% per $\hbar k$ [103] allowing to transfer a large number of photon recoils onto the atomic clouds. Its properties, including transfer efficiencies, loading into the lattice and lattice depth calibration, are investigated within this section. Due to the larger interaction time and higher lattice depths compared to Bragg diffraction, spontaneous emission can not be neglected. For simplicity, part of the following measurements were done along the vertical direction, where the atoms effectively interact with only one lattice due to the Doppler shift. In addition, a combination of double Bragg diffraction with Bloch oscillation along the horizontal direction is presented to establish symmetric large momentum beam splitting. Hereby, double Bragg diffraction initially lifts the degeneracy between both lattices. The twin-lattice configuration deviates from acceleration in a single lattice, since the influence of the counterpropagating lattice as well as contributions from parasitic lattices due to imperfect polarization have to be taken into account. These disturbances can be reduced by a larger initial separation with double Bragg diffraction.

4.3.1 Lattice depth measurement

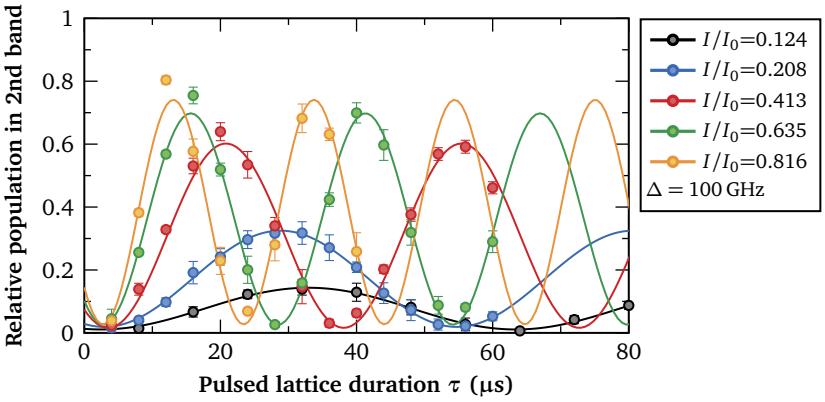

Figure 4.15: Oscillations between the fundamental and second excited Bloch band induced by a short lattice pulse for different relative laser intensities I/I_0. With a sinusoidal fit function to the data the oscillation period T can be extracted. T depends on the band gap $E_2 - E_0$ which can be related to a specific lattice depth V_0.

The lattice depth can be measured via Rabi oscillations with the double Bragg beam splitter as detailed in section 4.2.1. An alternative measurement employs a copropagating pulsed lattice to induce oscillations of the different momentum states.

If a BEC is not adiabatically but suddenly loaded into a comoving optical lattice, several bands are populated. The BEC can then be desribed as a superposition of Bloch states $|n, q\rangle$ with a momentum spectrum composed of peaks separated by momentum $2\hbar k$ [135]. It evolves in time according to the phase factor $\exp[-i\frac{E_n(q)}{\hbar}t]$. A sudden switch-off of the lattice after time τ projects the lattice state onto the plane-wave basis. The interference of the phase factors leads to oscillations of the population of the momentum components as a function of τ. For shallow lattices only the fundamental and second excited band are significantly

populated and the oscillation is almost purely sinusoidally. Due to the asymmetry of their eigenstates, odd bands are not populated by the BEC with its symmetric wavefunction. The period T of these oscillations depends on the band gap $\Omega_{\mathrm{bg}}^{02} = (E_2 - E_0)/\hbar$ as

$$T = \frac{2\pi}{\Omega_{\mathrm{bg}}^{02}}. \tag{4.9}$$

These oscillations can also be understood in terms of diffraction by a short pulse in the Kapitza-Dirac regime [182]. In this picture, the band gap is calculated from the respective Rabi frequency leading us to the same formula with the relation $\Omega_{\mathrm{bg}}^{02} \approx \Omega_{12} = V_0[E_r]\omega_r/2$ for a quasimomentum $q = 0$.

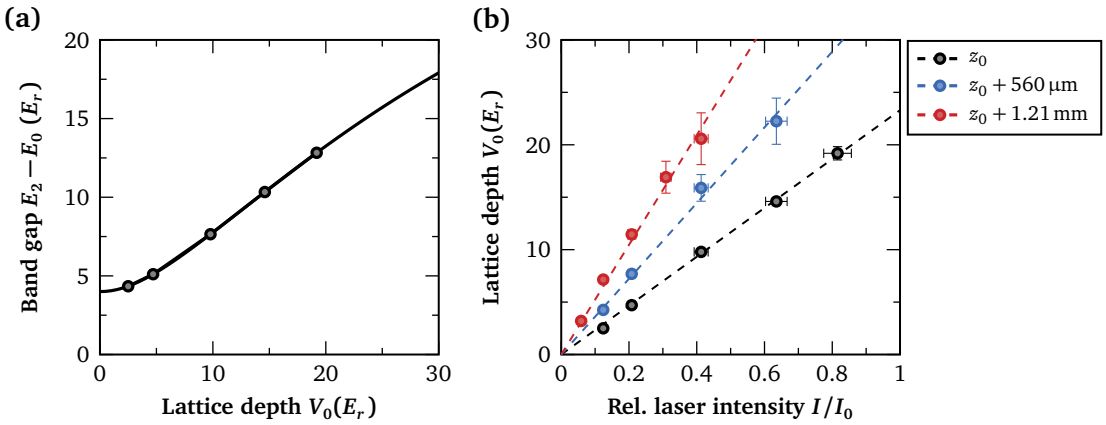

Figure 4.16: Lattice depth measurement. (a) Calculated band gap $\Omega_{\mathrm{bg}}^{02}$ between fundamental and second excited band for different lattice depths V_0. The markers indicate the band gaps extracted from the measurement depicted in Fig. 4.15. (b) The measured lattice depth V_0 depends linearly on the relative laser intensities measured in the fiber. The graph shows the evalutation of two other lattice depth calibrations performed at positions z closer to the center of the beam with a diameter of 7.5 mm.

To measure the twin lattice depth V_0, a superposition of momentum states $p_0 = \pm 4\hbar k$ is created via double Bragg diffraction and a sequential pulse. This separation should sufficiently minimize the effect of the non-resonant lattice contributions. A short pulse of a copropagating twin lattice induces oscillations between $p_0 = \pm 4\hbar k$ and the neighbouring momentum states $p_0 \pm 2\hbar k$ corresponding to the population in the second excited Bloch band. These oscillations are observed for different relative laser intensities I/I_0 (Fig. 4.15), where a value of $I/I_0 = 1$ corresponds to a total laser power of 1.06 W coupled into the fiber. Since the atomic position during the lattice pulse usually does not coincide with the beam center and laser light can be absorbed by optical elements between fiber and atoms, the actual power seen by the atoms is significantly less.

A sinusoidal fit to the data yields the period of the oscillations, which are translated into a band gap with (4.9). Figure 4.16(a) illustrates the relation between band gap and lattice depth V_0 taken from the band structure calculations in sec. 2.2.2. As shown in Fig. 4.16(b) the relation between lattice depth and the measured relative laser power is linear as expected. Lattice depths were also measured for other atomic positions closer to the beam center. Due to the higher local intensity, the measured lattice depths are larger for a specific power within the fiber.

4.3.2 Adiabatic loading

In contrast to the lattice calibration measurements, where several bands are populated, one usually wants to load the BEC into a single Bloch state $|n,q\rangle$ of the optical lattice. Similary, when unloading the atoms from the lattice, only one momentum class should be populated. This can be achieved by adiabatically increasing and decreasing the laser intensity during loading and unloading, respectively. When lowering the lattice depth V_0 the Wannier function in momentum space becomes constant over the first Brillouin zone and suppresses the population of other momentum states separated by multiples of $2\hbar k$ [44]. For an efficient loading procedure the lattice intensity has to follow an adiabatic ramp such that

$$|\langle n,q|\frac{\partial \hat{H}}{\partial t}|0,q\rangle| \ll \Delta E^2(q,t)/\hbar, \tag{4.10}$$

where $\Delta E = E_1 - E_0$ is the energy difference between the ground and the first excited state. The left-hand side of (4.10) is always less than $\frac{dV_0}{dt}$. At $q = 0$ the band gap energy ΔE never falls below $4E_r$ for any V_0 as can be seen in Fig. 2.7. Therefore, the adiabatic criterion can be satisfied by $\frac{dV_0}{dt} \ll 16E_r^2/\hbar$ [135]. In case of a lattice depth of $10\,E_r$, for example, the loading should take significantly longer than 26 µs.

Out of technical reasons usually a linear ramp is employed to adiabatically switch on and off the lattice depth. Since the band gap increases for larger values of V_0, adiabaticity is easier to fulfill and the ramp can be accelerated as the laser intensity increases. Indeed, the actual ramp in the experiment which is smoothed by the AOM response is a more efficient way to populate the fundamental Bloch state compared to a linear ramp. A non-adiabatic method for preparing a BEC in different bands of an optical lattice is presented in [183]. Via an optimized pulse sequence with a total duration of several tens of microseconds, atoms can be loaded into a single Bloch state with high efficiencies of more than 99%.

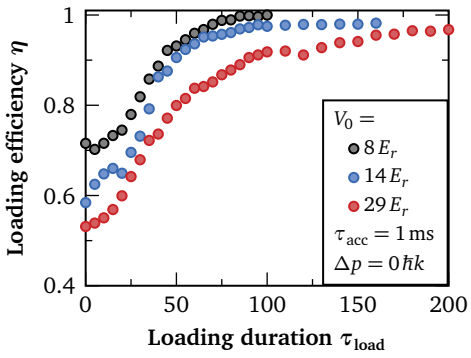

Fig. 4.17: Efficiency η for adiabatic loading into the fundamental Bloch band. The efficiency is plotted for different lattice depths V_0 depending on the duration τ_{load}.

In order to measure the loading efficiency into the fundamental band a BEC is loaded into a comoving lattice with a linear ramp of varying duration τ_{load}. It is held in the lattice for $\tau_{\text{acc}} = 1$ ms without any transfer of momentum and then released out of the lattice again via a linearly decreasing ramp of same duration τ_{load}. In case of a perfect loading efficiency, all atoms populate the initial momentum state and have not been transferred to neighboring states after this sequence. The experiment is performed along the vertical beam splitter direction and the lattice acceleration $a = \frac{\alpha}{2k}$ is matched to the gravitational acceleration g so that the lattice is always comoving with the atoms.

In Fig. 4.17 the loading behavior is displayed for three different lattice depths V_0. For shallow lattices $< 15\,E_r$, a duration of $\tau_{\text{load}} = 100$ µs is sufficient to efficiently populate the fundamental Bloch band. As the lattice depths increases, the adiabaticity criterion requires longer durations τ_{load}. In the majority of the performed experiments the lattice depth does not exceed $30\,E_r$ and a duration of $\tau_{\text{load}} = 200$ µs provides adequate efficiencies above 96%.

4.3.3 Transfer efficiency in a twin lattice

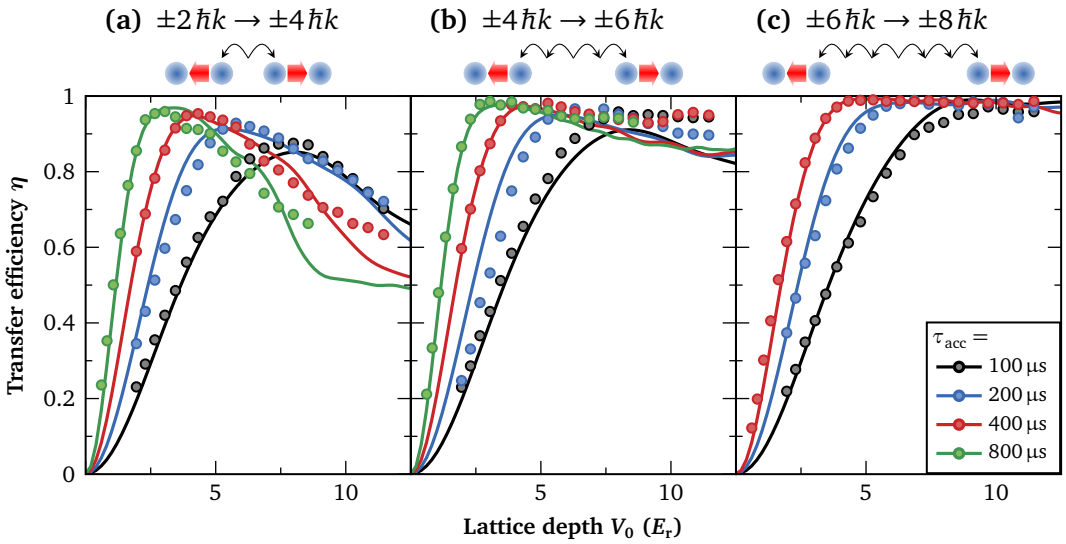

Figure 4.18: Transfer efficiency in the twin lattice starting with different initial superpositions of momentum states $\pm 2\hbar k$, $\pm 4\hbar k$ and $\pm 6\hbar k$. Via simultaneous lattice acceleration each cloud receives a momentum of $\pm 2\hbar k$ to increase the separation by $4\hbar k$. The efficiency is plotted for different durations τ_{acc} and in dependence of the lattice depth V_0. The markers represent experimental measurements and the lines are theoretical simulations.

As indicated in section 2.2.4 the transfer efficiency in a retroreflected scheme differs from a single lattice, since one lattice might disturb the acceleration within the other lattice. In order to measure efficiencies in our twin lattice, first a superposition of symmetric momentum states separated by $\Delta p = 4, 8, 12\hbar k$ is created by performing double Bragg diffraction and one or two successive Bragg pulses. Then, each cloud in $\pm 2\hbar k, \pm 4\hbar k$ or $\pm 6\hbar k$ is accelerated via Bloch oscillations by $\pm 2\hbar k$ for different durations τ_{acc}, which increases the inital momentum splitting by $4\hbar k$. Fig. 4.19(a) exemplary shows the relative population in the different momentum states for a transfer of $\pm 2\hbar k \rightarrow \pm 4\hbar k$ during $\tau_{\mathrm{acc}} = 200\,\mu\mathrm{s}$ depending on the lattice depth V_0. For the calculation of the transfer efficiency into the final momentum state as shown in Fig. 4.18 all loss channels detected on the CCD image are taken into account, which include momentum states up to $\pm 10\hbar k$.

As expected from Landau-Zener theory (sec. 2.2.4) the maximal transfer efficiency increases with τ_{acc}. Larger durations τ_{acc} correspond to smaller accelerations which lower the probability of non-adiabatic interband transitions. At the same time, the efficiency grows with larger momentum separation Δp and reaches almost 100% for $\Delta p = 12\hbar k$, while for smaller separations rather distinct maxima can be observed. Hereby, the declining transfer efficiencies for large lattice depths are mainly caused by losses into the state with $0\hbar k$. The experimental data (points) cannot be reproduced by simulations assuming an ideal twin lattice. In these calculations, no significant difference in the transfer efficiency is observed for different initial separations $\Delta p = 4, 8, 12\hbar k$. Furthermore they do not show a significant loss channel into $0\hbar k$. Only when imperfect polarizations of the light field are taken into account, the experiments can be explained.

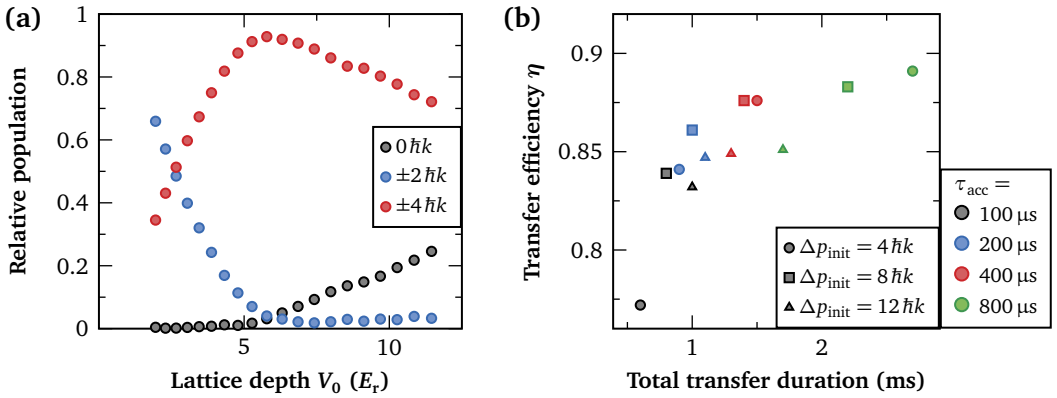

Figure 4.19: (a) Relative population in momentum states $0, \pm 2$ and $\pm 4\hbar k$ for a Bloch transfer $\pm 2\hbar k \rightarrow \pm 4\hbar k$ with duration $\tau_{acc} = 200\,\mu s$ depending on the twin lattice depth V_0. (b) Transfer efficiency in a twin lattice taking into account the double Bragg pulses for a total transfer of $0\hbar k \rightarrow \pm 8\hbar k$ depending on inital Bragg splitting Δp_{init} and lattice duration τ_{acc}.

The lines in Fig. 4.18 are the results of numerical calculations carried out by Jan-Niclas Siemß[1]. They take into account the twin-lattice potential and include imperfect polarizations characterized by σ_{pol} as detailed in (2.39). The simulations are based on an effective time-dependent Gross-Pitaevski model [170, 171] as introduced in section 3.2.2. The inital atomic state is generated by comparing the experimentally measured size and expansion rate of a lensed Bose-Einstein condensate to 3D Gross-Pitaevski simulations. For the simulations the release from a harmonic magnetic trap and a harmonic magnetic lensing potential is taken into account. The initial momentum transfer via double Bragg diffraction is simply realized by perfect momentum kicks, where the wave packet is multiplied with a phase factor $\phi_{DBD} = \Delta p \cdot y$.

Through a variation of the polarization error of σ_{pol} the simulations are fitted to the experimental data. An error of $\sigma_{pol} = 0.2688$ represents the best agreement between theory and data, which is compatible with experimental measurements of the polarization in the setup (sec. 3.3.2). While the influence of the beat term V_b is negligible, the interaction with a standing wave V_{St} significantly decreases the transfer efficiency in the twin lattice. Fortunately, this effect can be suppressed by starting Bloch oscillations with a larger inital momentum splitting, i.e. a larger detuning between atoms and the standing wave. A larger initial splitting, however, requires more initial Bragg pulses which are accompanied by additional atom losses. To achieve the most efficient transfer, one therefore has to find a compromise between both loss channels.

Fig. 4.19(b) sums up the results obtained from Fig. 4.18 and additionally takes into account the atom losses during the initial splitting through Bragg processes. It plots the total transfer efficiency for $0\hbar k \rightarrow \pm 8\hbar k$ for different initial momentum splittings $\Delta p_{init} = n \cdot 4\hbar k$ and different Bloch acceleration durations τ_{acc}, where the color coding is the same as in Figure 4.18. The total transfer duration corresponds to the respective sum of the pulse durations $n \cdot \tau_{Bragg} = n \cdot 300\,\mu s$ and acceleration durations $(4\text{-}n) \cdot \tau_{acc}$. For Bragg processes, an average efficiency of $\eta_{Bragg} = 95\%$ for one double or sequential pulse is assumed, corresponding to 98.8% per $\hbar k$. For each initial splitting and each duration τ_{acc} the maximum efficiency is extracted from

1 Institut für Theoretische Physik & Institut für Quantenoptik, Leibniz Universität Hannover

Fig. 4.18. The total transfer efficieny is then calculated as the product of the efficiency of each step. For example, for an initial momentum splitting of $\Delta p_{\text{init}} = 8\hbar k$ via Bragg diffraction and lattice durations of $\tau_{\text{acc}} = 200\,\mu\text{s}$ the efficiency and total duration τ are calculated in the following way:

$$\begin{aligned}\eta &= \eta_{\text{Bragg},0\to\pm 2\hbar k} \cdot \eta_{\text{Bragg},\pm 2\hbar k\to\pm 4\hbar k} \cdot \eta_{\tau_{\text{acc}}=200\,\mu\text{s},\pm 4\to\pm 6\hbar k} \cdot \eta_{\tau_{\text{acc}}=200\,\mu\text{s},\pm 6\to\pm 8\hbar k} \\ &= 0.95 \cdot 0.95 \cdot 0.966 \cdot 0.988 = 0.861, \\ \tau &= 300\,\mu\text{s} + 300\,\mu\text{s} + 200\,\mu\text{s} + 200\,\mu\text{s} = 1\,\text{ms}.\end{aligned}$$

Fig. 4.19(b) shows that an initial splitting of $\Delta p_{\text{init}} = 8\hbar k$ yields the highest overall efficiency. In case of an initial splitting of $\Delta p_{\text{init}} = 12\hbar k$, the total efficiency is limited by the Bragg processes to $(95\%)^3 = 85.7\%$, while starting Bloch oscillations directly after the first double Bragg pulse ($\Delta p_{\text{init}} = 4\hbar k$) is only worthwile if sufficiently long transfer durations are available in the experimental sequence. Hence, an initial superposition of $\pm 4\hbar k$ is chosen for starting acceleration in a twin lattice as a compromise between losses due to parasitic standing waves and the lower efficiency of Bragg diffraction .

4.3.4 Spontaneous emission in a twin lattice

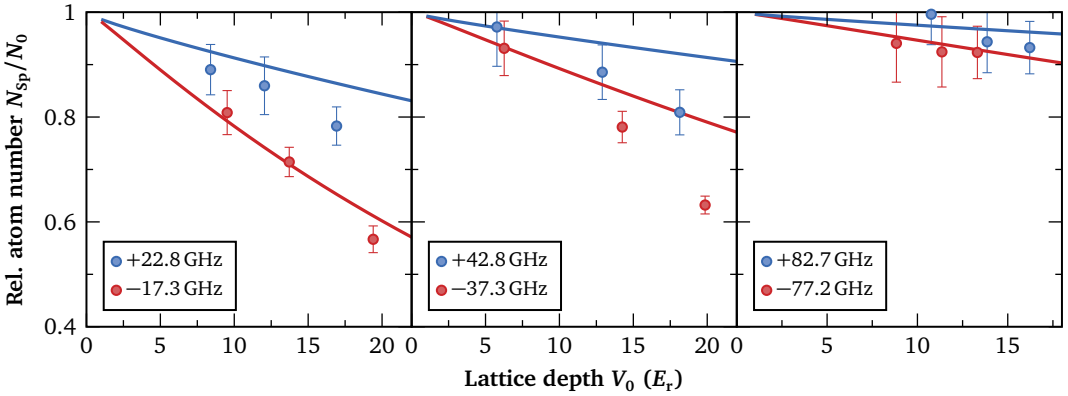

Figure 4.20: Residual atom number N_{Sp}/N_0 due to spontaneous emission losses in a twin lattice for different blue (——) and red (——) detunings $\Delta/(2\pi)$ depending on the lattice depth V_0. The lines are theoretical calculations according to Eq. (2.62) and (4.11).

The spontaneous emission rate for an atom copropagating in a blue-detuned twin-lattice potential has been derived in Eq. (2.62). In case of a red-detuned potential we similarly find

$$P_{\text{twin,red}} = \frac{V_0[E_r]\omega_r}{\Delta[\Gamma]}\left(1.5 - \frac{1}{2\sqrt{V_0[E_r]}}\right). \tag{4.11}$$

In both cases, the terms due to imperfect polarization do not contribute to the scattering rate since the temporal average over the interference terms yields zero.

The atom losses due to spontaneous emission are measured for a red and blue detuning of the twin lattice light. Fig. 4.20 details the results for six different detunings Δ, where the relative residual atom number is measured in dependence of the lattice depth V_0. For the measurement, the atom clouds are transferred into momentum states $\pm 16\hbar k$ in order to

exclude the probability of any influences of standing waves. The atom number in $\pm 16\hbar k$ is then measured repeatedly, yielding the amount of atoms N_0 without spontaneous emission losses. Afterwards, a comoving lattice is linearly ramped up, kept at a constant intensity V_0 during τ_{acc} and ramped down again during τ_{load}. Then, the residual atom number N_{Sp} in $\pm 16\hbar k$ is measured. The subsequent time-of-flight is sufficient to separate spontaneously scattered atoms from the output ports. After a total interaction time of $\tau_{\mathrm{acc}} + \tau_{\mathrm{load}}$ with the lattice, the atom number decreases with rate P_{twin} as

$$N_{\mathrm{Sp}} = N_0 \mathrm{e}^{-P_{\mathrm{twin}}(\tau_{\mathrm{acc}}+\tau_{\mathrm{load}})}. \tag{4.12}$$

Since the lattice depth during loading and unloading is on average $V_0/2$, the duration for loading and unloading has been multiplied by a factor $\frac{1}{2}$.

The experimental results confirm that a blue-detuned lattice suppresses spontaneous emission losses in a twin lattice, in our case by roughly a factor of two. The suppression is lower than in a single optical lattice due to the influence of the counterpropagating twin. A slight intensity imbalance between the two laser beams additionally can reduce the suppression of spontaneous emission losses in a blue detuned lattice [44]. The lines in Fig. 4.20 represent the theoretical calculations for the applied lattice depth and detuning as described in Eq. (2.62) and (4.11).

4.3.5 Phase shift

After loading the atoms into the lattice, the latter is accelerated to manipulate the atomic motion. The corresponding force acting on the lattice leads to a sudden shift of the local minimum of the lattice potential and induces oscillations of the atoms at the bottom of the lattice which result in lower transfer efficiencies [139]. This shift can be mitigated either by a shift of the lattice position, i.e. a phase shift, or with an adiabatic acceleration sequence.

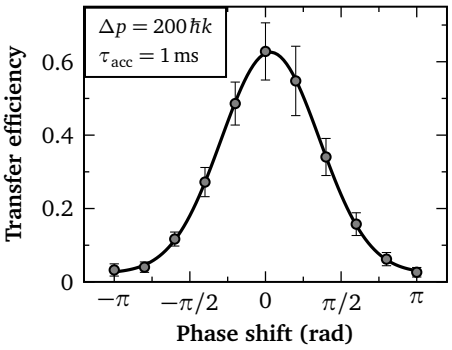

Fig. 4.21: Bloch transfer efficiency (Bloch period $T_B = 10\,\mu\mathrm{s}$) depending on a phase shift at the start of the acceleration and Gaussian fit to the data.

A phase shift can be applied via the AOMs on either one of the frequency components of the light field. Its influence on the transfer efficiency of Bloch oscillations is illustrated in Figure 4.21 for a transfer of $200\hbar k$ in direction of gravity. With an acceleration duration of $\tau_{\mathrm{acc}} = 1\,\mathrm{ms}$ the Bloch period corresponds to $T_B = 10\,\mu\mathrm{s}$. The atoms are loaded into a comoving lattice via linearly ramping up the lattice depth up to $30\,E_r$ while the lattice acceleration is matched to the gravitational acceleration. A phase shift is applied to the lattice after loading and before acceleration. Each data point corresponds to an average of 20 measurements. The data clearly shows a significant dependence of the transfer efficiency on the phase shift. For a phase shift of $\pm\pi$ the transfer efficiency almost drops to zero. Experimentally, the maximum efficiency is reached for zero phase shift. A Gaussian fit to the data exhibits a maximum at 0.1 rad where the transfer efficiency is merely larger by 0.5% compared to the value of 0 rad.

4.4 Extended diffraction techniques

As a conclusion to the current chapter, the following section comprises the presentation of some diffraction techniques which exceed the methods of double Bragg diffraction and Bloch oscillations as described previously. These techniques, which include symmetric beam splitting along gravity, an adiabatic-rapid-passage pulse and simultaneous beam splitting along two axes, each come with benefits for the implementation in atomic sensors.

4.4.1 Double diffraction along gravity

Double diffraction is intrinsically restricted to atoms with zero Doppler shift. However, when three frequencies are employed, it is possible to drive symmetric transitions in a cold cloud with a non-vanishing velocity and double the momentum transfer [62, 67]. In contrast to conventional double diffraction, however, the two simultaneous two-photon transitions only share one frequency component making the process not completely symmetric. This scheme is technically more complex to implement, since most frequency sources only feature two output ports. Therefore, usually two devices have to be employed which might complicate a synchronous operation and symmetric intensities for all three frequencies. Any asynchronisms in time, amplitude or phase of the frequencies which are not common to both transitions may decrease the contrast in an interfermeter.

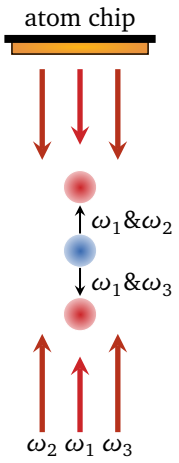

Fig. 4.22: Double diffraction scheme along gravity.

In our setup, double diffraction with three frequencies is realized along the axis parallel to gravity, where the Doppler shift $\omega_D = k_{eff} g t_{tof}$ increases linearly with time-of-flight and depends on the gravitational acceleration g and the time of flight t_{tof}. The atom chip serves as retroreflector and inertial reference for the light fields. The three different frequencies for first order double diffraction equal

$$\omega_1, \qquad \omega_2 = \omega_1 + k_{eff} g t_{tof} + \omega_{eff} \qquad \text{and} \qquad \omega_3 = \omega_1 + k_{eff} g t_{tof} - \omega_{eff}\,. \tag{4.13}$$

Compared to classical double diffraction, this scheme features also some advantages. For once, the minimum beat frequency equals $\Delta\omega = 2\omega_{eff}$, i.e. the frequency of the amplitude modulation, is twice as large as the one in first order double diffraction (see sec. 4.2.2). Therfore, pulse stability is reached for shorter pulse durations τ which increase the momentum acceptance. As illustrated in Fig. 4.23(a), already a pulse with $\tau = 200$ µs delivers a sufficiently high stability which is not further improved by a larger duration $\tau = 300$ µs.

Furthermore, already few milliseconds after release any influences caused by standing waves are sufficiently suppressed due to the Doppler shift. As long as the cloud's velocity does not approach zero, there is no need to use orthogonal incoming polarizations, which simplifies the setup. Indeed, our vertical beam splitter setup uses only parallel polarizations. A dual lattice with orthogonal polarizations would require to insert a quarter-wave plate in front of the atom chip.

Figure 4.23(b) plots the transfer efficiency for an acceleration via Bloch oscillations of a superposition of momenta $p_0 \pm 2\hbar k$ by $\pm 2\hbar k$ into $p_0 \pm 4\hbar k$. Analog to the measurements

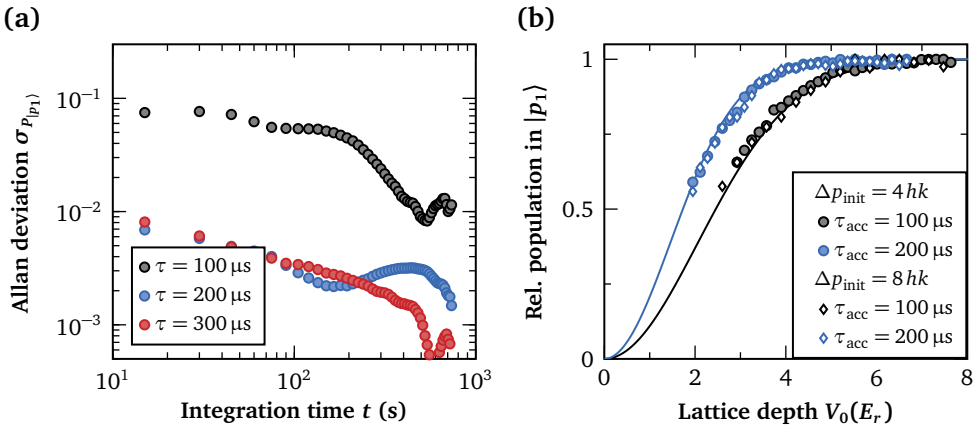

Figure 4.23: (a) Beam splitter stability of a double diffraction pulse along gravity for different pulse durations. (b) Acceleration with Bloch oscillations by $2\hbar k$ for different durations t_{acc} and two different initial splittings $\Delta p_{\text{init}} = 4\hbar k$ and $8\hbar k$. Theoretical Landau-Zener calculations for a single lattice are depicted as well (lines).

described in section 4.3.3 the initial separation $\Delta p_{\text{init}} = 4\hbar k$ is achieved via Bragg diffraction. Landau-Zener curves are also measured for an initial separation of $\Delta p_{\text{init}} = 8\hbar k$. In contrast to the horizontal twin lattice, the transfer efficiency in this setup is equal for both data series. The data points agree very well with the Landau-Zener theory for a single optical lattice (lines in Fig. 4.23(b)). This confirms that the limited efficiencies in Fig. 4.18 only result from standing waves and are not present in an ideal twin lattice with perfect polarizations.

Finally, a gravimeter is realized in order to prove the coherence of this type of beam splitter. Three first order pulses are applied to span a symmetric Mach-Zehnder-type interferometer, which is able to measure the gravitational acceleration. The lattice acceleration $\alpha = \frac{d\omega}{dt}$ is scanned in order to obtain fringes. Hereby, the relative population in the two outer output ports $p_1 = p_0 \pm 2\hbar k$ evolves as

$$P_{|p_1\rangle} = 1 - \cos((k_{\text{eff}} g - \alpha) T^2). \qquad (4.14)$$

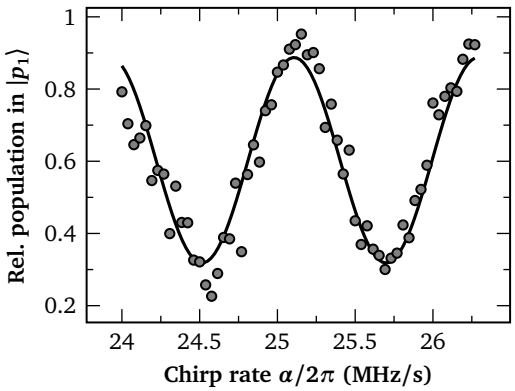

Fig. 4.24: Scanning the acceleration of the lattice results in interference fringes and allows one to obtain the value for local gravity.

Out of technical reasons a constant frequency chirp throughout the interferometer sequence can not be applied. To accumulate the same laser phase imprinted on to the atoms, the frequency can be changed in the temporal middle between the pulses [116, 177]. The measured fringe is shown in Fig. 4.24. From the fit to the data the gravitational acceleration is extracted to be $g = (9.986 \pm 0.002)\,\text{m/s}^2$.

4.4.2 Adiabatic-rapid-passage Bragg pulse

The combination of Bragg diffraction with an adiabatic rapid passage (ARP) leads to an efficient technique for transferring large momentum onto a cold atom cloud. In comparison to conventional box or Gaussian-shaped pulses, this method is more robust against fluctuations of pulse intensity and detuning and eases the requirements on the velocity spread of the atomic source. This makes it especially suited for large momentum transfer, where the effect of laser intensity noise might be increased due to the multitude of atom-light interactions.

For an ARP pulse the laser intensity has the shape of a hyperbolic tangent (tanh), while the two-photon detuning $\delta(t)$ is linearly swept through resonance during the pulse (Fig. 4.25). This technique can also be applied to higher order transitions. As in [73] the intensity profile follows

$$\Omega(t) = \tanh(8t)\tanh[8(1-t)] \quad \text{for} \quad 0 < t < \tau. \tag{4.15}$$

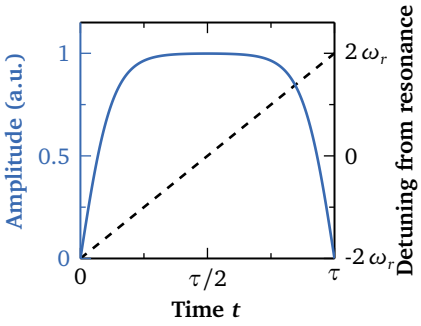

Fig. 4.25: Amplitude and detuning for an ARP tanh pulse of duration τ [73].

$\delta(t)$ is linearly swept from $-2\omega_r + \delta_0$ to $+2\omega_r + \delta_0$, where δ_0 is the resonance frequency. Tanh pulses of 300 µs duration, transferring $10\hbar k$ with a high efficiency of 99.7% per $\hbar k$ could be demonstrated [73]. 0.2% per $\hbar k$ of these losses were caused by spontaneous emission.

Figure 4.26 contrasts transfer efficiencies achieved in our experiment for a Gaussian pulse with $\sigma_t = 35$ µs and tanh pulses with two different durations $\tau = 300$ µs and $\tau = 1$ ms for first order and sequential double Bragg diffraction. For first order double diffraction the maximum transfer efficiencies are similar in all cases, while a tanh pulse achieves a better efficiency for sequential diffraction. The limited transfer for sequential Gaussian pulses probably results from an offset velocity due to an imperfect beam splitter alignment. In general, the tanh pulses exhibit a broader peak structure and therefore a larger acceptance both to fluctuations in intensity as well as in the detuning. However, these benefits decline with decreasing pulse duration τ as the adiabaticity of the process is lowered.

Although the beam splitting efficiencies seem promising, the method is not suited for interferometry with double Bragg diffraction. The adiabatic ramp destroys the symmetry and simultaneity of the process since the frequency chirp does not address momentum classes symmetrically. This results in an unequal population of momentum states $|+2\hbar k\rangle$ and $|-2\hbar k\rangle$, making it unsuitable for the use inside an atom interferometer (see inset Fig. 4.26). Symmetric diffraction would require to sweep the frequency difference in each arm oppositely to each other, which is impossible in our retroreflex configuration. For a single diffraction process, though, tanh pulses represent a good technique to improve current transfer efficiencies as demonstrated for sequential double diffraction. Currently, technical problems such as timing asymmetries prevent the application together with Bloch oscillations (see sec. 3.3.1).

In addition to the transfer efficiency, it is also important to look at the phase imprinted on the atoms during such pulses. If the phase of the different velocity components varies by more than 2π, the contrast in an interferometer vanishes. Whereas the dependence of the phase shift on velocity is negligible for standard Gaussian pulses, it is of much more importance for tanh pulses. Since, for example in a Mach-Zehnder interferometer the output phase is the

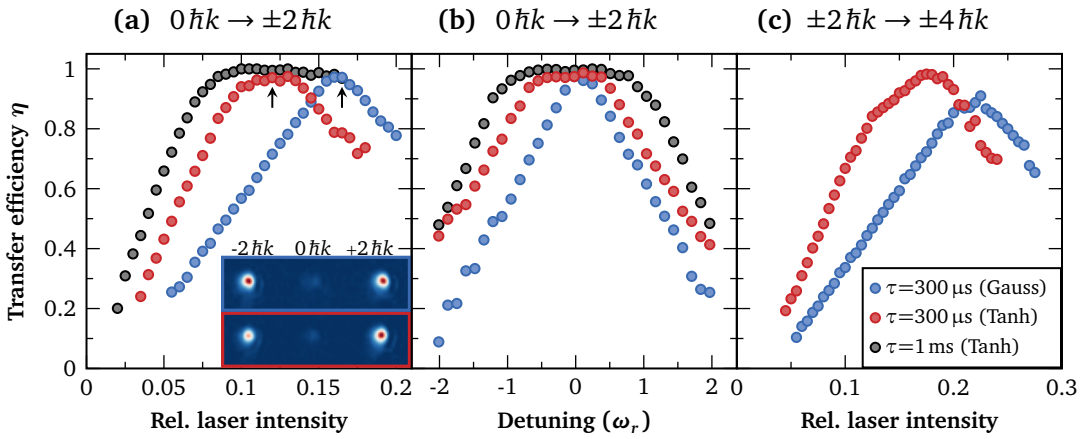

Figure 4.26: Comparison between a Gaussian pulse of width $\sigma_t = 35$ µs (●) and two tanh pulses of duration $\tau = 300$ µs (●) and $\tau = 1$ ms (●). For these pulses the transfer efficiency is measured for first order (a,b) as well as sequential (c) double diffraction depending on the relative laser intensity (a,c) and the detuning from resonance (b). The arrows in (a) mark the data points which correspond to the absorption images below. These show exemplarily that for first order double diffraction a tanh pulse (——) leads to an asymmetric population of momentum states $|+2\hbar k\rangle$ and $|-2\hbar k\rangle$, while the population is symmetric for a Gaussian pulse (——).

difference of its π and $\pi/2$ pulses, a proper choice of pulse parameters can still lead to a high contrast interferometer, where the phase shifts of each velocity component cancel out [73].

4.4.3 2D beam splitter

The unique beam splitting setup in QUANTUS-1 offers the possibility to combine horizontal with vertical atomic manipulation and create a 2D beam splitter. Multidimensional atom optic manipulation has been proposed in [184] to simultaneously probe accelerations and rotations in three dimensions or suppress parasitic inertial forces in a compact sensor. So far, this has only been achieved in sequential measurements [185, 186]. Another possible application represents a state-selective blow-away which can be implemented within our twin-lattice interferometer.

Spurious atoms in the output ports of an interferometer result in a loss of contrast, since they generate background noise or even form parasitic interferometers. In contrast to Bragg transitions, the internal state labeling of Raman diffraction allows a state-selective removal of residual atoms in a double diffraction scheme [66, 67] or a symmetric composite-pulse interferometer [24]. In the twin-lattice geometry, the limited efficiency of the initial sequential double Bragg process leads to residual atoms in momentum states $0\hbar k$ and $\pm 2\hbar k$. These atoms can only be addressed selectively via their horizontal momentum. Another Bragg pulse in horizontal direction, however, would not move these atoms out of the interferometer region. By employing a combination of vertical and horizontal light fields, instead, it is possible to address a particular horizontal momentum class and vertically separate it from the interferometer atoms.

As depicted in Figure 4.27(a,b) the blow-away pulse employs a single frequency component from each direction with frequencies $\omega_1 = 2\pi \cdot 10$ kHz and $\omega_2 = 2\pi \cdot 155$ kHz in horizontal

and vertical direction for a duration of $\tau = 500\,\mu s$. The atoms do not receive a particular momentum but get diffracted into a variety of states. The population in the initial spurious states is reduced with an efficiency of 90%. Despite of the promising results this technique was not applied in the twin-lattice interferometers described in the next chapter, since a first analysis could not demonstrate any improvement on the measured contrast.

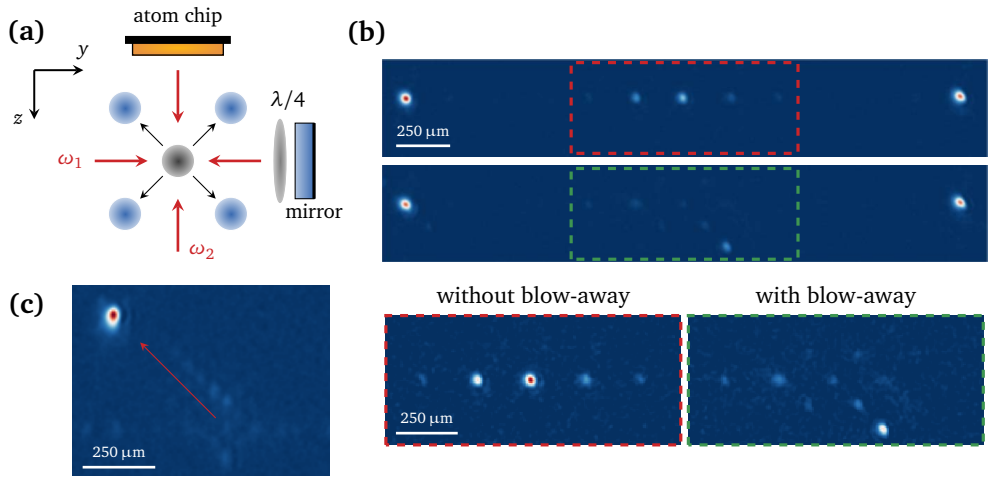

Figure 4.27: (a) The combination of two frequency components ω_1, ω_2 in y and z direction results in a 2D beam splitter. (b) This type of beam splitter can be used to remove spurious atoms in momentum states $0\hbar k, \pm 2\hbar k$, which are left over after a large momentum transfer beam splitter. (c) Realization of nine 2D Bloch oscillations by sweeping both frequencies by +80 kHz and −44 kHz, respectively.

Apart from populating a variety of different momentum states, Figure 4.27(c) also illustrates an example, where a mainly unidirectional transfer in $y - z$ direction has been achieved via Bloch oscillations. After a time-of-flight of $t_{\mathrm{tof}} = 27.5\,\mathrm{ms}$ the BEC undergoes nine Bloch oscillations and is diffracted diagonally by sweeping the initial frequencies of $f_1 = 0\,\mathrm{kHz}$ and $f_2 = 340\,\mathrm{kHz}$ within $\tau_{\mathrm{acc}} = 1\,\mathrm{ms}$ by +80 kHz and −44 kHz, respectively. The transfer exhibits a relatively high efficiency of more than 90%.

LARGE MOMENTUM INTERFEROMETRY IN A TWIN LATTICE

5

Large momentum transfer in atom interferometry represents one of the key elements to reach the required sensitivities for gravitational wave detection on ground [49–51] and in space [52, 53]. Additionally, the precision of h/m measurements [44–46] and inertial sensors [19, 25–27, 47] benefits from an increase in momentum separation between the two wave packets in the interferometer. As detailed in section 1.1.1, the transfer of multiples of photon recoils in an interferometer has been realized with Bragg [57, 68, 71, 73] or Raman diffraction [24, 66, 72, 74] as well as with Bloch oscillations [69] and a combination of both [59, 60, 62]. While atom interferometers with multiple light pulses are rather limited by atom loss caused by non-ideal beam splitter efficiencies, acceleration in a lattice rather suffers from a dephasing due to light shifts.

The twin-lattice interferometer approaches both of these problems. It is based on a sequential double Bragg diffraction interferometer [68] extended by the simultaneous acceleration of both clouds by Bloch oscillations. The high efficiency of Bloch oscillations provides a scalable setup, while the symmetric manipulation in a retroreflected geometry suppresses systematic effects such as laser phase noise as well as presumably diffraction phases [68, 69]. Such a combination was initially proposed in [61]. In Ref. [62] simultaneous acceleration in a dual lattice was implemented along gravity via superimposing two beams with a total of three frequency components. This technique is similar to double diffraction along gravity, as described in section 4.4.1.

The following section starts with a description of the temporal interferometer sequence. Owing to the large vibrations in the experiment the contrast of the interferometer is analyzed by statistical means (sec. 5.1). Possible contrast loss mechanisms are investigated in detail both experimentally as well as with theoretical simulations (sec. 5.2). We will see that the contrast in the twin-lattice interferometer is mainly limited by technical constraints due to limited transfer efficiencies and a dephasing arising from light field inhomogeneities. A preliminary way to overcome the current limitations is to employ a smaller beam size which reduces the amount of light distortions caused by spurious diffraction (sec. 5.3). The chapter closes with a presentation of different techniques which seem promising to improve on the current results in the future (sec. 5.4). The most important results presented in the following, including the realization and analysis of the twin-lattice geometry to achieve the largest separation in an atom interferometer so far, have been published in Ref. [104].

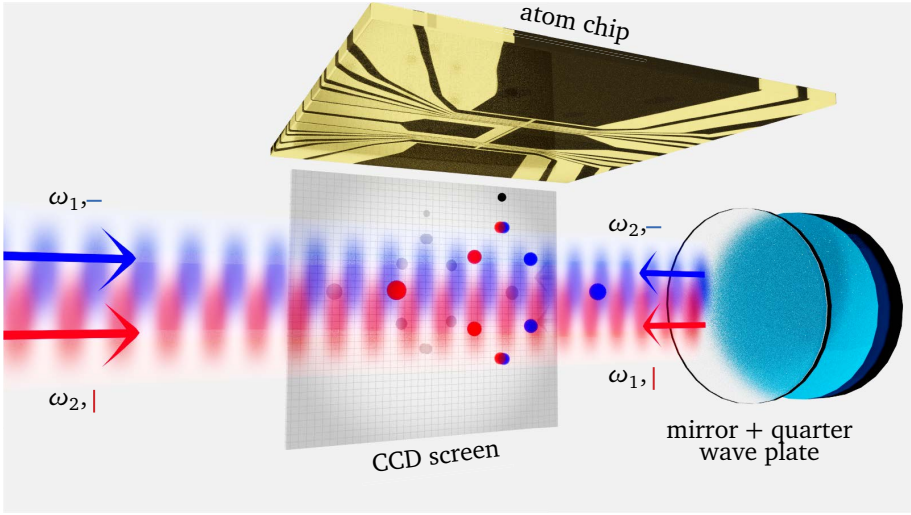

Figure 5.1: 3D-scheme of the twin-lattice interferometer. After release from the atom-chip trap and state preparation the BEC is manipulated by two counterpropagating lattices of orthogonal polarization, the so-called twin lattice. With the twin lattice, a sequence of double Bragg diffraction and Bloch oscillations is driven to form a symmetric atom interferometer. Published in [104].

5.1 Interferometer scheme

The total interferometer duration is limited by the size of the detection area. In the QUANTUS-1 experiment, the imaging system provides an observable free fall time of roughly 35 ms. Afterwards, atomic clouds can not be detected anymore. Given the time required for state preparation in the beginning and sufficient spatial separation of the momentum states in the end, a duration of about 12 ms is available for twin-lattice interferometry. During this time, a Mach-Zehnder-type sequence is driven, where the twin-lattice beam splitter serves for splitting, redirection and recombination of the BECs. In the following, stability and efficiency, two important properties of a beam splitter, are analyzed and the interferometer sequence is explained in detail.

5.1.1 Beam splitter

A twin lattice beam splitter starts with a sequential first order double Bragg process creating an initial superposition of momentum states $\pm 4\hbar k$. Each Bragg pulse is of Gaussian shape and has a width of $\sigma_t = 37.5\,\mu s$. The splitting of $\Delta p_{\text{init}} = 8\hbar k$ suppresses non-adiabatic losses during the following Bloch oscillation sequence as discussed in sec. 4.3.3. Both atom clouds are loaded into a copropagating lattice during $\tau_{\text{load}} = 200\,\mu s$, where they are accelerated up to a momentum of $\pm 204\hbar k$, and then unloaded from the lattice during $\tau_{\text{load}} = 200\,\mu s$. The sequence of the beam splitter is illustrated in Fig. 5.4(c). The applied twin-lattice depth V_0 increases with the maximum momentum separation Δp in order to compensate for rising Landau-Zener losses (Fig. 5.4(d)). Up to 1.2 W of laser power are available. For momentum splittings up to $100\hbar k$ the lattice acceleration is constant over the acceleration duration $\tau_{\text{acc}} = 2\,\text{ms}$. Faster accelerations than $100\hbar k$ per 2 ms, however, increase losses at the

beginning of the acceleration sequence due to the parasitic standing wave in the twin lattice (sec. 4.3.3). Therefore, a sequence comprising two acceleration steps is applied in these cases. For $\Delta p = 128, 208, 308$ and $408\,\hbar k$ a differential momentum of $12\,\hbar k$ is transferred during the first 500, 400, 300 and 300 µs, respectively, while the residual transfer takes place in the time that remains of 2 ms. In each step the lattice depth is optimized for low atom losses. In this way, the losses can be kept sufficiently small making these beam splitters well suitable for the application within an interferometer.

Fig. 5.2 shows density plots for different realizations of a twin-lattice beam splitter ranging from a separation of $\Delta p = 24\,\hbar k$ up to $\Delta p = 1008\,\hbar k$. The transfer efficiency is calculated by measuring the atom number in the target momentum class relative to the total atom number, neglecting spontaneous emission losses, which, for the most part, are not counted by the detection system. Substracting the losses from the initial Bragg process, the effective Bloch efficiency equals 99.5% per $\hbar k$ for $\Delta p = 24\,\hbar k$, 99.75% per $\hbar k$ for $\Delta p = 128\,\hbar k$ and reaches 99.95% per $\hbar k$ for $\Delta p = 408\,\hbar k$. The nonconstant transfer efficiency per $\hbar k$ partly results from abandoning the weak-binding limit, where the Landau-Zener formalism is no longer valid [139]. In addition, the parasitic interference terms of the twin lattice reduce the efficiency for small splittings Δp due to the influence of the standing wave.

For the realization of a $\Delta p = 1008\,\hbar k$ beam splitter, where the clouds have a differential velocity of 5.9 mm/s, τ_{acc} is increased from 2 ms to 3.5 ms. The relative population in $\pm 504\,\hbar k$ amounts to 28%, while the efficiency solely for Bloch oscillations corresponds to $\eta = 99.87\%$ per $\hbar k$. The efficiency is not limited fundamentally but by the available laser intensity as well as by the bounded detection size limiting τ_{acc} and thereby the adiabaticity of the process. For large Δp the atomic clouds seem slightly elongated along the y-axis. This is due to the high atomic velocity in this direction leading to a significant movement of the atoms during the 100 µs duration of image aquisition.

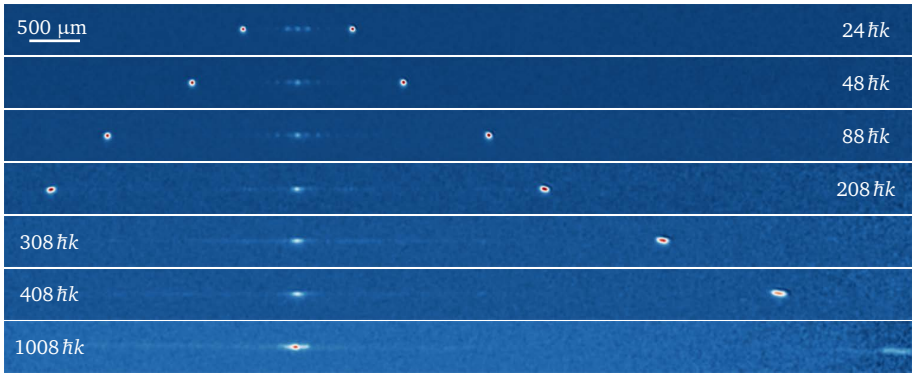

Figure 5.2: Density plots of different twin-lattice beam splitters with separations ranging from $\Delta p = 24\,\hbar k$ up to $\Delta p = 1008\,\hbar k$.

Beam splitter stability

Similarly as in section 4.2.2, the stability of the large momentum beam splitter is examined. Since large momentum transfer involves a multitude of atom-light interactions it is usually more sensitive to laser intensity fluctuations compared to beam splitters containing only a

single two-photon process. Changing beam splitter efficiencies can decrease the interferometric contrast and disturb the phase readout. Bloch oscillations present a good choice to provide stable transfer efficiencies, since they are based on adiabatic transfer, which is more robust against amplitude fluctuations.

The total diffraction efficiency of the first-order double diffraction beam splitter is measured via a double Gaussian fit (sec. 4.2.1). Because of the multitude of momentum states, the efficiency of larger momentum beam splitters can not be evaluated in the same manner. Instead, it is calculated by measuring the atom number in the final ports as well as the total atom number in all momentum states with individual Gaussian fits. This method intrinsically leads to a larger noise due to the absence of a common offset level (see sec. 3.1.2).

To estimate the impact of this detection method, the $4\hbar k$ beam splitter is evaluated both by measuring the absolute atom numbers in each state individually as well as by a direct measurement of the relative populations through a double Gaussian fit. Comparing both evaluations (Fig. 5.3(a)) reveals that the measurement of individual absolute atom numbers increases the detection noise by almost a factor of ten.

Figure 5.3(b) illustrates the stability of a first-order and a sequential double diffraction pulse with momentum separation $\Delta p = 4\hbar k$ and $\Delta p = 8\hbar k$ as well as of a beam splitter with additional Bloch oscillations ($\Delta p = 128\hbar k$). The diffraction efficiency is evaluated with individual Gaussian fits. In all cases, the beam splitter noise reaches a level below 10^{-2} after roughly 10^3 s of integration time. Surprisingly, the stability of the sequential double Bragg process ($\Delta p = 8\hbar k$) is slightly better compared to the first order pulse ($\Delta p = 4\hbar k$). This is most likely caused by a better performance of the experiment, since the measurements were realized at different times. Fluctuating environmental conditions like temperature can temporarily improve or degrade the experimental performance. Even the $\Delta p = 128\hbar k$ beam splitter does not show an increased noise level compared to the $\Delta p = 4\hbar k$ process, which is promising for the application in an interferometer. For the latter, a modulation can be observed, that likely results from the air-conditioning system in the laboratory which exhibits a period of around 15 minutes.

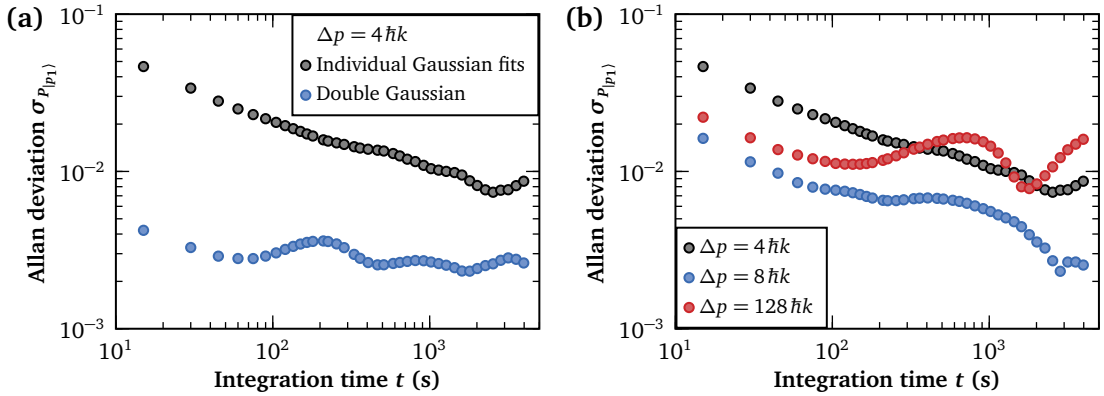

Figure 5.3: Stability of the large momentum beam splitter. (a) Comparison of the beam splitter stability for $\Delta p = 4\hbar k$ evaluated either by two individual Gaussian fits or one single fit consisting of two Gaussians with same background. (b) The overlapping Allan deviation of the transfer efficiency for a beam splitter without ($\Delta p = 4, 8\hbar k$) and with ($\Delta p = 128\hbar k$) Bloch oscillations. Evaluation in all cases with individual Gaussian fits.

5.1.2 Twin-lattice interferometry sequence

The twin-lattice interferometer sequence is depicted in Fig. 5.4, showing the trajectories during the interferometer (a) as well as the temporal sequence of the light field intensity and the momentum separation (c). The BEC is released from the magnetic trap with frequencies $\omega_{x,y,z} = 2\pi \cdot (43, 325, 327)\,\mathrm{Hz}$. DKC of duration $\tau_{\mathrm{dkc}} = 0.3\,\mathrm{ms}$ is performed 5.4 ms after release (sec. 4.1.2). Subsequently, the BEC is transferred to the non-magnetic state by an adiabatic rapid passage with a total duration of 9 ms (sec. 4.1.3).

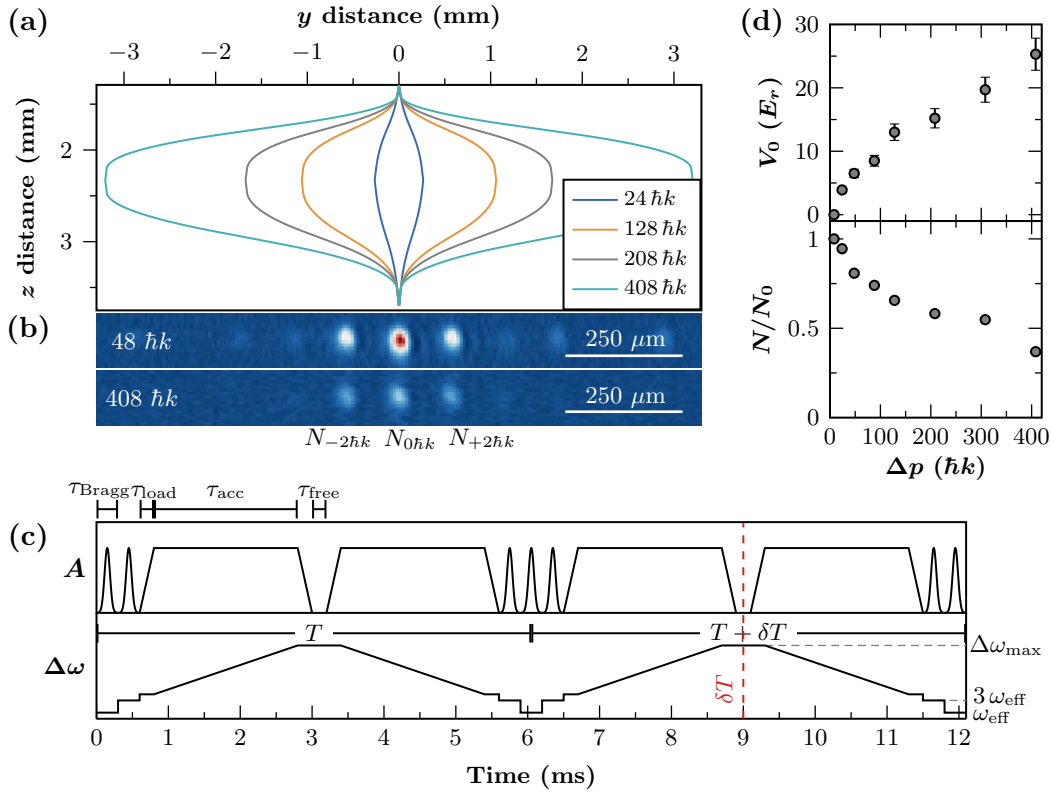

Figure 5.4: (a) Trajectories of the atom clouds during the twin-lattice interferometer. Distances are given relative to the center of the atom chip. (b) Interferometer output ports for $\Delta p = 48\,\hbar k$ and $\Delta p = 408\,\hbar k$. (c) Temporal sequence of the twin-lattice amplitude A (not to scale) controlled by AOMs and the frequency difference $\Delta\omega$ between the lattices. (d) Twin-lattice depth V_0 in units of recoil energy E_r and normalized atom number in the output ports for different interferometer realizations.

The interferometer sequence starts with the beam splitter described in section 5.1.1 consisting of a sequential double Bragg diffraction process and an acceleration via Bloch oscillations. During the following free evolution time of $\tau_{\mathrm{free}} = 200\,\mu\mathrm{s}$ the clouds are maximally separated in momentum by Δp. Afterwards, both momentum states are loaded into the twin lattice again and decelerated up to $\pm 4\hbar k$ via Bloch oscillations. A sequential double Bragg π-pulse inverts the atomic velocity resulting in a symmetric distribution in $\mp 4\hbar k$. Both clouds are then accelerated and after a second free evolution time decelerated again in the twin lattice before they are finally brought to interference by a last sequential double Bragg pulse. Each Gaussian pulse has a width of $\sigma_t = 37.5\,\mu\mathrm{s}$ and a duration of $\tau_{\mathrm{Bragg}} = 300\,\mu\mathrm{s}$, the duration for acceleration and deceleration correspond to $\tau_{\mathrm{acc}} = 2\,\mathrm{ms}$, while the loading and unloading

times amount to $\tau_{\mathrm{load}} = 200\,\mu\mathrm{s}$ in all cases. This results in a total interferometer duration of $2T = 12.1\,\mathrm{ms}$. For an interferometer solely based on double Bragg diffraction, the absence of Bloch oscillations leads to a free evolution time of $\tau_{\mathrm{free}} = 5\,\mathrm{ms}$ in each interferometer half.

After the interferometer, $\tau_{\mathrm{sep}} = 9\,\mathrm{ms}$ remain for the different momentum states to separate spatially before the output ports are detected via absorption imaging. Two exemplary interferometer output ports are depicted in Figure 5.4(b). During the interferometer Stern-Gerlach type deflection is employed to prevent atoms with nonzero magnetic moment from overlapping with the output ports (sec. 4.1.3). The interferometer signal P depends on the atom number in the two outer ports $N_{\pm 2\hbar k}$ and the inner port $N_{0\hbar k}$

$$P = \frac{N_{-2\hbar k} + N_{+2\hbar k}}{N_{-2\hbar k} + N_{0\hbar k} + N_{+2\hbar k}}. \tag{5.1}$$

In the following, a twin lattice interferometer is characterized by its maximum momentum separation Δp reached during the free evolution time. Interferometers are realized for separations ranging from $\Delta p = 8\hbar k$ (without Bloch oscillations), up to $\Delta p = 408\hbar k$ using beam splitters with 100 Bloch oscillations in each arm.

Figure 5.4(d) depicts the average lattice depth V_0 during the Bloch acceleration sequences, which is optimized for each step in order to minimize Landau-Zener losses. During the 2 ms of acceleration the atoms are falling through the twin lattice beam along the z-axis. Since the laser power can only be changed linearly, it is not possible to maintain a constant lattice depth during these 2 ms. The lattice depth calculation takes into account the vertical beam profile as measured via Rabi oscillations in section 4.10. Furthermore, the laser intensity decreases slightly with the applied frequency difference $\Delta\omega$, since the AOMs are aligned for zero detuning $\Delta\omega = 0$. For a maximum separation of $\Delta p = 408\hbar k$, where the AOMs are detuned by $+100\,\omega_{\mathrm{eff}}$ and $-100\,\omega_{\mathrm{eff}}$, respectively, an intensity reduction of 10% is observed.

The total atom number $N = N_{-2\hbar\mathrm{k}} + N_{0\hbar\mathrm{k}} + N_{+2\hbar\mathrm{k}}$ measured in the output ports is plotted in the lower part of Fig. 5.4(d) relative to the atom number N_0 of the interferometer without Bloch processes ($\Delta p = 8\hbar k$). It decreases due to non-adiabatic losses as well as increasing spontaneous emission rates. In case of the largest interferometer with $\Delta p = 408\hbar k$ still 35% of the atoms are present in the output ports. For a total transfer of $1600\hbar k$ via Bloch oscillations this yields an efficiency of 99.93% per $\hbar k$.

5.1.3 Statistical contrast analysis

To calculate the interferometric contrast according to Eq. (2.77) usually a phase scan is performed to observe fringes, i.e. oscillations of the relative population P in one of the output ports. Since the QUANTUS-1 experiment lacks any vibrational isolation, the interferometer phase is strongly perturbed by inertial vibrations in the order of $10^{-2}\,\mathrm{m/s^2}/\sqrt{\mathrm{Hz}}$ [116]. They lead to phase fluctuations of more than 2π from shot-to-shot and prevent the observation of fringes already for an interferometer with $\Delta p = 8\hbar k$. The phase is assumed to change randomly corresponding to white phase noise.

Therefore, the interference contrast of the twin-lattice interferometers is analyzed statistically [47, 71]. In detail, a timing asymmetry δT is introduced in the second half of the interferometer as indicated in Fig. 5.4(c) to change the spatial overlap of the BECs at the last double diffraction pulse. The contrast decreases with larger displacement $\Delta y = \delta T \Delta p/m$, where $\Delta p/m = \hbar\Delta k/m$ is the relative atomic velocity. This decrease depends on the coherence

length of the atomic ensemble characterized by the expansion rate σ_v in beam splitter direction [187]. Keeping in mind that the underlying signal is a sine function of the interferometer phase with an amplitude A, the contrast $C = 2A$ for $\delta T = 0$ is given by $2\sqrt{2}\sigma_P$, where σ_P is the standard deviation of the relative population P[71]. The contrast in dependence of the asymmetry δT is thus given by the Gaussian function [47]

$$C(\delta T) = 2\sqrt{2}\sigma_P(\delta T)\mathrm{e}^{-\frac{1}{2}\Delta k^2\sigma_v^2\delta T^2}. \tag{5.2}$$

To calculate the standard deviation σ_P of the output port fluctuations 40 data points are recorded for each value of δT. To suppress the effect of possible temporal drifts caused e.g. by thermal variations in the laboratory, one data point is taken for each uniformly distributed δT before the measurement is repeated. Additionally, δT is not scanned linearly but in an alternating way starting with $\delta T = 0$ followed by alternating positive and negative values. In case of the $\Delta p = 8\hbar k$-interferometer this implies $\delta T = 0, +40\,\mu\mathrm{s}, -40\,\mu\mathrm{s}, +80\,\mu\mathrm{s}, .. -240\,\mu\mathrm{s}$. Fig. 5.5 exemplary depicts the relative population P for a $\Delta p = 8\hbar k$-interferometer as a function of the timing asymmetry δT.

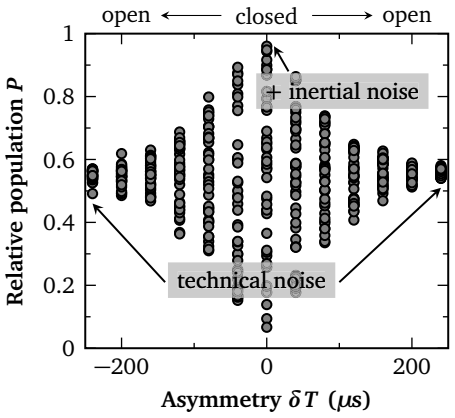

Fig. 5.5: Interferometer signal P depending on asymmetry δT for $\Delta p = 8\hbar k$.

Large values of δT correspond to an open interferometer with an insufficient overlap of the atomic wave functions at the interferometer ports for interference. From the measured output port fluctuations at large δT the technical or non-inertial noise in our interferometer is read out, which stems from fluctuations of the experimental parameters such as laser intensity. The largest value of σ_P is expected for $\delta T = 0$, where the interferometer is closed and fully sensitive to inertial noise. The width of the Gaussian distribution $\hbar/(\Delta p\sigma_v)$ is a measure of the coherence time during which the signal decays due to insufficient overlap. It has been shown that the coherence length remains constant in a free-space interferometer while the wave packet's size evolves [188]. The coherence length therefore only depends on the initial momentum distribution.

Figure 5.6(a) shows the experimentally measured fluctuations $2\sqrt{2}\sigma_P$ as a function of the timing asymmetry δT for twin-lattice interferometers with $\Delta p = 8\hbar k$ to $\Delta p = 408\hbar k$. In all cases, a Gaussian distribution according to (5.2) with four free parameters matches the data well. The free fit parameters determine the peak contrast, the technical noise, the center position and the width of the Gaussian distribution.

The peak contrast decreases with increasing number of Bloch oscillations (Fig. 5.6(b)). A thourough analysis of contrast decay mechanisms is performed in the next section. The technical noise, produced e.g. by laser intensity fluctuations, is constant for the different interferometer realizations indicating a stable system over weeks of data aquisition. In addition, its value of ≈ 0.03 is relatively low (compared e.g. to Ref. [47]). This is also a result of the stable beam splitter operation (sec. 5.1.1). Since the spatial displacement increases with $\delta T\Delta p$, the width $\sigma_{\delta T}$ is inversely proportional to Δp for a constant spatial coherence length. This behavior is well reproduced by our data as shown in Fig. 5.6(c) demonstrating that the manipulation by the twin lattice does not effect the coherence length of the BEC.

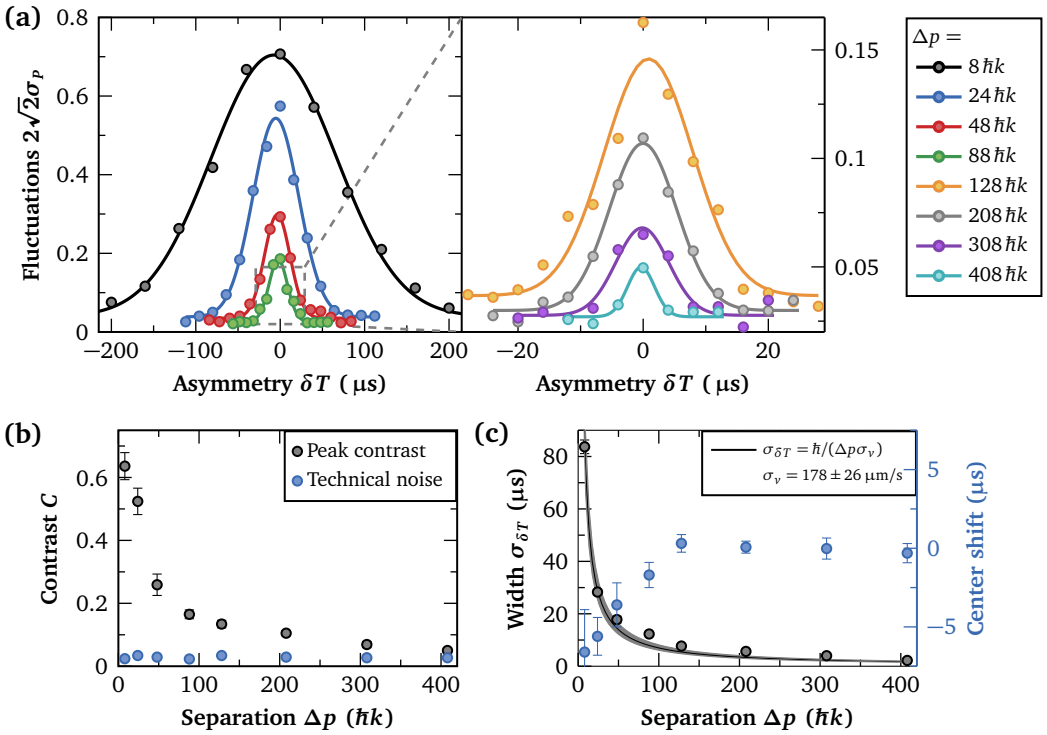

Figure 5.6: (a) Fluctuations $2\sqrt{2}\sigma_P$ of the output port population P for twin-lattice interferometers with different maximum momentum separations Δp in dependence of the timing asymmetry δT. The latter determines the spatial displacement at the last double diffraction pulse. A Gaussian bell-shaped curve is fitted to the data points. $2\sqrt{2}\sigma_P$ is approximately equal to the contrast [47, 71]. (b) Peak contrast and technical noise as well as (c) width $\sigma_{\delta T}$ and center shift determined by the fit parameters. Error bars result solely from the fit uncertainties. The line in (c) represents the theoretically expected width $\sigma_{\delta T}$ calculated for the expansion rate σ_v of the delta-kicked BEC.

5.2 Contrast loss mechanisms

As displayed in Fig. 5.6(b) the contrast decays rapidly for small Δp and more slowly for larger separations. Considering Fig. 5.4 there are essentially three parameters which change between the different interferometer realizations, namely the residual atom number N/N_0, the lattice depth V_0 and the transferred momentum Δp causing different spatial trajectories. Atom loss as indicated by the decreasing number N/N_0 is a common reason for contrast decay [57]. It reduces the number of coherently oscillating atoms in the output ports compared to an incoherent background and therefore lowers the signal of the interferometer. However, the atom number does not reduce as fast with Δp as the contrast and can therefore not solely explain its course.

Contrast loss can also be caused by shortcomings of the light field. Its effect may be influenced by the lattice depth and the atomic trajectories within the lattice beam.

The deviation of the Gaussian beam from a plane wave leads to a Gouy phase shift due to the dispersion of the wave vector and a wavefront curvature depending on the distance from the propagation axis of the beam [44]. Both contributions result in a correction of the photon

momentum k causing a systematic uncertainty. For an ideal Gaussian beam this effect should be negligible and suppressed in our geometry.

Local distortions of the beam can severely impact the measurement. Lately is has been shown, that not wavefront distortions but intensity variations arising due to light distortions contribute dominantly to a change of the photon momentum [189]. Imperfections in the beam profile may result from parasitic reflections, speckle pattern through scattering at optical elements or diffraction at apertures and lead to a local intensity gradient which in turn changes the atomic velocity through the dipole force $F = \partial V/\partial x$ [44]. Random changes of the atomic velocity δv, induce random phase shifts $k_{\text{eff}}\delta v T$ which lead to a reduction of the interference contrast. For a Ramsey-Bordé interferometer with time T between $\pi/2$ pulses and a probability distribution $P(\delta v)$ of the velocity variation it has been demonstrated that the contrast decays as

$$C = C_0 \int P(\delta v)\cos(k_{\text{eff}}\,\delta v\, T)\mathrm{d}\delta v, \tag{5.3}$$

where C_0 corresponds to the contrast without random velocity changes [131, 190].

Random velocity variations δv can also be caused by spontaneous emission, where an atom absorbs a photon from one of the lattice beams and spontaneously emits a photon in a random direction. This leads to a random momentum change of up to $\pm 2\hbar k$ in beam splitter direction. Assuming a momentum acceptance of $2\hbar k$ for the fundamental Bloch band, a spontaneous emission event leaves approximately half of the atoms trapped in the lattice, while the other half is lost [131]. The probability distribution of δv for remaining atoms in the lattice has a width of roughly v_{rec}. However, due to the small spatial extent of the delta-kick collimated BEC in our case, the vast majority of spontaneously scattered atoms is separated spatially from the interferometer ports. In the twin-lattice interferometer the average time for an atom between scattering and detection equals $T + \tau_{\text{sep}} = 15.05\,\text{ms}$. With an output port extent of roughly $60\,\mu\text{m}$ the gain in velocity has to be smaller than $30\,\mu\text{m}/15.05\,\text{ms} = 0.34\,v_{\text{rec}}$ to be counted in the port. This implies that the direction of the absorbed and spontaneously emitted photon has to coincide within an angle of 10°, which only adds up for rougly 7.5% of the scattered atoms.

Apart from a random velocity variation the atomic clouds can also experience a momentum shift δp common for each arm leading to an open interferometer. This induces a common phase shift $\delta\phi = \frac{\delta p x}{\hbar}$ which imprints a spatial fringe pattern in the output ports [191]. If the associated fringe spacings are smaller than the atomic cloud, this leads to a contrast reduction [192]

$$C = \left| \int \mathrm{e}^{-\frac{i}{\hbar}\delta p\cdot x} |\Psi(x)|^2 \mathrm{d}x \right|. \tag{5.4}$$

A large momentum offset in beam splitter direction would be noticeable either through a shift of the center of the contrast envelope or a change in the measured coherence width.

To conclude the considerations made so far, atom loss and light field distortions represent the most probable cause for loss of contrast in the twin-lattice interferometer. To support these assumptions, different experimental studies are performed as detailed in the following sections 5.2.1 and 5.2.2. Moreover, the contrast loss of the twin-lattice interferometer is calculated theoretically and compared to the experimental results by simulating both contrast loss mechanisms (sec. 5.2.3).

5.2.1 Experimental study of atom loss

In this section, we will investigate the atom loss channels of the interferometer. After an examination of the transfer efficiencies of each interferometer step, the contrast of a double Bragg interferometer is compared for different beam splitting efficiencies. At last, the impact of an acceleration with Bloch oscillations on non-resonant atoms is investigated.

As long as the detected atom number still lies significantly above the detection noise, atom loss only reduces the contrast if the lost atoms are not separated spatially from the interferometer output ports. Here, they either lead to a constant offset signal or to a dephased oscillating signal in case spurious ports should close an interferometer geometry.

Relative atom number in interferometer states

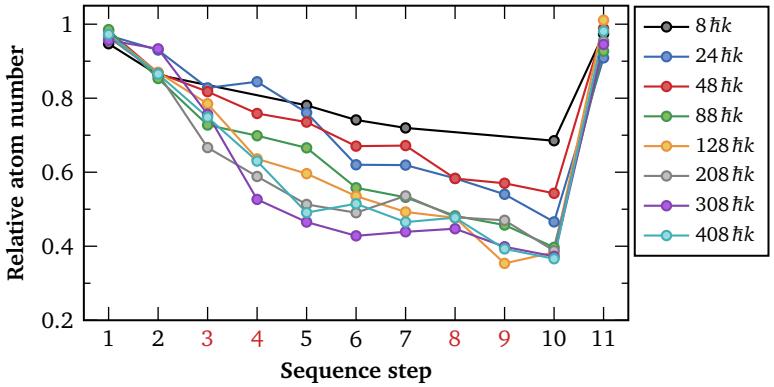

Figure 5.7: Relative atom number observed during the optimization of a specific step of the interferometer sequence, which either corresponds to a Bragg process (1,2,5,6,...) or a Bloch acceleration (3,4,8,9). While for optimization of the last pulse solely the pulse itself was applied, in the other cases all previous steps were performed.

Fig. 5.7 depicts the atom number in the desired momentum states relative to the total number of detected atoms as measured during the optimization of the interferometer sequence. Each step either corresponds to one Bragg or Bloch process. Seven Bragg pulses together with four Bloch accelerations yield a sum of eleven steps. By comparing the atom numbers of successive steps it is possible to estimate the respective transfer efficiency. The data exhibits some uncertainty since each data point relies solely on a single measurement. In addition, in case of larger momentum separations, partially only one of the desired momentum states can be observed on the camera while the population of the state is assumed to be equal to its counterpart.

As expected, Fig. 5.7 shows, how each step leads to additional atom losses, which are slightly higher for a larger amount of transfer. Apart from few exceptions, the relative atom number does not increase with the next step. This indicates that, once an atom is lost from the desired momentum state, it mostly does not get back into the interferometer ports, where it would cause dephasing. The impact of Bloch oscillations on these spurious atoms will be investigated further down.

Contrast for different beam splitting efficiencies

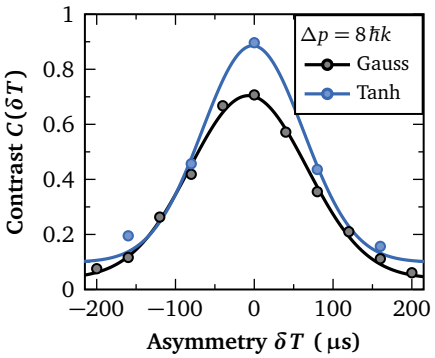

Fig. 5.8: $8\hbar k$ interferometer contrast with solely Gaussian or partially Tanh pulses.

In case of the sequential double Bragg interferometer ($\Delta p = 8\hbar k$) the contrast is measured for two realizations with different pulse efficiencies and otherwise equal parameters. The $\Delta p = 8\hbar k$ interferometer explained in sec. 5.1 is compared to an interferometer, where the sequential Bragg processes are realized via tanh shaped pulses with a frequency ramp and a length of 300 µs (sec. 4.4.2). The application of these adiabatic-rapid-passage pulses for sequential Bragg processes leads to an augmentation of the respective transfer efficiencies from roughly 95% to 98%. Figure 5.8 depicts the contrast envelopes for these two interferometers where either solely Gaussian pulses are applied or where sequential processes are realized via tanh shaped pulses. The measured contrast amounts to 70.6% and 88.6%, respectively. This result indicates that limited beam splitting efficiencies represent a major cause for a non-ideal contrast in case of the $8\hbar k$ double Bragg interferometer. They lead to a background of atoms in the interferometer ports, which does not oscillate with the interferometer phase.

Impact of Bloch oscillations on spurious atoms

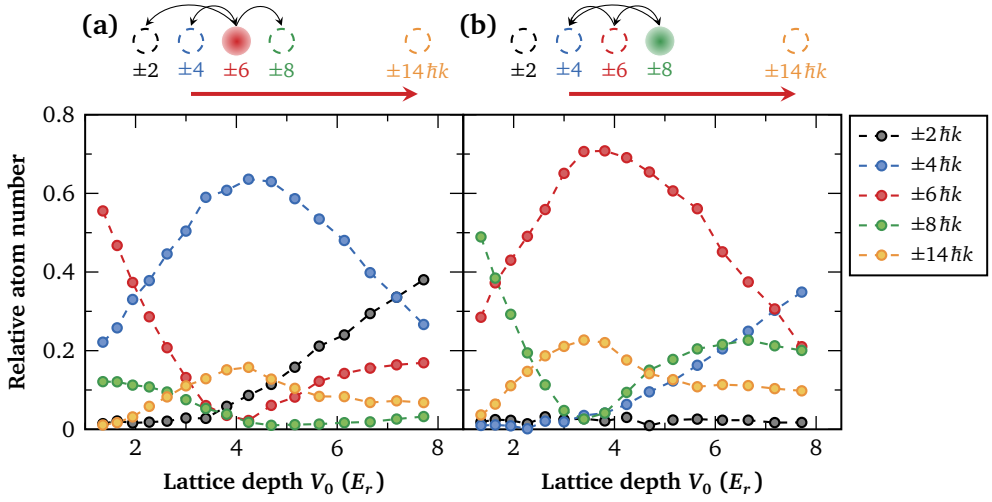

Figure 5.9: Off-resonant coupling during Bloch acceleration. A transfer sequence from $\pm 4\hbar k$ into $\pm 14\hbar k$ via Bloch oscillations ($\tau_{\mathrm{load}} = 200\,\mu\mathrm{s}$, $\tau_{\mathrm{acc}} = 1\,\mathrm{ms}$) is driven. The graphs depict the relative atom number of atoms for initial off-resonant momentum states $\pm 6\hbar k$ (a) and $\pm 8\hbar k$ (b) in dependence of the lattice depth V_0.

The addition of Bloch oscillations to the interferometer sequence increases the number of loss channels. In the following, it shall be examined whether atoms lost from the interferometer states can be coupled back into the interferometer output ports via Bloch oscillations. In the experiment, the BEC is prepared in a superposition of momentum states $\pm 6\hbar k$ or $\pm 8\hbar k$. Then,

an off-resonant Bloch sequence is driven with $\tau_{\mathrm{load}} = 200\,\mu\mathrm{s}$ and of duration $\tau_{\mathrm{acc}} = 1\,\mathrm{ms}$. The frequency sweep corresponds to an acceleration of atoms from $\pm 4\hbar k$ into $\pm 14\hbar k$. Depending on the applied lattice depth, the Bloch sequence affects the prepared momentum states and changes their velocity. Figure 5.9 plots the final relative population in all relevant momentum states.

The measurement indicates that the majority of off-resonant atoms is not "picked up" and accelerated via Bloch oscillations but rather scattered into neighboring momentum states via first and second-order Bragg diffraction. During the Bloch sequence the frequency difference of the twin lattice is swept from $\delta = 4\,\omega_{\mathrm{eff}}$ to $\delta = 14\,\omega_{\mathrm{eff}}$. For an initial atomic distribution in $\pm 6\hbar k$ (Fig. 5.9(a)) atoms are mainly diffracted via a first-order Bragg process from $\pm 6\hbar k$ into $\pm 4\hbar k$ exhibiting a resonance frequency of $\delta = 5\,\omega_{\mathrm{eff}}$. Other possible mechanisms include the first-order process $\pm 6\hbar k \leftrightarrow \pm 8\hbar k$ ($7\,\omega_{\mathrm{eff}}$) and second-order diffraction $\pm 6\hbar k \leftrightarrow \pm 2\hbar k$ ($4\,\omega_{\mathrm{eff}}$). The latter becomes important for larger lattice depths and happens already during the loading phase at the beginning of the Bloch sequence where the frequency difference equals $4\,\omega_{\mathrm{eff}}$. In case of an initial distribution in $\pm 8\hbar k$ (Fig. 5.9(b)), similarly, the following first- and second-order Bragg transitions are most likely: $\pm 8\hbar k \leftrightarrow \pm 6\hbar k$ ($7\,\omega_{\mathrm{eff}}$), $\pm 6\hbar k \leftrightarrow \pm 4\hbar k$ ($5\,\omega_{\mathrm{eff}}$) and $\pm 8\hbar k \leftrightarrow \pm 4\hbar k$ ($6\,\omega_{\mathrm{eff}}$). In both cases, a fraction of roughly 10% ends up in the states $\pm 14\hbar k$ where these atoms would cause a dephasing.

To sum up, Bloch oscillations do not significantly increase the number of possible offset atoms, which are present in the interferometer output port without contributing to the coherently oscillating signal. Off-resonant Bloch oscillations rather induce additional Bragg scattering when crossing the respective resonances. This results in a variety of loss channels of which the great majority is expected to be spatially separated from the interferometer ports.

5.2.2 Experimental study of light field

To study the impact of the light field, the twin-lattice beam is examined with a beam profiling camera in order to detect local intensity fluctuations. Furthermore, the influence of an iris diaphragm as well as the lattice depth and duration on the contrast is investigated.

Insertion of an iris

In order to ensure sufficient laser intensities at the atomic position the center of the beam is only at a distance of about 3 mm away from the atom chip. Due to the relatively large beam diameter of 7.5 mm the beam gets clipped at the atom chip, which can be observed when examining the beam with an infrared viewer behind the chamber. To avoid clipping, an iris diaphragm is inserted into the beam path directly behind the collimator for all interferometer realizations described above.

Without iris	With iris
$C = 0.43 \pm 0.03$	$C = 0.52 \pm 0.03$
$C = 0.42 \pm 0.03$	$C = 0.53 \pm 0.04$

Table 5.1: Interferometric contrast ($\Delta p = 24\hbar k$) with and without the insertion of an iris into the beam path. Two measurements have been performed for each case.

The effect of the iris on the contrast is observed by realizing an interferometer with $\Delta p = 24\hbar k$ and $2T = 7.05\,\mathrm{ms}$. The contrast is measured statistically in each case twice with and without the

insertion of an iris into the beam path. Table 5.1 sums up the results. The measurement has been performed at an earlier stage, where the parameters for Bragg and Bloch oscillation were not fully optimized leading to a lower interferometric contrast. The other parameters equal $\tau_{\mathrm{Bragg}} = 150\,\mu\mathrm{s}$, $\tau_{\mathrm{load}} = 100\,\mu\mathrm{s}$, $\tau_{\mathrm{acc}} = 800\,\mu\mathrm{s}$ and $\tau_{\mathrm{free}} = 1\,\mathrm{ms}$. The experimental data shows an increase of the interferometric contrast by roughly 20% when inserting an additional aperture into the beam path. As anticipated, the distortions caused by the clipping of the beam at the atom chip lead to a loss of coherence. This can be mitigated by reducing the aperture at the beginning of the beam path to prevent any cut-off by successive elements.

Distortion on the beam profile

In order to get a better understanding of the observed contrast loss, the beam profile of the twin lattice light is examined carefully with a beam imaging camera (`WinCam D, DataRay Inc.`). Figure 5.10 shows images of the beam directly behind the collimator (a) and after passing through the vacuum chamber without (c) and with (d) the insertion of an iris into the beam path. To reduce the optical power on the beam cam, which saturates at intensities of $\mu\mathrm{W/cm}^2$, a neutral density filter is inserted into the beam path. For each image a vertical and a horizontal cross section through the center of the beam is shown, to which a Gaussian distribution is fitted.

Already the beam profile directly behind the collimator deviates from a perfect Gaussian form and features intensity fluctuations in the order of 10%. These distortions can be caused by the optical elements involved in the beam imaging, namely the optical fiber, the collimator, the neutral density filter and the camera itself. The profile could neither be improved by a change of the fiber nor by a tilt of the collimator, which should exclude any position dependent effects. It is assumed that the distortions are a property of this type of collimators. However, it is not possible to exclude any impacts of the image acquisition, since another beam cam could not be tested.

The beam image without an iris shows distinct fringes running parallel to the atom chip resulting from diffraction at the edge of the chip. They can also be distinguished well in the cross section of the beam along the z-axis. The magnitude of the ripples is in the order of 10-15% of the maximal intensity. While the insertion of an iris suppresses diffraction at the chip's edge, the iris itself leads to a diffraction pattern and intensity modulation. Although the measured interference contrast can be improved by adding an iris into the beam path, a remaining influence of the light field on the contrast is very likely.

For the three beam images in Fig 5.10 the intensity inhomogeneity, also called roughness, is calculated relative to the Gaussian fit to the cross section. Let $h(j,k)$ be the measured intensity at pixel number j,k in x and z direction, respectively. Assuming a vertical cross section through the beam, i.e. $j = \mathrm{const.}$, and a Gaussian fit $g_j(k)$ the uniformity u is calculated by the normalized root mean square (rms) deviation

$$u_j = \sqrt{\frac{1}{N}\sum_{k=1}^{N}\left(\frac{h(j,k)-g_j(k)}{g_j(k)}\right)^2}. \tag{5.5}$$

The rms value for the inhomogeneity is calculated around the center of the beam in x and z direction.

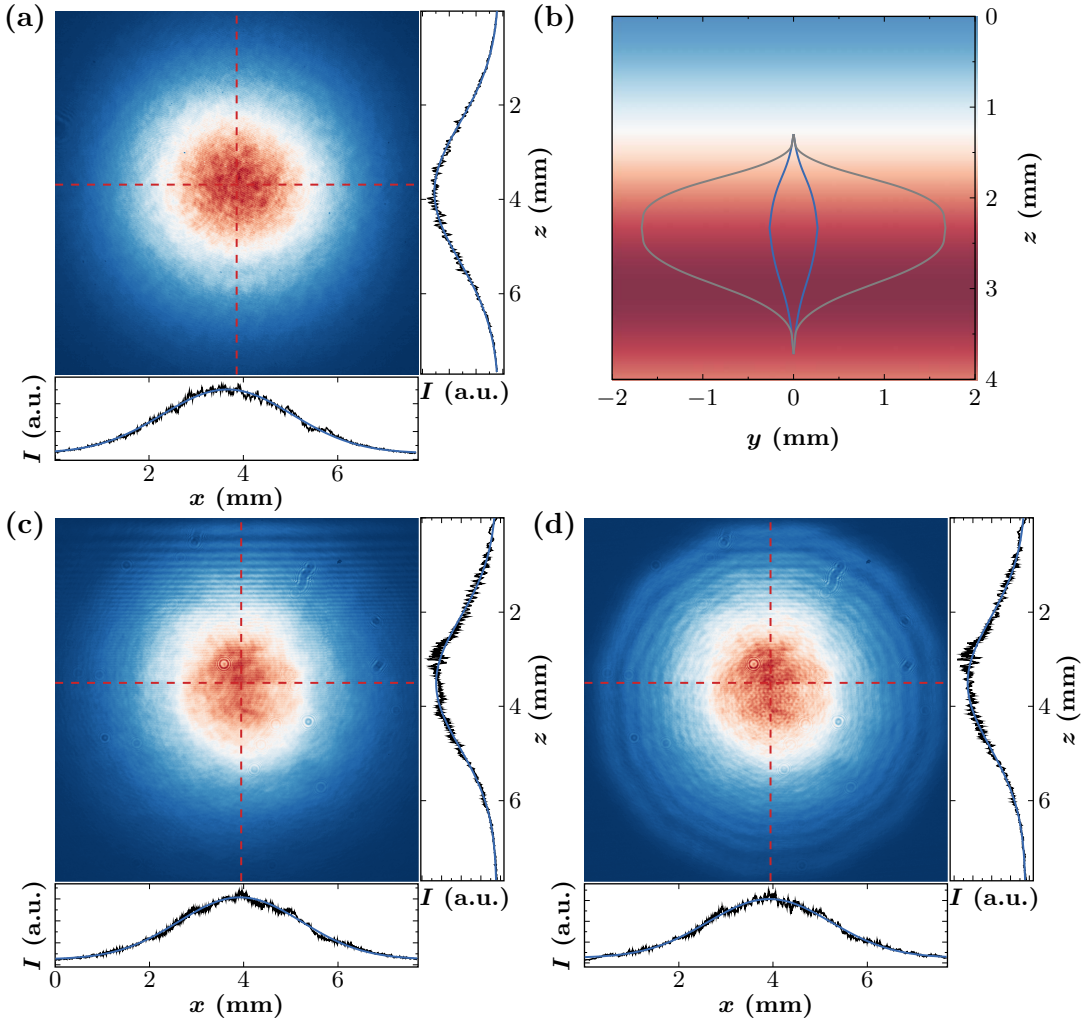

Figure 5.10: Twin lattice beam with a diameter of 7.5 mm imaged with a beam camera directly behind the collimator (a) and after passing through the vacuum chamber without (c) and with (d) an iris inserted into the beam path. The graphs on the right and bottom of the beam image show cross sections through the beam center (——) as indicated by the red dashed lines. The blue lines (——) in (a,c,d) resemble a Gaussian fit to the data. (b) Trajectories for $\Delta p = 24\,\hbar k$ (——) and $\Delta p = 208\,\hbar k$ (——) relative to the beam.

The beam which is imaged directly behind the collimator, features a roughness of 0.06 rms. This value increases after propagation through the vacuum chamber. In case of an iris the roughness caused by the diffraction pattern amounts to 0.11 rms in both directions. Without an additional aperture the inhomogeneity along the horizontal direction only corresponds to 0.08 rms, while along the vertical direction this values equals 0.11 rms. However, if one only considers the upper half of the beam, where the distortions due to the atom chip are strongest, the vertical roughness amounts to 0.14 rms.

Impact of lattice depth and duration

The impact of the light field and its distortions can be tuned via its intensity V_0 and the interaction duration with the lattice. Therefore, these parameters have been varied to investigate the contrast loss in combination with the light field.

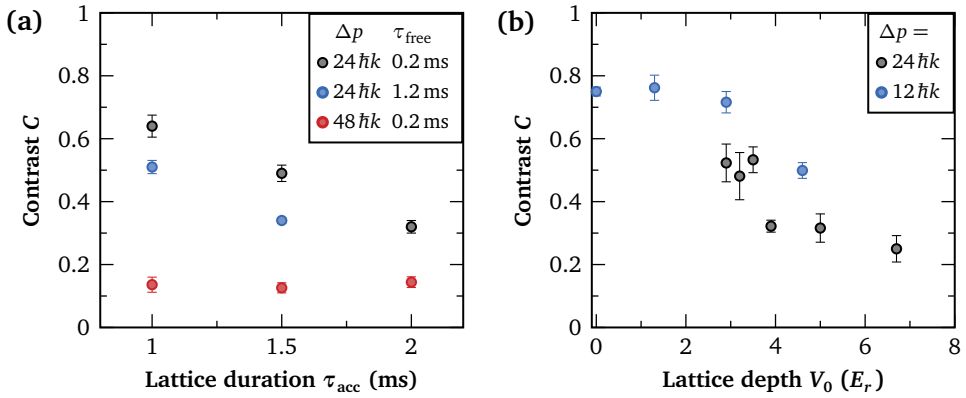

Figure 5.11: Influence of the lattice on the interference contrast. (a) Measured contrast for interferometers with $\Delta p = 24\hbar k$ and $48\hbar k$ as a function of the acceleration duration τ_{acc}. For each series the free evolution time τ_{free} is fixed at 0.2 ms or 1.2 ms, respectively. (b) Contrast for a $\Delta p = 12\hbar k$ interferometer, solely based on double Bragg diffraction, where a comoving lattice of depth V_0 is applied during free evolution and an interferometer with $\Delta p = 24\hbar k$ where the lattice depth during Bloch oscillations is varied.

The measurements described in the following have been realized with an arbitrary waveform generator (`ArbStudio 1104`, see sec. 3.3.1), which enables the use of tanh pulses but features a temporal delay. These properties lead to larger contrast for interferometers relying solely on double diffraction, where a small timing delay is insignificant, whereas they decrease the measured interference amplitude for interferometers using Bloch oscillations.

In Fig. 5.11(a) the contrast is plotted in dependence of the acceleration duration τ_{acc} for $\Delta p = 24\hbar k$ and $48\hbar k$. For interferometers with $\Delta p = 24\hbar k$ and free evolution times of $\tau_{free} = 0.2$ ms and 1.2 ms, respectively, the contrast decreases with τ_{acc}. Furthermore the contrast is almost the same for an equal interferometer duration $2T$, which is the case for $2\tau_{acc} + \tau_{free} = \text{const}$. In case of $\Delta p = 48\hbar k$ this effect seems to be saturated and no significant influence on the contrast can be observed.

Additionally, the influence of the lattice depth is investigated as depicted in Fig. 5.11(b). In case of $\Delta p = 24\hbar k$ an increase of the lattice depth during Bloch oscillations from $3\,E_r$ to $4\,E_r$ or $6.7\,E_r$ reduces the contrast by 40% or 50%, respectively. A similar behavior is observed

when atoms in an interferometer only involving Bragg pulses ($\Delta p = 12\hbar k$) are exposed to a comoving lattice which features zero momentum transfer and is switched on for 2.6 ms during free evolution time. A comoving lattice of depth $V_0 = 4.6\,E_r$ leads to a contrast reduction of 34%. In these experiments, the lattice depth was kept sufficiently low to not induce atom loss due to transitions into other momentum states. In that way, the contrast should only be affected by the light field and its distortions.

5.2.3 Simulations

The observed contrast loss with increasing Δp is calculated taking into account two main mechanisms, namely atom loss and light field distortions, as identified by the previously described experimental studies. The simulations only rely on two experimentally determined parameters: The lattice depth V_0 during Bloch oscillations and the relative atom number N/N_0 in the interferometer output ports (Fig. 5.4(d)). Both of these parameters depend on the momentum transfer Δp. Within our model, the contrast decay is solely caused by two effects:

- Losses during the Bloch oscillation sequences caused by non-adiabatic transitions which reduce the number of atoms contributing to the interferometer signal.
- Light distortions of the twin-lattice beam resulting in decoherence and dephasing.

Atom loss model

This section contains our description about possible atom loss channels and how they impact the contrast. We express the contrast as the minimum and maximum values of the relative population P (Eq. (2.77))

$$C = \frac{P_{\max} - P_{\min}}{P_{\max} + P_{\min}}. \tag{5.6}$$

In a simple picture, the total number of atoms in the interferometer output ports $N = N_{\mathrm{Sig}} + N_{\mathrm{bg}}$ consists of a signal N_{Sig}, which coherently oscillates with the interferometer phase $\Delta\phi$, and a background or offset N_{bg} of atoms exhibiting no oscillations at all. For an equal distribution of N_{bg} among the ports the extreme values for the relative population P can then be written as

$$P_{\min} = \frac{N_{\mathrm{bg}}/2}{N} \qquad \text{and} \qquad P_{\max} = \frac{N_{\mathrm{Sig}} + N_{\mathrm{bg}}/2}{N}\,. \tag{5.7}$$

This can be inserted into (5.6):

$$C = \frac{N_{\mathrm{Sig}}}{N_{\mathrm{bg}} + N_{\mathrm{Sig}}} = \frac{N - N_{\mathrm{bg}}}{N}\,. \tag{5.8}$$

In order to arrive at a relatively simple formula for the contrast C as a function of the experimental parameters the following assumptions are made:

(i) In principle, the spontaneous scattering rate depends on the relative velocity between an atom and the lattice. It has been calculated for an atom copropagating in one of the twins and for an atom at rest (sec. 2.2.4). The latter represents one possible loss channel. In case of our

twin lattice ($\sigma_{\mathrm{pol}} = 0.2688$, see sec. 2.2.1) both values only deviate on the few percent level. Additionally, as explained in the beginning of this section, the vast majority of spontaneously scattered atoms is spatially separated from the output ports and does not contribute to the measured number N. Therefore, we approximate that spontaneous emission equally removes atoms from N_{bg} and N_{Sig} with rate P_{twin} and, hence, has no impact on the contrast. The initial atom number N_0 detected in the output ports of the sequential double Bragg interferometer ($\Delta p = 8\hbar k$) decreases solely due to spontaneous emission as

$$N_{\mathrm{Sp}}(\Delta p) = N_0 \cdot e^{-P_{\mathrm{twin}}(V_0)\cdot\tau}, \tag{5.9}$$

as shown in Fig. 5.13(c). While P_{twin} varies with Δp because of different lattice depths V_0, the Bloch acceleration duration τ is equal in all interferometers depicted in Fig. 5.6.

(ii) The contrast of the sequential double Bragg interferometer $C(\Delta p = 8\hbar k) = 0.706 \pm 0.022$ solely originates from the limited beam splitter efficiencies as affirmed by experimental measurements (Fig. 5.8). Non-ideal efficiencies lead to a background of atoms N_{bg} and a reduction of the signal N_{Sig}. With $N(8\hbar k) = N_0$ Eq. (5.8) can be rephrased to express the background atom number

$$N_{\mathrm{bg}}(8\hbar k) = (1 - C(8\hbar k))N_0. \tag{5.10}$$

Previous phase sensitive measurements [68] confirm that the double Bragg interferometer does not feature any significant parasitic interferometers which would lead to a spurious signal with a dephased oscillation. Since each interferometer is based on the same double Bragg processes we assume that the backgound $N_{\mathrm{bg}}(8\hbar k)$ is present in all interferometer realizations. For larger Δp it is only reduced by spontaneous emission with rate P_{twin} as

$$N_{\mathrm{bg}}(\Delta p) = N_{\mathrm{bg}}(8\hbar k)e^{-P_{\mathrm{twin}}(V_0)\cdot\tau} = (1 - C(8\hbar k))N_{\mathrm{Sp}}(\Delta p), \tag{5.11}$$

where (5.9) and (5.10) have been used.

(iii) With the addition of Bloch oscillations, Landau-Zener losses reduce the signal N_{Sig} but the lost atoms do not couple back into the output ports because of their spatial separation (sec. 5.2.1). Since we assume that background atoms are not accelerated by the lattice, N_{bg} is not influenced. In this way, the reduction in N_{Sig} lowers the contrast.

With these assumptions at hand, the contrast in (5.8) for any Δp can be expressed in the following way

$$C_{\mathrm{loss}}(\Delta p) = \frac{N(\Delta p) - N_{\mathrm{bg}}(\Delta p)}{N(\Delta p)} = 1 - \frac{1 - C(8\hbar k)}{N(\Delta p)/N_{\mathrm{Sp}}(\Delta p)}. \tag{5.12}$$

It solely depends on the experimentally measured contrast $C(8\hbar k)$ and number $N(\Delta p)$ as well as on the calculated spontaneous emission losses $N_{\mathrm{Sp}}(\Delta p)$.

Light field model

As detailed in the beginning of this section local intensity variations of the twin-lattice beam may reduce the contrast as they lead to local dipole forces resulting in additional momenta δp [44, 131, 190, 193]. These forces depend on the exact trajectory of an atom and, thus, deviate between the different interferometer arms as well as across an atom cloud. The

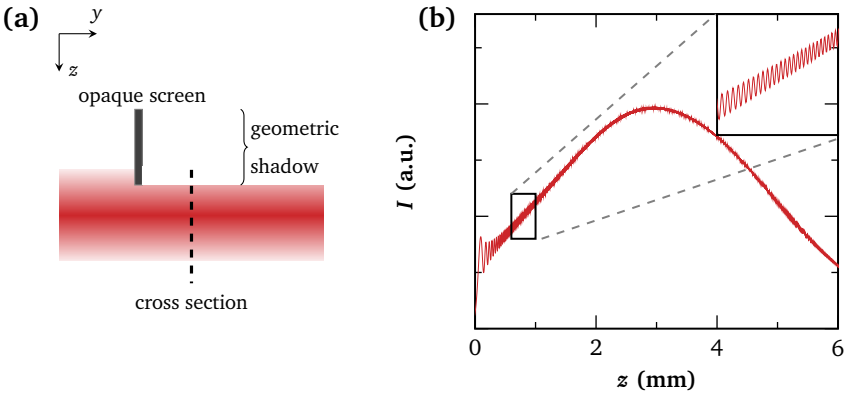

Figure 5.12: (a) Scheme for the simulated light field distortions. A Gaussian shaped beam is diffracted at a sharp edge. (b) Vertical intensity profile of the simulated beam.

influence of this effect in our experiment is gauged via calculating the contrast for a simulated intensity profile featuring spatial variations. The simulations have been carried out by Jan-Niclas Siemß[1].

In the experiment, light field distortions arise mainly due to diffraction at the iris and the atom chip. Therefore, for our simulations we use a Gaussian shaped beam that has been diffracted at a sharp edge of an opaque screen [194] giving rise to a normalized intensity distribution $I(x,y,z)/I_0$ (Fig. 5.12). The resulting dipole potential of the beam is scaled by the lattice depth $V_0(\Delta p)$ employed for the different interferometer realizations in the experiment. For a certain trajectory s, i.e. an interferometer arm, the additional momentum in direction $j = x,y,z$ is calculated by integrating the dipole force along s during the interferometer duration $t = [0,2T]$

$$p_{j,s} = \int_0^{2T} \frac{V_0}{I_0} \frac{\partial}{\partial j} I\left(x(t),y(t),z(t)\right) \mathrm{d}t \,. \tag{5.13}$$

In this way, the differential momentum $\delta p_j = p_{j,\mathrm{arm1}} - p_{j,\mathrm{arm2}}$ between both interferometer arms can be determined. The trajectories, i.e. $x(t),y(t),z(t)$, are depicted in Figure 5.4(a) for different momentum separation Δp. δp_j implicates a phase difference $\delta\varphi_j = \delta p_j \cdot j/\hbar$ which affects the contrast as in [192]

$$C = \left| \iiint |\Psi_{\mathrm{end}}(x,y,z,t=2T)|^2 \; e^{-\frac{i}{\hbar}(\delta p_x \cdot x + \delta p_y \cdot y + \delta p_z \cdot z)} \mathrm{d}x\mathrm{d}y\mathrm{d}z \right| . \tag{5.14}$$

Hereby, $|\Psi_{\mathrm{end}}(x,y,z,t=2T)|^2$ describes the density distribution of the interferometer output ports in momentum states $0\hbar k, \pm 2\hbar k$ at the end of the interferometer and the integral is evaluated over the positions in the output ports. Their size is given by experimental measurements which do not indicate any deformation of the cloud caused by the light field within our detection resolution. Therefore, $|\Psi_{\mathrm{end}}(x,y,z,t=2T)|^2$ is given by a Thomas-Fermi distribution.

In addition to the considerations mentioned above, we take into account the spatial extent of the atomic wave packet. According to the initial spatial distribution of the cloud

1 Institut für Theoretische Physik & Institut für Quantenoptik, Leibniz Universität Hannover

$|\Psi_{\text{init}}(x_i, y_i, z_i, t = 0)|^2$ at the beginning of the interferometer slightly different single-particle trajectories $x(t), y(t), z(t)$ arise. For each of these trajectories the differential momentum $\delta p_j = \delta p_j(x_i, y_i, z_i)$ can be calculated according to (5.13) which in turn leads to different contrast values $C(x_i, y_i, z_i)$ in Eq. (5.14). Finally, the contrast value $C_{\text{light}}(\Delta p)$ for one interferometer realization is obtained by averaging over these values weighted with the initial density distribution $|\Psi_{\text{init}}(x_i, y_i, z_i, t = 0)|^2$.

Comparison with experiment

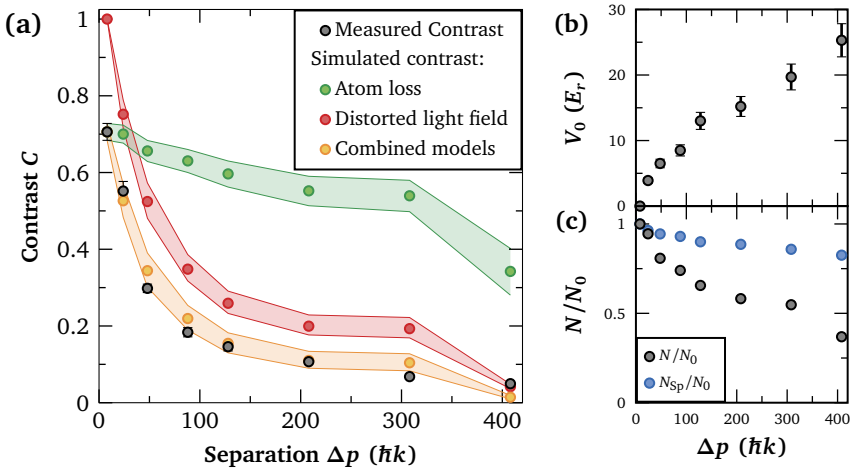

Figure 5.13: (a) Experimentally measured contrast in comparison to the calculated results. The simulated contrast is the product of a contrast decay arising through atom losses and the effect of a distorted Gaussian beam with inhomogeneities of 9% V_0. (b,c) The measured lattice depth V_0 and relative atom number N/N_0 serve as input parameters for the simulations. Additionally, the residual atom number N_{Sp} due to spontaneous emission is taken into account.

To compare the simulations with the experiment, the result of both models is multiplied $C(\Delta p) = C_{\text{loss}}(\Delta p) \cdot C_{\text{light}}(\Delta p)$. In order to match the experiment results the contrast decay $C_{\text{light}}(\Delta p)$ due to distortions has to be increased. Comparing the intensity variations of the simple model of a clipped Gaussian beam $I(x, y, z)$ with the light field of the lattice beam depicted in section 5.2.2 already indicates that the model underestimates the observed distortions. The simulated beam features inhomogeneities merely in the order of 1%, while they correspond to roughly 10% in the experiment, where diffraction not only occurs at a single edge but at different apertures. The simulated intensity profile $I(x, y, z)/I_0$ is fixed for the given assumption of a Gaussian beam which is cut off a sharp edge. Therefore, the dipole potential is scaled up by a factor of 9 in order to increase the distortions to an absolute value of 9% V_0. In case of a perfect Gaussian beam, an increase of the lattice depth has a vanishing effect on the contrast.

As depicted in Figure 5.13 the simulated contrast is in very good agreement with the measured contrast values. The contrast drop for $\Delta p = 408\,\hbar k$ results both from the increase in the applied lattice depth as well as from the significantly lower measured atom number compared to $\Delta p = 308\,\hbar k$. Based on our calculations we assume that the limited transfer efficiency as well as light distortions in the order of 9% V_0 currently represent the main

limitations in our experiment. Both of these limits are of technical nature and it is possible to overcome them in a dedicated setup. A decrease of the intensity fluctuations to a level of 0.5% for example, would maintain a contrast of $C_{\text{light}} = 0.9$ up to $\Delta p = 408\,\hbar k$. The following section 5.3 illustrates a first demonstration, how a larger contrast can be achieved with a smaller beam diameter which decreases the amount of light distortions.

5.3 Small beam interferometer

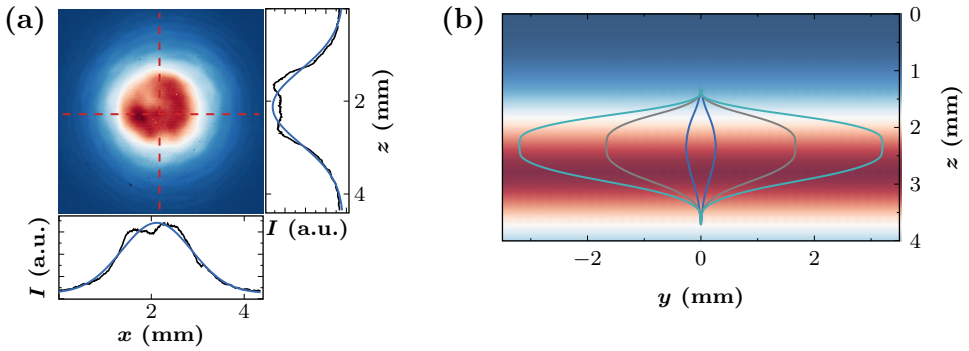

Figure 5.14: (a) Beam with a diameter of 3.3 mm imaged with a beam camera after passing through the vacuum chamber. (b) Trajectories for $\Delta p = 24\,\hbar k$ (——), $\Delta p = 208\,\hbar k$ (——) and $\Delta p = 408\,\hbar k$ (——) relative to the beam.

As we have seen so far, the light field presents the main reason for a limited contrast, mainly caused by the atom chip itself or an additional aperture intended to prevent clipping at the chip. However, the proximity of the chip to the atom interferometer can not be changed easily. In order to avoid the cut-off at the chip, the beam center would have to be positioned much below the interferometer region. This would lead to significantly lower laser intensities at the atomic trajectories preventing large accelerations in the lattice.

In order to confirm that distortions are mainly responsible for the loss of contrast, the $1/e^2$ beam diameter is reduced from 7.5 mm to 3.3 mm by changing the fiber collimator. The beam profile behind the chamber with the new collimator (`SuK, 60FC-4-A15-02`) is depicted in Fig. 5.14. In contrast to the previous configuration, the beam does not feature any diffraction patterns after passing through the vacuum chamber. However, the beam profile also deviates from a perfect Gaussian form, which is mainly a property of the collimator itself. In this new configuration different twin-lattice interferometers similar to the ones described in section 5.1.2 are realized.

To reduce the interferometer region, the lattice duration is initially set to $\tau_{\text{acc}} = 1\,\text{ms}$ and the loading times to $\tau_{\text{load}} = 150\,\mu\text{s}$ which results in a total duration of $2T = 7.7\,\text{ms}$. Furthermore, the interferometer is not initiated directly after the adiabatic rapid passage but with a delay of 2 ms time-of-flight. This increases the proximity to the beam's center and, thus, the laser intensity at the beginning of the interferometer which otherwise would be too low.

In this way, twin-lattice interferometers with $\Delta p = 8, 24, 88, 128$ and $208\,\hbar k$ are realized. Larger momentum separations are not possible within the limited time of $\tau_{\text{acc}} = 1\,\text{ms}$ due to the available laser power. Accelerations up to momentum splittings of 308 and $408\,\hbar k$ are

therefore performed with $\tau_{\mathrm{acc}} = 2\,\mathrm{ms}$. The total interferometer time of $2T = 11.7\,\mathrm{ms}$ together with the 2 ms delay reduces the remaining time for the atomic clouds to separate spatially after the last interferometer pulse to 7.4 ms. Due to the small spatial width of the delta-kicked BEC the interferometer ports are still sufficiently isolated for a spatial detection. The large intensity gradient of the small beam represents a challenge for the implementation of these interferometers, since the lattice depth changes significantly during free fall. Especially in case of smaller momentum splittings excessive lattice depths cause atom losses due to the interaction with standing waves. To compensate for the strongly changing lattice depth, the laser intensity is not constant during one acceleration sequence but linearly ramped during τ_{acc}. The ramp is optimized for highest transfer efficiency.

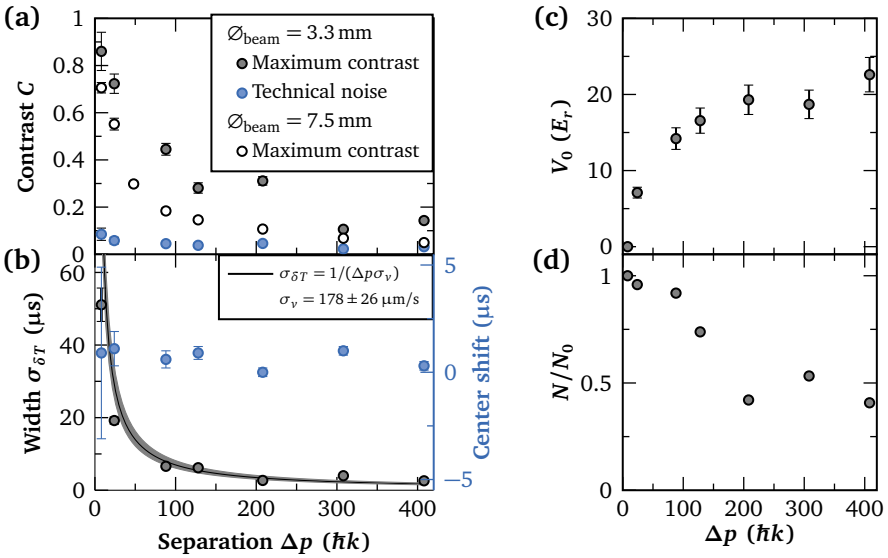

Figure 5.15: Results and parameters for the twin-lattice interferometer realized with a beam diameter of $\varnothing_{\mathrm{beam}} = 3.3\,\mathrm{mm}$ in dependence of the momentum separation Δp. (a) Contrast and technical noise extracted from the Gaussian fit parameters. For comparison the results from the data series with $\varnothing_{\mathrm{beam}} = 7.5\,\mathrm{mm}$ (sec. 5.1.3) are plotted as well. (b) Width $\sigma_{\delta T}$ and center shift. (c) Average applied lattice depth V_0 during Bloch oscillations and (d) normalized atom number in output ports. Up to $\Delta p = 208\,\hbar k$ the interferometer time equals $2T = 7.7\,\mathrm{ms}$. For $\Delta p = 308\,\hbar k$ and $408\,\hbar k$ the duration is increased to $2T = 11.7\,\mathrm{ms}$.

The results from the statistical contrast analysis, the utilized lattice depth V_0 as well as the normalized atom number N/N_0 in the interferometer ports are presented in Fig. 5.15. The amount of data taken to evaluate the contrast of these interferometers is slightly lower compared to the data series with $\varnothing_{\mathrm{beam}} = 7.5\,\mathrm{mm}$ which leads to a larger uncertainty in the fit parameters. The relative atom numbers during the optimization of each step are depicted in Fig. 5.16. Since the available acceleration time τ_{acc} is twice as large for $\Delta p = 308\,\hbar k$ and $\Delta p = 408\,\hbar k$ compared to interferometers with smaller momentum splitting, the respective atom numbers are larger than for $\Delta p = 128\,\hbar k$ and $\Delta p = 208\,\hbar k$.

In general, the contrast values obtained with a twin-lattice beam of 3.3 mm diameter are larger than the ones measured in the first data series (sec. 5.1.3). This confirms the assumption of light field distortions being mainly responsible for the observed contrast loss. However, there are other mechanisms to consider: Already the $\Delta p = 8\,\hbar k$ interferometer exhibits a

contrast 20% higher than measured in the first series. Since the diffraction efficiencies in this case were not larger compared to the first series, this might be explained by a lower interrogation time T. Also, an influence of the superior light field can not be excluded. For small momentum separations up to $208\,\hbar k$ it has to be noted that the acceleration durations were only equal to $\tau_{\mathrm{acc}} = 1\,\mathrm{ms}$. In section 5.2.2 it could be observed that for $\Delta p = 24\,\hbar k$ a bisection of τ_{acc} increases the contrast by roughly 75%. However, this effect saturated already for $\Delta p = 48\,\hbar k$.

Smaller interrogation durations are not sufficient to explain the increase in contrast observed with a beam diameter of 3.3 mm. This confirms that light field distortions are mainly responsible for an increasing constrast loss with Δp. A small beam, that does not get clipped at apertures or the atom chip, increases the interference contrast despite its strong intensity gradients. The results presented in this section are only a first study to demonstrate the ability to increase the contrast in our setup and enable the realization of interferometers with even larger momentum separation. The large intensity gradient and small interrogation area of the 3.3 mm beam, however, do not present ideal conditions for further improvements. In the next section possible improvements are introduced which might pave the way for momentum splittings in the order of $1000\,\hbar k$.

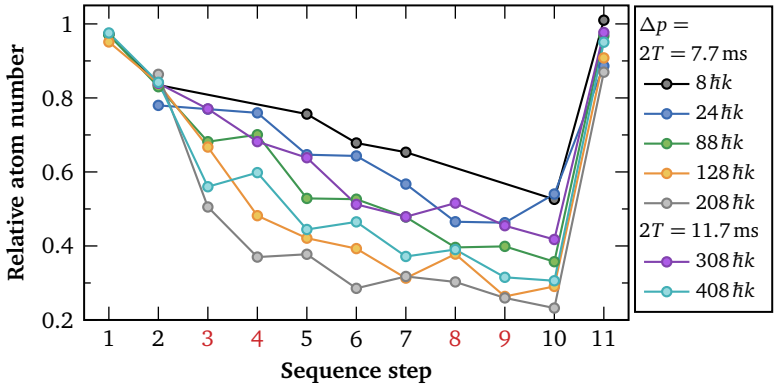

Figure 5.16: Relative atom number observed at a specific step during the optimization of the interferometer sequence. A step either corresponds to a Bragg process (1,2,5,6,...) or a Bloch acceleration (3,4,8,9).

5.4 Future improvements for large momentum interferometry

Currently, the performance of the twin-lattice interferometer is restricted by distortions of the light field as well as limited transfer efficiencies. In the following, some ideas will be presented to overcome the current limitations and increase the possible momentum transfer.

The combination of the twin-lattice interferometer with the atomic fountain as developed within QUANTUS-1 [88, 116] seems promising. The fountain employs a vertical lattice which is retroreflected from the atom chip. Via a combination of Bloch oscillations in a single lattice and double Bragg diffraction, an atomic cloud falling towards the ground can be launched up again to enlarge the time-of-flight by roughly a factor of three. The small velocity around the fountain's apex is particularly useful for a horizontal beam since it increases the available

interrogation time within the beam or allows for the use of a smaller beam diameter. Longer interferometer times can be used to increase the duration and thereby the adiabaticity of the Bloch processes to reach even larger momentum separations. In the current setup, however, the implementation of a fountain leads to a momentum broadening caused by defects on the atom chip [116]. The broadening can only be minimized but not fully avoided by changing the beam's position relative to the chip. It diminishes the efficiency of double Bragg diffraction as well as the coherence of the beam splitting. The combination of a twin-lattice interferometer with the fountain therefore already revealed a vanishing contrast for $\Delta p = 88\hbar k$. In a setup with a decent retroreflection mirror for the vertical light field, however, the launch mechanism should not affect the interferometric contrast but instead offer several advantages as mentioned above.

5.4.1 Atom loss

Spontaneous emission An atomic fraction of 18% is lost due to spontaneous scattering in case of the $\Delta p = 408\hbar k$ interferometer. Spontaneous emission losses lead to a decrease of the signal-to-noise ratio (SNR) which scales with $\sqrt{N}$. If the SNR becomes smaller than the detection noise, it is not possible to detect a signal anymore. The application of a larger detuning Δ represents the only way to decrease the scattering rate P_{twin} which scales inversely proportional with the square of Δ. Since the lattice depth V_0 is inversely proportional to Δ the laser intensity has to be increased for larger Δ in order to maintain a sufficiently large lattice depth.

Bragg beam splitting efficiency The efficiency for sequential Bragg pulses can be increased by employing an adiabatic rapid passage with a tanh-shaped intensity envelope as detailed in section 4.4.2. However, it is not possible to apply this method to the symmetric double Bragg beam splitter. Here, only a proper alignment of the twin-lattice beam in horizontal direction along with an atom source exhibiting a small momentum distribution and offset velocity can improve on the efficiency, which already reaches very good values of 98.8% per $\hbar k$.

Transfer efficiency during Bloch oscillations The Bloch state does not represent the optimal solution for high transfer efficiencies with Bloch oscillations [139]. Better survival probabilities can be achieved by preparing the atoms in a Wannier-Bloch state [138], which can be experimentally achieved by adiabatically switching on and off the acceleration instead of applying a uniform force. A sudden switch-on of the acceleration leads to a sudden shift of the position of the potential minimum and induces oscillations of the atoms in the lattice. These can be suppressed by an adiabatic turning-on. For a lattice depth of $V_0 = 50\,E_r$ and a Bloch period of $T_B = 10\,\mu$s already a linearly increasing acceleration for few tens of μs before and after the constant acceleration significantly increases the efficiency [139]. A similar effect can be achieved by introducing a phase shift as tested in sec. 4.3.5.

An adiabatically increasing lattice acceleration is in particular important for the twin-lattice configuration, where for small separations Δp large lattice depths and forces increase the losses caused by parasitic standing waves (sec. 4.3.3). Furthermore, a constantly increasing acceleration leads to an even faster scaling of the space-time area enclosed by the interferometer trajectories proportional to T^4 [58]. Currently, a non-linear frequency change cannot

be implemented technically, which is why the acceleration sequence at times had to be split into parts of different absolute acceleration. New devices such as the RF synthesizer `MOGLabs XRF021` should in principle open up the possibility of applying arbitrary frequency ramps.

5.4.2 Light field

Beam shaping The beam itself presents a major limitation for the realization of twin-lattice interferometers with large momentum transfer. Large beam diameters require high laser powers and might lead to clipping at various apertures or the atom chip. In contrast, a small beam restricts the available interferometer region, where sufficiently large lattice depths can be reached, and thus limits the interferometer duration. Furthermore, large intensity gradients of Gaussian beams impede an efficient acceleration since they make it difficult to properly adjust the lattice depth. In the current setup, intensity inhomogeneities across the delta-kick collimated cloud are negligible but might become important when using smaller beam sizes or larger clouds.

A top-hat beam features a uniform intensity distribution in the central part as well as a relatively sharp cut-off at the edges. Both of these properties are beneficial for interferometry. However, the creation of the uniform intensity profile involving a multitude of optical elements might lead to inhomogeneities of the laser phase and therefore has to be investigated carefully. In a retroreflected scheme the requirements on the phase homogeneity can be relaxed and only the relative phase arising due to the propagation between atom cloud and mirror has to be considered.

In Ref. [195] a top-hat beam is examined regarding its intensity and phase profile as well as its application as a beam splitter for atoms. Calculations show that the relative phase inhomogeneities for a propagated ideal top-hat beam, which is expressed as a sum of Laguerre-Gauss modes, are sufficiently low with values well below 1 mrad in the central part of the beam. Experimentally, the beam shaping is done via an assembly of aspheric optics fabricated by the Asphericon Company. Beam shaping is also possible with a simple apodizing filter [46] or via spatial light modulators [196]. However, these suffer either from a significant loss of laser intensity or a bulky setup including potential drifts and limited peak intensities. In [195] the application of the top-hat beam in combination with a source of laser-cooled atoms led to significantly enhanced Rabi oscillations as well as a larger interferometric contrast. In this case, the advantages of the top-hat beam mainly arise because of the large cloud size compared to the Gaussian beam waist leading to a varying Rabi frequency across the cloud. However, the operation of an interferometer with laser-cooled atoms and an interrogation time of $2T = 294\,\mathrm{ms}$ at a contrast of 35% demonstrates that the top-hat beam can be applied in highly sensitive atom interferometric measurements.

Optical cavity Using an optical cavity provides another option to improve on the beam quality and overcome dephasing caused by the optical lattice [130, 197]. Because of its resonant enhancement, it requires only a small amount of input power. Moreover, a cavity offers spatial filtering of the interferometer beam to suppress wavefront distortions as well as an intrinsic alignment of the beams. On the downside, the operation requires atoms to stay in the relatively small cavity mode volume.

AC-Stark compensation Residual imperfections of the lattice beam can be compensated by employing an absolute light shift compensation [47, 193]. Intensity gradients lead to dipole forces since the energy of an atomic state is shifted proportional to the local laser intensity, and induce an additional phase shift which can vary across the cloud and between the interferometer arms leading to a contrast reduction. To suppress this effect a contribution with opposite single-photon detuning Δ can be added to the lattice beam. Being out of resonance it does not drive any transitions, but passes through the same optics as the beam for interferometry and therefore features equal distortions. By adjusting the relative intensities of the red- and blue-detuned beam the light shift of both parts can cancel each other out [47]. The second frequency contribution can be established by a second laser or modulation with an electro-optical modulator.

6 OPTICAL DIPOLE TRAP

An important lever for increasing the sensitivity of an atom interferometer is the interrogation time. In a Mach-Zehnder-type geometry, the scale factor increases quadratically with the duration T between beam splitter and mirror pulse. Seconds of interrogation time can be realized in large atomic fountains [35, 47], under microgravity conditions [39–41] or even in space [42]. Alternatively, atoms can be suspended against gravity in optical lattices [130, 131, 190] or in an optical or magnetic waveguide [36–38]. These techniques are in particular promising for the construction of compact inertial sensors for mobile applications on ground. While the twin-lattice interferometer does not provide sufficient confinement for the suspension against gravity, it already constitutes a type of guided interferometer. Here, the atoms spend the majority of the interrogation time in a lattice, contrary to typical light-pulse interferometers which exhibit a negligible beam splitter duration. With an increase of the lattice depth one could create an optical lattice acting simultaneously as a guide and a beam splitter as proposed in [70]. An increase in laser power entails the use of a larger detuning to keep spontaneous emission losses at a sufficiently low level.

In this chapter, a step towards atom interferometry in an optical waveguide is realized within QUANTUS-1, namely the generation and loading of a far-detuned optical dipole trap. While atom-chip traps feature steep gradients and allow for fast and efficient evaporation, a dipole trap provides a more harmonic potential which is beneficial for the realization of delta-kick collimation via optical lensing [86]. Additionally, it offers the possibility to steer the atomic interactions by an external magnetic field via Feshbach resonances [105] and to trap different hyperfine levels enabling the realization of a magnetometer inside the trap [198]. At the same time, loading an optical dipole trap from an atom chip within QUANTUS-1, serves as a testbed for the future MAIUS-2/3 missions [41, 199]. In these missions atom interferometry with rubidium and potassium is to be performed during a parabolic flight on a sounding rocket. The two species will first be trapped and cooled with an atom chip, before they are transferred to an optical dipole trap. In comparison to a magnetic trap, the corresponding possibility to tune the atomic interactions via Feshbach resonances allows not only for efficient evaporation of potassium via sympathetic cooling [106] but also for a better spatial overlap of both species [107]. The latter is important since a displacement between both clouds represents a main source for systematic uncertainties in a dual-species atom interferometer. Additionally, both species can be optically lensed with the dipole beam.

This chapter starts with the theoretical concepts for optical dipole trapping in a single red-detuned focused beam (sec. 6.1). It is followed by a short description of the setup and integration of the dipole trap into the QUANTUS-1 experiment (sec. 6.2). Finally, in section 6.3 the loading procedure from the chip trap into the dipole trap is investigated in detail as well as properties of the dipole trap such as lifetime, trap frequencies and expansion rates.

6.1 Optical dipole traps with far-detuned light

A dipole trap is based on the atomic dipole interaction with the laser light field. The dipole potential V_{dip} and scattering rate P_{Sp} have already been introduced in section 2.2.1

$$V_{\mathrm{dip}}(\mathbf{r}) = \frac{3\pi c^2}{2\omega_0^3}\frac{\Gamma}{\Delta}I(\mathbf{r}), \qquad P_{\mathrm{Sp}} = \frac{\Gamma}{\Delta}\frac{V_{\mathrm{dip}}(\mathbf{r})}{\hbar}. \tag{6.1}$$

They depend on the resonance frequency ω_0, the line width Γ, detuning Δ and intensity I. In the following we will consider a far-detuned light field, where radiation pressure caused by photon scattering is negligible compared to the dipole force [134].

In case of a red-detuned light field the dipole force points in direction of higher intensity and the focus of a single laser beam represents an easy implementation for a three-dimensional optical dipole trap. The focused beam trap was first proposed by Ashkin in 1978 [5] and could be realized experimentally in 1986 with sodium atoms [200]. Since trap depths are in the microkelvin range, the atoms have to be precooled by means of a magneto-optical trap. The intensity distribution of a focused Gaussian beam with a total power P propagating along the y direction depends on the distance $r = \sqrt{x^2+y^2}$ from the center as

$$I(r,y) = \frac{2P}{\pi w^2(y)}\exp\left(-2\frac{r^2}{w^2(y)}\right), \tag{6.2}$$

where the beam waist $w(y)$ given by the $1/e^2$ radius can be calculated with the minimum waist w_0 and the Rayleigh length $y_R = \pi w_o^2/\lambda$

$$w(y) = w_0\sqrt{1+\left(\frac{y}{y_R}\right)^2}. \tag{6.3}$$

Close to the trap center the optical potential of a focused Gaussian beam can be approximated by a harmonic oscillator as illustrated in Fig. 6.1(a)

$$V_{\mathrm{dip}}(r,z) \approx V_0\left[1-2\left(\frac{r}{w_0}^2\right)-\left(\frac{z}{z_r}^2\right)\right] = V_0\left[1+\frac{1}{2}m\omega_r^2 r^2+\frac{1}{2}m\omega_y^2 y^2\right]. \tag{6.4}$$

This is valid for an atomic cloud with a thermal energy $k_B T$ significantly smaller than the potential depth V_0, whose spatial extent in radial and axial direction is small compared to the beam waist and the Rayleigh length. The trap depth is commonly expressed in units of temperature V_{dip}/k_B, where k_B is the Boltzmann constant. To efficiently load atoms into the dipole trap, their temperature should be about an order of magnitude smaller than V_0/k_B. In the harmonic approximation, the trap frequencies in radial and axial direction are given by

$$\omega_r = \sqrt{\frac{4V_0}{mw_0^2}} \propto \frac{\sqrt{P}}{w_0^2}, \qquad \omega_y = \sqrt{\frac{2V_0}{my_R^2}} \propto \frac{\sqrt{P}}{w_0^3}. \tag{6.5}$$

The ratio between radial and axial confinement follows

$$\frac{\omega_r}{\omega_y} = \sqrt{2}\frac{y_R}{w_0} = \sqrt{\frac{2\pi}{\lambda}y_R}. \tag{6.6}$$

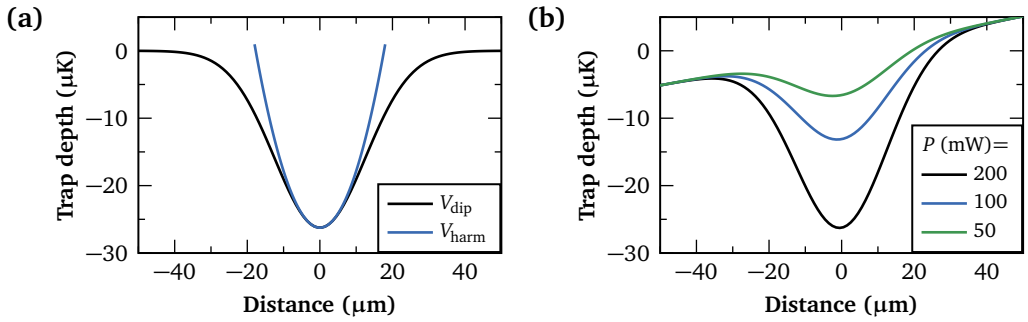

Figure 6.1: (a) Potential of a dipole trap V_{dip} along the radial direction compared to the harmonic approximation V_{harm} calculated for the following parameters: $P = 200\,\text{mW}$, $w_0 = 25\,\mu\text{m}$ and $\lambda = 1064\,\text{nm}$. (b) Sum of dipole and gravitational potential $V = V_{dip} + V_{grav}$ along the z-axis for three different laser powers.

Since usually $y_R \gg w_0$ the trap is highly anisotropic and exhibits a much larger confinement in radial than in axial direction. For typical parameters the radial trap frequencies exceed the axial ones by two orders of magnitude. To suspend the atoms against gravity, the trap is therefore commonly aligned horizontally. In the presence of an external gravitational field along the z-axis the atoms are subject to a total potential [201]

$$V = V_{dip} + V_{grav} \qquad \text{with} \qquad V_{grav} = mgz. \tag{6.7}$$

In consequence, the potential exhibits a tilt which reduces the effective trap depth as depicted in Fig. 6.1(b). Additionally, the position of the potential minimum is slightly shifted along the y-axis by $2g/\omega_r^2$, the so-called gravitational sag.

The focused single-beam trap with its weak axial confinement is easy to implement experimentally, but might not be the best choice for trapping atoms. Alternatively, dipole traps can be generated by retroreflecting the beam to create a standing wave offering very strong confinement in axial direction [134]. Another possibility represent crossed-beam traps which also overcome the very low trap frequencies in the axial direction of a single beam trap. Overlapping two beams with orthogonal polarizations and equal waist under an angle of 90° generates a trap with almost isotropic confiment. These traps are well suited to perform evaporative cooling, since they exhibit higher collision rates for rethermalization [134]. To achieve a larger trapping volume, the intersection angle can chosen to be smaller than 90°.

6.2 Experimental setup

In this section, a short description of the optical dipole system for QUANTUS-1 is given. Since the system simultaneously serves as a testbed for the MAIUS mission, some components have been designed for the application on a sounding rocket featuring a high mechanical and thermal stability as well as a compact volume. More information on the optical setup as well as a charactization and environmental tests performed by Simon Kanthak can be found in [202]. A wavelength of $\lambda = 1064\,\text{nm}$ is chosen for dipole trapping which constitutes a compromise between sufficiently low scattering rates and sufficiently high trap depths given

that the optical power available aboard a sounding rocket is restricted. Furthermore, the wavelength choice permits to employ the same optics as for 780 nm laser light.

Laser and distribution

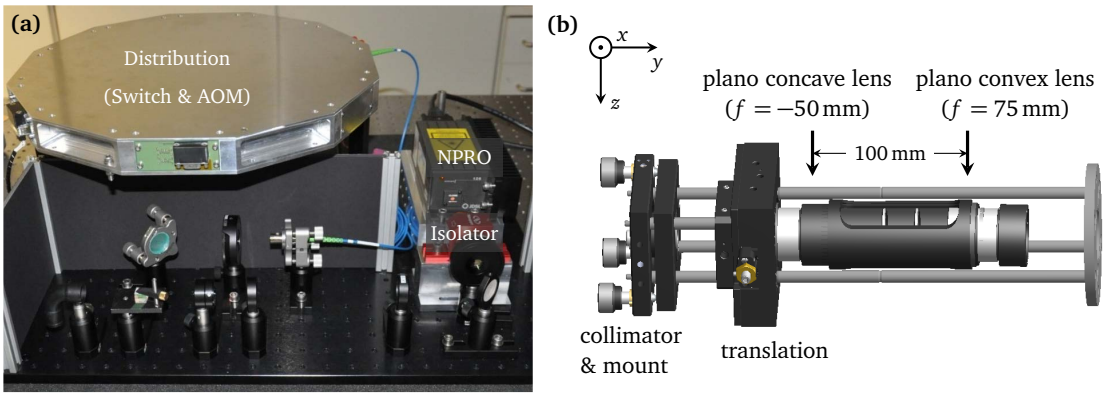

Figure 6.2: Dipole trap setup in QUANTUS-1. (a) The light emitted from the NPRO laser passes an isolator is guided to the distribution module via an optical fiber. The module houses a switch and an AOM to control the laser intensity. (b) Optical assembly for alignment of the dipole beam.

Whereas a micro-integrated laser module (MILAS) developed by the Ferdinand Braun Institut is employed during the MAIUS mission, the ground testbed is operated with a nonplanar ring oscillator (NPRO) Nd:YAG laser. Both devices have similar properties and exhibit an output power of 550 mW at 1064 nm. The laser is mounted on a breadboard together with an optical isolator to prevent back-coupling of the light (Fig. 6.2(a)). The emitted light is coupled into a polarization-maintaining fiber and guided to the distribution module. The module contains a fiber coupled optical switch (`LEONI`) with two output ports which is used as an optical shutter exhibiting an extinction of -88 dB and a rise-and-fall time of roughly 5 ms [202]. The second port offers the possibility of monitoring the power of the dipol laser. Additionally, a fiber-coupled AOM (`Gooch & Housgo`) is used to control and shape the amplitude of the dipole beam. The AOM is fed with a 150 MHz signal generated by a DDS. Its amplitude is modulated via an attenuator (`MiniCircuits ZMAS-3`) which is controlled by an arbitrary waveform generator (`ArbStudio 1104`). This allows the realization of linear ramps or a sinusoidal signal required for the determination of trap frequencies. The limited response time of 20 µs associated with the attenuator is not critical in case of the dipole trap, where typical switching times lie in the millisecond range. From the distribution module, the light is guided to the viewports of the vacuum chamber via a 10 m long single mode fiber (`Thorlabs`).

Optomechanical assembly

The optomechanis required for the optical dipole trap are installed along the y-axis replacing the optical assembly used for beam splitting along the horizontal axis with the twin lattice. The anti-reflection coating of the vacuum windows also provides transmission for the near-infrared spectrum. Similar to the interferometry components, the optical dipole system is based on a cage system (`Thorlabs`) as depicted in Figure 6.2(b). The 1064 nm light is emitted

from a fiber collimator (SuK) featuring a small beam diameter of 675 µm. The collimator is mounted in a kinematic mount to adjust its angle. The beam is focused to a waist of 25 µm by passing a plano concave and a plano convex lens with focal lengths of $f = -50$ mm and $f = 75$ mm, respectively. Both lenses are mounted in a lens tube with a variable distance of roughly 100 mm to determine the size of the beam waist. The focus position of the dipole beam along its propagation axis can be adjusted by moving the lens tube along the y direction. The focus position in x and z direction is adapted with a translation mount.

The dipole beam is measured with a beam profiling camera to determine its waist and focus position [202]. While the focus is at the expected position, the beam waist is slightly larger than specified exhibiting a value of $w_0 \approx 35$ µm. This is caused by deviation of the dipole beam from a perfect Gaussian beam characterized by a beam quality factor of $M^2 \neq 1$.

6.3 Characterization of the dipole trap in QUANTUS-1

	f_x (Hz)	f_y (Hz)	f_z (Hz)
Chip trap	17	47	31
ODT, $w_0 = 25$ µm	638	6.1	638
ODT, $w_0 = 35$ µm	326	2.2	326

Table 6.1: Trap frequencies of the shallow chip release trap compared to the dipole trap (ODT) with $P = 200$ mW for the specified and measured waist, $w_0 = 25$ µm and $w_0 = 35$ µm, respectively.

In this section, the experimental realization of a dipole trap in QUANTUS-1 is described. First, the atoms have to be efficiently loaded into the dipole trap, while atom loss and heating is to be minimized. In case of loading from a MOT, this step can be optimized by varying several parameters such as cooling light intensity and detuning as well as dipole trap depth and alignment, which has been studied in detail [203, 204]. In our configuration, the depth of the dipole trap does not suffice to load atoms from a MOT. Instead, a Bose-Einstein condensate is transferred to the dipole trap which at the same time allows to profit from the fast evaporation on the atom chip. Overlapping the focus of the dipole trap with a waist of 25 µm with the BEC having about the same size represents a challenge and requires precise alignment. The transfer is further impeded by the different aspect ratios, i.e. the mode mismatch of both traps possibly which might lead to atom loss and heating [167]. Table 6.1 compares the trap frequencies of the shallow release trap with the ones of the dipole trap. The latter have been calculated for an optical power of 200 mW, a specified waist of $w_0 = 25$ µm and a Rayleigh length of $y_R = 1.85$ mm. Table 6.1 additionally shows values for the measured waist of $w_0 = 35$ µm, corresponding to a Rayleigh length of $y_R = 3.6$ mm which deviate from the specified ones by roughly a factor of two. In both cases, the dipole trap frequencies in radial and axial direction differ by two orders of magnitude. While the atom chip features a weak axis along the x direction, the dipole trap exhibits a weak confinement along the y-axis.

In addition to the loading procedure, this section comprises a characterization of the dipole trap which includes measurements of expansion rates, lifetime as well as trap frequencies.

6.3.1 Spatial overlap of dipole and magnetic trap

One possible way to achieve a spatial overlap between a condensed cloud and a focused dipole beam is to image both positions on a CCD camera [205]. Given that the BEC is in the focal plane of the camera, the focus of the dipole beam can be adjusted by minimizing its size so it overlaps with the camera focus. This procedure has already been implemented to transfer an atom cloud from a chip trap to a dipole trap [206, 207]. Due to the absence of a detection system along the y-axis another procedure is performed within QUANTUS-1, which is depicted in Figure 6.3.

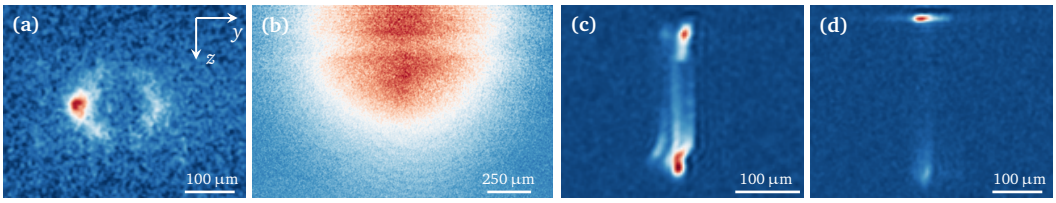

Figure 6.3: Alignment of the dipole beam. (a) Initially, a near resonant 780 nm beam is overlapped with the atomic cloud by maximizing spontaneous emission visible as a halo next to the cloud. (b) Focusing this beam leaves a trace of low atomic density in a large non-condensed cloud. (c) After alignment of the focused 780 nm beam the 1064 nm dipole laser is attached to the optics and already a significant amount of atoms can be optically trapped. (d) Further adjustment of the position of the dipole beam and the magnetic trap leads to a transfer efficiency of almost 100%.

First, the 1064 nm light is replaced with 780 nm laser light resonant to the D_2 line of ^{87}Rb. The bandwidth of the utilized optics is sufficiently broad to be employed with both wavelengths. The lens is removed and the collimated 780 nm beam is aligned horizontally by deflecting it via a pentaprism from a water surface analog to the procedure described in section 3.3.2. The overlap with the atomic cloud is optimized by maximizing spontaneous emission scattering with the translation mount. Hereby, light pulses with a power of 2.5 mW and a duration of 500 µs are applied. Absorption from the beam and subsequent isotropic spontaneous emission lead to the formation of a halo next to the original cloud (Fig. 6.3(a)). To prevent any damage from laser induced heating to the atom chip, the BEC is released from the shallow chip trap ($I_{\mathrm{Bias}} = 0.36\,\mathrm{A}$, $\omega_{x,y,z} = 17, 47, 31\,\mathrm{Hz}$) which exhibits a larger distance from the chip surface, namely 700 µm, compared to steeper traps (Fig. 4.2). The resonant laser pulse is applied after a time-of-flight of 6 ms leading to an additional distance of 180 µm from the atom chip. A larger distance between chip and dipole trap also avoids clipping of the dipole beam which would lead to a serious degradation of the beam quality.

Subsequently, the lens is inserted into the optical assembly to achieve a more precise alignment, and the focused 780 nm beam is again overlapped with the BEC by means of spontaneous emission. The vertical position of the focused beam can be monitored well by employing a resonant laser pulse to a large atom cloud, where its position corresponds to a trail of lower atomic density caused by spontaneously scattered atoms (Fig. 6.3(b)). A large cloud extent is achieved, when evaporative cooling is not performed and non-condensed atoms are released from the chip-based Ioffe-Pritchard trap (see sec. 3.2.1). The high temperatures of these non-condensed atoms, however, do enable trapping with the dipole trap configuration. Therefore, the vertical position of the dipole trap is moved to the position of the shallow release trap at a distance of 700 µm from the chip surface.

At this point, the 1064 nm laser light is connected to the fiber collimator. Without any further alignment, already a fraction of atoms can be trapped optically (Fig. 6.3(c)). For an adiabatic loading the power of the dipole beam is ramped from 0 mW to 260 mW within $t_{\mathrm{ramp}} = 10\,\mathrm{ms}$. The power is constant for another 20 ms, of which the last $t_{\mathrm{odt}} = 7\,\mathrm{ms}$ constitute a pure dipole trap without any magnetic trap present (see Fig. 6.4). Atoms, which are not held in the dipole trap can therefore be detected a few hundred of micrometers below the optically trapped cloud. Further adjustment of the beam position in x and z direction along with a slight adjustment of the location of the chip trap via the K2 coils allows for a transfer efficiency close to 100% from the magnetic into the dipole trap (Fig. 6.3(d)). The loading efficiency can be further increased by adjusting the durations of the ramp of the dipole laser power as well as the temporal overlap with the magnetic trap which will be investigated in the next section.

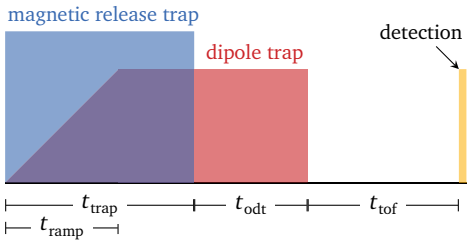

Figure 6.4: Temporal sequence of loading into the dipole trap and subsequent time-of-flight.

6.3.2 Optimization of dipole trap loading

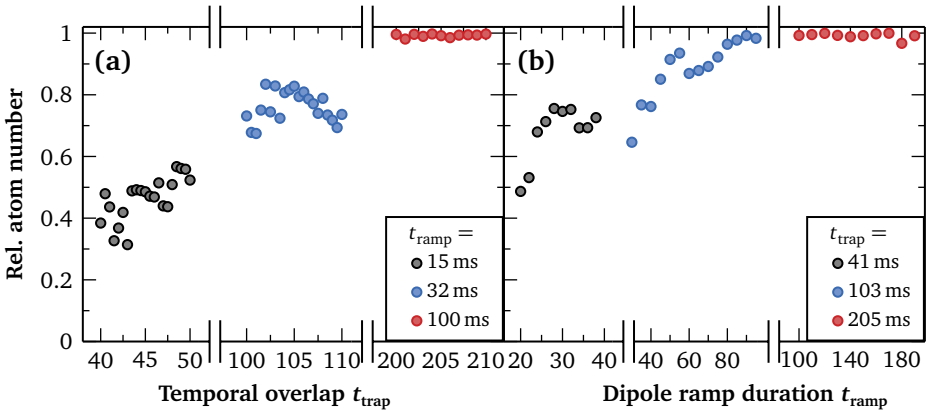

Figure 6.5: Optimization of the transfer between chip trap and dipole trap. The relative number of optically trapped atoms is recorded for various temporal overlaps t_{trap} of the optical and magnetic release trap (a) as well as for different ramp durations t_{ramp} of the dipole power (b). In all cases $t_{\mathrm{tof}} = 6\,\mathrm{ms}$ and $t_{\mathrm{odt}} = 18\,\mathrm{ms}$.

Apart from the spatial overlap between dipole trap and chip trap, the loading efficiency depends on additional parameters such as temporal overlap of both traps and the trap depth. For a more adiabatic loading into the dipole trap and to minimize heating, the laser power, corresponding to the trap depth, is linearly ramped up at the beginning of the magnetic release

trap during t_{ramp} as schematically depicted in Figure 6.4. Hereby, a fully adiabatic transfer from the magnetic potential into the dipole potential is hindered by the mode mismatch of both traps. Dipole and release trap are then simultaneously operated for a few more milliseconds before the chip trap is switched off. The total duration of the release trap corresponds to t_{trap}. The dipole trap is kept on for a duration t_{odt} to separate the trap volume from atoms that have not been trapped optically. Its total duration therefore equals $t_{\mathrm{trap}} + t_{\mathrm{odt}}$

Figure 6.5 illustrates the gain in loading efficiency by increasing the temporal overlap between both traps t_{trap} as well as the ramp duration t_{ramp}. In all cases, the dipole trap is operated for a time $t_{\mathrm{odt}} = 18\,\mathrm{ms}$ after switching off the magnetic release trap. The atom number is measured after a time-of-flight of $t_{\mathrm{tof}} = 6\,\mathrm{ms}$. Figure 6.5(a) depicts the relative number of optically trapped atoms for three different ramp durations $t_{\mathrm{ramp}} = 15\,\mathrm{ms}$, 32 ms, and 100 ms in dependence of the temporal overlap of release and dipole trap scaling with t_{trap}. For values of t_{trap} smaller than 100 ms a longer overlap between magnetic and dipole trap increases the trapped atom number. For $t_{\mathrm{trap}} > 100\,\mathrm{ms}$ and a given ramp duration an increase of the temporal overlap does not lead to a gain in transfer efficiency. A dependence on the phase of the oscillation in the release trap, which results in slightly different center-of-mass positions and velocities (see sec. 4.1.1) can not be observed.

In Figure 6.5(b) the ramp duration t_{ramp} is variied for constant durations $t_{\mathrm{trap}} = 41\,\mathrm{ms}$, 103 ms, and 205 ms. In general, longer ramps are beneficial since they lead to a more adiabatic transfer. The loading efficiency increases with t_{ramp} and reaches 100% for durations $t_{\mathrm{ramp}} \gtrsim 90\,\mathrm{ms}$. For the following measurements, unless stated otherwise, a trap duration of $t_{\mathrm{trap}} = 103\,\mathrm{ms}$ together with a ramping time of $t_{\mathrm{ramp}} = 90\,\mathrm{ms}$ is employed.

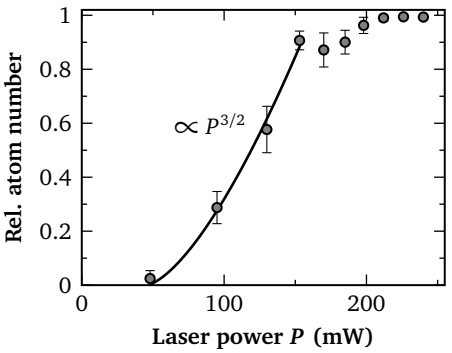

Fig. 6.6: Relative number of optically trapped atoms depending on the applied laser power. $t_{\mathrm{trap}} = 100\,\mathrm{ms}$, $t_{\mathrm{ramp}} = 90\,\mathrm{ms}$, $t_{\mathrm{odt}} = 18\,\mathrm{ms}$, $t_{\mathrm{tof}} = 6\,\mathrm{ms}$. A power dependence of $N \propto P^{3/2}$ can be recognized.

The loading efficiency is additionally recorded for different laser intensities, corresponding to different trap depths and frequencies of the dipole trap according to (6.5). As depicted in Figure 6.6, for small laser intensities ($P < 50\,\mathrm{mW}$) the trap depth is not sufficient to capture atoms and suspend them against gravity. For 50 mW< P <150 mW the trapped atom number increases with the laser power as atoms with higher energy can be loaded into the dipole trap. In this region, the trapped atom number shows a power dependence of $P^{3/2}$ as in [208], which can be theoretically derived by assuming a Maxwell velocity distribution for the atoms. For laser powers above 200 mW the loading efficiency reaches 100%.

6.3.3 Expansion rates

The width of a thermal atomic cloud with an initial size of σ_0 at release from a trap evolves during free evolution with time t_{tof} as [167]

$$\sigma(t) = \sqrt{\sigma_0^2 + \sigma_v^2 t_{\mathrm{tof}}^2}. \tag{6.8}$$

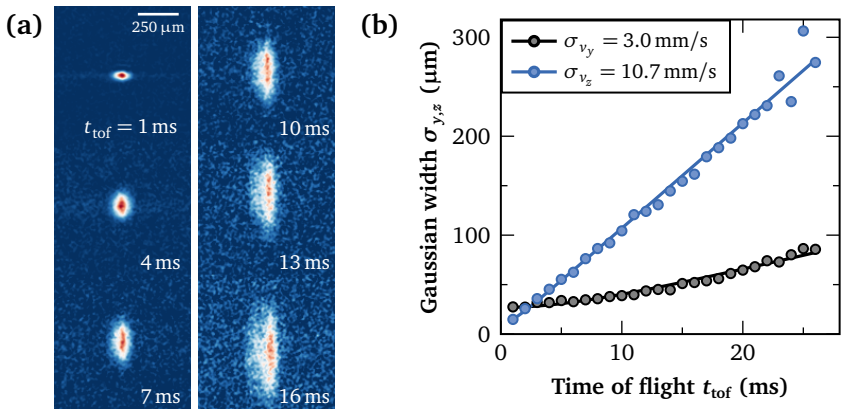

Figure 6.7: Expansion of an optically trapped atomic ensemble ($t_{odt} = 100$ ms). (a) Density images for different time-of-flights t_{tof}. (b) Atomic size in horizontal and vertical direction determined by the Gaussian width of the cloud. Velocity widths are calculated via Eq. (6.8).

The velocity width $\sigma_{v,i}$ along each dimension i is a measure for the effective temperature in this direction

$$k_B T_i = m\sigma_{v,i}^2, \tag{6.9}$$

where m is the atomic mass and k_B the Boltzmann constant. In case of a partly condensed cloud of atoms the temperature can be obtained by fitting a bimodal distribution to the column density and evaluating the Gaussian width σ of the thermal part in order to extract the temperature of the atomic cloud.

Figure 6.7(a) shows absorption images taken at different time-of-flights t_{tof} after a dipole trap duration of $t_{odt} = 100$ ms. The shape of the atomic cloud impedes fitting a bimodal distribution to the column density and might be the result of a non-perfect transfer from chip trap to dipole trap which leads to additional atomic motions. Instead, the cloud's size is extracted by a Gaussian fit to the whole ensemble. For this fit, the fraction of atoms which has already started spreading along the waveguide during the 100 ms of optical trapping is neglected. The Gaussian widths in y and z direction, σ_y and σ_z, are displayed in Figure 6.7(b). Directly after release, the cloud is elongated in y direction due to the low trap frequencies along this axis. After a few milliseconds of time-of-flight, however, σ_z becomes larger than σ_y. A changing aspect ratio represents an indicator for a condensed cloud and results from the conversion of mean-field energy to kinetic energy. A fit to the data according to (6.8) allows to calculate the respective velocity widths and yields values of $\sigma_{v_y} = 3.0$ mm/s and $\sigma_{v_z} = 10.7$ mm/s corresponding to effective temperatures of $T_y = 94$ nK and $T_z = 1.19$ µK.

Compared to the shallow magnetic trap, the cloud released from the dipole trap exhibits larger expansion rates. Heating occurs from a non-adiabatic transfer from the chip trap into the dipole trap which is impeded by the mode mismatch of both traps. The atoms spread along the y-axis due to the weak confinement in this direction and have not yet reached equilibrium. In z direction, higher trap frequencies additionally lead to larger mean-field energy which is converted into kinetic energy. Still, it is possible to load a Bose-Einstein condensate from a chip trap into a dipole trap and obtain effective 1D-temperatures in the nK regime.

6.3.4 Lifetime

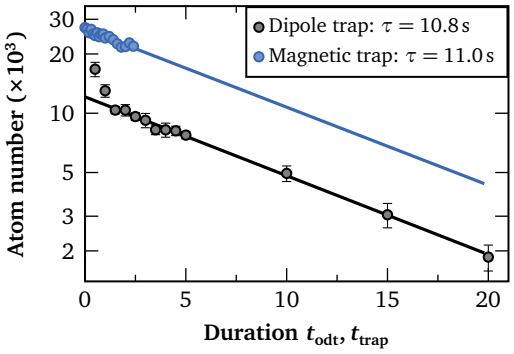

Figure 6.8: Measuring of the lifetime in the dipole trap compared to the chip trap.

The lifetime of atoms in a trap is limited by collisions causing atoms to the escape the trap. In general, the atom number decay can be expressed by the following equation [134]

$$\frac{\mathrm{d}N}{\mathrm{d}t} = -\alpha N(t) - \beta \int_V n^2(\mathbf{r},t)\mathrm{d}^3r - \gamma \int_V n^3(\mathbf{r},t)\mathrm{d}^3r. \tag{6.10}$$

Density-independent loss mechanisms are described by the single-particle coefficient α which accounts for collisions with the background gas in the vacuum chamber. At a pressure of $3\cdot10^{-9}$ mbar one expects a 1/e lifetime of roughly $\tau = 1/\alpha \approx 1\,\mathrm{s}$ [134]. Since the QUANTUS-1 experiment exhibits a pressure in the order of 10^{-11} mbar the measured lifetime should be significantly larger. The coefficient α also comprises photon scattering which can be neglected in a far-detuned trap as well as external heating processes, caused e.g. by laser intensity noise. Two-body losses characterized by β are relevant if the atoms are not in their absolute ground state and include hyperfine-changing collisions. During this process the atoms gain kinetic energy expelling the atoms from the trap. Changes of the hyperfine state from $|F=2\rangle$ to $|F=1\rangle$ can be prohibited by preparing the atoms in the outermost Zeeman sublevels $|F=2, m_F=\pm2\rangle$ due to conservation of angular momentum [209]. Therefore, two-body losses can be neglected in our case. Interactions between three atoms become relevant in case of high densities. In this case, a molecule is formed out of two particles, while the third atom absorbs the released energy and all three atoms are lost from the trap. Due to the coherence properties of Bose-Einstein condensates the rate of three-body recombinations given by γ is predicted to be a factor of 6 lower compared to thermal atoms [210, 211].

The lifetime in the optical dipole trap is examined by measuring the atom number for holding times up to $t_{\mathrm{odt}} = 20\,\mathrm{s}$. For comparison, Fig. 6.8 additionally shows a lifetime measurement in the magnetic release trap. The safety protocol for the atom chip prevents exceedingly long currents and limits the maximum duration in the release trap to $t_{\mathrm{trap}} = 2.4\,\mathrm{s}$. Both, the data points obtained with the magnetic trap as well as the data associated with the dipole trap for durations $t_{\mathrm{odt}} > 1\,\mathrm{s}$, follow an exponential behavior and can be fitted with a single exponential function indicating solely density independent loss mechanisms

$$N(t) = N_0 \mathrm{e}^{-t/\tau}. \tag{6.11}$$

In case of the magnetic trap the fit yields a lifetime of $\tau = (11.0 \pm 1.0)\,\mathrm{s}$, limited primarily by the vacuum quality of the experiment. In the dipole trap, high initial densities causing

three-body collisions lead to a more rapid atom number decay for small durations $t_{\mathrm{odt}} \leq 1\,\mathrm{s}$. For $t_{\mathrm{odt}} > 1\,\mathrm{s}$, however, the dominant loss process is given by collisions with the background vapor and the single exponential fit agrees very well with the data indicating a lifetime of $\tau = (10.8 \pm 0.5)\,\mathrm{s}$ very similar to the one of the magnetic trap.

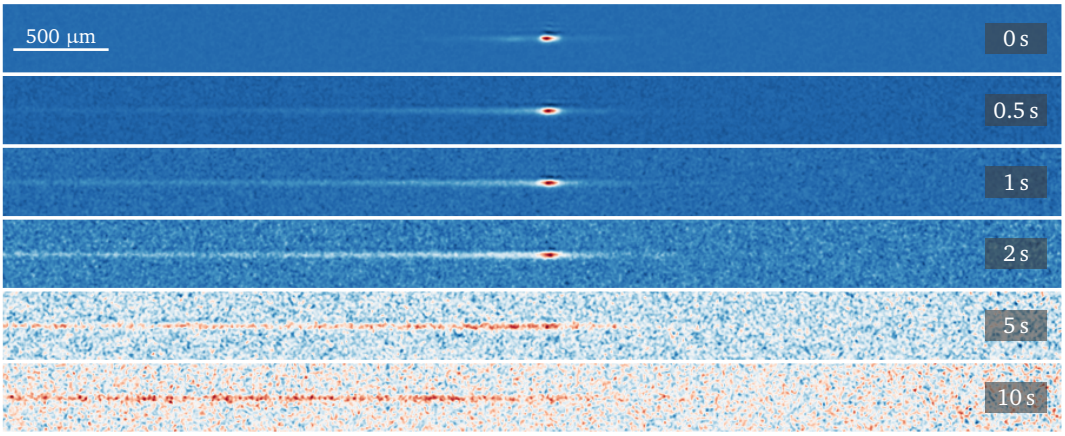

Figure 6.9: Density plots of the atomic cloud in the dipole trap for different durations $t_{\mathrm{odt}} = 0...10\,\mathrm{s}$. With increasing time t_{odt} the cloud starts spreading along the axial direction exhibiting a weak confinement. The asymmetric spreading is probably caused by a slight tilt of the dipole trap.

Figure 6.9 shows the density plots corresponding to the lifetime measurement for durations ranging from $t_{\mathrm{odt}} = 0\,\mathrm{s}$ to $10\,\mathrm{s}$. While the atom cloud released from the magnetic trap exhibits similar dimensions in y and z direction, the focused single beam trap is highly anisotropic. Atoms with highest energy are able to overcome the weak confinement in axial direction. They start spreading along the y direction with increasing holding time, while the atom cloud maintains its extent in radial direction. The spread is not symmetric but atoms mainly propagate in one direction, which might indicate a slight tilt of the dipole beam towards gravity. For small t_{odt} the high densities of the atomic cloud lead to a diffraction of the detection light causing an interference pattern.

6.3.5 Trap frequencies

Trap frequencies are an important property of a trapping potential and determine the motion of atoms inside the trap. They can be measured via a parametric heating technique where the dipole laser power is modulated sinusoidally with a relative amplitude $\beta \ll 1$ and a frequency ω_{mod} [212]. The corresponding equation of motion yields

$$\ddot{x} + \omega_{\mathrm{trap}}^2 [1 + \beta \cos(\omega_{\mathrm{mod}} t)]\, x = 0\,, \tag{6.12}$$

where ω_{trap} is the oscillator's resonance frequency, i.e. the trap frequency of the dipole potential [213]. If the modulation frequency matches twice the trap frequency or a subharmonic $\omega_{\mathrm{mod}} = \frac{2\omega_{\mathrm{trap}}}{n}$, n being an integer, the atoms are resonantly driven which increases their temperature and leads to trap losses. Due to the damping of the resonances with increasing n usually only two resonances are observable, namely $\omega_{\mathrm{mod}} = 2\omega_{\mathrm{trap}}$ and $\omega_{\mathrm{mod}} = \omega_{\mathrm{trap}}$.

For this purpose, the atoms are first loaded into the dipole trap using the common protocol with $t_{\mathrm{ramp}} = 90\,\mathrm{ms}$ and $t_{\mathrm{trap}} = 103\,\mathrm{ms}$ described in section 6.3.2. After a dipole trap duration

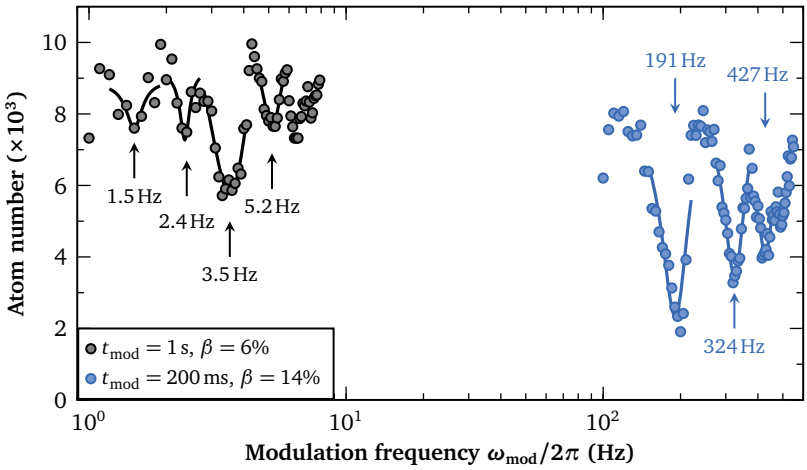

Figure 6.10: Determination of the trap frequencies in the optical dipole trap via parametric driving. The laser power of 210 mW is modulated at a frequency of ω_{mod} and a modulation amplitude of β during t_{mod}. The position of the resonances is determined via Lorentzian fits.

of $t_{\mathrm{odt}} = 10\,\mathrm{ms}$ the laser power is modulated during t_{mod} by changing the amplitude of the AOM. The atomic population is monitored as the modulation frequency ω_{mod} is scanned over the values of the trap frequency. To determine the radial frequencies of our dipole trap the laser power is modulated by ±14% for a duration of 200 ms. The chosen modulation amplitude represents a compromise between a clearly visible signal at parametric resonances and low atom losses in between. However, even at modulation frequencies far off resonance an overall atom loss occurs caused by heating and an escape of atoms with the highest energy from the trap. This process can even be utilized as a technique for evaporative cooling [208, 214]. Parametric resonances are determined via Lorentzian fits and can be observed at frequencies of 191 Hz, 324 Hz and 427 Hz. For the observation of the axial frequencies in the regime of several Hz the duration t_{mod} is increased to 1 s with a reduced modulation amplitude of ±6%. The most prominent resonance is positioned at $\omega_{\mathrm{mod}} = 2\pi \cdot 3.5\,\mathrm{Hz}$. Other dips can be found at 1.5 Hz, 2.4 Hz and 5.2 Hz. Given the low signal-to-noise ratio the determination of those positions is not definite. The relatively long modulation duration of 1 s results in atom losses due to the limited lifetime as well as in a spatial spread of the atom cloud making it more difficult to measure the axial trap frequencies.

The measurement can be interpreted in the following way: It reveals a radial trap frequency of $f_r \approx 200\,\mathrm{Hz}$ with a resonance at twice the value at $2f_r \approx 420\,\mathrm{Hz}$. In case of the axial direction, the dip at $\omega_{\mathrm{mod}} = 2\pi \cdot 3.5\,\mathrm{Hz}$ corresponds to the second harmonic of the axial trap frequency, while the resonance can be observed at $\omega_{\mathrm{mod}} = 2\pi \cdot 1.5\,\mathrm{Hz}$. These values would correspond to a beam waist of roughly $w_0 \approx 40\,\mu\mathrm{m}$ at a power of $P = 200\,\mathrm{mW}$ which is only slighty larger than the waist measured with the beam profiling camera. Additionally, another resonance for the radial trap frequency at $f_r \approx 320\,\mathrm{Hz}$ can be identified which might be connected with the small dips at $f_y = 2.4\,\mathrm{Hz}$ and 5.2 Hz for the frequency in axial direction. These could in principle be explained by another waist of $w_0 \approx 35\,\mu\mathrm{m}$ originating from an astigmatism of the dipole beam.

The measured trap frequencies are in reasonable agreement with the ones calculated from the measured beam waist and laser power (Table 6.1). The measurement of slightly lower

trap frequencies than expected can have several reasons. First of all, the optical power of the dipole beam is measured directly at the fiber output. Subsequent optics such as telescopes, lenses and vacuum windows degrade the laser power by a few percent. Anharmonics of the trapping potential also shift the resonances to lower frequencies [208]. The local beam waist also has a large effect. If the atomic position does not match the beam's focus by a distance of 1 mm due to insufficient alignment, the waist $w(y)$ already increases from 35 µm to 40 µm.

6.3.6 Dipole trapping depending on the evaporation sequence

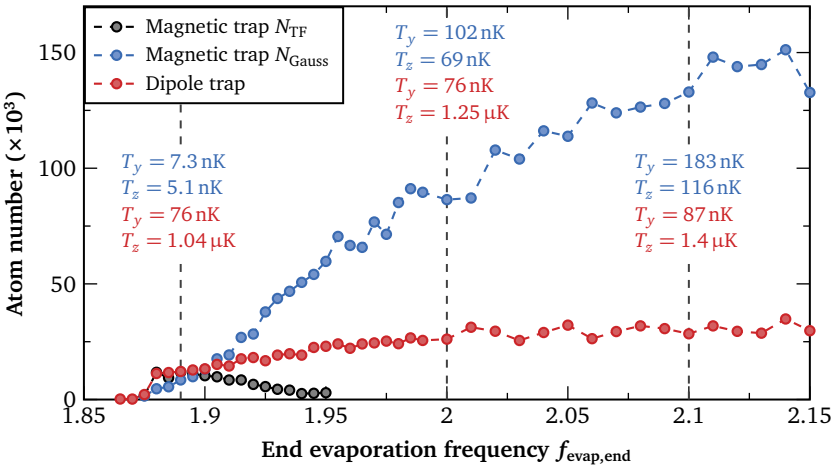

Figure 6.11: Atom number as a function of the final frequency of the evaporation $f_{\mathrm{evap,end}}$ for a release from the chip trap and the dipole trap, respectively. In case of the chip trap, the atom number is composed of a Thomas-Fermi and a Gaussian part. The effective temperatures in y and z direction is calculated from the expansion rates (Table 6.2) for three different frequencies $f_{\mathrm{evap,end}} = 1.89\,\mathrm{MHz}$, 2 MHz and 2.1 MHz.

The sequence for evaporative cooling influences the number of atoms in the final release trap and their kinetic energy. In the following it will be investigated, how this affects the transfer into the dipole trap. So far, the dipole trap has been loaded after evaporation down to a frequency of $f_{\mathrm{evap,end}} = 1.89\,\mathrm{MHz}$. This yields a condensed atomic fraction of more than 50% after release from the chip trap. For higher frequencies $f_{\mathrm{evap,end}}$, less atoms are expelled from the trap and the atomic ensemble exhibits a higher temperature. For $f_{\mathrm{evap,end}} = 1.95\,\mathrm{MHz}$ the condensed fraction, which is determined by a Thomas-Fermi fit, drops to zero. At the same time, the number of thermal atoms, calculated with a Gaussian distribution, significantly increases with $f_{\mathrm{evap,end}}$ (Fig. 6.11). Their temperature also rises from few nK to more than 100 nK. The temperature is calculated from the velocity width of the Gaussian part of a bimodal distribution via time-of-flight measurements (Table 6.2).

The higher overall atom number allows to increase the number of atoms transferred to the dipole trap. When $f_{\mathrm{evap,end}}$ is increased from 1.89 MHz to 2 MHz the optically trapped atom number is approximately doubled, while the corresponding expansion rates do not rise by a significant amount. At the same time, the transfer efficiency decreases from 100% to 25% due to the higher temperature and larger spatial extent of the atom cloud which prohibits

	$f_{\mathrm{evap,end}}$	**1.89 MHz**	**2 Mhz**	**2.1 MHz**
Chip trap	σ_{v_y} (mm/s)	0.84 ± 0.01	3.12 ± 0.01	4.19 ± 0.02
	σ_{v_z} (mm/s)	0.70 ± 0.02	2.57 ± 0.03	3.33 ± 0.04
Dipole trap	σ_{v_y} (mm/s)	2.70 ± 0.06	2.70 ± 0.06	2.88 ± 0.09
	σ_{v_z} (mm/s)	10.0 ± 0.2	10.9 ± 0.06	11.56 ± 0.06

Table 6.2: Velocity width σ_v in y and z direction for a release from the atom chip trap and the dipole trap for different evaporation end frequencies $f_{\mathrm{evap,end}}$.

loading all atoms into the dipole trap. A further augmentation of $f_{\mathrm{evap,end}}$ does not lead to a higher atom number, since the optical trap depth is not sufficient for higher energetic atoms.

7 CONCLUSION AND OUTLOOK

7.1 Summary

Within the scope of this thesis, the coherent manipulation of Bose-Einstein condensates with optical lattices was studied in a compact atom-chip experiment. The main achievements are the development of a large momentum transfer beam splitter and the realization of a so-called twin-lattice interferometer with a wave-packet separation of up to $408\,\hbar k$. This represents the largest momentum splitting in an interferometer reported so far. In detail, the main results cover the following topics:

Large momentum transfer beam splitter

Combining double Bragg diffraction with Bloch oscillations in a twin-lattice configuration allows for a symmetric and scalable beam splitter for the transfer of many photon recoils onto an atom cloud. The twin lattice is built in an elegant way by simply retroreflecting a single beam containing two frequency components with orthogonal polarization. The double Bragg process serves for the initial creation of a superposition of symmetric momentum states as well as for the redirection and recombination in the interferometer. A delta-kicked collimated ensemble with a velocity width of $0.03\,\hbar k$ together with a well-aligned beam enabled high beam splitting efficiencies of 98.8% per $\hbar k$. The pulse stability was studied in dependence on the pulse duration. Applying a duration of $\tau = 300\,\mu s$, the noise caused by amplitude fluctuations could be suppressed, and high stability was reached.

Going beyond the standard Landau-Zener calculations, the Bloch transfer efficiency was investigated in an extension of the non-ideal twin lattice. For small initial momentum splittings, additional atom losses occur. The reproduction of the experimental data with theoretical simulations confirmed that the interaction with parasitic standing waves causes these losses. Standing waves originate from imperfect polarizations arising, for example, from the vacuum windows and cannot be fully suppressed in the current setup. An initial splitting of $8\,\hbar k$ by sequential double Bragg diffraction was chosen as a trade-off between losses caused by parasitic lattices and lower Bragg efficiencies. In that way, Bloch transfer efficiencies in the order of 99.9% could be achieved, and the favorable scaling behavior allowed for a beam splitter with a separation of $1008\,\hbar k$. In our setup, spontaneous emission losses can be suppressed by a factor of two due to the blue detuning of the lattice laser.

Twin-lattice interferometer and contrast analysis

Utilizing the large momentum beam splitter, a Mach-Zehnder-type atom interferometer was formed, whose symmetry promises the suppression of systematic errors encountered in current devices. Since both interferometer arms are manipulated by the same light fields, diffraction phases should be suppressed at least as good as in Ref. [69], where only one frequency component is common to both arms. The interferometric contrast was evaluated for different scalings via a statistical method. It decreases from 70% for an $8\hbar k$ interferometer to 5% for the realization with the largest momentum splitting of $408\hbar k$. This value corresponds to the quadruple of the splitting achieved in Ref. [57] and almost the double of the recent result of Ref. [69]. The observed contrast decay was studied in detail. In combination with simulations, a very good understanding could be achieved. The loss of contrast is mainly caused by two mechanisms, namely atom loss as well as local intensity variations caused by diffraction of the laser beam at different apertures. The effect of atom loss can approximately be expressed by a relatively simple formula relying only on two experimental parameters. Hereby, non-adiabatic losses during Bloch oscillations reduce the interferometer signal. To gauge the second effect, the contrast was calculated for the experimental trajectories in a modeled distorted light field giving rise to dephasing. The current limitations are of technical nature and can probably be easily solved in a dedicated setup. Compared to previous schemes, the twin-lattice interferometer features more scalability marked by low atom number and contrast loss. This opens up exciting perspectives for its implementation in future sensors.

Loading an atom-chip BEC into an optical dipole trap

The setup was extended with a far-detuned 1064 nm laser system to generate an optical dipole trap. After spatially overlapping dipole and chip trap, the Bose-Einstein condensate could be efficiently loaded into the optical trap. With a temporal overlap of roughly 100 ms a transfer efficiency close to unity was reached. The observed lifetime of 11 s is similar to the one in the magnetic trap, and the measured trap frequencies agree with the calculations based on the experimental parameters. The successful operation of a dipole trap within the QUANTUS-1 apparatus is encouraging for its integration in future experiments.

7.2 Perspectives for QUANTUS-1

7.2.1 Maximizing the momentum separation

The large momentum beam splitter presented in this thesis represents a promising tool for the implementation in a variety of experiments. Apart from gravitational wave detection possible application areas include compact devices, such as atomic gyroscopes [23–25], gravimeters [19, 48], quantum tiltmeters [68, 215] or gravity gradiometers [27] possibly in planned spaceborne instruments [26, 216]. These devices, in which laser power and free-fall distance are often constrained, can benefit from the twin-lattice technique to efficiently transfer momentum and maximize their sensitivity.

Ongoing work within the QUANTUS-1 apparatus strives for further improvements on the current results. Since light field distortions presently constitute the main limitation, current investigations include the application of a top-hat beam [195] offering a homogeneous intensity profile. Its benefits include a constant lattice depth throughout the interferometer as well as a relatively sharp cutoff at the edges of the beam to minimize clipping at different apertures. Additionally, the installation of a camera with a larger CCD chip is planned to increase the detection size. This might open up the possibility to augment the interferometer region for larger interrogation times and move it away from the atom chip to reduce distortions arising from clipping at the chip.

At the same time, technological development is made in the field of controlling the RF frequency of the AOMs. The possibility of driving arbitrary intensity and frequency ramps enables the realization of more efficient transfer sequences for Bloch oscillations. Currently, a parasitic standing wave impedes the momentum transfer for small initial separations between both wave packets. An adiabatically increasing acceleration rate exhibiting a small initial acceleration and lattice depth is expected to reduce the corresponding atom loss [58] and is, in general, more suited for the transfer of many photon recoils in a deep lattice [139]. Such a sequence will be realized by combining the amplitude curve of an arbitrary waveform generator (`ArbStudio 1104`) with the frequency sweep of an RF synthesizer (`MOGLabs XRF021`). Atom losses will be further reduced by utilizing a new laser system detuned $\Delta = 2\pi \cdot 300\,\mathrm{GHz}$ from resonance suppressing spontaneous emission by a factor of 3 compared to the currently used system exhibiting a detuning of $\Delta = 2\pi \cdot 100\,\mathrm{GHz}$. Future enhancements might also include an AC-Stark compensation [47, 193] to suppress the effect of residual local intensity inhomogeneities.

7.2.2 Optical dipole potentials

Apart from forming optical traps for atoms, a dipole potential can also be used to generate an optical lens to reduce the atomic expansion rate. While the magnetic lens already yields very good results for our condensate, an optical lens or a combination of both may have some benefit. First, it gives access to the weak axis parallel to the central wire of the chip, which is hardly manipulated with the magnetic lens. Besides, it might solve the problem of the anharmonicity of the chip trap perpendicular to its surface, leading to deformations of the atomic density profile as observed in Ref. [98, 99]. Recently, a new 1064 nm laser system has been added to the experiment and the first studies of optical lensing seem promising.

The optics associated with the new dipole laser system also allow for the implementation of a waveguide [37] for the investigation of atom interferometry in a compact volume. In particular, one has to study possible dephasing mechanisms in the guide arising, for example, through mechanical instability or intensity fluctuations. An interesting approach is proposed in Ref. [70], where a lattice simultaneously serves as a beam splitter and guide. In detail, one would use two optical lattice waveguides to separate the interferometer arms, then sustain both arms in a single common lattice, and finally recombine the arms using both lattices again. Apart from inertial measurements, the proximity of the atom chip to the waveguide within QUANTUS-1 offers the possibility of measuring short-ranged forces such as predicted by certain models for dark energy [32] or the Casimir-Polder force [34]. On the other hand,

waveguides also offer the possibility to move the interferometer region away from the atom chip to suppress systematic effects related to its surface or mass distribution.

A lot of interesting applications arise when one uses painted potentials to create a variety of geometries. These can be created with acousto-optic deflectors (AODs), allowing for rapid modulation. While slow movements of the dipole beam induce heating, atoms are not capable of following oscillations faster than the trap frequency and will only experience a time-averaged potential [217]. In this way, arbitrary and potentially dynamic potentials for trapping cold atoms can be created, such as toroids or ring lattices. The latter are interesting due to their periodic boundary conditions and the ability to realize vortices.

7.3 Application in future devices

The studies presented within this thesis do not solely have the purpose of advancing the QUANTUS-1 experiment but are equally important for future quantum sensors on ground or in space. The areas of applications for these devices are broad and range from tests of the Equivalence Principle to Earth observation up to gravitational wave detection. The following paragraphs comprise a selection of planned instruments.

7.3.1 Gravitational wave antenna

One particular field of application for the twin-lattice beam splitter is the planned hybrid atom-laser interferometer MIGA (**M**atter wave-laser based **I**nterferometer **G**ravitation **A**ntenna), a demonstrator for the measurement of space-time strain in the infrasound [49]. Apart from MIGA, there exist proposals for other ground-based instruments [51, 218, 219], which will complement each other in the detection of infrasound gravitational waves and the research on gravitation. MIGA will be installed 500 m underground in an environment characterized by very low noise and seismic disturbances. In the first realization, the detector consists of a set of three atom interferometers interrogated by the light field of an ultra-stable optical cavity. The corresponding high beam quality will eliminate the most severe error encountered in our twin-lattice interferometer caused by light field distortions. Variations of the strain inside the cavity, induced by a gravitational wave, modify the optical phase. It is linked to the phase of the atom interferometers through the interaction during the interferometer pulses. Apart from the application of an optical cavity, the instrument will rely on standard, well-proven techniques including laser-cooled rubidium atoms, two-photon Bragg diffraction, and shot-noise limited sensitivity. For a resonator length of $L = 200\,\mathrm{m}$, an interrogation time of $2T = 500\,\mathrm{ms}$, Bragg diffraction of order $n = 1$ and 10^6 laser-cooled atoms, the expected peak strain sensitivity will be $2 \cdot 10^{-13}/\sqrt{\mathrm{Hz}}$ at 2 Hz.

Newtonian noise, caused by fluctuations of the terrestrial gravity field, is considered to be a limiting noise source at low frequencies for the next generation of gravitational-wave detectors. A future device, which is built of two orthogonal arms interrogated by the same laser, will therefore consist of an array of atomic gradiometers to reduce the effect of this particular noise source [56]. Since gravitational wave signals and Newtonian noise are characterized by different length scales along the detector's size, it is possible to distinguish between them when using a network of sensors. Assuming an ambitious configuration with 80 gradiometers,

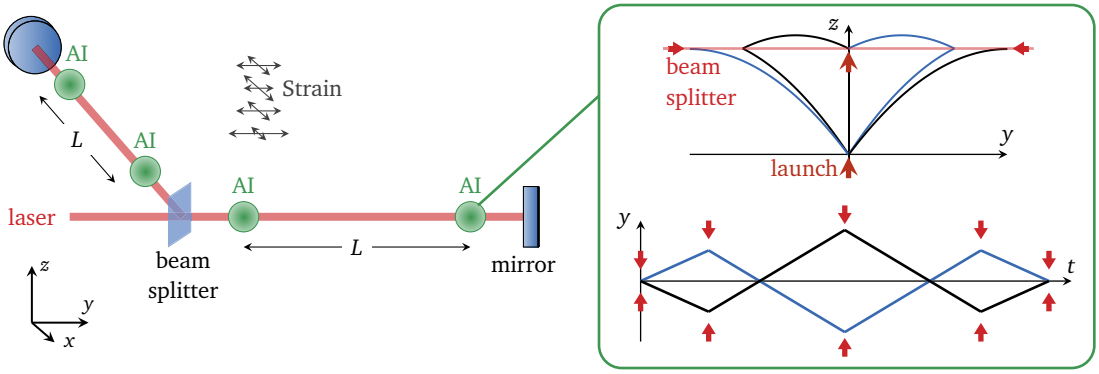

Figure 7.1: Scheme of a gravitational wave detector with two horizontal arms, which is maximally sensitive to a wave traveling in the vertical direction. Shown is an exemplary interferometer geometry with three loops, three vertical launches and five beam-splitting pulses for the suppression of noise sources. Adapted from [50]

a total arm length of $L = 16.3\,\mathrm{km}$, an interrogation time of $2T = 0.6\,\mathrm{s}$, large momentum transfer of order $n = 1000$ and an atom flux of $10^{12}/\mathrm{s}$ strain sensitivities below $1 \cdot 10^{-19}/\sqrt{\mathrm{Hz}}$ in the 0.3—3 Hz frequency domain are accessible along with a peak sensitivity of $3 \cdot 10^{-23}/\sqrt{\mathrm{Hz}}$ at 2 Hz. Applying our twin-lattice beam splitter in a dedicated setup, the required momentum separation of $2000\,\hbar k$ seems to be in reach.

Ref. [50] elaborates on interferometer schemes for the use in terrestrial detectors, making particular use of our symmetric twin-lattice beam splitter. In a multi-loop sequence, where symmetric beam splitting is combined with vertical relaunches to fold the interferometer geometry, some noise sources are suppressed (Fig. 7.1). In particular, this geometry is insensitive to the initial position and velocity of the atomic cloud, causing spurious phase terms due to the Sagnac effect. Therefore, it eases the requirements on the atomic expansion rate which, otherwise, would require energy levels of femtokelvins.

7.3.2 Very large baseline atom interferometer (VLBAI)

Another testbed for new beam-splitting techniques constitutes the VLBAI which is currently being installed in the HITec building in Hannover (Fig. 7.2). Its 10 m baseline allows for an extended free-fall time aiming at high-precision tests of the equivalence principle employing mixtures of ytterbium and rubidium [221]. Apart from the implementation of a fountain mode, large momentum beam splitters represent one factor for increasing the sensitivity in an advanced setup. At the same time, the device can be used for highly accurate absolute gravimetry, gradiometry or exploring methods for gravitational wave detection. To suppress spurious noise sources such as vibrations and magnetic field gradients, the instrument is equipped with a seismic attenuation system as well as a ten-meter long magnetic shield making it possible to perform outstanding measurements.

The combination of large momentum transfer with long interrogation times allows to create atomic superpositions over macroscopic distances and, in this way, search for the quantum-to-classical transition of an object. Motivated amongst others by the search for compatibility between quantum theory and general relativity, the question arises, whether quantum mechanics loses its validity beyond a specific mass or complexity of the test ob-

ject [222]. To address this question, interference experiments with matter-waves play an essential role. In these experiments, it is crucial to shield the system from dephasing and decoherence stemming from technical or other non-fundamental sources.

A measure for the macroscopicity of a specific superposition state was developed in Ref. [223]. It rates the superposition according to its ability to rule out possible modifications of quantum mechanics, which comprise a violation of the superposition principle on macroscopic scales. If an experiment does not reveal physics 'beyond the Schrödinger equation', a certain parameter region can be ruled out. The larger the excluded region, the more macroscopic the experiment. The macroscopicity μ can be quantified by the largest excluded coherence time parameter τ of a reference particle such as an electron: $\mu = \log_{10}(\frac{\tau_e}{1\,\mathrm{s}})$. For interference experiments one can approximate

$$\mu = \log_{10}\left[\left|\frac{1}{\ln f}\right|\left(\frac{m}{m_e}\right)^2 \frac{t}{1\,\mathrm{s}}\right], \tag{7.1}$$

where f is the measured fraction of the expected interference contrast, m the mass of the test particle, m_e the electron mass and t the period during which coherence is maintained. The largest macroscopicity values with grades of about 12 have been achieved by interfering molecules with masses above 10 000 amu [224] or in atom interferometers with long interrogation times of $T = 1.04s$ [47]. In comparison, proposed interference experiments with nanospheres would achieve a rate of 20, while the spatial superposition of a cat along 10 cm would show a score of 57.

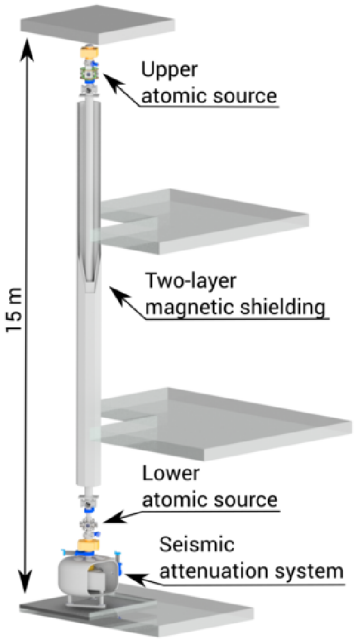

Fig. 7.2: Scheme of the VLBAI [220].

Eq. (7.1) does not consider the wave packet separation since the latter does not impact the maximally excluded time parameter. Given the lower contrast, the value μ calculated for the $90\,\hbar k$ interferometer in Ref. [47] therefore falls below the one of the $2\,\hbar k$ realization, although a large atomic wave packet separation of 54 cm could be demonstrated. However, a higher wave packet separation allows excluding another dimension of the parameter region, namely the critical length scale $\hbar/\sigma_q$ [223], where σ_q is the standard deviation of the momentum variable. It is therefore also crucial for ruling out possible modifications.

7.3.3 Missions in space

By developing and investigating new beam splitting techniques as well as by studying the interplay between atom chip and optical dipole trap, the QUANTUS-1 experiment serves as a testbed for quantum sensors onboard future space missions. The twin-lattice beam splitter, in particular, is suitable for the implementation in microgravity environments, since it requires a vanishing velocity in beam splitter direction.

The outcomes achieved with the QUANTUS-1 and QUANTUS-2 experiments directly impact the strategies for the MAIUS sounding rocket missions. After the successful launch of MAIUS-1, the successors MAIUS-2 and MAIUS-3 aim to perform dual-species experiments with rubidium

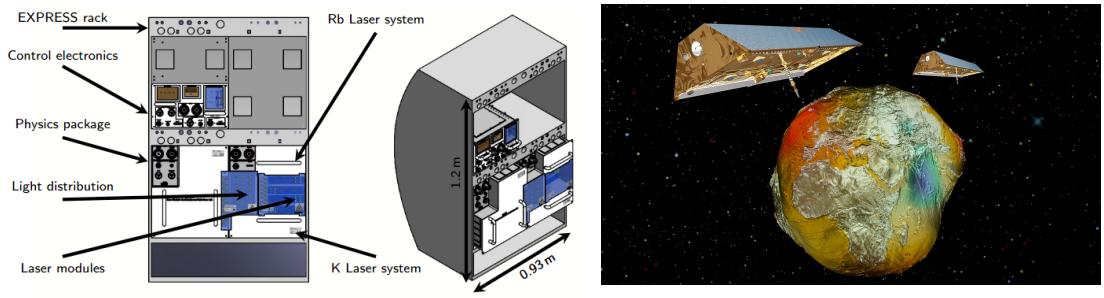

Figure 7.3: (Left) BECCAL apparatus housed in a standardized rack system for the ISS. The payload consists of three subsystems, namely the physics package, the laser system, and the control electronics [43]. (Right) Future quantum sensors will likely be installed onboard satellites, mapping, for example, Earth's gravity field [26, 216]. The picture shows the twin satellites of the mission GRACE [225], which performed detailed measurements of Earth's gravity field anomalies (source: [226]).

and potassium [41, 199]. Besides, an optical dipole trap will be added in MAIUS-3 to study hybrid or purely optical traps. Dipole traps allow for tuning the interactions between the different atomic species and enable a transfer away from the chip to suppress systematic effects associated with its surface and mass.

The BECCAL project relies on the expertise of the QUANTUS consortium together with JPL/NASA to build and operate miniaturized quantum sensors [43]. A panel of experts in the field of ultra-cold atoms has gathered a variety of possible experiments to be performed on the ISS. Among others, these experiments include dual-species atom interferometry with extended interrogation times as well as strongly interacting atoms and molecules. Furthermore, degenerate gases shall be investigated in different trapping geometries such as blue box potentials or shell-like geometries, which are inaccessible in ground-based setups.

While the ISS already allows for a variety of intriguing experiments in extended free fall, the vibrational noise on the space station sets a limit for high precision measurements. Therefore, proposals take one step further and exploit the superior microgravity conditions on satellites. With this, benefits may also arise from highly elliptic orbits, which induce significant variations of the gravitational potential. Besides, a configuration based on two or more satellites provides large relative distances, undisturbed by atmosphere, which can be exploited to increase the sensitivity of gravitational wave detectors. The goal of the STE-QUEST mission, which was selected for a phase A study in ESA's Cosmic Vision Programme, was to perform high-precision tests of general relativity using atomic clocks and matter-wave interferometry [227, 228]. The proposed measurements include a test of the gravitational redshift of the sun and moon as well as dual-species interferometry with ^{87}Rb and ^{85}Rb to probe the universality of free fall at a targeted level of 10^{-15}. Although STE-QUEST was finally not selected, the study provides significant scientific knowledge and experience for future satellite missions. Hereby, the fields of application are versatile, ranging from gravity gradiometry to map the Earth's gravity field [26, 216] up to gravitational wave detection [52, 53]. Several fundamental topics are addressed within the mission "Space Atomic Gravity Explorer" (SAGE) [229]. The proposal envisages a multi-satellite configuration to house atomic clocks and interferometers based on ultracold strontium atoms. In addition to the topics mentioned above, the multi-purpose mission aims for the investigation of dark matter and fundamental aspects of quantum mechanics such as quantum correlations and Bell inequalities.

BIBLIOGRAPHY

[1] T. H. Maiman. “Stimulated Optical Radiation in Ruby.” *Nature* **187** (1960), 493–494 (cit. on p. 1).

[2] J. Aasi et al. “Enhanced sensitivity of the LIGO gravitational wave detector by using squeezed states of light.” *Nat. Phot.* **7** (2013), 613–619 (cit. on p. 1).

[3] B. P. Abbott et al. “Observation of Gravitational Waves from a Binary Black Hole Merger.” *Phys. Rev. Lett.* **116** (2016), 061102 (cit. on pp. 1, 28).

[4] T. Hänsch and A. Schawlow. “Cooling of gases by laser radiation.” *Optics Communications* **13** (1975), 68 –69 (cit. on p. 1).

[5] A. Ashkin. “Trapping of Atoms by Resonance Radiation Pressure.” *Phys. Rev. Lett.* **40** (1978), 729–732 (cit. on pp. 1, 104).

[6] P. D. Lett, R. N. Watts, C. I. Westbrook, W. D. Phillips, P. L. Gould, and H. J. Metcalf. “Observation of Atoms Laser Cooled below the Doppler Limit.” *Phys. Rev. Lett.* **61** (1988), 169–172 (cit. on p. 1).

[7] M. Kasevich and S. Chu. “Laser cooling below a photon recoil with three-level atoms.” *Phys. Rev. Lett.* **69** (1992), 1741–1744 (cit. on p. 1).

[8] D. W. Sesko and C. E. Wieman. “Observation of the cesium clock transition in laser-cooled atoms.” *Opt. Lett.* **14** (1989), 269–271 (cit. on p. 1).

[9] J. L. Hall, M. Zhu, and P. Buch. “Prospects for using laser-prepared atomic fountains for optical frequency standards applications.” *J. Opt. Soc. Am. B* **6** (1989), 2194–2205 (cit. on p. 1).

[10] S. A. Werner, J. L. Staudenmann, and R. Colella. “Effect of Earth’s Rotation on the Quantum Mechanical Phase of the Neutron.” *Phys. Rev. Lett.* **42** (1979), 1103–1106 (cit. on p. 1).

[11] D. M. Greenberger and A. W. Overhauser. “Coherence effects in neutron diffraction and gravity experiments.” *Rev. Mod. Phys.* **51** (1979), 43–78 (cit. on p. 1).

[12] O. Carnal and J. Mlynek. “Young’s double-slit experiment with atoms: A simple atom interferometer.” *Phys. Rev. Lett.* **66** (1991), 2689–2692 (cit. on p. 1).

[13] D. W. Keith, C. R. Ekstrom, Q. A. Turchette, and D. E. Pritchard. “An interferometer for atoms.” *Phys. Rev. Lett.* **66** (1991), 2693–2696 (cit. on p. 1).

[14] F. Riehle, T. Kisters, A. Witte, J. Helmcke, and C. J. Bordé. “Optical Ramsey spectroscopy in a rotating frame: Sagnac effect in a matter-wave interferometer.” *Phys. Rev. Lett.* **67** (1991), 177–180 (cit. on p. 1).

[15] M. Kasevich and S. Chu. “Atomic interferometry using stimulated Raman transitions.” *Phys. Rev. Lett.* **67** (1991), 181–184 (cit. on pp. 1, 2, 10).

[16] P. J. Martin, B. G. Oldaker, A. H. Miklich, and D. E. Pritchard. “Bragg scattering of atoms from a standing light wave.” *Phys. Rev. Lett.* **60** (1988), 515–518 (cit. on pp. 2, 10).

[17] E. M. Rasel, M. K. Oberthaler, H. Batelaan, J. Schmiedmayer, and A. Zeilinger. “Atom Wave Interferometry with Diffraction Gratings of Light.” *Phys. Rev. Lett.* **75** (1995), 2633–2637 (cit. on p. 2).

[18] A Peters, K. Y. Chung, and S Chu. “High-precision gravity measurements using atom interferometry.” *Metrologia* **38** (2001), 25–61 (cit. on pp. 2, 17, 29, 33).

[19] C. Freier, M. Hauth, V. Schkolnik, B. Leykauf, M. Schilling, H. Wziontek, H.-G. Scherneck, J. Müller, and A. Peters. “Mobile quantum gravity sensor with unprecedented stability.” *J. Phys.: Conf. Ser.* **723**.1 (2016), 012050 (cit. on pp. 2, 3, 78, 118).

[20] Z.-K. Hu, B.-L. Sun, X.-C. Duan, M.-K. Zhou, L.-L. Chen, S. Zhan, Q.-Z. Zhang, and J. Luo. “Demonstration of an ultrahigh-sensitivity atom-interferometry absolute gravimeter.” *Phys. Rev. A* **88** (2013), 043610 (cit. on p. 2).

[21] *Muquans*. `https://www.muquans.com/`. Accessed 19/08/20 (cit. on p. 2).

[22] *AOSense*. `https://aosense.com/`. Accessed 19/08/20 (cit. on p. 2).

[23] J. K. Stockton, K. Takase, and M. A. Kasevich. “Absolute Geodetic Rotation Measurement Using Atom Interferometry.” *Phys. Rev. Lett.* **107** (2011), 133001 (cit. on pp. 2, 118).

[24] P. Berg, S. Abend, G. Tackmann, C. Schubert, E. Giese, W. P. Schleich, F. A. Narducci, W. Ertmer, and E. M. Rasel. “Composite-Light-Pulse Technique for High-Precision Atom Interferometry.” *Phys. Rev. Lett.* **114** (2015), 063002 (cit. on pp. 2, 4, 76, 78, 118).

[25] I. Dutta, D. Savoie, B. Fang, B. Venon, C. L. Garrido Alzar, R. Geiger, and A. Landragin. “Continuous Cold-Atom Inertial Sensor with 1 nrad/sec Rotation Stability.” *Phys. Rev. Lett.* **116** (2016), 183003 (cit. on pp. 2, 78, 118).

[26] O. Carraz, C. Siemes, L. Massotti, R. Haagmans, and P. Silvestrin. “A Spaceborne Gravity Gradiometer Concept Based on Cold Atom Interferometers for Measuring Earth’s Gravity Field.” *Microgravity Sci. Technol.* **26** (2014), 139–145 (cit. on pp. 2, 78, 118, 123).

[27] P. Asenbaum, C. Overstreet, T. Kovachy, D. D. Brown, J. M. Hogan, and M. A. Kasevich. “Phase shift in an atom interferometer due to spacetime curvature across its wave function.” *Phys. Rev. Lett.* **118** (2017), 183602 (cit. on pp. 2, 3, 78, 118).

[28] S. Herrmann, E. Göklü, H. Müntinga, A. Resch, T. van Zoest, H. Dittus, and C. Lämmerzahl. “Testing Fundamental Physics with Degenerate Quantum Gases in Microgravity.” *Microgravity Sci. Technol.* **22** (2010), 529–538 (cit. on p. 2).

[29] S. Dimopoulos, P. W. Graham, J. M. Hogan, and M. A. Kasevich. “General relativistic effects in atom interferometry.” *Phys. Rev. D* **78** (2008), 042003 (cit. on p. 2).

[30] D. Schlippert, J. Hartwig, H. Albers, L. L. Richardson, C. Schubert, A. Roura, W. P. Schleich, W. Ertmer, and E. M. Rasel. “Quantum Test of the Universality of Free Fall.” *Phys. Rev. Lett.* **112** (2014), 203002 (cit. on p. 2).

[31] L. Zhou, S. Long, B. Tang, X. Chen, F. Gao, W. Peng, W. Duan, J. Zhong, Z. Xiong, J. Wang, Y. Zhang, and M. Zhan. "Test of Equivalence Principle at 10^{-8} Level by a Dual-Species Double-Diffraction Raman Atom Interferometer." *Phys. Rev. Lett.* **115** (2015), 013004 (cit. on p. 2).

[32] M. Jaffe, P. Haslinger, V. Xu, P. Hamilton, U. Amol, B. Elder, J. Khoury, and H. Müller. "Testing sub-gravitational forces on atoms from a miniature in-vacuum source mass." *Nature Physics* **13** (2017), 938–942 (cit. on pp. 2, 119).

[33] M. A. Hohensee, B. Estey, P. Hamilton, A. Zeilinger, and H. Müller. "Force-Free Gravitational Redshift: Proposed Gravitational Aharonov-Bohm Experiment." *Phys. Rev. Lett.* **108** (2012), 230404 (cit. on p. 2).

[34] D. M. Harber, J. M. Obrecht, J. M. McGuirk, and E. A. Cornell. "Measurement of the Casimir-Polder force through center-of-mass oscillations of a Bose-Einstein condensate." *Phys. Rev. A* **72** (2005), 033610 (cit. on pp. 2, 119).

[35] S. M. Dickerson, J. M. Hogan, A. Sugarbaker, D. M. S. Johnson, and M. A. Kasevich. "Multiaxis Inertial Sensing with Long-Time Point Source Atom Interferometry." *Phys. Rev. Lett.* **111** (2013), 083001 (cit. on pp. 2, 5, 17, 103).

[36] O. Garcia, B. Deissler, K. J. Hughes, J. M. Reeves, and C. A. Sackett. "Bose-Einstein-condensate interferometer with macroscopic arm separation." *Phys. Rev. A* **74** (2006), 031601 (cit. on pp. 2, 103).

[37] G. D. McDonald, H. Keal, P. A. Altin, J. E. Debs, S. Bennetts, C. C. N. Kuhn, K. S. Hardman, M. T. Johnsson, J. D. Close, and N. P. Robins. "Optically guided linear Mach-Zehnder atom interferometer." *Phys. Rev. A* **87** (2013), 013632 (cit. on pp. 2, 8, 103, 119).

[38] T. Akatsuka, T. Takahashi, and H. Katori. "Optically guided atom interferometer tuned to magic wavelength." *Appl. Phys. Expr.* **10** (2017), 112501 (cit. on pp. 2, 8, 103).

[39] B. Barrett, L. Antoni-Micollier, L. Chichet, B. Battelier, T Lévèque, A. Landragin, and P. Bouyer. "Dual matter-wave inertial sensors in weightlessness." *Nat. Com.* **7** (2016), 13786 (cit. on pp. 2, 103).

[40] H. Müntinga et al. "Interferometry with Bose-Einstein condensates in microgravity." *Phys. Rev. Lett.* **110** (2013), 093602 (cit. on pp. 2, 5, 6, 34, 103).

[41] D. Becker et al. "Space-borne Bose–Einstein condensation for precision interferometry." *Nature* **562** (2018), 391–395 (cit. on pp. 2, 5, 7, 103, 123).

[42] E. Elliott, M. Krutzik, J. Williams, R. Thompson, and D. Aveline. "NASA's Cold Atom Lab (CAL): system development and ground test status." *npj Microgravity* **4** (2018), 16 (cit. on pp. 2, 5, 7, 103).

[43] K. Frye et al. "The Bose-Einstein Condensate and Cold Atom Laboratory." *arXiv:1912.04849* (2019) (cit. on pp. 2, 5, 7, 123).

[44] P. Cladé, E. de Mirandes, M. Cadoret, S. Guellati-Khélifa, C. Schwob, F. Nez, L. Julien, and F. Biraben. "Precise measurement of h/m_{Rb} using Bloch oscillations in a vertical optical lattice: Determination of the fine-structure constant." *Phys. Rev. A* **74** (2006), 052109 (cit. on pp. 2, 27, 68, 72, 78, 85, 86, 94).

[45] R. Bouchendira, P. Cladé, S. Guellati-Khélifa, F. Nez, and F. Biraben. “New Determination of the Fine Structure Constant and Test of the Quantum Electrodynamics.” *Phys. Rev. Lett.* **106** (2011), 080801 (cit. on pp. 2, 19, 78).

[46] R. H. Parker, C. Yu, W. Zhong, B. Estey, and H. Müller. “Measurement of the fine-structure constant as a test of the Standard Model.” *Science* **360** (2018), 191–195 (cit. on pp. 2, 4, 19, 78, 101).

[47] T. Kovachy, P. Asenbaum, C. Overstreet, C. A. Donnelly, S. M. Dickerson, A. Sugarbaker, J. M. Hogan, and M. A. Kasevich. “Quantum superposition at the half-metre scale.” *Nature* **528** (2015), 530–533 (cit. on pp. 3, 4, 78, 83–85, 102, 103, 119, 122).

[48] X. Wu, Z. Pagel, B. S. Malek, T. H. Nguyen, F. Zi, D. S. Scheirer, and H. Müller. “Gravity surveys using a mobile atom interferometer.” *arXiv:1904.09084* (2019) (cit. on pp. 3, 118).

[49] B. Canuel et al. “Exploring gravity with the MIGA large scale atom interferometer.” *Scientific Reports* **8** (2018), 14064 (cit. on pp. 3, 78, 120).

[50] C. Schubert, D. Schlippert, S. Abend, E. Giese, A. Roura, W. P. Schleich, W. Ertmer, and E. M. Rasel. “Scalable, symmetric atom interferometer for infrasound gravitational wave detection.” *arXiv:1909.01951* (2019) (cit. on pp. 3, 78, 121).

[51] M.-S. Zhan et al. “ZAIGA: Zhaoshan long-baseline atom interferometer gravitation antenna.” *Int. J. Mod. Phys. D* **0** (0), 1940005 (cit. on pp. 3, 78, 120).

[52] J. M. Hogan et al. “An atomic gravitational wave interferometric sensor in low earth orbit (AGIS-LEO).” *Gen. Relativ. Gravit.* **43** (2011), 1953–2009 (cit. on pp. 3, 5, 78, 123).

[53] P. W. Graham, J. M. Hogan, M. A. Kasevich, and S. Rajendran. “New Method for Gravitational Wave Detection with Atomic Sensors.” *Phys. Rev. Lett.* **110** (2013), 171102 (cit. on pp. 3, 12, 78, 123).

[54] M. Punturo et al. “The Einstein Telescope: a third-generation gravitational wave observatory.” *Classical and Quantum Gravity* **27** (2010), 194002 (cit. on p. 3).

[55] J. Harms, B. J. J. Slagmolen, R. X. Adhikari, M. C. Miller, M. Evans, Y. Chen, H. Müller, and M. Ando. “Low-frequency terrestrial gravitational-wave detectors.” *Phys. Rev. D* **88** (2013), 122003 (cit. on p. 3).

[56] W. Chaibi, R. Geiger, B. Canuel, A. Bertoldi, A. Landragin, and P. Bouyer. “Low frequency gravitational wave detection with ground-based atom interferometer arrays.” *Phys. Rev. D* **93** (2016), 021101 (cit. on pp. 3, 120).

[57] S.-w. Chiow, T. Kovachy, H.-C. Chien, and M. A. Kasevich. “102$\hbar$k large area atom interferometers.” *Phys. Rev. Lett.* **107**.13 (2011), 130403 (cit. on pp. 3–5, 78, 85, 118).

[58] G. D. McDonald, C. C. N. Kuhn, S. Bennetts, J. E. Debs, K. S. Hardman, J. D. Close, and N. P. Robins. “A faster scaling in acceleration-sensitive atom interferometers.” *EPL (Europhysics Letters)* **105** (2014), 63001 (cit. on pp. 4, 31, 32, 100, 119).

[59] G. D. McDonald, C. C. N. Kuhn, S. Bennetts, J. E. Debs, K. S. Hardman, M. Johnsson, J. D. Close, and N. P. Robins. "80$\hbar k$ momentum separation with Bloch oscillations in an optically guided atom interferometer." *Phys. Rev. A* **88** (2013), 053620 (cit. on pp. 4, 5, 78).

[60] P. Cladé, S. Guellati-Khélifa, F. Nez, and F. Biraben. "Large Momentum Beam Splitter Using Bloch Oscillations." *Phys. Rev. Lett.* **102** (2009), 240402 (cit. on pp. 4, 19, 24, 31, 78).

[61] P. Cladé, T. Plisson, S. Guellati-Khélifa, F. Nez, and F. Biraben. "Theoretical analysis of a large momentum beamsplitter using Bloch oscillations." *The European Physical Journal D* **59** (2010), 349–360 (cit. on pp. 4, 26, 78).

[62] H. Müller, S.-w. Chiow, S. Herrmann, and S. Chu. "Atom Interferometers with Scalable Enclosed Area." *Phys. Rev. Lett.* **102** (2009), 240403 (cit. on pp. 4, 19, 31, 73, 78).

[63] M. Büchner, R. Delhuille, A. Miffre, C. Robilliard, J. Vigué, and C. Champenois. "Diffraction phases in atom interferometers." *Phys. Rev. A* **68** (2003), 013607 (cit. on pp. 4, 30).

[64] B. Estey, C. Yu, H. Müller, P.-C. Kuan, and S.-Y. Lan. "High-Resolution Atom Interferometers with Suppressed Diffraction Phases." *Phys. Rev. Lett.* **115** (2015), 083002 (cit. on pp. 4, 30).

[65] D. Gochnauer, K. E. McAlpine, B. Plotkin-Swing, A. O. Jamison, and S. Gupta. "Bloch-band picture for light-pulse atom diffraction and interferometry." *Phys. Rev. A* **100** (2019), 043611 (cit. on pp. 4, 16).

[66] T. Lévèque, A. Gauguet, F. Michaud, F. Pereira Dos Santos, and A. Landragin. "Enhancing the Area of a Raman Atom Interferometer Using a Versatile Double-Diffraction Technique." *Phys. Rev. Lett.* **103** (2009), 080405 (cit. on pp. 4, 18, 28, 76, 78).

[67] N. Malossi, Q. Bodart, S. Merlet, T. Lévèque, A. Landragin, and F. P. D. Santos. "Double diffraction in an atomic gravimeter." *Phys. Rev. A* **81** (2010), 013617 (cit. on pp. 4, 73, 76).

[68] H. Ahlers et al. "Double Bragg Interferometry." *Phys. Rev. Lett.* **116** (2016), 173601 (cit. on pp. 4, 6, 8, 18, 30, 34, 61, 62, 78, 94, 118).

[69] Z. Pagel, W. Zhong, R. H. Parker, C. T. Olund, N. Y. Yao, and H. Müller. "Bloch beamsplitters and dual-lattice methods for atom interferometry." *arXiv:1907.05994* (2019) (cit. on pp. 4, 78, 118).

[70] T. Kovachy, J. M. Hogan, D. M. S. Johnson, and M. A. Kasevich. "Optical lattices as waveguides and beam splitters for atom interferometry: An analytical treatment and proposal of applications." *Phys. Rev. A* **82** (2010), 013638 (cit. on pp. 4, 103, 119).

[71] H. Müller, S.-w. Chiow, Q. Long, S. Herrmann, and S. Chu. "Atom Interferometry with up to 24-Photon-Momentum-Transfer Beam Splitters." *Phys. Rev. Lett.* **100** (2008), 180405 (cit. on pp. 4, 5, 15, 16, 78, 83–85).

[72] J. M. McGuirk, M. J. Snadden, and M. A. Kasevich. "Large Area Light-Pulse Atom Interferometry." *Phys. Rev. Lett.* **85** (2000), 4498–4501 (cit. on pp. 4, 78).

[73] T. Kovachy, S.-w. Chiow, and M. A. Kasevich. "Adiabatic-rapid-passage multiphoton Bragg atom optics." *Phys. Rev. A* **86** (2012), 011606 (cit. on pp. 4, 75, 76, 78).

[74] K. Kotru, D. L. Butts, J. M. Kinast, and R. E. Stoner. "Large-Area Atom Interferometry with Frequency-Swept Raman Adiabatic Passage." *Phys. Rev. Lett.* **115** (2015), 103001 (cit. on pp. 4, 78).

[75] B. Plotkin-Swing, D. Gochnauer, K. E. McAlpine, E. S. Cooper, A. O. Jamison, and S. Gupta. "Three-Path Atom Interferometry with Large Momentum Separation." *Phys. Rev. Lett.* **121** (2018), 133201 (cit. on p. 4).

[76] M. H. Anderson, J. R. Ensher, M. R. Matthews, C. E. Wieman, and E. A. Cornell. "Observation of Bose-Einstein Condensation in a Dilute Atomic Vapor." *Science* **269** (1995), 198–201 (cit. on pp. 4, 43, 46).

[77] K. B. Davis, M. O. Mewes, M. R. Andrews, N. J. van Druten, D. S. Durfee, D. M. Kurn, and W. Ketterle. "Bose-Einstein Condensation in a Gas of Sodium Atoms." *Phys. Rev. Lett.* **75** (1995), 3969–3973 (cit. on pp. 4, 43, 46).

[78] C. C. Bradley, C. A. Sackett, J. J. Tollett, and R. G. Hulet. "Evidence of Bose-Einstein Condensation in an Atomic Gas with Attractive Interactions." *Phys. Rev. Lett.* **75** (1995), 1687–1690 (cit. on pp. 4, 43).

[79] Bose. "Plancks Gesetz und Lichtquantenhypothese." *Zeitschrift für Physik* **26** (1924), 178–181 (cit. on pp. 4, 43).

[80] A. Einstein. "Quantentheorie des einatomigen idealen Gases." *S. B. Preuss. Akad. Wiss. phys.-math. Klasse* (1924) (cit. on pp. 4, 43).

[81] M. R. Andrews, C. G. Townsend, H.-J. Miesner, D. S. Durfee, D. M. Kurn, and W. Ketterle. "Observation of Interference Between Two Bose Condensates." *Science* **275** (1997), 637–641 (cit. on p. 5).

[82] M. Kasevich, D. S. Weiss, E. Riis, K. Moler, S. Kasapi, and S. Chu. "Atomic velocity selection using stimulated Raman transitions." *Phys. Rev. Lett.* **66** (1991), 2297–2300 (cit. on p. 5).

[83] J. Rudolph, W. Herr, C. Grzeschik, T. Sternke, A. Grote, M. Popp, D. Becker, H. Müntinga, H. Ahlers, A. Peters, C. Lämmerzahl, K. Sengstock, N. Gaaloul, W. Ertmer, and E. M. Rasel. "A high-flux BEC source for mobile atom interferometers." *New J. Phys.* **17** (2015), 065001 (cit. on pp. 5, 6, 42).

[84] M. Fattori, B. Deissler, C. D'Errico, M.Jona-Lasinio, M. Modugno, G. Roati, L. Santos, A. Simoni, M. Zaccanti, M. Inguscio, and G. Modugno. "Atom interferometry with a weakly interaction Bose-Einstein condensate." In: *Pushing the Frontiers of Atomic Physics*. 2009, 251–262 (cit. on pp. 5, 55).

[85] J. E. Debs, P. A. Altin, T. H. Barter, D. Döring, G. R. Dennis, G. McDonald, R. P. Anderson, J. D. Close, and N. P. Robins. "Cold-atom gravimetry with a Bose-Einstein condensate." *Phys. Rev. A* **84** (2011), 033610 (cit. on pp. 5, 28, 55).

[86] T. Kovachy, J. M. Hogan, A. Sugarbaker, S. M. Dickerson, C. A. Donnelly, C. Overstreet, and M. A. Kasevich. "Matter Wave Lensing to Picokelvin Temperatures." *Phys. Rev. Lett.* **114** (2015), 143004 (cit. on pp. 5, 103).

[87] S. S. Szigeti, J. E. Debs, J. J. Hope, N. P. Robins, and J. D. Close. "Why momentum width matters for atom interferometry with Bragg pulses." *New J. Phys.* **14** (2012), 023009 (cit. on pp. 5, 16, 55, 58).

[88] S. Abend, M. Gebbe, M. Gersemann, H. Ahlers, H. Müntinga, E. Giese, N. Gaaloul, C. Schubert, C. Lämmerzahl, W. Ertmer, W. P. Schleich, and E. M. Rasel. "Atom-Chip Fountain Gravimeter." *Phys. Rev. Lett.* **117** (2016), 203003 (cit. on pp. 5, 6, 8, 28, 34, 99).

[89] A. Louchet-Chauvet, T. Farah, Q. Bodart, A. Clairon, A. Landragin, S. Merlet, and F. P. D. Santos. "The influence of transverse motion within an atomic gravimeter." *New J. Phys.* **13** (2011), 065025 (cit. on p. 5).

[90] V. Schkolnik, B. Leykauf, M. Hauth, C. Freier, and A. Peters. "The effect of wavefront aberrations in atom interferometry." *Appl. Phys. B* **120** (2015), 311–316 (cit. on p. 5).

[91] G Tackmann, P Berg, C Schubert, S Abend, M Gilowski, W Ertmer, and E. M. Rasel. "Self-alignment of a compact large-area atomic Sagnac interferometer." *New J. Phys.* **14** (2012), 015002 (cit. on pp. 5, 55, 57).

[92] A. Sugarbaker, S. M. Dickerson, J. M. Hogan, D. M. S. Johnson, and M. A. Kasevich. "Enhanced Atom Interferometer Readout through the Application of Phase Shear." *Phys. Rev. Lett.* **111** (2013), 113002 (cit. on p. 5).

[93] C. Gross, T. Zibold, E. Nicklas, J. Estève, and M. K. Oberthaler. "Nonlinear atom interferometer surpasses classical precision limit." *Nature* **464** (2010), 1165–1169 (cit. on p. 6).

[94] M. F. Riedel, P. Böhi, Y. Li, T. W. Hänsch, A. Sinatra, and P. Treutlein. "Atom-chip-based generation of entanglement for quantum metrology." *Nature* **464** (2010), 1170–1173 (cit. on p. 6).

[95] N. Yu, J. Kohel, J. Kellogg, and L. Maleki. "Development of an atom-interferometer gravity gradiometer for gravity measurement from space." *Appl. Phys. B* **84** (2006), 647–652 (cit. on p. 6).

[96] N. Lundblad, T. Jarvis, and T. Correia. "Design of a microgravity shell-geometry Bose-Einstein condensate experiment." In: *APS Division of Atomic, Molecular and Optical Physics Meeting Abstracts*. 2017, Q1.106 (cit. on p. 6).

[97] K. Padavić, K. Sun, C. Lannert, and S. Vishveshwara. "Physics of hollow Bose-Einstein condensates." *EPL (Europhysics Letters)* **120** (2017), 20004 (cit. on p. 6).

[98] J. Rudolph. "Matter-Wave Optics with Bose-Einstein Condensates in Microgravity." PhD thesis. Leibniz Universität Hannover, 2016 (cit. on pp. 6, 59, 119).

[99] T. Sternke. "An Ultracold High-Flux Source for Matter-Wave Interferometry in Microgravity." PhD thesis. Universität Oldenburg, 2018 (cit. on pp. 6, 59, 119).

[100] S. Kulas et al. "Miniaturized Lab System for Future Cold Atom Experiments in Microgravity." *Microgravity Sci. Technol.* **29** (2017), 37–48 (cit. on p. 6).

[101] C. Vogt, M. Woltmann, H. Albers, D. Schlippert, S. Herrmann, E. M. Rasel, and C. Lämmerzahl. "Evaporative cooling from an optical dipole trap in microgravity." *arXiv:1909.03800* (2019) (cit. on p. 6).

[102] *ZARM*. `https://www.zarm.uni-bremen.de/`. Accessed 19/09/13 (cit. on p. 7).

[103] P. Cladé, E. de Mirandes, M. Cadoret, S. Guellati-Khélifa, C. Schwob, F. Nez, L. Julien, and F. Biraben. "Determination of the Fine Structure Constant Based on Bloch Oscillations of Ultracold Atoms in a Vertical Optical Lattice." *Phys. Rev. Lett.* **96** (2006), 033001 (cit. on pp. 8, 19, 66).

[104] M. Gebbe, S. Abend, J. N. Siemß, M. Gersemann, H. Ahlers, H. Müntinga, S. Herrmann, N. Gaaloul, C. Schubert, K. Hammerer, C. Lämmerzahl, W. Ertmer, and E. M. Rasel. "Twin-lattice atom interferometry." *arXiv:1907.08416* (2019) (cit. on pp. 8, 78, 79).

[105] C. Chin, R. Grimm, P. Julienne, and E. Tiesinga. "Feshbach resonances in ultracold gases." *Rev. Mod. Phys.* **82** (2010), 1225–1286 (cit. on pp. 8, 103).

[106] G. Modugno, G. Ferrari, G. Roati, R. J. Brecha, A. Simoni, and M. Inguscio. "Bose-Einstein Condensation of Potassium Atoms by Sympathetic Cooling." *Science* **294** (2001), 1320–1322 (cit. on pp. 8, 103).

[107] S. B. Papp, J. M. Pino, and C. E. Wieman. "Tunable Miscibility in a Dual-Species Bose-Einstein Condensate." *Phys. Rev. Lett.* **101** (2008), 040402 (cit. on pp. 8, 103).

[108] D. M. Giltner, R. W. McGowan, and S. A. Lee. "Atom Interferometer Based on Bragg Scattering from Standing Light Waves." *Phys. Rev. Lett.* **75** (1995), 2638–2641 (cit. on p. 10).

[109] A. O. Jamison, B. Plotkin-Swing, and S. Gupta. "Advances in precision contrast interferometry with Yb Bose-Einstein condensates." *Phys. Rev. A* **90** (2014), 063606 (cit. on p. 10).

[110] T. Mazzoni, X. Zhang, R. Del Aguila, L. Salvi, N. Poli, and G. M. Tino. "Large-momentum-transfer Bragg interferometer with strontium atoms." *Phys. Rev. A* **92** (2015), 053619 (cit. on p. 10).

[111] B. Young, M. Kasevich, and S. Chu. "Precision Atom Interferometry with Light Pulses." In: *Atom Interferometry*. Ed. by P. R. Berman. San Diego: Academic Press, 1997, 363 –406 (cit. on pp. 11, 12).

[112] L. Hu, N. Poli, L. Salvi, and G. M. Tino. "Atom Interferometry with the Sr Optical Clock Transition." *Phys. Rev. Lett.* **119** (2017), 263601 (cit. on p. 12).

[113] T. Petelski. "Atom interferometers for precision gravity measurements." PhD thesis. 2005 (cit. on pp. 13, 14).

[114] C. Foot. *Atomic Physics*. Oxford University Press, 2005 (cit. on pp. 14, 37).

[115] A. D. Cronin, J. Schmiedmayer, and D. E. Pritchard. "Optics and interferometry with atoms and molecules." *Rev. Mod. Phys.* **81** (2009), 1051–1129 (cit. on p. 15).

[116] S. Abend. "Atom-chip Gravimeter with Bose-Einstein Condensates." PhD thesis. Leibniz Universität Hannover, 2017 (cit. on pp. 15, 22, 26, 74, 83, 99, 100).

[117] W. L. Bragg. "The Specular Reflection of X-rays." *Nature* **90** (1912), 410 (cit. on p. 14).

[118] W. Friedrich, P. Knipping, and M. Laue. "Interferenzerscheinungen bei Röntgenstrahlen." *Annalen der Physik* **346** (1913), 971–988 (cit. on p. 14).

[119] P. L. Kapitza and P. A. M. Dirac. "The reflection of electrons from standing light waves." *Proc. Cambridge Phil. Soc.* **29** (1933), 297–300 (cit. on p. 14).

[120] H. Müller, S.-w. Chiow, and S. Chu. “Atom-wave diffraction between the Raman-Nath and the Bragg regime: Effective Rabi frequency, losses, and phase shifts.” *Phys. Rev. A* **77** (2008), 023609 (cit. on pp. 16, 62).

[121] B. Fang, N. Mielec, D. Savoie, M. Altorio, A. Landragin, and R. Geiger. “Improving the phase response of an atom interferometer by means of temporal pulse shaping.” *New J. Phys.* **20** (2018), 023020 (cit. on p. 16).

[122] E. Giese, A. Friedrich, S. Abend, E. M. Rasel, and W. P. Schleich. “Light shifts in atomic Bragg diffraction.” *Phys. Rev. A* **94** (2016), 063619 (cit. on pp. 16, 30).

[123] P. L. Gould, G. A. Ruff, and D. E. Pritchard. “Diffraction of atoms by light: The near-resonant Kapitza-Dirac effect.” *Phys. Rev. Lett.* **56** (1986), 827–830 (cit. on p. 17).

[124] E. Giese, A. Roura, G. Tackmann, E. M. Rasel, and W. P. Schleich. “Double Bragg diffraction: A tool for atom optics.” *Phys. Rev. A* **88** (2013), 053608 (cit. on pp. 18, 62).

[125] H. Müntinga. “Matter-wave interferometry for space-borne inertial sensors.” PhD thesis. Universität Bremen, 2019 (cit. on pp. 18, 30, 34, 37, 40, 42, 56, 60).

[126] C. Zener. “A theory of the electrical breakdown of solid dielectrics.” *Proc. R. Soc. Lond.* **145** (1934) (cit. on pp. 19, 25).

[127] F. Bloch. “Bemerkung zur Elektronentheorie des Ferromagnetismus und der elektrischen Leitfähigkeit.” *Zeitschrift für Physik* **57** (1929), 545–555 (cit. on p. 19).

[128] S. R. Wilkinson, C. F. Bharucha, K. W. Madison, Q. Niu, and M. G. Raizen. “Observation of Atomic Wannier-Stark Ladders in an Accelerating Optical Potential.” *Phys. Rev. Lett.* **76** (1996), 4512–4515 (cit. on p. 19).

[129] M. Ben Dahan, E. Peik, J. Reichel, Y. Castin, and C. Salomon. “Bloch Oscillations of Atoms in an Optical Potential.” *Phys. Rev. Lett.* **76** (1996), 4508–4511 (cit. on pp. 19, 22).

[130] V. Xu, M. Jaffe, C. D. Panda, S. L. Kristensen, L. W. Clark, and H. Müller. “Probing gravity by holding atoms for 20 seconds.” *Science* **366** (2019), 745–749 (cit. on pp. 19, 101, 103).

[131] R. Charrière, M. Cadoret, N. Zahzam, Y. Bidel, and A. Bresson. “Local gravity measurement with the combination of atom interferometry and Bloch oscillations.” *Phys. Rev. A* **85** (2012), 013639 (cit. on pp. 19, 86, 94, 103).

[132] M. Andia, R. Jannin, F. Nez, F. Biraben, S. Guellati-Khélifa, and P. Cladé. “Compact atomic gravimeter based on a pulsed and accelerated optical lattice.” *Phys. Rev. A* **88** (2013), 031605 (cit. on p. 19).

[133] E. Peik, M. Ben Dahan, I. Bouchoule, Y. Castin, and C. Salomon. “Bloch oscillations of atoms, adiabatic rapid passage, and monokinetic atomic beams.” *Phys. Rev. A* **55** (1997), 2989–3001 (cit. on pp. 19, 22, 24, 25, 32).

[134] R. Grimm, M. Weidemüller, and Y. B. Ovchinnikov. “Optical Dipole Traps for Neutral Atoms.” *Advances In Atomic, Molecular, and Optical Physics* **42** (2000), 95 –170 (cit. on pp. 19, 104, 105, 112).

[135] J. H. Denschlag, J. E. Simsarian, H. Häffner, C. McKenzie, A. Browaeys, D. Cho, K. Helmerson, S. L. Rolston, and W. D. Phillips. "A Bose-Einstein condensate in an optical lattice." *J. Phys. B* **35** (2002), 3095–3110 (cit. on pp. 21, 22, 66, 68).

[136] N. Ashcroft and N. Mermin. *Solid State Physics*. Philadelphia: Saunders College, 1976 (cit. on p. 22).

[137] M. Glück, A. Kolovsky, H. Korsch, and N. Moiseyev. "Calculation of Wannier-Bloch and Wannier-Stark states." *Eur. Phys. J. D* **4** (1998), 239–246 (cit. on p. 22).

[138] M. Glück, A. R. Kolovsky, and H. J. Korsch. "Wannier–Stark resonances in optical and semiconductor superlattices." *Physics Reports* **366** (2002), 103 –182 (cit. on pp. 22, 26, 100).

[139] P. Cladé, M. Andia, and S. Guellati-Khélifa. "Improving efficiency of Bloch oscillations in the tight-binding limit." *Phys. Rev. A* **95** (2017), 063604 (cit. on pp. 26, 72, 80, 100, 119).

[140] C. Sias, A. Zenesini, H. Lignier, S. Wimberger, D. Ciampini, O. Morsch, and E. Arimondo. "Resonantly Enhanced Tunneling of Bose-Einstein Condensates in Periodic Potentials." *Phys. Rev. Lett.* **98** (2007), 120403 (cit. on p. 26).

[141] A. Michelson and E. Morley. "On the relative motion of the Earth and the luminiferous ether." *American Journal of Science* **34** (1887), 333–345 (cit. on p. 28).

[142] B. Décamps, M. Bordoux, J. Alibert, B. Allard, and A. Gauguet. "Phase response of atom interferometers based on sequential Bragg diffractions." *J. Phys. B* **52** (2018), 015003 (cit. on pp. 30, 31).

[143] P. Cheinet, B. Canuel, F. Pereira Dos Santos, A. Gauguet, F. Yver-Leduc, and A. Landragin. "Measurement of the Sensitivity Function in a Time-Domain Atomic Interferometer." *IEEE Trans. Instrum. Meas.* **57** (2008), 1141–1148 (cit. on p. 30).

[144] A. Gauguet, T. E. Mehlstäubler, T. Lévèque, J. Le Gouët, W. Chaibi, B. Canuel, A. Clairon, F. P. Dos Santos, and A. Landragin. "Off-resonant Raman transition impact in an atom interferometer." *Phys. Rev. A* **78** (2008), 043615 (cit. on p. 30).

[145] W. M. Itano, J. C. Bergquist, J. J. Bollinger, J. M. Gilligan, D. J. Heinzen, F. L. Moore, M. G. Raizen, and D. J. Wineland. "Quantum projection noise: Population fluctuations in two-level systems." *Phys. Rev. A* **47** (1993), 3554–3570 (cit. on p. 32).

[146] T. van Zoest et al. "Bose-Einstein condensation in microgravity." *Science* **328** (2010), 1540 (cit. on p. 34).

[147] T. van Zoest. "Realisierung erster quantenentarteter Gase unter Schwerelosigkeit." PhD thesis. Leibniz Universität Hannover, 2008 (cit. on pp. 34, 36, 41).

[148] W. Lewoczko-Adamczyk. "Bose-Einstein Condensation in Microgravity." PhD thesis. Humboldt-Universität zu Berlin, 2008 (cit. on pp. 34, 41).

[149] M. Krutzik. "Matter wave interferometry in microgravity." PhD thesis. Humboldt-Universität zu Berlin, 2014 (cit. on pp. 34, 57, 60).

[150] J. Reichel, W. Hänsel, P. Hommelhoff, and T. Hänsch. "Applications of integrated magnetic microtraps." *Appl. Phys. B* **72** (2001), 81–89 (cit. on pp. 36, 38).

[151] W. Hänsel, P. Hommelhoff, T. W. Hänsch, and J. Reichel. “Bose–Einstein condensation on a microelectronic chip.” *Nature* **413** (2011), 498–501 (cit. on p. 36).

[152] Y. Gott, M. Ioffe, and V. Telkovskii. *Nucl. Fusion Suppl.* **3** (1962), 1045 (cit. on pp. 36, 37).

[153] D. E. Pritchard. “Cooling Neutral Atoms in a Magnetic Trap for Precision Spectroscopy.” *Phys. Rev. Lett.* **51** (1983), 1336–1339 (cit. on pp. 36, 37).

[154] E. Majorana. “Atomi orientati in campo magnetico variabile.” *Il Nuovo Cimento (1924-1942)* **9** (1932), 43–50 (cit. on p. 37).

[155] C. V. Sukumar and D. M. Brink. “Spin-flip transitions in a magnetic trap.” *Phys. Rev. A* **56** (1997), 2451–2454 (cit. on p. 37).

[156] V. S. Bagnato, G. P. Lafyatis, A. G. Martin, E. L. Raab, R. N. Ahmad-Bitar, and D. E. Pritchard. “Continuous Stopping and Trapping of Neutral Atoms.” *Phys. Rev. Lett.* **58** (1987), 2194–2197 (cit. on p. 37).

[157] J. Reichel and V. Vuletic. *Atom chips*. John Wiley & Sons, 2011 (cit. on p. 37).

[158] D. A. Steck. *Rubidium 85 D Line Data*. `https://steck.us/alkalidata/rubidium85numbers.pdf`. Accessed 19/06/20 (cit. on p. 39).

[159] D. A. Steck. *Rubidium 87 D Line Data*. `https://steck.us/alkalidata/rubidium87numbers.pdf`. Accessed 19/06/20 (cit. on pp. 39, 40, 141).

[160] J. H. Shirley. “Modulation transfer processes in optical heterodyne saturation spectroscopy.” *Opt. Lett.* **7** (1982), 537–539 (cit. on p. 38).

[161] G. Reinaudi, T. Lahaye, Z. Wang, and D. Guéry-Odelin. “Strong saturation absorption imaging of dense clouds of ultracold atoms.” *Opt. Lett.* **32** (2007), 3143–3145 (cit. on p. 40).

[162] W. D. Phillips and H. Metcalf. “Laser Deceleration of an Atomic Beam.” *Phys. Rev. Lett.* **48** (1982), 596–599 (cit. on p. 41).

[163] S. Chu, L. Hollberg, J. E. Bjorkholm, A. Cable, and A. Ashkin. “Three-dimensional viscous confinement and cooling of atoms by resonance radiation pressure.” *Phys. Rev. Lett.* **55** (1985), 48–51 (cit. on p. 41).

[164] C. Pethick and H. Smith. *Bose-Einstein condensation in dilute gases*. Cambridge University Press, 2002 (cit. on pp. 42, 43, 46).

[165] W. D. Phillips. “Nobel Lecture: Laser cooling and trapping of neutral atoms.” *Rev. Mod. Phys.* **70** (1998), 721–741 (cit. on p. 42).

[166] K. B. Davis, M.-O. Mewes, M. A. Joffe, M. R. Andrews, and W. Ketterle. “Evaporative Cooling of Sodium Atoms.” *Phys. Rev. Lett.* **74** (1995), 5202–5205 (cit. on p. 42).

[167] W. Ketterle, D. Durfee, and D. Stamper-Kurn. “Making, probing and understanding Bose- Einstein condensates.” *Proc. Int. School Phys. Enrico Fermi* **Course 140** (1999), 67–176 (cit. on pp. 43, 107, 110).

[168] Y. Castin and R. Dum. “Bose-Einstein Condensates in Time Dependent Traps.” *Phys. Rev. Lett.* **77** (1996), 5315–5319 (cit. on p. 46).

[169] Y. Kagan, E. L. Surkov, and G. V. Shlyapnikov. “Evolution of a Bose-condensed gas under variations of the confining potential.” *Phys. Rev. A* **54** (1996), R1753–R1756 (cit. on p. 46).

[170] L. Salasnich, A. Parola, and L. Reatto. “Effective wave equations for the dynamics of cigar-shaped and disk-shaped Bose condensates.” *Phys. Rev. A* **65** (2002), 043614 (cit. on pp. 46, 70).

[171] J.-N. Siemß. “Simulations of Bose-Einstein Condensate Dynamics in Optical Lattices for Large Momentum Transfer Experiments.” Master’s thesis. Leibniz Universität Hannover., 2016 (cit. on pp. 46, 47, 70).

[172] *NKT Photonics*. `https://www.nktphotonics.com/`. Accessed 19/06/26 (cit. on p. 47).

[173] F. Lienhart, S. Boussen, O. Carraz, N. Zahzam, Y. Bidel, and A. Bresson. “Compact and robust laser system for rubidium laser cooling based on the frequency doubling of a fiber bench at 1560 nm.” *Appl. Phys. B* **89** (2007), 177–180 (cit. on p. 47).

[174] R. W. P. Drever, J. L. Hall, F. V. Kowalski, J. Hough, G. M. Ford, A. J. Munley, and H. Ward. “Laser phase and frequency stabilization using an optical resonator.” *Appl. Phys. B* **31** (1983), 97–105 (cit. on p. 48).

[175] P. Brozynski. “Demonstration eines Chip-Gravimeters in QUANTUS-I.” Bachelor thesis. Leibniz Universität Hannover, 2014 (cit. on p. 52).

[176] A. Steffen, W. Alt, M. Genske, D. Meschede, C. Robens, and A. Alberti. “Note: In situ measurement of vacuum window birefringence by atomic spectroscopy.” *Rev. Sci. Instrum.* **84** (2013), 126103 (cit. on p. 54).

[177] M. Gebbe. “Determination of local gravity with an atom chip based matter wave interferometer.” Master’s thesis. Universität Bremen, 2015 (cit. on pp. 57, 74).

[178] H. Ammann and N. Christensen. “Delta Kick Cooling: A New Method for Cooling Atoms.” *Phys. Rev. Lett.* **78** (1997), 2088–2091 (cit. on pp. 57, 58).

[179] T. Aoki, T. Kato, Y. Tanami, and H. Nakamatsu. “δ-kick cooling using the Ioffe-Pritchard potential.” *Phys. Rev. A* **73** (2006), 063603 (cit. on p. 57).

[180] A. Wenzlawski. “Matter-wave optics in microgravity: Laser technology and applications.” PhD thesis. Universität Hamburg, 2013 (cit. on p. 60).

[181] D. Allan. “Statistics of atomic frequency standards.” *Proc. IEEE* **54** (1966), 221–230 (cit. on p. 63).

[182] Y. B. Ovchinnikov, J. H. Müller, M. R. Doery, E. J. D. Vredenbregt, K. Helmerson, S. L. Rolston, and W. D. Phillips. “Diffraction of a Released Bose-Einstein Condensate by a Pulsed Standing Light Wave.” *Phys. Rev. Lett.* **83** (1999), 284–287 (cit. on p. 67).

[183] X. Zhou, S. Jin, and J. Schmiedmayer. “Shortcut loading a Bose-Einstein condensate into an optical lattice.” *New J. Phys.* **20** (2018), 055005 (cit. on p. 68).

[184] B. Barrett, P. Cheiney, B. Battelier, F. Napolitano, and P. Bouyer. “Multidimensional Atom Optics and Interferometry.” *Phys. Rev. Lett.* **122** (2019), 043604 (cit. on p. 76).

[185] B. Canuel, F. Leduc, D. Holleville, A. Gauguet, J. Fils, A. Virdis, A. Clairon, N. Dimarcq, C. J. Bordé, A. Landragin, and P. Bouyer. "Six-Axis Inertial Sensor Using Cold-Atom Interferometry." *Phys. Rev. Lett.* **97** (2006), 010402 (cit. on p. 76).

[186] X. Wu, F. Zi, J. Dudley, R. J. Bilotta, P. Canoza, and H. Müller. "Multiaxis atom interferometry with a single-diode laser and a pyramidal magneto-optical trap." *Optica* **4** (2017), 1545–1551 (cit. on p. 76).

[187] L. P. Parazzoli, A. M. Hankin, and G. W. Biedermann. "Observation of Free-Space Single-Atom Matter Wave Interference." *Phys. Rev. Lett.* **109** (2012), 230401 (cit. on p. 84).

[188] J. R. Kellogg, N. Yu, J. M. Kohel, R. J. Thompson, D. C. Aveline, and L. Maleki. "Longitudinal coherence in cold atom interferometry." *J. Mod. Opt.* **54** (2007), 2533–2540 (cit. on p. 84).

[189] S. Bade, L. Djadaojee, M. Andia, P. Cladé, and S. Guellati-Khelifa. "Observation of extra photon recoil in a distorted optical field." *Phys. Rev. Lett.* **121** (2018), 073603 (cit. on p. 86).

[190] X. Zhang, R. P. del Aguila, T. Mazzoni, N. Poli, and G. M. Tino. "Trapped-atom interferometer with ultracold Sr atoms." *Phys. Rev. A* **94** (2016), 043608 (cit. on pp. 86, 94, 103).

[191] J. M. Hogan, D. M. S. Johnson, and M. A. Kasevich. "Light-pulse atom interferometry." *Proc. Int. School Phys. Enrico Fermi* **168** (2009), 411–446 (cit. on p. 86).

[192] A. Roura, W. Zeller, and W. P. Schleich. "Overcoming loss of contrast in atom interferometry due to gravity gradients." *New J. Phys.* **16** (2014), 123012 (cit. on pp. 86, 95).

[193] R. H. Parker, C. Yu, B. Estey, W. Zhong, E. Huang, and H. Müller. "Controlling the multiport nature of Bragg diffraction in atom interferometry." *Phys. Rev. A* **94** (2016), 053618 (cit. on pp. 94, 102, 119).

[194] S. P. Anokhov, R. A. Lymarenko, and A. I. Khizhnyak. "Wide-angle diffraction of the laser beam by a sharp edge." *Radiophysics and Quantum Electronics* **47** (2004), 926–932 (cit. on p. 95).

[195] N. Mielec, M. Altorio, R. Sapam, D. Horville, D. Holleville, L. A. Sidorenkov, A. Landragin, and R. Geiger. "Atom interferometry with top-hat laser beams." *Appl. Phys. Lett.* **113** (2018), 161108 (cit. on pp. 101, 119).

[196] H. Ma, Z. Liu, P. Zhou, X. Wang, Y. Ma, and X. Xu. "Generation of flat-top beam with phase-only liquid crystal spatial light modulators." *J. Opt.* **12** (2010), 045704 (cit. on p. 101).

[197] P. Hamilton, M. Jaffe, J. M. Brown, L. Maisenbacher, B. Estey, and H. Müller. "Atom Interferometry in an Optical Cavity." *Phys. Rev. Lett.* **114** (2015), 100405 (cit. on p. 101).

[198] M. Vengalattore, J. M. Higbie, S. R. Leslie, J. Guzman, L. E. Sadler, and D. M. Stamper-Kurn. "High-Resolution Magnetometry with a Spinor Bose-Einstein Condensate." *Phys. Rev. Lett.* **98** (2007), 200801 (cit. on p. 103).

[199] T. Schuldt et al. “Design of a dual species atom interferometer for space.” *Exp. Astron.* **39** (2015), 167–206 (cit. on pp. 103, 123).

[200] S. Chu, J. E. Bjorkholm, A. Ashkin, and A. Cable. “Experimental Observation of Optically Trapped Atoms.” *Phys. Rev. Lett.* **57** (1986), 314–317 (cit. on p. 104).

[201] S. Will. *From Atom Optics to Quantum Simulation*. Springer Theses, 2013 (cit. on p. 105).

[202] S. Kanthak. “An optical dipole trap for dual-species atom interferometry in microgravity.” Master’s thesis. Humboldt-Universität zu Berlin, 2018 (cit. on pp. 105–107).

[203] S. J. M. Kuppens, K. L. Corwin, K. W. Miller, T. E. Chupp, and C. E. Wieman. “Loading an optical dipole trap.” *Phys. Rev. A* **62** (2000), 013406 (cit. on p. 107).

[204] A. Szczepkowicz, L. Krzemien, A. Wojciechowski, K. Brzozowski, M. Krüger, M. Zawada, M. Witkowski, J. Zachorowski, and W. Gawlik. “Optimal geometry for efficient loading of an optical dipole trap.” *Phys. Rev. A* **79** (2009), 013408 (cit. on p. 107).

[205] D. M. Stamper-Kurn, H.-J. Miesner, A. P. Chikkatur, S. Inouye, J. Stenger, and W. Ketterle. “Reversible Formation of a Bose-Einstein Condensate.” *Phys. Rev. Lett.* **81** (1998), 2194–2197 (cit. on p. 108).

[206] M. K. Ivory, A. R. Ziltz, C. T. Fancher, A. J. Pyle, A. Sensharma, B. Chase, J. P. Field, A. Garcia, D. Jervis, and S. Aubin. “Atom chip apparatus for experiments with ultracold rubidium and potassium gases.” *Rev. Sci. Instrum.* **85** (2014), 043102 (cit. on p. 108).

[207] M. K. Ivory. “Experimental Apparatus for Quantum Pumping with a Bose-Einstein Condensate.” PhD thesis. The College of William and Mary, 2016 (cit. on p. 108).

[208] J. Wu, R. Newell, M. Hausmann, D. J. Vieira, and X. Zhao. “Loading dynamics of optical trap and parametric excitation resonances of trapped atoms.” *J. Appl. Phys.* **100** (2006), 054903 (cit. on pp. 110, 114, 115).

[209] W. Hung, P. Huang, F.-C. Wu, M. Bruvelis, H.-Y. Xiao, A. Ekers, and I. A. Yu. “Storage time of cold Rb atoms in an optical dipole trap formed by a multimode fiber laser.” *J. Opt. Soc. Am. B* **32** (2015), B32–B36 (cit. on p. 112).

[210] Y. Kagan, B. V. Svistunov, and G. V. Shlyapnikov. “Effect of Bose condensation on inelastic processes in gases.” *Sov. JETP Lett.* **42** (1985), 209 (cit. on p. 112).

[211] E. A. Burt, R. W. Ghrist, C. J. Myatt, M. J. Holland, E. A. Cornell, and C. E. Wieman. “Coherence, Correlations, and Collisions: What One Learns about Bose-Einstein Condensates from Their Decay.” *Phys. Rev. Lett.* **79** (1997), 337–340 (cit. on p. 112).

[212] S. Friebel, C. D’Andrea, J. Walz, M. Weitz, and T. W. Hänsch. “CO_2-laser optical lattice with cold rubidium atoms.” *Phys. Rev. A* **57** (1998), R20–R23 (cit. on p. 113).

[213] L. Landau and E. Lifshitz. *Mechanics (Third Edition)*. Oxford: Butterworth-Heinemann, 1976 (cit. on p. 113).

[214] N. Poli, R. J. Brecha, G. Roati, and G. Modugno. “Cooling atoms in an optical trap by selective parametric excitation.” *Phys. Rev. A* **65** (2002), 021401 (cit. on p. 114).

[215] W.-J. Xu, M.-K. Zhou, M.-M. Zhao, K. Zhang, and Z.-K. Hu. “Quantum tiltmeter with atom interferometry.” *Phys. Rev. A* **96** (2017), 063606 (cit. on p. 118).

[216] A. Trimeche et al. “Concept study and preliminary design of a cold atom interferometer for space gravity gradiometry.” *arXiv:1903.09828* (2019) (cit. on pp. 118, 123).

[217] K. Henderson, C. Ryu, C. MacCormick, and M. G. Boshier. “Experimental demonstration of painting arbitrary and dynamic potentials for Bose–Einstein condensates.” *New J. Phys.* **11** (2009), 043030 (cit. on p. 120).

[218] J. Coleman. “MAGIS-100 at Fermilab.” *arXiv:1812.00482* (2018) (cit. on p. 120).

[219] B. Canuel et al. “ELGAR – a European Laboratory for Gravitation and Atom-interferometric Research.” *arXiv:1911.03701* (2019) (cit. on p. 120).

[220] *Gravity sensing with very long baseline atom interferometry*. `https://www.geoq.uni-hannover.de/a02.html/`. Accessed 19/09/11 (cit. on p. 122).

[221] J. Hartwig, S. Abend, C. Schubert, D. Schlippert, H. Ahlers, K. Posso-Trujillo, N. Gaaloul, W. Ertmer, and E. M. Rasel. “Testing the universality of free fall with rubidium and ytterbium in a very large baseline atom interferometer.” *New J. Phys.* **17** (2015), 035011 (cit. on p. 121).

[222] M. Arndt and K. Hornberger. “Testing the limits of quantum mechanical superpositions.” *Nature Physics* **10** (2014), 271 (cit. on p. 122).

[223] S. Nimmrichter and K. Hornberger. “Macroscopicity of Mechanical Quantum Superposition States.” *Phys. Rev. Lett.* **110** (2013), 160403 (cit. on p. 122).

[224] S. Eibenberger, S. Gerlich, M. Arndt, M. Mayor, and J. Tüxen. “Matter–wave interference of particles selected from a molecular library with masses exceeding 10 000 amu.” *Phys. Chem. Chem. Phys.* **15** (2013), 14696–14700 (cit. on p. 122).

[225] B. Tapley, J. Ries, S. Bettadpur, D. Chambers, M. Cheng, F. Condi, B. Gunter, Z. Kang, P. Nagel, R. Pastor, T. Pekker, S. Poole, and F. Wang. “GGM02 – An improved Earth gravity field model from GRACE.” *Journal of Geodesy* **79** (2005), 467–478 (cit. on p. 123).

[226] *Mission GRACE: Die Vermesser der Erdgravitation*. `https://www.br.de/themen/wissen/grace-satelliten-mission-erdgravitation-gfz-dlr-nasa-100.html`. Accessed 19/12/16 (cit. on p. 123).

[227] D. N. Aguilera et al. “STE-QUEST—test of the universality of free fall using cold atom interferometry.” *Class. Quantum Grav.* **31** (2014), 115010 (cit. on p. 123).

[228] B. Altschul et al. “Quantum tests of the Einstein Equivalence Principle with the STE–QUEST space mission.” *Advances in Space Research* **55** (2015), 501 –524 (cit. on p. 123).

[229] G. M. Tino et al. “SAGE: A proposal for a space atomic gravity explorer.” *Eur. Phys. J. D.* **73** (2019), 228 (cit. on p. 123).

[230] E. Tiesinga, P. J. Mohr, D. B. Newell, and B. N. Taylor. *CODATA Recommended Values of the Fundamental Physical Constants: 2018*. `https://physics.nist.gov/cuu/Constants/index.html`. Accessed 19/09/27 (cit. on p. 141).

ACRONYMS

AOM Acousto-optical modulator

AOD Acousto-optical deflector

ARP Adiabatic rapid passage

BEC Bose-Einstein condensate

BECCAL Bose-Einstein condensate and cold atom lab

CAL Cold atom laboratory

CCD Charge-coupled device

DDS Direct-digital synthesizer

DLR Deutsches Zentrum für Luft- und Raumfahrt

DFB Distributed feedback

ESA European Space Agency

HITec Hanover Institute of Technology

IGP Ion-getter pump

IPT Ioffe-Pritchard trap

ISS International space station

JPL Jet Propulsion Laboratory

LIGO Laser interferometer gravitational-wave observatory

MIGA Matter wave-laser based Interferometer Gravitation Antenna

MAIUS Materiewelleninterferometrie unter Schwerelosigkeit

MILAS Micro-integrated laser module

MOT Magneto-optical trap

NPRO Nonplanar ring oscillator

NASA National Aeronautics and Space Administration

PM Polarization-maintaining

PBS Polarizing beam splitter

PER Polarization extinction ratio

PRIMUS Präzisionsinterferometrie mit Materiewellen unter Schwerelosigkeit

PXI PCI Extensions for Instrumentation

QUANTUS Quantengase unter Schwerelosigkeit

RF Radio frequency

rms Root mean square

RWA Rotating wave approximation

SAGE Space Atomic Gravity Explorer

SHG Second harmonic generation

SNR Signal-to-noise ratio

STE-QUEST Spacetime explorer and quantum equivalence principle space test

TA Tapered amplifier

TTL Transistor–transistor logic

UHV Ultra-high vacuum

URL Uniform resource locator

VLBAI Very large baseline atom interferometer

LIST OF CONSTANTS

Fundamental physical constants (CODATA 2018 recommended value) [230].

Symbol	Quantity	Value	Unit
c	Speed of light in vacuum	299 792 458	$\mathrm{m\,s^{-1}}$
h	Planck constant $h = 2\pi\hbar$	$6.626\,070\,15 \cdot 10^{-34}$	$\mathrm{J\,Hz^{-1}}$
e	Elementary charge	$1.602\,176\,634 \cdot 10^{-19}$	C
μ_0	Vacuum magnetic permeability	$4\pi \times 1.000\,000\,000\,55(15)$	$\mathrm{N\,A^{-2}}$
ϵ_0	Vacuum electric permittivity $1/\mu_0 c^2$	$8.854\,187\,8128(13) \times 10^{-12}$	$\mathrm{F\,m^{-1}}$
μ_B	Bohr magneton	$9.274\,010\,0783(28) \times 10^{-24}$	$\mathrm{J\,T^{-1}}$
a_B	Bohr radius	$5.291\,772\,109\,03(80) \times 10^{-11}$	m
k_B	Boltzmann constant	$1.380\,649 \times 10^{-23}$	$\mathrm{J\,K^{-1}}$
u	Atomic mass unit	$1.660\,539\,066\,60(50) \times 10^{-27}$	kg

Rubidium 87 D_2 line data [159].

Symbol	Quantity	Value	Unit
m	Atomic mass	$1.443\,160\,648(72) \times 10^{-25}$	kg
ω	Frequency	$2\pi \cdot 384.2304844685(62)$	THz
λ	Wavelength (vacuum)	780.241 209 686(13)	nm
l	Wave number	12 816.549 389 93(21)	$\mathrm{cm^{-1}}$
τ	Lifetime	26.2348(77)	ns
Γ	Natural line width (FWHM)	$2\pi \cdot 6.0666(18)$	MHz
v_rec	Recoil velocity	5.8845	$\mathrm{mm\,s^{-1}}$
ω_r	Recoil energy	$2\pi \cdot 3.7710$	kHz
T_r	Recoil temperature	361.96	nK
T_D	Doppler temperature	145.57	µK
I_sat	Saturation intensity	1.669 33(35)	$\mathrm{mW\,cm^{-2}}$

LIST OF FIGURES

LIST OF TABLES

ACKNOWLEDGMENTS

Zum Gelingen dieser Arbeit haben einige Menschen beigetragen, bei denen ich mich an dieser Stelle bedanken möchte.

Nachdem ich schon während meiner Masterarbeit einen Einblick in das QUANTUS-Projekt erhalten hatte, bekam ich die Möglichkeit, weiter als Doktorandin am ZARM in diesem spannenden Projekt zu arbeiten. Dafür möchte ich mich bei Claus Lämmerzahl bedanken, der mit viel Engagement unsere breit aufgestellte Arbeitsgruppe leitet. Ebenso danke ich dafür unserem Gruppenleiter Sven Herrmann, an den ich mich bei verschiedensten Problemen und Fragen, sei es wissenschaftlicher oder organisatorischer Art, stets wenden konnte. Der Erfolg des Projekts und das Erreichen immer weiterer Meilensteine wären ohne Ernst Rasel nicht möglich gewesen. Er hat unser Experiment und unsere Veröffentlichungen durch viele wertvolle Anstöße unterstützt. Danke auch an das DLR, welches die QUANTUS-Projekte seit Jahren finanziell fördert und begleitet.

Die hier vorgestellten Ergebnissen konnten nur durch gemeinschaftliche Arbeit im Team erreicht werden. Zusammen mit Matthias und Sven hatte ich das Glück, ein funktionierendes und robustes Experiment übernehmen zu können, welches von mehreren Doktoranden vor uns, zuletzt von Holger und Hauke, aufgebaut und weiterentwickelt wurde. Die gemeinsame Arbeit hat viel Spaß gemacht und die gegenseitige Unterstützung habe ich sehr geschätzt. Seitdem haben wir einige tolle Ergebnisse erzielt, neue Physik gemacht und gezeigt, dass QUANTUS-1 noch lange kein Museumsstück ist. Bei diversen Problemen konnten wir dabei oft auf die Erfahrung von Hauke zugreifen. Von theoretischer Seite wurden wir in letzter Zeit vor allem von Jan-Niclas aus der Gruppe von Naceur unterstützt, der mit seinen Simulationen für ein besseres Verständnis unserer Daten gesorgt hat. Auch mit den Theorie-Gruppen aus Ulm und Darmstadt konnten wir uns immer wieder austauschen. Im Rahmen seiner Masterarbeit ist Simon aus Berlin zu QUANTUS-1 gestoßen und bildet seitdem eine tolle Bereicherung für unser Team.

Mehrere Kollegen haben das ein oder andere Kapitel Korrektur gelesen und somit dazu beigetragen, einige Fehler aus dem Dokument zu entfernen. Vielen Dank dafür an Matthias, Sven A., Sven H., Merle, Hauke, Christian V., Marian, Peter und Christian S.. Die Tikz-Vorlage, mit der all die schönen Bilder und Graphen dieser Arbeit erzeugt wurden, beruht auf Sven A. und Dennis. Danke an alle Kollegen, insbesondere unserer Bremer Gruppe, aber auch der gesamten QUANTUS-Kollaboration für vielfältige gegenseitige Hilfe, dem regen Austausch von Laborutensilien und interessanten Diskussionen. Genauso wichtig und bereichernd waren aber auch die Zeiten außerhalb der Arbeit, sei es nach Feierabend oder auf diversen Konferenzen und Meetings.

Schließlich möchte ich mich bei meiner Familie, meinen Eltern Marlies und Reinhold sowie meinem Bruder Christian, für ihren Rückhalt und ihre Unterstützung bedanken. Ebenso dankbar bin ich meinem Freund Basi, der während der letzten Jahre immer für mich da war.